

1



D4.4 - REPORT ON THE AERODYNAMIC AND ACOUSTIC ASSESSMENT OF LOW NOISE SLATS AND SLAT TRACKS IN THE F2 WIND TUNNEL

Document author	Éric MANOHA (ONERA)
Document contributors	
ONERA	Renaud DAVY, Thomas LE GARREC, Marc TERRACOL
DLR	Michael POTT-POLLENSKE, Malav SONI, Roland EWERT
Dassault-Aviation	Vincent FLEURY, Jean-Max HASHOLDER
UoB - University of Bristol	Mahdi AZARPEYVAND, Hasan Kamliya JAWAHAR
NLR	Johan KOK, Evelyn VAN BOKHORST, Marthjin TUINSTRA
TCD - Trinity College Dublin	Gareth BENNETT
RWTH - Aachen University	Sutharsan SATCUNANATHAN, Matthias MEINKE
TUD – Technical University Delft	Daniele RAGNI, Francesco AVALLONE

Abstract

This deliverable D4.4 covers activities in Task 4.3 "*Aerodynamic & acoustic assessment of low noise slats and slat tracks integrated on a F16 model*", dedicated to the integration, measurements and numerical simulation of slats porous inserts and generic / low noise slat tracks on the 3-element high-lift airfoil F16 model with a 30° sweep angle installed in ONERA's F2 aerodynamic WT. Note that these tests have been specified in Deliverable D2.7. The present report follows the organization of task 4.3.

Section 3 reports on the Subtask ST4.3.1 which was devoted to (i) the design/manufacture of new elements of the F16 model required for these tests, namely a new slat system with modular inboard/outboard slat side-edges, (ii) the selection of the tested porous slat inserts and slat tracks to be selected from the preliminary tests in AAWT@UBRI (Task 4.1) and AWT@NLR (Task 4.2) and (iii) the definition of the model instrumentation (static pressure taps and Kulite sensors), the flow conditions, and the acoustic (120-microphone array) and aerodynamic (LDV, PIV) instrumentation to be used in ONERA's F2 WT.

Section 4 reports on the Subtask ST4.3.2 which was devoted to the achievement and analysis of the aeroacoustic and aerodynamic measurements in the F2 wind tunnel of the selected low-noise devices installed on the F16 model.

Section 5 reports on the Subtask ST4.3.3 which was devoted to CFD/CAA computations of selected tested configurations of slat tracks achieved by DAV, ONERA, NLR and DLR with the objective to recover the trends observed in the experiments, with and without generic and low noise slat tracks, thus assess the noise reduction potential of the best and low-noise slat track concepts.


Finally, Section 6 reports on the Subtask ST4.1.6, part of Task T4.1 "Preliminary assessment of slat noise reduction by innovative materials". Subtask ST4.1.6 was devoted to numerical simulations, achieved by RWTH, of the slat porous inserts installed on the flapless (VALIANT-like) configuration of the F16 model with 0° sweep, as it was tested in the acoustic windtunnel of the University of Bristol. Note that these computations should have been reported in the deliverable D4.1 "Parametric study on slat noise reduction and selection of best NRTs based on porous treatments".

Keywords

Slat track noise, Slat noise, Porous materials, High lift wing, Aeroacoustic measurements, CFD-CAA computations

1 Information Table

Project information	
PROJECT ID	860538
PROJECT FULL TITLE	INnoVative dEsign of iNstalled airframe componenTs for aircraft nOise Reduction
PROJECT ACRONYM	INVENTOR
FUNDING SCHEME	RIA -Research and Innovation Action
START DATE OF THE PROJECT	01-05-2020
DURATION	54 months
CALL IDENTIFIER	H2020-MG-2018-2019-2020

Deliverable information	
DELIVERABLE No AND TITLE	D4.4 - REPORT ON THE AERODYNAMIC AND ACOUSTIC ASSESSMENT OF LOW NOISE SLATS AND SLAT TRACKS IN THE F2 WIND TUNNEL
TYPE OF DELIVERABLE (1)	R (Report)
DISSEMINATION LEVEL (2)	PU (Public)
BENEFICIARY NUMBER AND NAME	1-Onera, 3-DaV, 5-DLR, 8-TCD, 9-NLR, 10-RWTH, 13-UoB, 14-TUD
AUTHOR	Éric MANOHA (ONERA)
CONTRIBUTORS	See front page
WORK PACKAGE No	WP4
WORK PACKAGE LEADER WP LEADER VALIDATION DATE	Michael Pott-Pollenske, DLR, 25.07.2024
COORDINATOR VALIDATION DATE	Eric MANOHA, ONERA 25.07.2024
Coordinator signature	 E. MANOHA

· Use one of the following codes: R=Document, report (excluding the periodic and final reports)
 DEM=Demonstrator, pilot, prototype, plan designs
 DEC=Websites, patents filing, press & media actions, videos, etc.
 OTHER=Software, technical diagram, etc.
 · Use one of the following codes: PU=Public, fully open, e.g. web
 CO=Confidential, restricted under conditions set out in Model Grant Agreement
 CI=Classified, information as referred to in Commission Decision 2001/844/EC.

2 Table of Contents

1	Information Table	3
2	Table of Contents	4
3	Introduction, context and objectives.....	8
3.1	INVENTOR objectives	8
3.2	Objectives of Task T4.3	8
3.2.1	Experimental	8
3.2.2	Numerical	8
3.3	The LEISA2/SWAHILI/HiLiNo context	9
3.3.1	Introduction	9
3.3.2	F2-windtunnel	9
3.3.3	F16 model.....	10
3.3.4	The LEISA2 aerodynamic program	11
3.3.5	The SWAHILI aerodynamic program.....	13
3.3.6	LEISA2/SWAHILI acoustic outcomes.....	14
3.3.7	The HiLiNo program.....	14
3.4	Down selection of slat porous inserts and slat tracks in INVENTOR.....	15
3.4.1	Introduction	15
3.4.2	Down selection of slat porous inserts in AAWT@UoB	16
3.4.3	Down selection of low noise slat tracks at AWT@NLR	18
4	INVENTOR's tests in F2	20
4.1	Test set-up	20
4.1.1	Introduction	20
4.1.2	F16 model section.....	20
4.1.3	Implementation in the F2 windtunnel: from 0° to 30° sweep.....	21
4.1.4	Note on the 2.5D continuous slat system and brackets.....	22
4.1.5	Note on the SWAHILI flap system (not used in INVENTOR).....	23
4.1.6	Model on-board instrumentation	23
4.1.6.1	Static pressure taps.....	23
4.1.6.2	Kulite unsteady pressure sensors.....	25
4.1.7	New slat system with slat side-edges on the F16 model	25
4.1.7.1	Objectives	25
4.1.7.2	Inboard slat side edge	25
4.1.7.3	Outboard slat side edge case	25
4.1.7.4	Static pressure taps on slat	27
4.1.7.5	Retracted slat elements	27
4.1.7.6	Proximity between a slat bracket (suction side) and a slat track (pressure side).27	

4.1.8	Model arm fairings.....	28
4.1.9	Flow conditions.....	30
4.1.9.1	Model incidences.....	30
4.1.9.2	Wind velocities.....	30
4.1.10	Microphone array.....	30
4.1.11	Slat tracks.....	31
4.1.11.1	Slat tracks designs	31
4.1.11.2	Slat tracks implementation	33
4.1.12	Slat porous inserts	33
4.1.12.1	Synthesis of tested porous inserts.....	33
4.1.12.2	Adjustment of central slat elements "J" and "N".....	35
4.1.13	Combination of slat track / slat side edges and slat porous insert.....	36
4.2	Model deformation under aerodynamic loads.....	36
4.3	Wall pressure measurements.....	37
4.3.1	Introduction and test matrix	37
4.3.2	Wall static pressure measurements	38
4.3.3	Wall unsteady pressure measurements	39
4.3.3.1	Influence of slat track.....	39
4.3.3.2	Influence of slat porous insert.....	40
4.4	Acoustic measurement.....	42
4.4.1	Introduction and test matrix	42
4.4.2	Signal processing description	42
4.4.3	Slat track noise detection with the continuous slat.....	43
4.4.4	Acoustic ranking of slat track designs with the continuous slat.....	44
4.4.5	Slat side edge noise analysis (no slat track)	46
4.4.6	Influence of the slat side edge on slat track noise.....	48
4.4.7	Slat porous inserts acoustic analysis	52
4.4.7.1	F2 results	52
4.4.7.2	Additional tests in AWB.....	55
4.4.8	Slat track noise mitigation using slat porous inserts	56
4.4.9	Comparison with numerical simulations	56
4.5	Aerodynamic measurements using PIV.....	57
4.5.1	PIV set-up.....	57
4.5.2	Velocity maps calibration	58
4.5.3	Typical flow field explorations	59
4.5.4	Axis frameworks of the final PIV database	61
4.5.4.1	"2D" maps.....	61
4.5.4.2	"3D" maps.....	61

4.5.5	Early comparison PIV/CFDdatabase.....	62
4.5.6	Using PIV for flow analysis	63
4.6	Aerodynamic measurements using LDV2D	64
4.6.1	Set-up	64
4.6.2	LDV2D geometrical calibration	65
4.6.3	LDV2D framework axis.....	65
4.6.3.1	Coordinates	65
4.6.3.2	Velocity components.....	66
4.6.4	LDV2D test matrix	66
4.6.5	Selection of LDV2D results and comparison with PIV.....	68
4.6.5.1	Continuous (2.5D) slat without slat track.....	68
4.6.5.2	Continuous (2.5D) slat with slat tracks #1 and #2	68
5	Slat tracks flow/noise numerical simulations.....	70
5.1	Context and objectives	70
5.2	Numerical simulations by Dassault-Aviation	70
5.2.1	Objectives.....	70
5.2.2	Geometry.....	70
5.2.3	Numerical strategy.....	71
5.2.4	Results	72
5.2.4.1	Mean aerodynamic data.....	72
5.2.4.2	Fluctuations of velocity	75
5.2.4.3	Fluctuations of pressure.....	81
5.2.4.4	Acoustics via virtual beamforming.....	82
5.2.4.5	Additional acoustic analysis	84
5.3	Numerical simulations by ONERA.....	89
5.3.1	Context and objectives.....	89
5.3.2	Configuration and computational grid	90
5.3.3	Numerical strategy.....	91
5.3.4	Physical analysis of the flow	92
5.3.4.1	No-track configuration	92
5.3.4.2	Track #2 configuration	93
5.3.5	Mean flow statistics.....	95
5.3.5.1	No-track configuration	95
5.3.5.2	Track #2 configuration	97
5.3.6	Wall pressure power spectral densities	100
5.3.7	Acoustics	101
5.3.7.1	Local noise source.....	101
5.3.7.2	Farfield noise using a Ffowcs Williams-Hawkings solver	101

5.3.7.3	Virtual beamforming.....	102
5.4	Numerical simulations by NLR	105
5.4.1	Context and objectives.....	105
5.4.2	Geometry and flow conditions.....	105
5.4.3	Grid set-up.....	105
5.4.4	Steady RANS result.....	106
5.4.5	Hybrid RANS–LES set-up	106
5.4.6	Validation with PIV measurements	108
5.4.7	Validation with Kulite data	113
5.4.8	Far-field noise computation and virtual beamforming	115
5.5	Numerical simulations by DLR	117
5.5.1	Introduction	117
5.5.2	Numerical strategy and settings	118
5.5.3	Adding sweep and slat-track.....	119
5.5.3.1	F16 without and with sweep.....	119
5.5.3.2	F16 without and with slat-track	120
5.5.4	Active noise control.....	123
5.5.4.1	Concept.....	123
5.5.4.2	Variants.....	123
5.5.5	Passive noise control.....	125
5.5.6	Conclusions	126
5.5.7	Outlook.....	127
5.5.8	Acknowledgements.....	127
5.6	Cross comparisons of computed and measured noise spectra.....	127
5.6.1	Introduction	127
5.6.2	Cross-comparisons of computations of the baseline case (no slat track)	128
5.6.3	Cross-comparisons of computations with the slat track ST#2.....	128
6	Low noise slats numerical simulations by RWTH	130
6.1	Context	130
6.2	Objectives	130
6.3	Incidence adjustment	130
6.4	Flow field results	131
6.5	Acoustic Field Results	132
6.6	Summary.....	135
7	Acknowledgments.....	136
8	References.....	136

3 Introduction, context and objectives

3.1 INVENTOR objectives

The INVENTOR project aims at

- better understanding the physics of airframe noise generated by landing gear and high lift devices,
- assessing innovative technologies to mitigate airframe noise, through experiments and computations.

The technical work of the project is split in Workpackage 3 (landing gears), Workpackage 4 (high lift devices) and Workpackage 5 (assessment at aircraft level). It starts with Workpackage 2, where the specifications for WP3, 4 and 5 are described.

The present report, Deliverable D4.4, details activities in Task 4.3 "Aerodynamic & acoustic assessment of low noise slats and slat tracks integrated on a F16 model", dedicated to the integration, measurements and numerical simulation of slats porous inserts and generic / low noise slat tracks on the 3-element high-lift airfoil F16 model with a 30° sweep angle installed in ONERA's F2 aerodynamic WT.

3.2 Objectives of Task T4.3

3.2.1 Experimental

The first objective of Task 4.3 (Subtasks 4.3.1 and 4.3.2) is to achieve and analyze experimental activities based on testing low noise slat tracks and slat porous inserts on the 3-element high-lift airfoil F16 model with a 30° sweep angle in ONERA's F2 aerodynamic windtunnel.

The objective of the tests in F2 is to characterize the steady/unsteady flow and radiated noise generated by a range of low noise slat tracks and slat porous inserts, and the combination of both. Aerodynamic measurements included wall static pressure probes, PIV and LDV, whereas acoustic measurements involved Kulite wall pressure sensors installed on the model and a microphone array implemented in the windtunnel ceiling.

This aerodynamic/acoustic characterization covered three aspects:

- (i) to acoustically assess the best noise reduction designs/technologies for slat and slat tracks,
- (ii) to provide experimental validation to numerical simulations and,
- (iii) to tentatively improve our knowledge on the physics of noise generation by the slat system of high lift wings of transport and business aircraft.

3.2.2 Numerical

The second objective of Task 4.3 (Subtask 4.3.3) was to achieve CFD/CAA computations of selected tested configurations of the baseline configuration and several slat tracks configurations. The objectives are:

- to recover the trends observed in the experiments,
- to globally validate of the CFD/CAA solvers,
- to help understanding the physical mechanisms of noise generation,
- to assess the noise reduction potential of the best low-noise slat track concepts.

The last section of the present deliverable reports on the Subtask ST4.1.6, part of Task T4.1 "Preliminary assessment of slat noise reduction by innovative materials". Subtask ST4.1.6 was devoted to numerical simulations, achieved by RWTH, of the slat porous inserts installed on the flapless (VALIANT-like) configuration of the F16 model with 0° sweep, as it was tested in the acoustic windtunnel of the University of Bristol. Note that these computations should have been reported in the deliverable D4.1 "Parametric study on slat noise reduction and selection of best NRTs based on porous treatments".



3.3 The LEISA2/SWAHILI/HiLiNo context

3.3.1 Introduction

The model set-up in F2 for INVENTOR has been already used in former ONERA-DLR cooperations named LEISA2, SWAHILI and HiLiNo based on tests of the same F16 model in F2@ONERA, AWB@DLR and NWB@DNW. Therefore, the present report starts with a summary of these activities, focusing on the experimental capabilities of the F2 windtunnel with this F16 model.

LEISA2 (Silent Take-Off and Landing, 2010-2013) [1], SWAHILI (SWept Airfoil with HIgh Lift, 2014-2017) [2] and HiLiNo (High lift Noise, 2019-2023) [3] are Common Research Projects (CRP), in which ONERA and DLR have built experimental databases for the validation of CFD/CAA codes applied to the simulation of the unsteady flow and noise generation from a high-lift profile with deployed slat and flap. Both projects relied on DLR's model F16, a two-dimensional airfoil (constant section in the span direction), with a clean (retracted) chord equal to 300 mm and an (original) span of 800 mm. In the LEISA2 project, a first database has been constructed with the F16 model tested without sweep angle, or with its trailing edge perpendicular to the windtunnel flow. Then, in the SWAHILI project, the same model has been tested with a sweep angle of 30°.

During the course of the SWAHILI project, Dassault-Aviation has partnered with ONERA and DLR, contributing to the project with two additional configurations of flap side-edge, with the same aerodynamic and acoustic experimental approach.

In both LEISA2 and SWAHILI projects, the model has been tested in F2, an aerodynamic, closed section wind tunnel located in ONERA-Le Fauga, with intensive aerodynamic measurements, including wall pressure steady/unsteady sensors, optical devices such as PIV and steady/unsteady LDV and a hot wire probe. Acoustic measurements were also achieved with a wall 120-microphone array mounted in the windtunnel ceiling.

In the LEISA2 project, the un-swept model has been also tested in AWB, an anechoic open-jet windtunnel located in DLR-Braunschweig for acoustic data acquisition. In the SWAHILI context, similar tests have been achieved in AWB with the swept model.

Since 2014, the LEISA2 database has been included by NASA and AIAA in the Benchmark for Airframe Noise Computations (BANC). The SWAHILI database has been also presented in 2016 as a potential candidate for inclusion in the BANC (Benchmark for Airframe Noise Computations) activities.

3.3.2 F2-windtunnel

The F2 wind tunnel circuit is presented in Figure 1. F2 is an atmospheric subsonic continuous flow wind tunnel located at ONERA-Le Fauga near Toulouse. The rectangular test section is 1.8 m high, 1.4 m wide and 5 m long. The side walls of the test section are parallel, made up of removable opaque or transparent panels are adapted according to the requirements of each test.

The test section is at atmospheric pressure. This pressure level is regulated with a chimney starting at the beginning of the first diffuser and going outside the building.

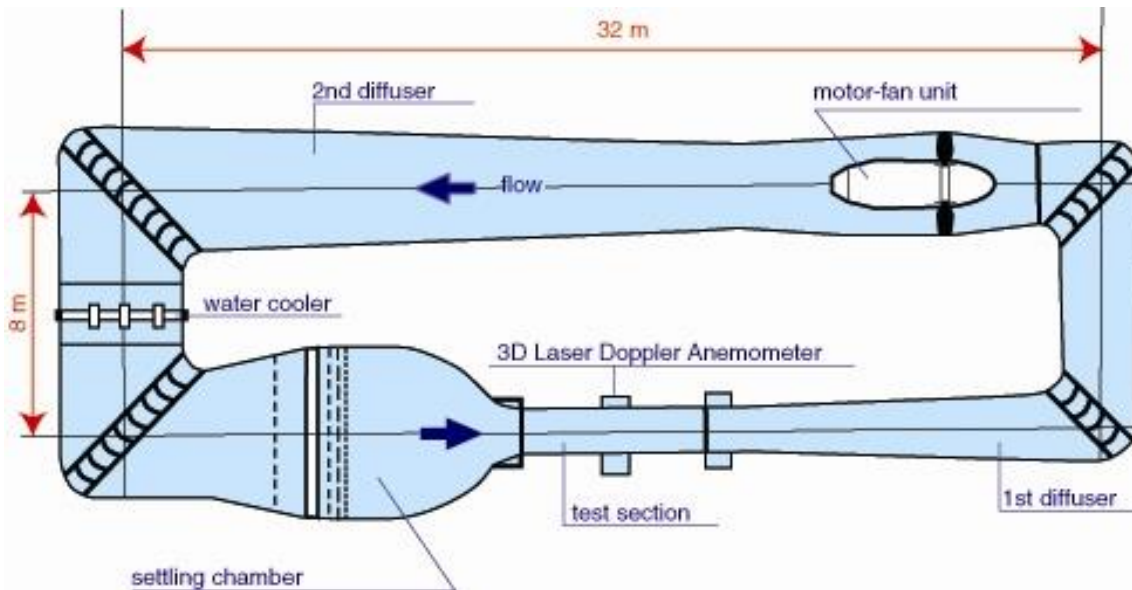


Figure 1: Drawing of F2 wind tunnel

The windtunnel has been specifically designed for efficient use of optical aerodynamic measurement devices such as LDV and PIV. For this purpose, the whole test section is circled with a massive frame supporting optical instrumentation (emission and reception) that can be moved in three directions with high precision and efficiency. Indeed, the measured spot (a single point for LDV, or a 2D planar image for PIV) can be moved rapidly from a position to another without modifying the optical adjustment.

Although the windtunnel test section is noisy and reverberant, it is possible to achieve acoustic measurements of localized noise sources using a 120-microphone array implemented in the WT ceiling beneath a wiremesh cloth. The acoustic sources over the model are identified by a beamforming technique and their acoustic level is obtained by a dedicated deconvolution process (DAMAS).

3.3.3 F16 model

The cross section of DLR's F16 model is an Airbus design denoted FNG. This 2D airfoil is derived from a 3D section (at a normalized span 0.511) of a swept wing (sweep angle 30°) coming from a single-aisle short- and medium-range aircraft (Figure 2). The cruise wing has been designed by Airbus and the high lift elements were designed by DLR. The transformation from the 3D section to the 2D airfoil assumes that the distribution of lift and drag coefficients remains constant, while levels may change. The "clean" (flap/slat retracted) chord of the F16 airfoil is 300 mm. Figure 3 shows the F16 airfoil in configurations with deployed/retracted slat and flap (top) and a view of an unsteady flow computation via LES (bottom).

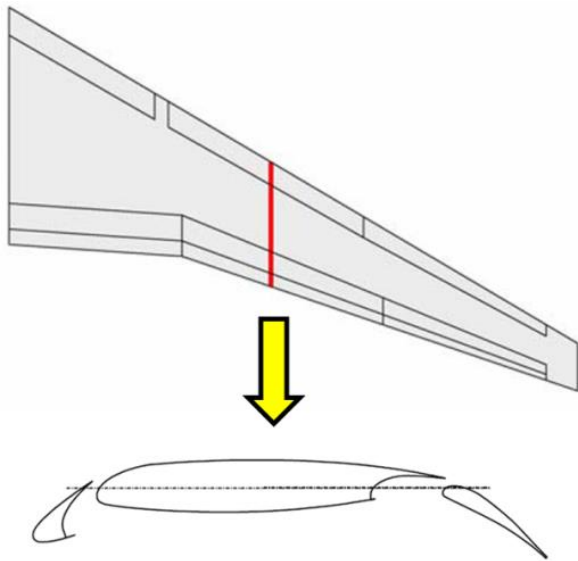


Figure 2: Derivation of the FNG design from a 3D Airbus wing

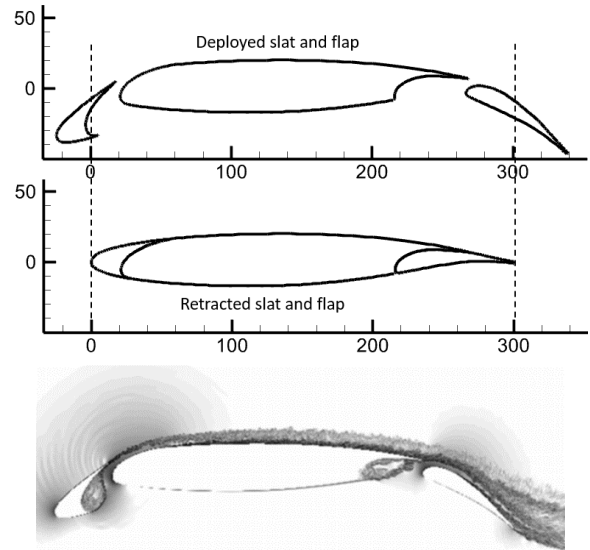


Figure 3: F16 model section. Top: configurations with deployed/retracted slat and flap. Bottom: unsteady flow (LES).

3.3.4 The LEISA2 aerodynamic program

The F16 model was originally designed for tests with 0° sweep in AWB@DLR, with a span of 800 mm. In the LEISA2 program [1], the F16 model was mounted between the parallel glass walls of F2 with a 0° sweep angle, thanks to two model extensions of span 0.3 m designed and manufactured by DLR (Figure 4). New slat brackets were designed and manufactured to attach the slat from the suction side to maximize the optical access in the slat cove (Figure 3, bottom). The global incidence of the model can be adjusted continuously. A 120-microphone array was installed beneath a wiremesh at the ceiling of the test section.

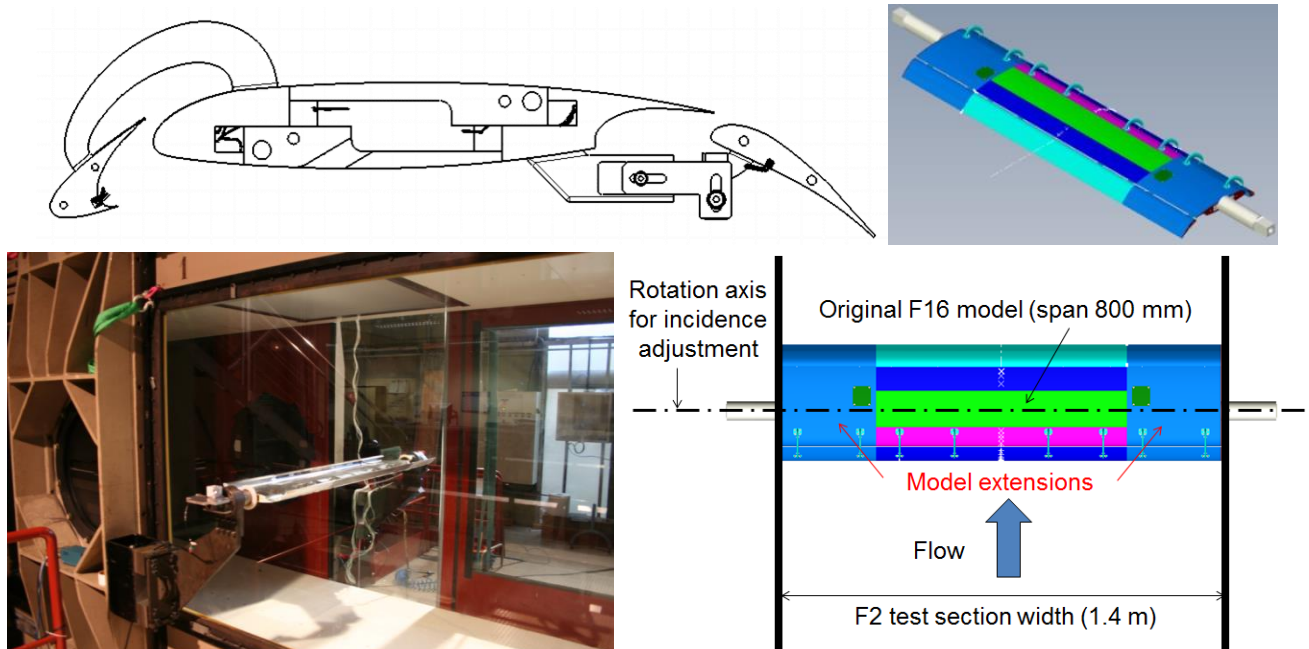


Figure 4: Top left: F16 model CAD section with slat and flap bracket (bottom). Top right: model with span extensions and rotation axis for incidence adjustment. Bottom: model in F2 with a 0° sweep angle and microphone array beneath Kevlar at the WT ceiling;

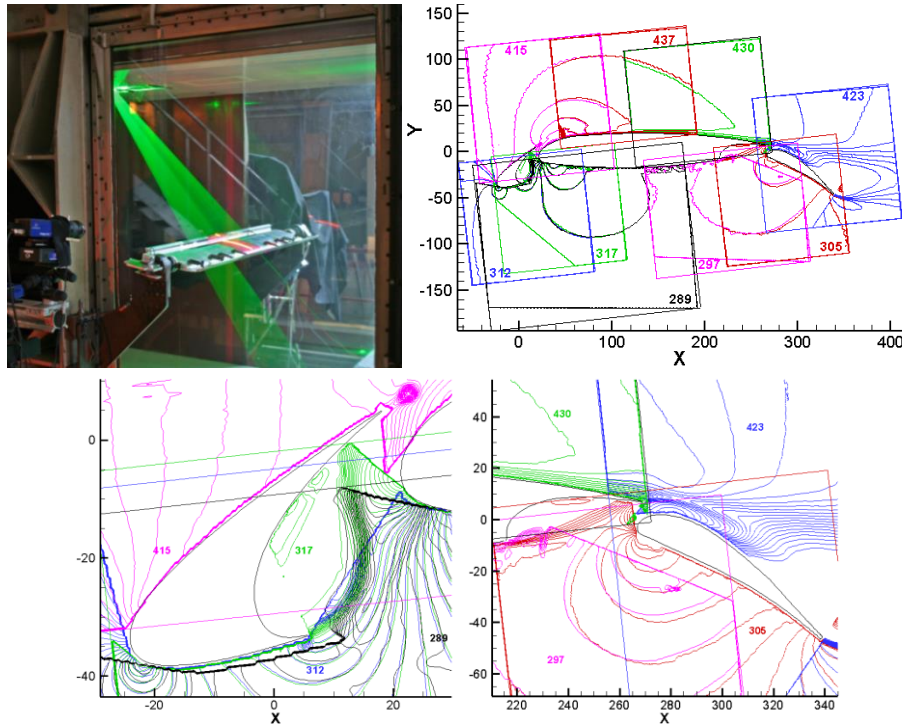


Figure 5: LEISA2 PIV-3C set-up and examples of mean velocity maps

Extensive PIV and LDV measurements were achieved at a reference windtunnel flow velocity of 61.5 m/s and a model angle of attack of 6.15°. Figure 5 shows an example of PIC-3C set-up with the laser sheet emitted from the ceiling, and several assemblies of mean velocity maps. Figure 6 shows an example of LDV-2D set-up, with the location of measurements points in slat cove and comparison with PIV on traverse 11107-2 which crosses the slat shear layer.

Note that, in the same program, the F16 model has been also tested in the open-jet acoustic windtunnel AWB at DLR-BS, with its original span of 0.8 m.

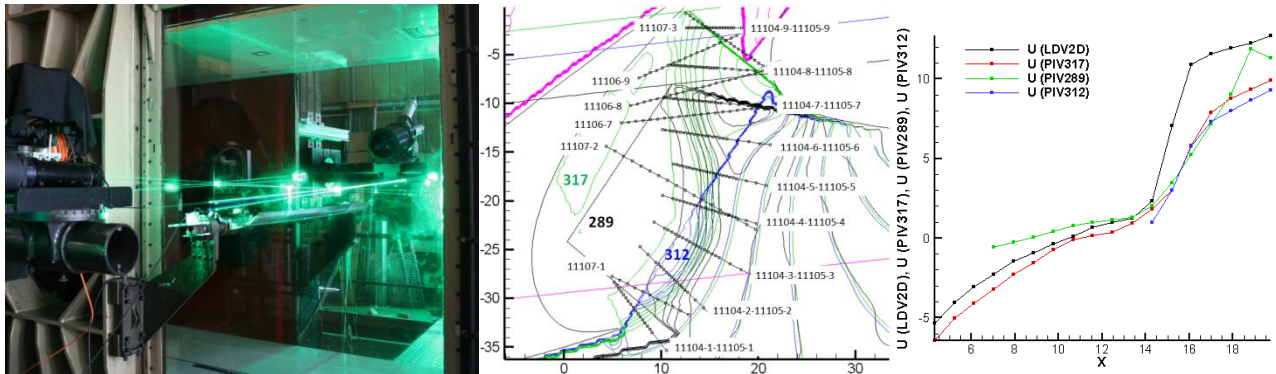


Figure 6: LEISA2 LDV2D set-up, location of measurements in slat cove and comparison with PIV on traverse 11107-2

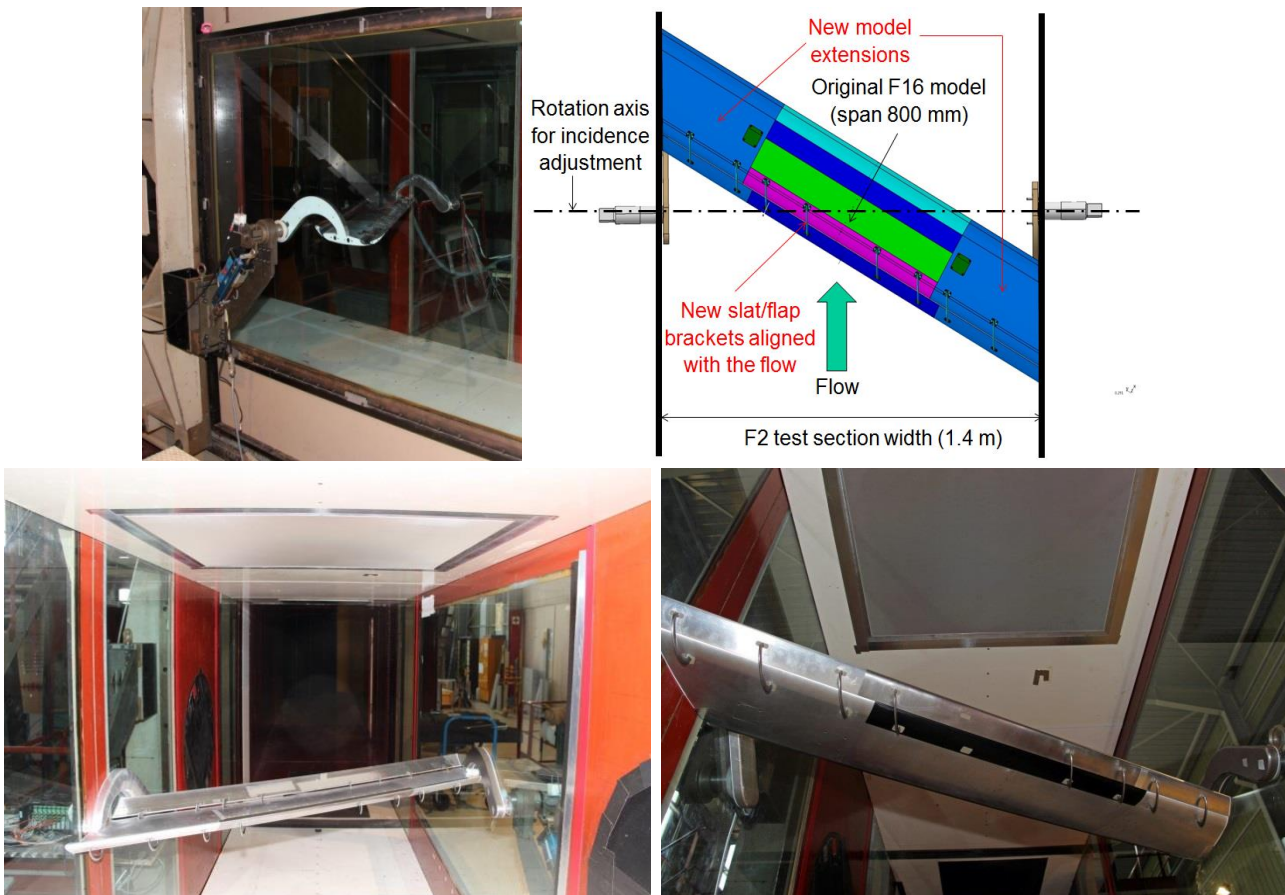


Figure 7: Model in F2 with a 30° sweep angle, slat and flap brackets aligned with the flow
Microphone array beneath Kevlar at the WT ceiling

3.3.5 The SWAHILI aerodynamic program

SWAHILI [2] is a continuation of LEISA2 aiming at investigating the influence of:

- a 30° sweep angle and
- several flap side-edge configurations proposed by Dassault-Aviation,

on the steady/unsteady flow and generated noise. For this purpose, the same F16 model was rotated by 30° and new model extensions and slat/flap bracket aligned with the flow were designed and manufactured by DLR (Figure 7).

For fair acoustic comparisons, a special care was taken to ensure that, for both sweep angle cases 0° and 30°, the same model element of given span provide the same lift. This led to adjust the global reference model incidence to 5.3° and the windtunnel flow velocity was set to $61.5/\cos(30^\circ)$ or 71 m/s.

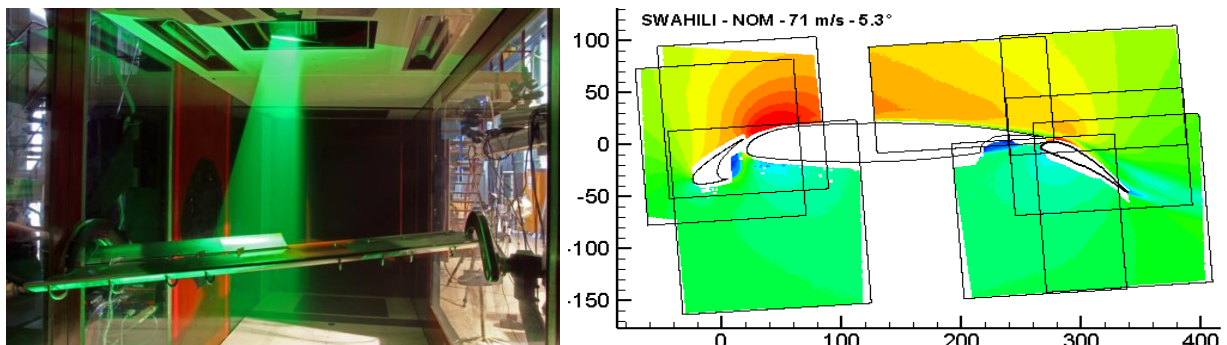


Figure 8: SWAHILI PIV set-up with the model in flap side-edge configuration
Mean velocity map in a plane parallel to the airfoil section

A full program of aerodynamic measurements based on PIV has been achieved. For easier comparison with the unswept configuration LEISA2, measurements were achieved in planes oriented along the airfoil section at 30° from the flow direction. Figure 8 shows the PIV set-up and mean flow maps.

A survey of the local 3D flow in the vicinity of the flap side-edge was also obtained using 2 normal vertical planes (Figure 9).

LDV was also used for

- mean velocity measurements along the same location as for the unswept airfoil, and
- unsteady velocity flow measurements at a limited number of locations.

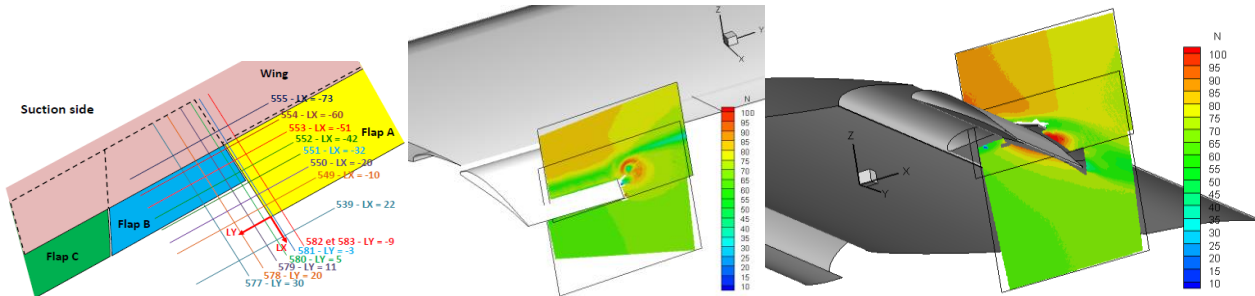


Figure 9: survey of the local 3D flow in the vicinity of the flap side-edge with PIV in 2 normal vertical planes.

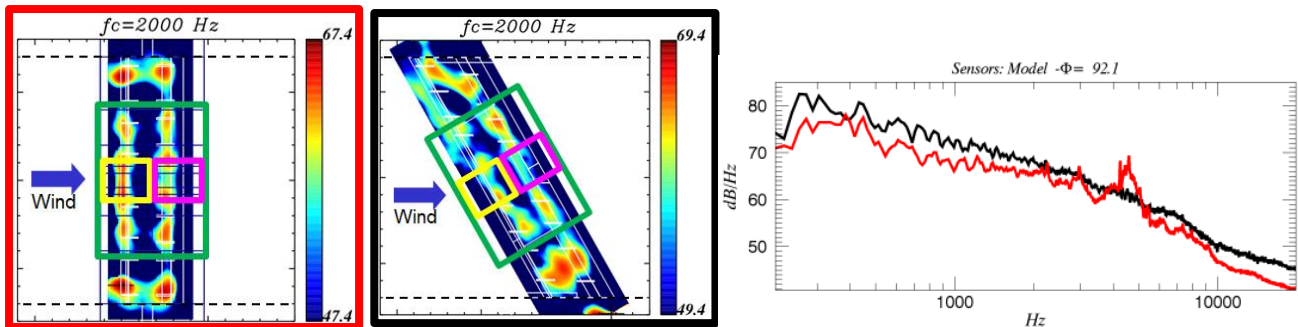


Figure 10: Left: noise maps (DAMAS) over the unswept and swept models. Right: noise spectra from the integration of the noise maps

3.3.6 LEISA2/SWAHILI acoustic outcomes

Finally, the 120-microphone array installed at the windtunnel ceiling was used to compute DAMAS noise maps of the 0° sweep case at incidence 6.15° and flow velocity 61.5 m/s (LEISA2) and the 30° sweep case at incidence 5.3° and flow velocity 71 m/s (SWAHILI) (Figure 10, right). Noise spectra were computed from the integration of these noise maps, showing that the 30° sweep angle is globally mmoier than the 0° sweep angle.

3.3.7 The HiLiNo program

In the SWAHILI program, the F16 model was tentatively tested with the 30° sweep in DLR's AWB facility, an anechoic open-jet windtunnel with a test section of 1.2×0.8 m. Unfortunately, the combination of a (required) large incidence angle and the sweep angle generated a significant blockage effect with strong 3D aerodynamic effects. Consequently, the mean flow was much degraded. Even though these issues could be solved by improvements of the setup, the subsequent second test was too short to achieve a meaningful database over a range of angles of attack and flow speeds respectively.

In order to get reliable acoustic data, in a continuing project named HiLiNo (High Lift Noise) [3], DLR had the opportunity to test the F16 model in the LEISA2 (0° sweep) and SWAHILI (30° sweep) configurations in the larger open jet acoustic facility NWB (Figure 11, left), which section is 2.8×3.2 m, ensuring much better aerodynamic condition. ONERA and DLR both achieved analysis of microphone array measurements and comparison with similar data from F2. Figure 11 (right) shows

a first comparison (with excellent agreement) by DLR, of spectra integrated in the slat area, from noise maps measured in F2 (SWAHILI) and NWB (HiLiNo) with the F16 model and 30° sweep. The same comparison from the same measurements led by ONERA provided spectra from F2 about 4 dB higher than those from NWB, a difference that is still under investigation. Note that these new measurements will also be an opportunity to confirm the acoustic influence of the sweep angle, already evaluated from F2 data in LEISA2/SWAHILI (Figure 10, right).

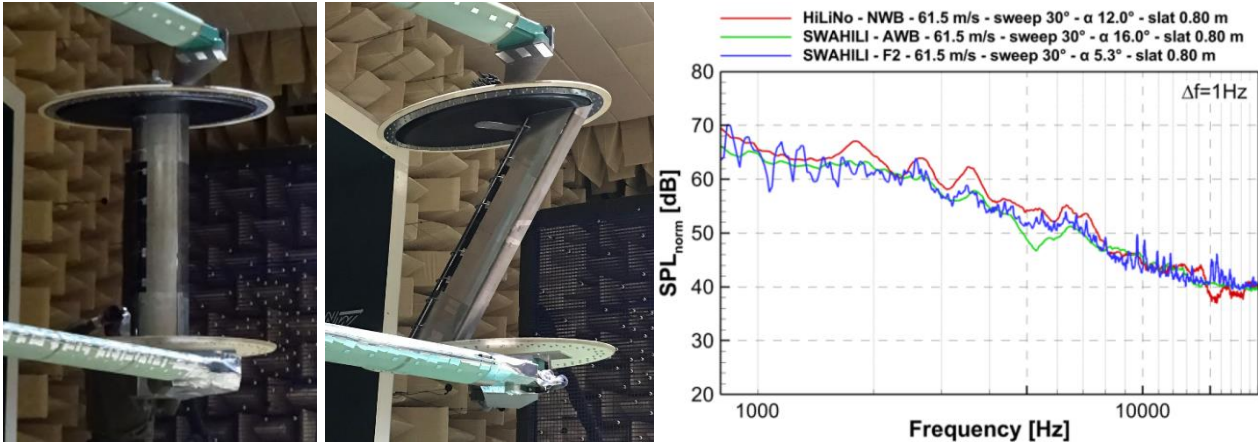


Figure 11: HiLiNo test of the F16 model in NWB. Left: test set-ups. Right: comparison of spectra integrated in the slat area, from noise maps measured in F2 (SWAHILI) and NWB (HiLiNo) with the F16 model and 30° sweep [3].

3.4 Down selection of slat porous inserts and slat tracks in INVENTOR

3.4.1 Introduction

In the INVENTOR workflow, the F2 test campaign is a continuation of two former preliminary experimental acoustic assessments achieved on the same model derived from the F16:

- the first one was achieved with a 0° sweep angle on various slat porous inserts in the aeroacoustic wind tunnel AAWT facility at University of Bristol (specifications described in D2.5 [4], experiment described and analyzed in D4.1 [5]) and
- the second one was achieved with a 30° sweep angle on several generic and low-noise slat tracks in the aeroacoustic wind tunnel AWT in NLR (specifications described in D2.3 [6], experiment described and analyzed in D4.2 [7]).

Both windtunnels AWT@NLR and AAWT@UoB are laboratory open jet facilities, and the experience at AWB@DLR has shown that a high lift wing might considerably deviate the wind tunnel open jet, leading to highly degraded aerodynamic conditions. Following the same approach as for tests of this airfoil in such a small open-jet facility at ECL (Ecole Centrale de Lyon) in the FP6 project VALIANT, a flapless version of the F16 has been designed by ONERA, with the objective of correctly reproducing the mean/unsteady flow in the slat region while considerably decreasing the total lift of the model. This was obtained by keeping unchanged the leading edge (in pink on Figure 12) and central (in green) elements of the F16 model and replacing the trailing edge element (in blue) by a new optimized element (in red line). Note that, in VALIANT, this optimization was achieved for tests with 0° sweep angle, so in INVENTOR the process had to be repeated accounting for the 30° sweep.

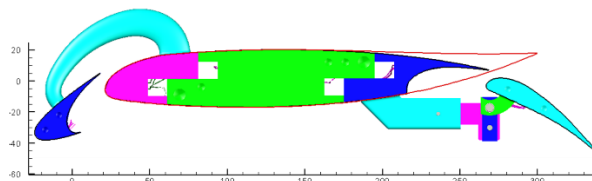


Figure 12: Cross section of original F16 model and designed flapless configuration shown in red

Experiments in AWT and AAWT aimed at checking and ranking at reduced cost the noise performances of a large range of slat tracks and slat porous inserts in a view to select the best ones for more detailed aerodynamic/acoustic measurements in F2.

3.4.2 Down selection of slat porous inserts in AAWT@UoB

INVENTOR focusses on reducing the noise generated by the slat, using porous surface materials installed in inserts at the slat pressure side in the slat cove. Several porous materials based on polyurethane foam and diamond lattice structures were designed and manufactured, mainly using 3D printing (Figure 13). The global goal is to experimentally assess the slat noise mitigation brought by such porous inserts, to better understand the mechanism of this noise mitigation, and improve our ability to numerically predict this physics. Moreover, these measurements will be used to validate models of such surface porous materials implemented in CFD/CAA solvers.

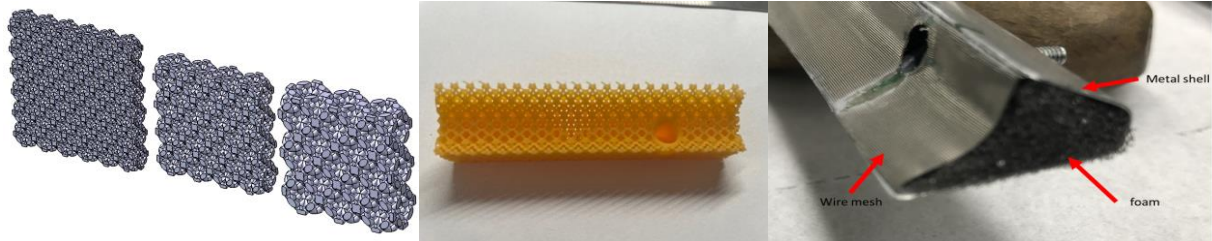


Figure 13: Porous materials to be tested as inserts at the slat pressure side (diamond lattice and polyurethane foam)

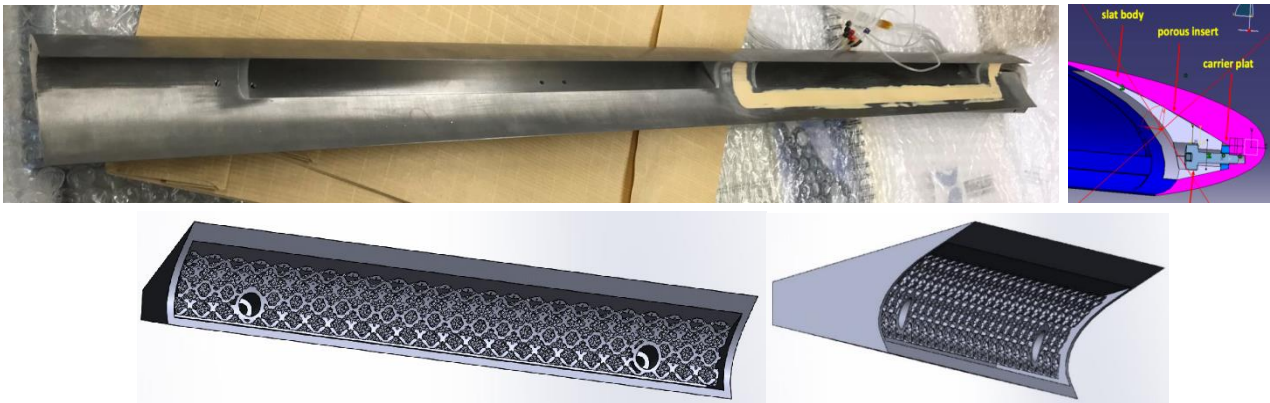


Figure 14: implementation of porous inserts at the F16 slat pressure side at the bottom of the slat cavity: two inserts are available on the 800 mm span slat element "J".

Preliminary experimental activities have been achieved in Task 4.1, including:

- Characterization of porous material planar samples in the WAABLIEF facility at VKI.
- Experimental assessment of several porous inserts (Figure 14) installed at the slat pressure side of the flapless ("VALIANT-like") configuration of the F16 high lift wing with a 0° sweep in the AAWT aeroacoustic facility at University of Bristol (Figure 15) an open jet facility with a test section of 0.775×0.5 m. The best fit with the mean flow on the 3-element airfoil at 6° in free field was obtained with an airfoil geometrical incidence of 18° . The free stream velocity was $U = 30$ m/s and 37 m/s. A total of 6 cases were tested, the baseline (rigid surface) and 5 porous inserts, one provided by DLR (metallic foam), three provided by TUD (diamond lattice) and one provided by TCD (fabric) [5].

Note that numerical activities on porous slats were also being performed in Task 4.1:

- Development of numerical models to be implemented in CFD/CAA solvers, documented and validated against the results of characterization in VKI
- Numerical simulations of the unsteady flow in the slat cove with/without porous materials and reduction of noise level.

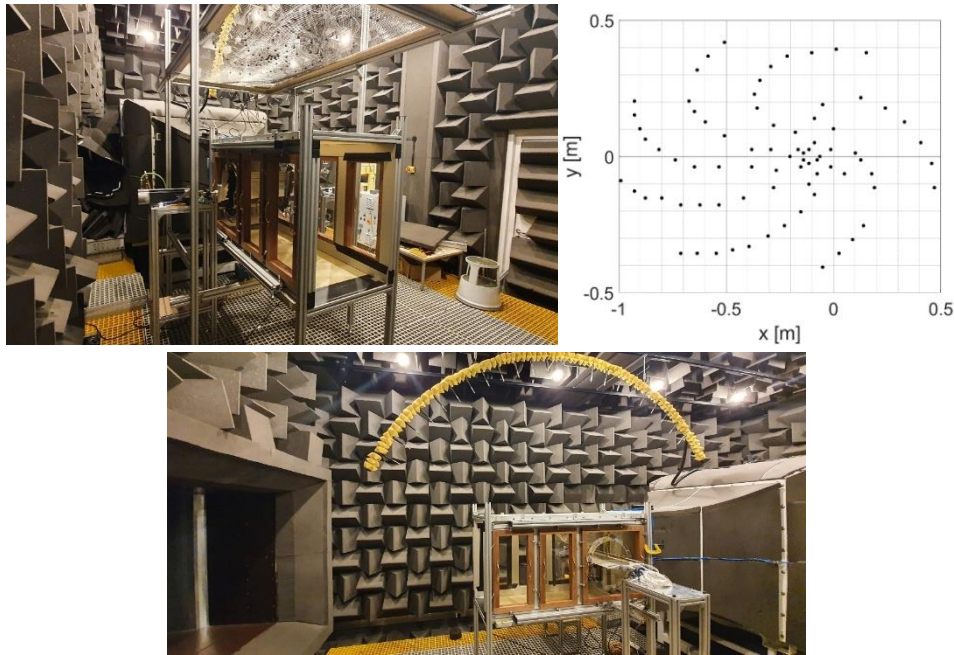


Figure 15: “VALIANT-like” flapless F16 airfoil tested in the AAWT facility (University of Bristol) with the test section equipped with Kevlar floor/ceiling. Top: configuration with the 80-microphone beamforming array (concentric elliptical spiral distribution). Bottom: configuration with a far-field arc of 16 microphone used for directivity measurements.

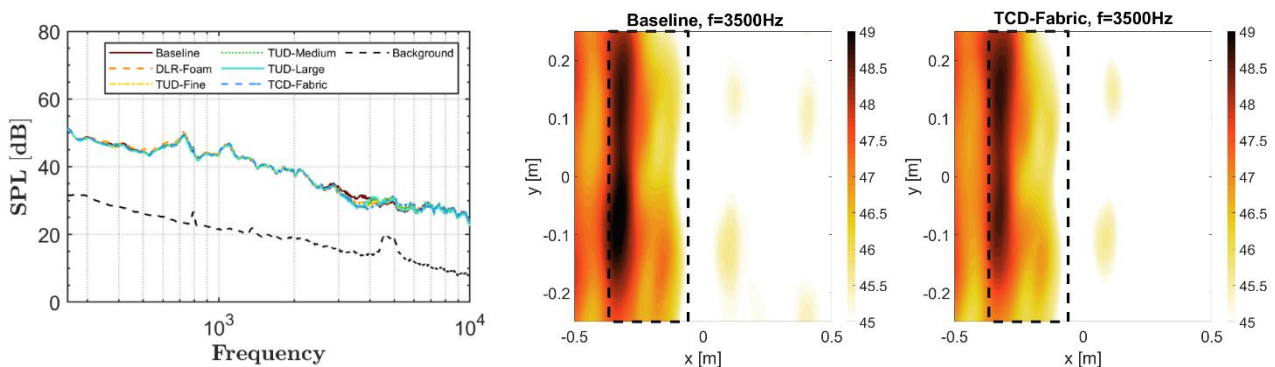


Figure 16: Acoustic results. Left: SPL spectra for all tested materials from the 90° microphone of the directivity arc. Right: noise maps for the baseline and the TCD-fabric, from the beamforming array at 3.5 kHz

Globally, the results of these tests were modest. The different tested porous inserts appeared to work as weak nearfield sound absorbers, with no or little influence on the local static pressure distribution and the wall pressure spectra measured by the Kulite sensors implemented at the wing leading edge. In terms of radiated noise, measurements by one microphone (at 90°) of the farfield directivity arc showed small differences (max 2-3 dB) between the baseline and most tested materials, and only in a limited frequency band [2.5 kHz– 4.5 kHz], as illustrated in Figure 16 (left). The noise maps obtained via the beamforming array at the frequency of 3.5 kHz do not show much visual differences, but perhaps spectra obtained via the integration of these maps in the slat region would show more differences.

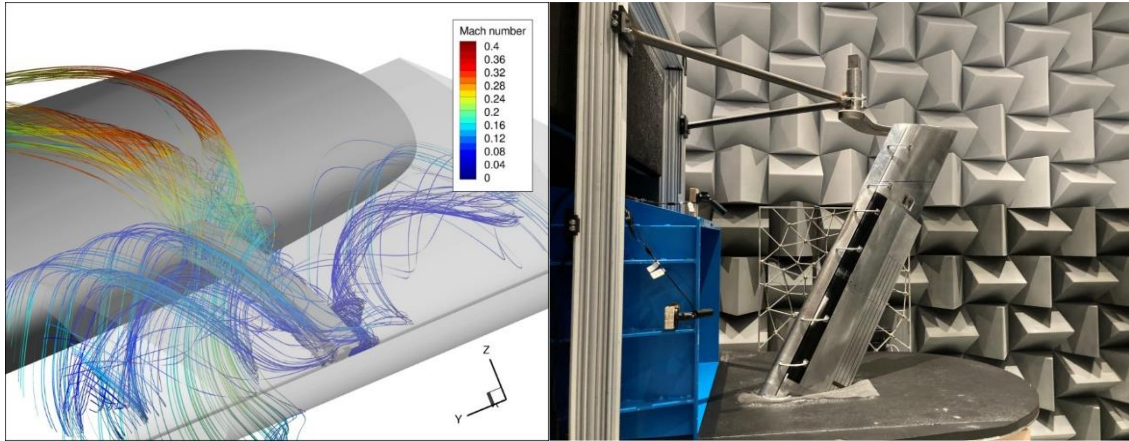


Figure 17: RANS numerical simulation of the mean flow by NLR (left) and test set-up in AWT@NLR (right)

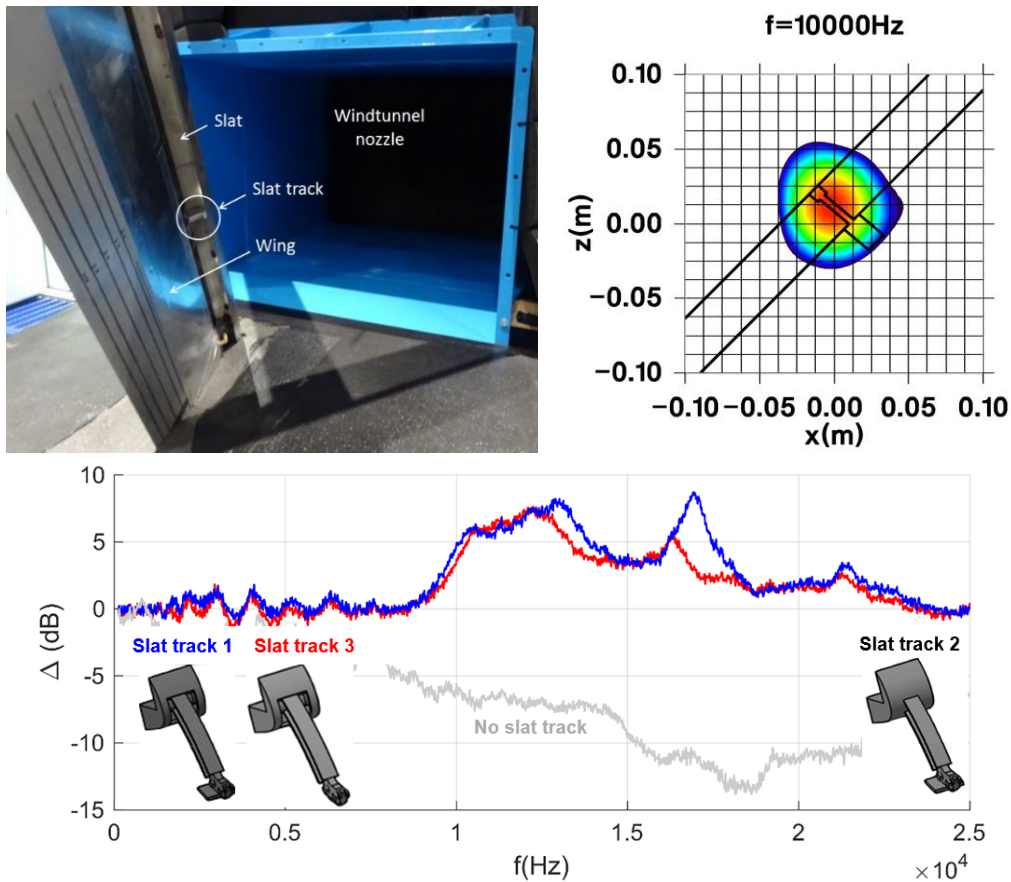


Figure 18: Slat track location (top left) – Noise map at frequency 10 kHz (NLR's results, top right) Bottom: power integrated spectra of baseline slat tracks (values are relative to the power integrated spectrum of slat track 2. Influence of the wing cavity (slat track #1) and the panel door (slat track #3)

3.4.3 Down selection of low noise slat tracks at AWT@NLR

INVENTOR focusses on reducing the noise generated by the slat tracks. The global goal is to better understand the mechanism of slat track noise generation, to quantify the relative weight between conventional slat noise sources (without slat track, nor any slat device) and slat track acoustic sources, and to assess alternative low noise slat track designs through experiments and numerical simulations.

In a preliminary activity (Task 4.2 [7]) the following actions have been achieved:

- numerical simulations of the complex mean flow in the slat track area have been achieved, suggesting possible noise generation mechanisms (Figure 17),
- a large number (14) of generic and low noise slat track designs proposed by Dassault-Aviation, and NLR have been tested on the flapless ("VALIANT-like") configuration of the F16 high lift

wing with a 30° sweep in the AWT aeroacoustic facility at NLR (Figure 17 and Figure 18), an open jet facility with a test section of 0.8×0.6 m. On its side, DLR has proposed conventional A/C slat tracks based on Airbus geometry to investigate the effect of slat size (thickness). The best fit with the mean flow on the 3-element airfoil at 6° in free field was obtained with an airfoil geometrical incidence of 21° . The free stream velocity was $U = 71$ m/s.

Farfield acoustic spectra have been obtained from the integration, in the slat track area, of noise maps obtained with a 64-microphone array installed in the flyover plane, showing that this small noise source has a significant contribution to the global airframe noise. This gives a preliminary qualitative answer to the general question on the relative weight of the contributions by conventional/classical slat noise and slat track noise (or other devices). Moreover, first tests on a generic slat track also revealed the influence of the wing cavity and the panel door.

In complement to this preliminary activity, the tests in F2 described in the next section planned to confirm the acoustic ranking of all tested generic and low noise slat tracks, with potential interaction with close slat side-edges, in combination with surface porous materials implemented in the slat cove, along with numerical activities.

4 INVENTOR's tests in F2

4.1 Test set-up

4.1.1 Introduction

The INVENTOR test set-up in F2 is very similar to the SWAHILI test set-up described on Figure 7, with the same F16 model oriented with a 30° sweep angle. Note that the model was also installed upside down with the pressure side facing the windtunnel ceiling (and the microphone array). The flap system is identical, but frozen in the "continuous" or 2.5D configuration (no flap side edge configuration). In the next sections we describe:

- the F16 model section main characteristics and related axis system,
- the implementation of the F16 model in the F2 windtunnel and related axis system,
- the model instrumentation (static pressure taps and Kulite sensors),
- the new slat system with modular inboard/outboard slat side-edges configurations,
- the model arm fairings,
- the flow conditions (model incidences, windtunnel velocities),
- the 120-microphone array,
- the tested slat porous inserts,
- the tested generic and low noise slat tracks.

4.1.2 F16 model section

The Airbus origin of this high lift airfoil is detailed in section 3.3.3 and Figure 2. Table 1 below shows the main dimensions of the F16 airfoil three elements. Note that this airfoil has been extensively used by DLR with several models at various scales. Compared to the present F16, which has a clean chord of 300 mm, the F15 has a double chord (600 mm) and the FTEG (only tested in DNW-LLF) has a quadruple chord of 1200 mm.

	Slat	Wing	Flap
Chord (mm)	55.8	247.2	84
Deflection angle (deg)	27.834	0	35.011
Gap (% of retracted chord)	2.265%	-	2.016%
Overlap(% of retracted. chord)	1.071%	-	0.55%

Table 1: Main dimensions (in mm) of F16 model's elements

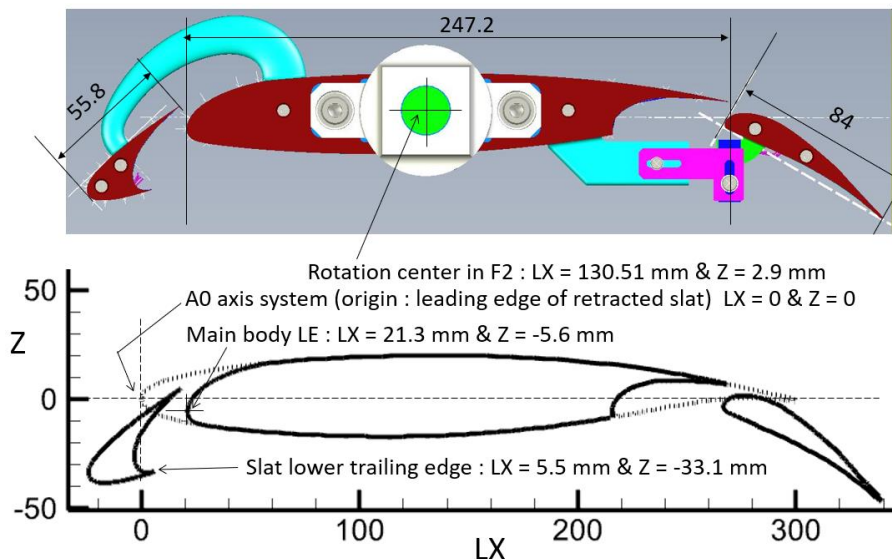


Figure 19: Top: CAD model section with key dimensions in mm (main elements chords, coordinates of main body leading edge, rotation center - Bottom: Origin (leading edge of retracted slat) of the reference framework axis A0 associated to the airfoil with an incidence of 0°.

Figure 19 (top) shows a CAD section of the F16 model in its LEISA2 (0° sweep) configuration (see Figure 4, bottom right). The position of this rotation center is given on Figure 19 (bottom) in the “AO axis system (LX, LY, Z)” linked to the airfoil section at an incidence of 0° with the origin at the leading edge of the retracted slat. LX is in the flow direction, LY in the span direction and Z in the vertical direction, oriented from the airfoil pressure side to the suction side. Note that the origin of the AO axis system (LX, LY, Z) might vary throughout this report, depending on what dimension is addressed, but it will be precised each time as necessary. This figure also provides the coordinates of (i) the slat lower trailing edge (also named “cusp” or “hook”) and (ii) the leading edge of the main wing element.

4.1.3 Implementation in the F2 windtunnel: from 0° to 30° sweep

The F2 windtunnel is described in Section 3.3.2 and Figure 1. The full test section is 5 m long and the entry section is 1.4 m in width and 1.8 m in height. The floor and ceiling are slightly divergent with angles of ± 0.29°, so the outlet section is approximately 1850 mm high.

Figure 20 illustrates how the model was implemented in F2 with a 0° sweep (LEISA2). As also shown on Figure 4, the model is installed with its original central element of span 800 mm and 2 extensions of 300 mm. It is installed in upside down position with the pressure side facing the ceiling where the microphone array is installed. Note that the windtunnel vertical axis Z is oriented downward, from the ceiling to the floor, so it is identical to the airfoil Z axis represented on Figure 19. The windtunnel X and Y axis are in the horizontal plane, X in the flow direction and Y in the direction of the airfoil span, so they are identical to the airfoil axis LX and LY. The “Rotation axis Y” used to adjust the model incidence is located 2.65 m downstream the test section entry, 905 mm above the floor and 925 mm below the ceiling. This axis corresponds to the “Rotation center in F2” identified on Figure 19.

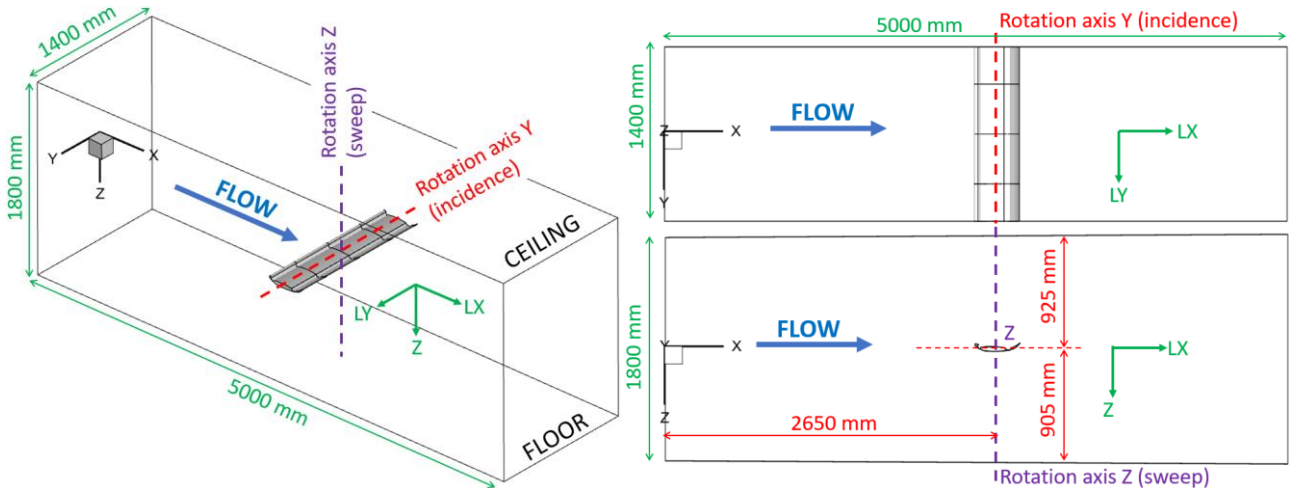


Figure 20: F16 model installation in F2 with 0° sweep (LEISA2)

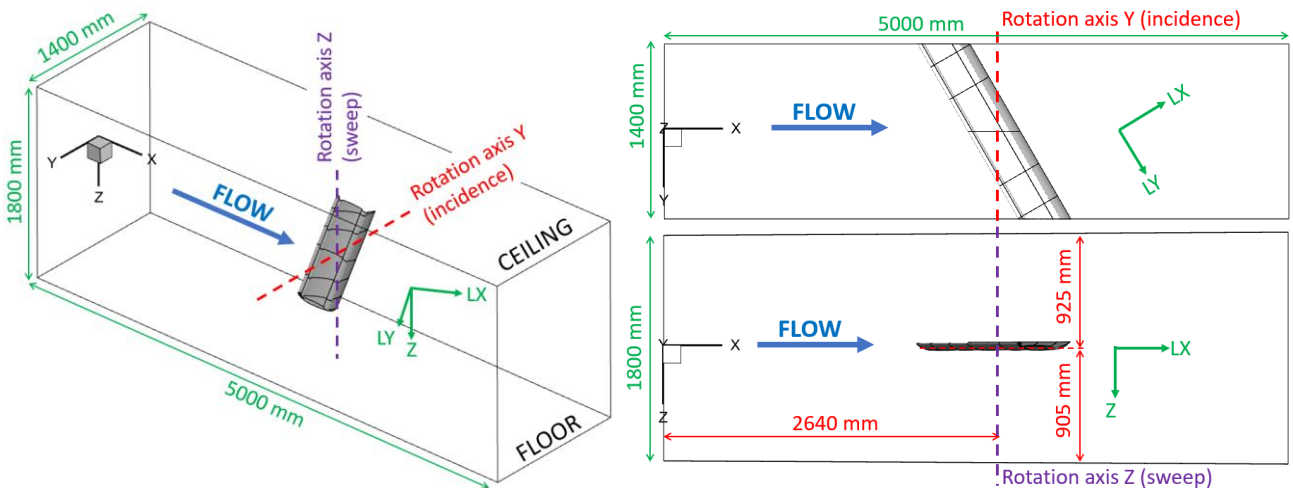


Figure 21: F16 model installation in F2 with 0° sweep (SWAHILI – INVENTOR)

As illustrated on Figure 21, the 30° sweep was simply obtained from a rotation of -30° of the model (at an incidence of 0°) around the vertical "Rotation axis Z" which intersects the horizontal "Rotation axis Y" at a position named the "Rotation center" at equal distances of the windtunnel walls. As also shown on Figure 7, new extensions of the 800 mm central element were built, but the "Rotation axis Y" remains the same, so that the incidence can be adjusted with the model ends smoothly following the lateral walls of the test section.

In the following, most views of the model will be represented as any classic lifting wing, which means with the airfoil pressure side (resp. suction side) facing the floor (resp. ceiling) and the positive lift oriented with the Z axis from the floor to the ceiling. This can be obtained by mentally rotating the full set-up by 180° around the X axis. A mnemotechnic representation is to consider that, in this position, the model corresponds to the right wing of a classic aircraft (with positive or rearward sweep).

4.1.4 Note on the 2.5D continuous slat system and brackets.

Figure 22 details the system of slat brackets in the 0° (LEISA2) and 30° (SWAHILI – INVENTOR) sweep configurations.

In the 0° sweep configuration, the central slat/wing element "E" (span 800 mm) has 4 symmetrical slat brackets located at $LY = \pm 150$ mm and ± 325 mm from the model mid span. The two extensions "G" (span 300 mm) have 2 slat brackets each, located at $LY = \pm 450$ mm and ± 650 mm from the model mid span.

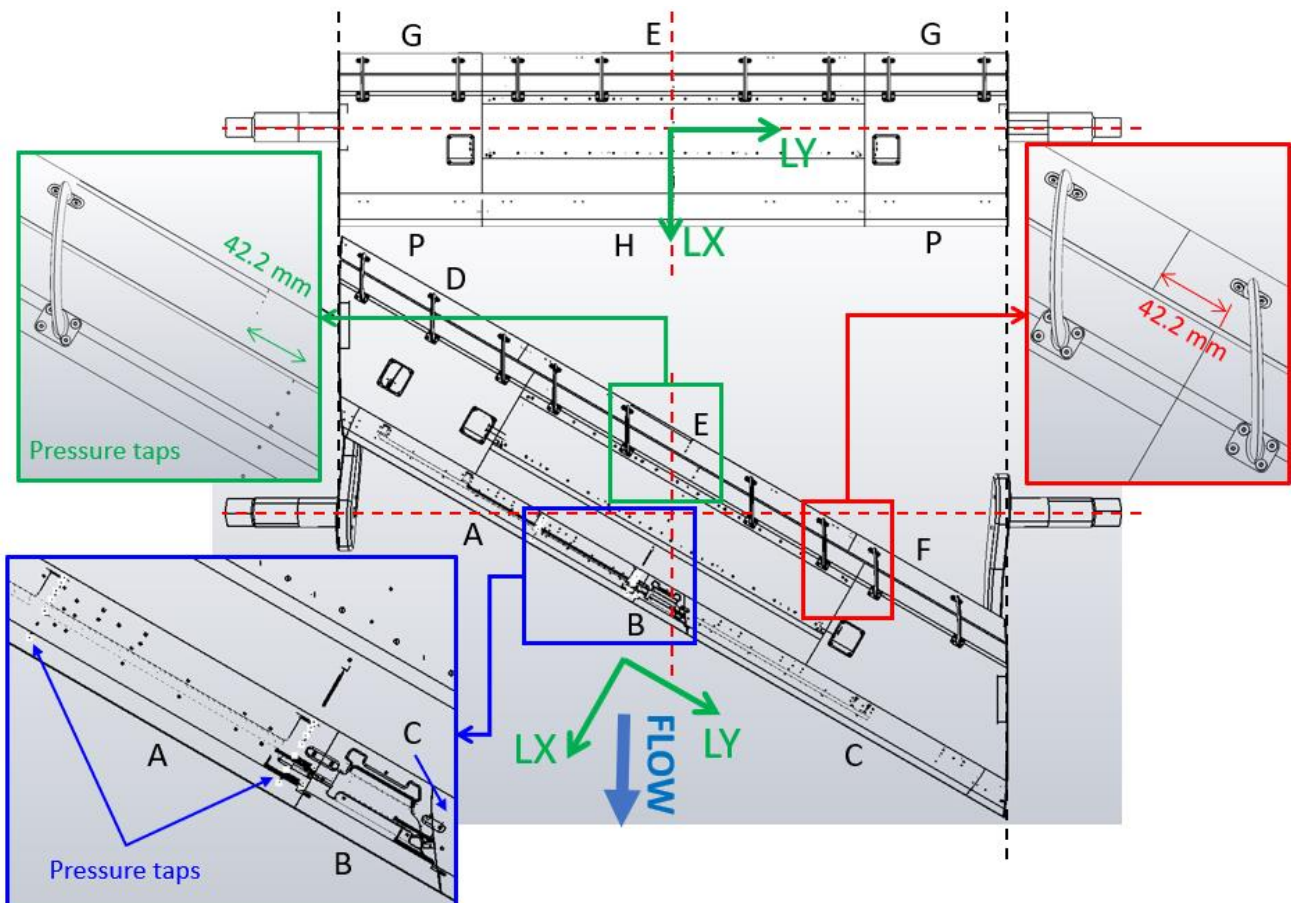


Figure 22: Implementation of slat and flap systems on the F16 with 0° and 30° sweep (suction side apparent)

In the 30° sweep configuration, new slat brackets aligned with the flow have been designed. One constraint was to avoid machining additional footprints on the central elements of span 800 mm (slat and main wing), so the existing footprints were re-used, with the slat element simply translated by $LY = -42.2$ mm. Each bracket can be easily located by the spanwise distance LY between the center

of its footprint on the main element and the model mid span section: the 4 brackets on the main wing central element are still at $LY = \pm 150$ mm and ± 325 mm. New slat and wing extensions were designed and manufactured accordingly. The right extension has two brackets located at $LY = +450$ mm and $+650$ mm, whereas the left extension has 3 brackets with their footprint located on the main wing at $LY = -450$ mm, -620 mm and -790 mm (note that the full span of the model is $1400/\cos(30^\circ) = 1616.6$ mm).

Figure 22 also shows that the static pressure taps on the slat element "E", which are aligned at the model mid span with the 0° sweep are now also shifted by $LY = -42.2$ mm.

4.1.5 Note on the SWAHILI flap system (not used in INVENTOR)

In the 0° sweep configuration (LEISA2) configuration, the flap was built from the original element "H" (span 800 mm) and two extensions "P" (span 300 mm) see Figure 22.

In the 30° configuration (SWAHILI), Dassault-Aviation has designed a completely new slat system in 3 elements (denoted "A", "B" and "C" on Figure 22) to allow 2 different flap side edge configurations, one aligned with the flow direction ("FSA": A and B deployed, C retracted) and one aligned in the airfoil chord direction ("FSD": A deployed, B and C retracted). In INVENTOR, only the "NOM" configuration with all 3 elements deployed will be used (same shape as element "H").

Finally, span extents of slat and flap elements are given in Table 2, measured at the flap trailing edge and slat cusp (or lower trailing edge). Note that elements in contact with the windtunnel walls were equipped with an additional friction seal of thickness 2.0 mm (LEISA2, elements G and P) or 2.3 mm (SWAHILI, elements A, C, D, F).

Element	Left (mm)	Center (mm)	Right (mm)	Total (mm)
Slat sweep 0° (LEISA2)	G: 298.0 + 2.0	E: 800.0	G: 298.0 + 2.0	1400.0
Flap sweep 0° (LEISA2)	P: 298.0 + 2.0	H: 800.0	P: 298.0 + 2.0	1400.0
Slat sweep 30° (SWAHILI)	D: 435.9 + 2.3	E: 800.0	F: 376.0 + 2.3	1616.5
Flap sweep 30° (SWAHILI)	A: 770.9 + 2.3	B: 134.2	C: 707.2 + 2.3	1616.4

Table 2: Span extent of slat/flap elements (Figure 22) measured at the trailing edge (lower TE or cusp for slat)

4.1.6 Model on-board instrumentation

4.1.6.1 Static pressure taps

The F16 model central section ($LY = 0$) is equipped with static pressure taps on the slat, wing and flap. Their number and positions varied throughout the experimental campaigns (Figure 23).

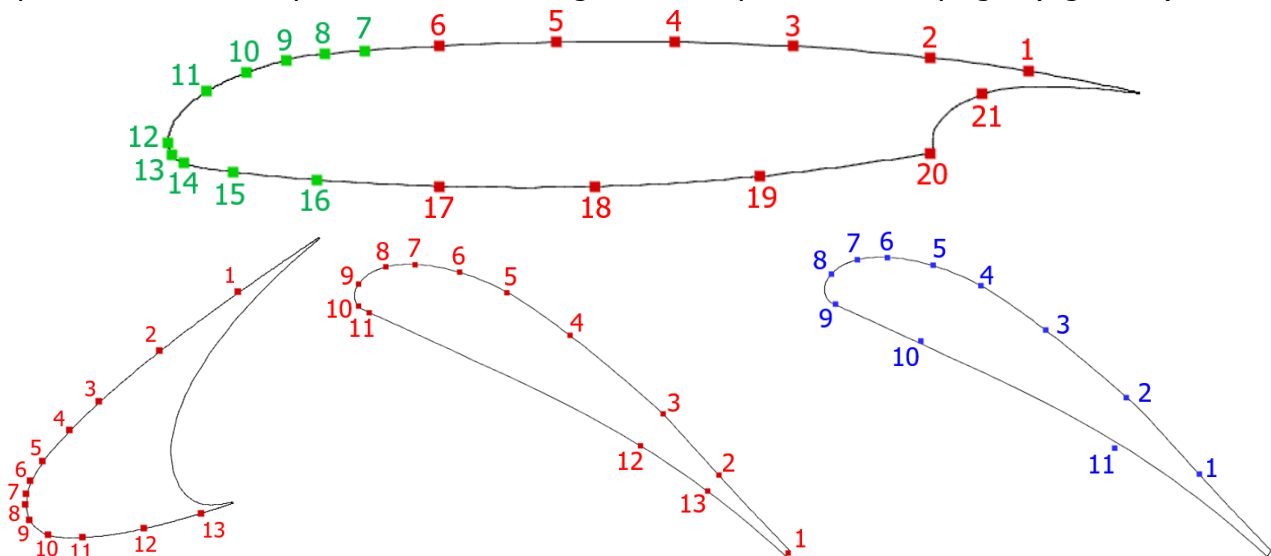


Figure 23: Location of static pressure taps on the slat, wing and flap. **In red:** original taps (LEISA2). **In blue:** SWAHILI new taps on flap (2 sections). **In green:** INVENTOR's new taps on main element.

- LEISA2 (sweep 0°): in red on Figure 23: all pressure taps (slat/wing/flap) were located in the same airfoil section at mid span ($LY=0$), 13 taps on the slat, 11 taps on the wing (#1 to #6

and #17 to #21) and 13 taps on the flap. Note that taps #7 to #16 did not exist and 8 Kulite unsteady pressure sensors were mounted in this region instead, see Figure 24. Note also that the tap #20 might not exist, as it was not found on the model at this position during the INVENTOR tests.

- SWAHILI/HiLiNo/INVENTOR (sweep 30°): in blue on Figure 23: the slat central element "E" (and its 13 pressure taps) was translated by LY = -41.8 mm in the span direction. On the new flap system (elements "A", "B" and "C") new flaps 2 sections of 11 pressure taps were created, one at LY = 0 mm and the other one at LY=-250 mm.
- INVENTOR: in green on Figure 23: for the INVENTOR tests, the 8 Kulites on the wing leading edge were maintained but additional pressure taps #7 to #16 were manufactured, in a section translated at LY = 35 mm in the span direction.

Slat			Wing			Flap (section 1 / 2)					
#	LX	LY	Z	#	LX	LY	Z	#	LX	LY	Z
1	6.32	-41.8	-2.88	1	240.33	0	12.63	1	327.46	0 / -250	-33.16
2	-5.01	-41.8	-11.29	2	215.34	0	16.05	2	315.69	0 / -250	-20.86
3	-13.76	-41.8	-18.63	3	180.24	0	18.96	3	302.63	0 / -250	-9.87
4	-17.93	-41.8	-22.68	4	150.33	0	20.04	4	292.21	0 / -250	-2.77
5	-21.86	-41.8	-27.2	5	120.18	0	20.04	5	284.40	0 / -250	0.58
6	-23.53	-41.8	-30.01	6	90.24	0	19.02	6	277.06	0 / -250	1.86
7	-24.13	-41.8	-31.86	7	71.3	35	17.8	7	272.22	0 / -250	1.47
8	-24.25	-41.8	-33.42	8	61.3	35	17	8	267.95	0 / -250	-0.83
9	-23.73	-41.8	-35.6	9	51.3	35	15.3	9	268.66	0 / -250	-5.74
10	-21.03	-41.8	-37.72	10	41.3	35	12.25	10	282.43	0 / -250	-11.63
11	-16.11	-41.8	-38.07	11	31.2	35	7.4	11	313.76	-2 / -252	-28.97
12	-7.3	-41.8	-36.84	12	21.3	35	-5.5				
13	1	-41.8	-34.64	13	22.3	35	-8.8				
				14	25.3	35	-10.8				
				15	37.9	35	-13.1				
				16	59.3	35	-15.1				
				17	90.24	0	-16.65				
				18	130.05	0	-16.74				
				19	172.08	0	-14.13				
				20	215.2	0	-8.33				
				21	228.45	0	6.93				

Table 3: Coordinates (in the axis framework A0, model at incidence 0°, see Figure 19) of all static pressure taps of the INVENTOR configuration

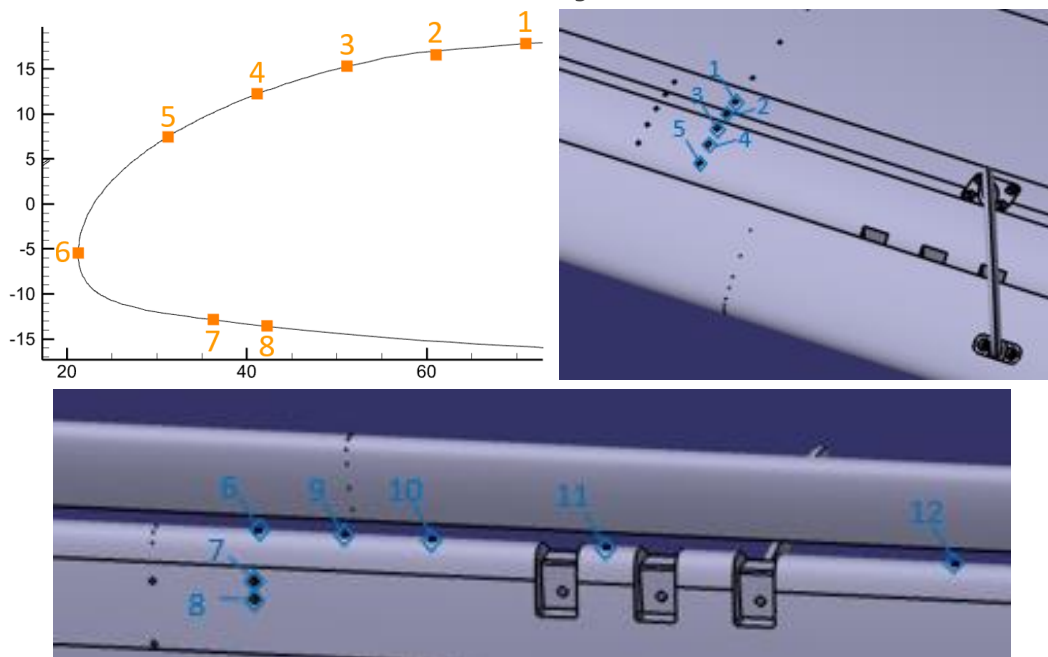


Figure 24: Positions of the 12 Kulite sensors (blue diamonds) on the main wing leading edge

Finally, the coordinates (in the axis framework A0, model at incidence 0° , see Figure 19) of all static pressure taps of the INVENTOR configuration are given in Table 3.

4.1.6.2 *Kulite unsteady pressure sensors*

The central element of the F16 model is also equipped with 12 unsteady pressure sensors (Kulite) located on the wing near the leading edge. Note that Kulite #9 to #12 are located at the same 2D position as Kulite #6 but with a span shift of respectively LY=-30, -60, -120 and -240 mm. An overview of the distribution of the pressure ports and Kulites is shown on Figure 24 and their coordinates in the AO axis system (see Figure 19) are given in Table 4.

#	LX	LY	Z
1	71.1	0.0	17.8
2	61.1	0.0	16.6
3	51.1	0.0	15.3
4	41.2	0.0	12.2
5	31.2	0.0	7.5
6	21.3	0.0	-5.4
7	36.3	0.0	-12.9
8	42.3	0.0	-13.6
9	21.3	-30.0	-5.4
10	21.3	-60.0	-5.4
11	21.3	-120.0	-5.4
12	21.3	-240.0	-5.4

Table 4: Coordinates (in the axis framework A0, model at incidence 0° , insee Figure 19) of the 12 Kulite sensors on the wing leading edge

4.1.7 New slat system with slat side-edges on the F16 model

4.1.7.1 *Objectives*

In addition to the mechanism of slat track noise occurring when the latter is placed in a continuous 2.5D slat (as they were tested in AAWT@NLR), the role of slat edges and the specific aerodynamic interaction with the closest slat track and the related noise generation are also of interest.

Moreover, the situation may completely differ whether the slat track is located close to an inboard slat side-edge (side-edge facing the aircraft fuselage) or close to an outboard slat side-edge (side-edge facing the wing tip). Moreover, the spanwise distance between the side edge and the closest slat track is also a parameter of interest, so 3 slat track pockets have been manufactured on the central wing element "E", providing 3 possible slat track positions. The pocket #1, #2 and #3 are located respectively at LY = -104, -138 and -172 mm from the mid span of the wing element "E".

Finally, two slat side edge configurations have been designed and manufactured with the following geometrical constraints and arrangements to tentatively re-use existing slat elements. Note that, in the next paragraph, C denotes the slat chord $C = 55.8$ mm, and "fuselage" and "wing tip" refer to the airfoil ends, when it is seen as the right wing of an aircraft with classic rearward sweep.

4.1.7.2 *Inboard slat side edge*

The inboard slat side edge configuration is described on Figure 25. The side-edge is (i) facing the "aircraft fuselage" (ii) aligned with the flow and (iii) located approximately $1.5C$ upstream the central slat track pocket #2, as prescribed by Dassault-Aviation on Figure 18 of the D2.7 deliverable. This has been simply obtained using the existing central slat element "E" (span 800 mm) and just requiring the design and manufacture of 2 new small slat elements "K" and "L" (in red on Figure 25, span extent of all slat elements are detailed in Table 5).

Note that the existing 800-mm span slat element "E" is equipped with 2 cavities designed to test the porous slat inserts, offering the opportunity to have such inserts close to the slat side-edge and evaluate their potential effect on slat side noise reduction. However, due to lack of time, this possibility was not exploited during the INVENTOR tests.

4.1.7.3 *Outboard slat side edge case*

The outboard slat side edge configuration is described on Figure 26. The side-edge is (i) facing the "aircraft wing tip" (ii) aligned with the airfoil chord and (iii) located approximately $1.5C$ downstream the central slat track pocket #2, as prescribed by Dassault-Aviation on Figure 18 of the D2.7 deliverable. This has been simply obtained using the existing extensions element "D" and "F" and just requiring the design and manufacture of the new small slat element "M" (in green on Figure 26, span extent of all slat elements are detailed in Table 5).

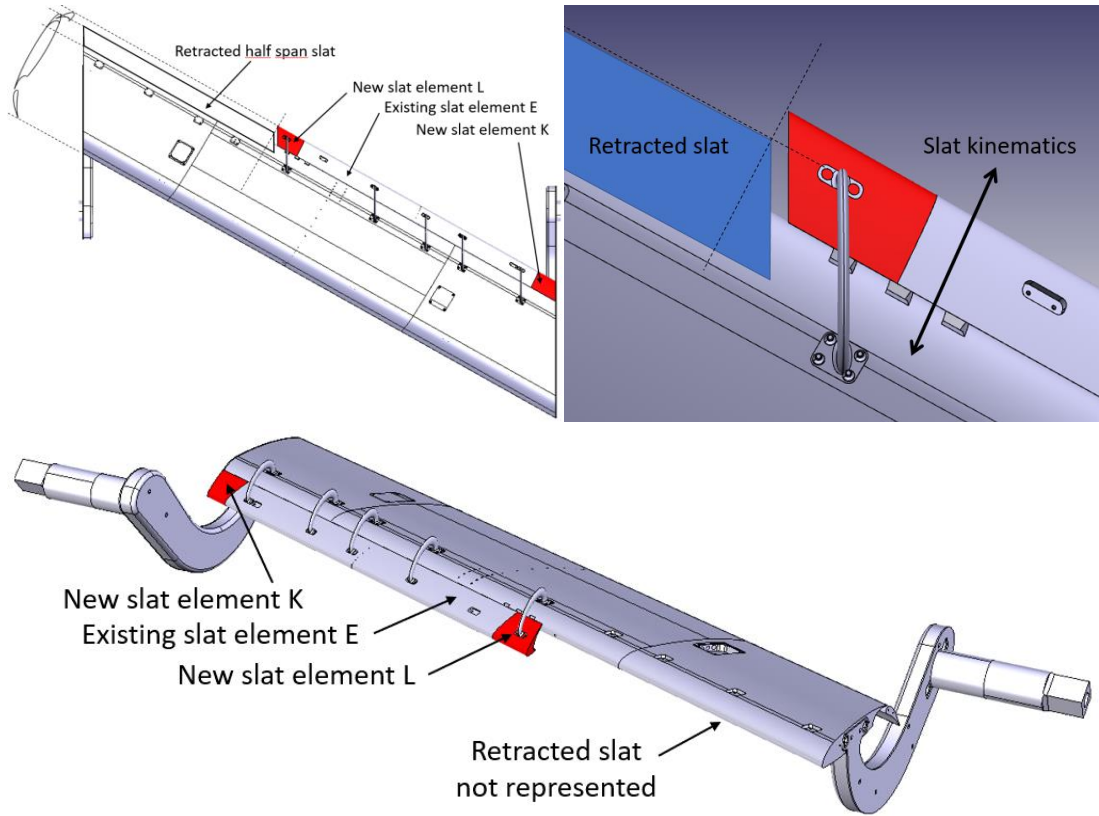


Figure 25: Inboard slat side-edge configuration

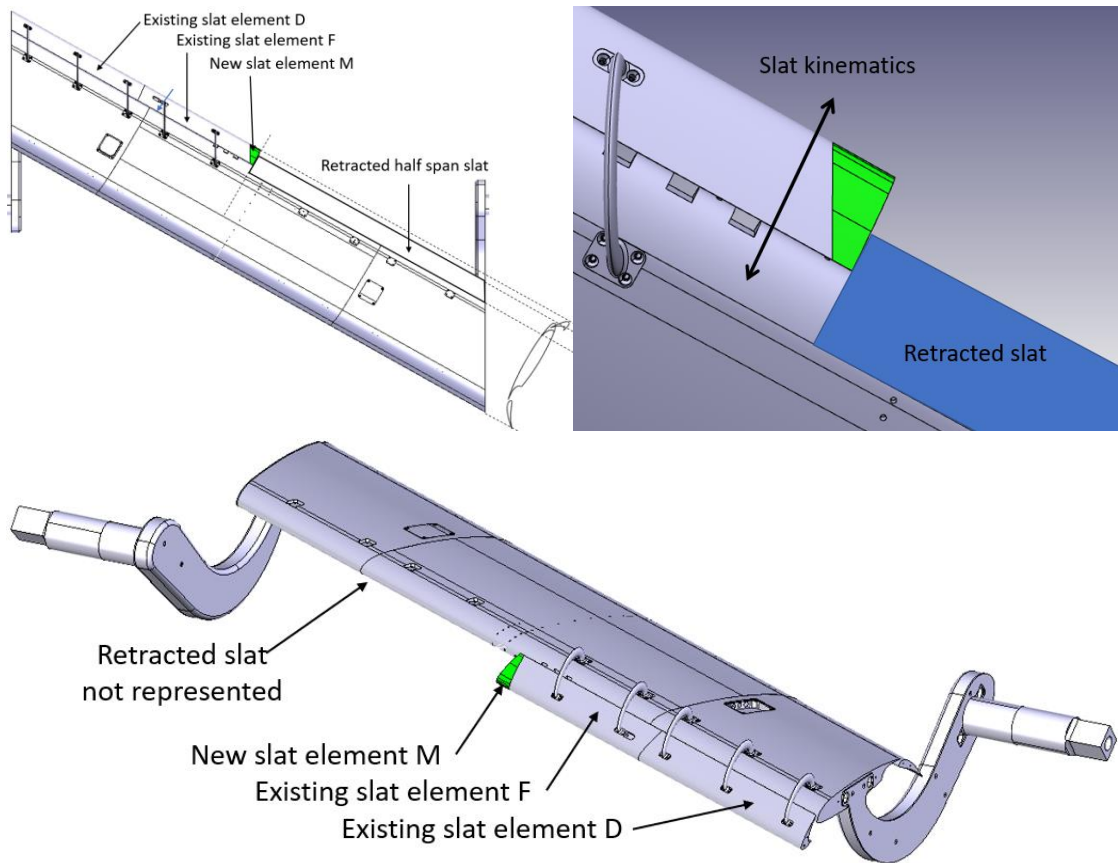


Figure 26: Outboard slat side-edge configuration

Note that, for this outboard slat side-edge case, there was no possibility to install any porous insert on the slat pressure side.

Finally, Table 5 provides the dimensions at the lower (cusp) and upper trailing edges of all slat elements used in both slat side edge configurations. Note that elements D and K in contact with the windtunnel walls were equipped with an additional friction seal of thickness 2.3 mm.

Slat element	Span at cusp (mm)	Span at upper TE (mm)	SSE configuration
D	435.9 + 2.3	428.6 + 2.3	Outboard
F	376.0	383.3	Outboard
M	18.2	11.0	Outboard
K	75.2 + 2.3	65.1 + 2.3	Inboard
E	800.0	800.0	Inboard
L	73.9	84.0	Inboard

Table 5: Spanwise dimensions at the cusp and trailing edge of all slat elements used in inboard/outboard slat side edge configurations

4.1.7.4 *Static pressure taps on slat*

The SWAHILI tests were achieved with the continuous 2.5D slat (elements "D", "E" and "F") with the 13 static pressure taps connected with their vinyl tubes routed to the main wing without connectors. For the INVENTOR tests we had to switch several times between the continuous and the slat side edges configurations, so new connectors had to be implemented to easily connect/disconnect the taps. These taps were actually present on the "E" slat element in the inboard slat side-edge configuration (see Figure 25), but it was not possible to connect them and route them to the main wing, so they were not used in this configuration.

In the outboard slat side-edge configuration (see Figure 26), the slat elements "D" and "F" do not have any static pressure taps, so such measurement were also not possible.

4.1.7.5 *Retracted slat elements*

In both slat side-edge configurations, the realism of the geometry assumes that one half-span slat element is retracted. Unfortunately, the corresponding slat elements were not included in the original CAD files (see Figure 25 and Figure 26) so they were not manufactured with the new element "K", "L" and "M", and this omission was discovered rather lately.

In order to rapidly solve the issue, DLR has proposed to design and "3D print" cheap slat elements, assuming that such retracted slat is not subjected to significant aerodynamic effort and can be directly attached to the wing leading edge with aluminum tape, without specific brackets. One risk was obviously to obtain different surface qualities (in terms of shape precision and surface roughness), but this was not considered as critical in these specific configurations. Moreover, we could not afford milling such new parts, in aluminum for example. It was of course impossible to "3D print" slat elements of about 700 mm long, so DLR manufactured several elements of span 200 mm and these elements were adjusted "on site" in the windtunnel. Note that a "calibre" part in aluminum was also provided to allow cutting the slat element with the correct sweep angle for the outboard slat side edge aligned in the flow direction.

Finally, the position of the side edges of these retracted slats was simply adjusted considering the kinematics of the deployed slat element in the direction normal to the wing leading edge, in such a way that, when this half-slat is deployed, the full slat is continuous, without any gaps. In this respect the situations are different for the inboard and outboard slat side edges (see Figure 25 and Figure 26).

4.1.7.6 *Proximity between a slat bracket (suction side) and a slat track (pressure side)*

During the slat track tests in AWT, NLR's colleagues observed that one slat bracket on the suction side was located at a spanwise position very close to the slat track pockets on the pressure side for acoustic characterization. The presence of an unwanted noise source close to the investigated noise

source is actually not favorable. NLR's colleagues did not take the risk to remove the slat bracket, and their results suggest that it had no significant influence on the results.

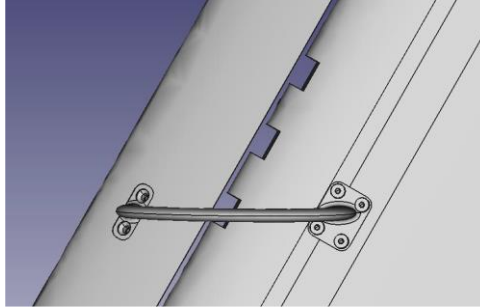


Figure 27: Proximity of a slat bracket (suction side) and the 3 pockets manufactured for the implementation of slat tracks on the pressure side

However, F2 windtunnel is way noisier than AWT, so the signal-to-noise ratio will be probably weaker, and it was considered wiser to prevent such situation. With the agreement of DLR, it has been decided to simply remove this slat bracket, without weakening the slat or generating slat vibrations, especially for the slat side-edge configurations. Note that this suppression is only possible for the continuous 2.5D slat configurations. Figure 25 and Figure 26 suggest that a similar issue might arise from the close proximity of a slat bracket and the inboard/outboard slat side edges (and especially in the inboard configuration), which might similarly generate spurious noise. However, for structural reasons, this slat brackets cannot be removed, nor replaced by something potentially more silent.

Note: in the SWAHILI program it was observed in the windtunnel that the wake of the same slat bracket directly hit one of the tested flap side-edge: it was decided to remove this slat bracket as well.

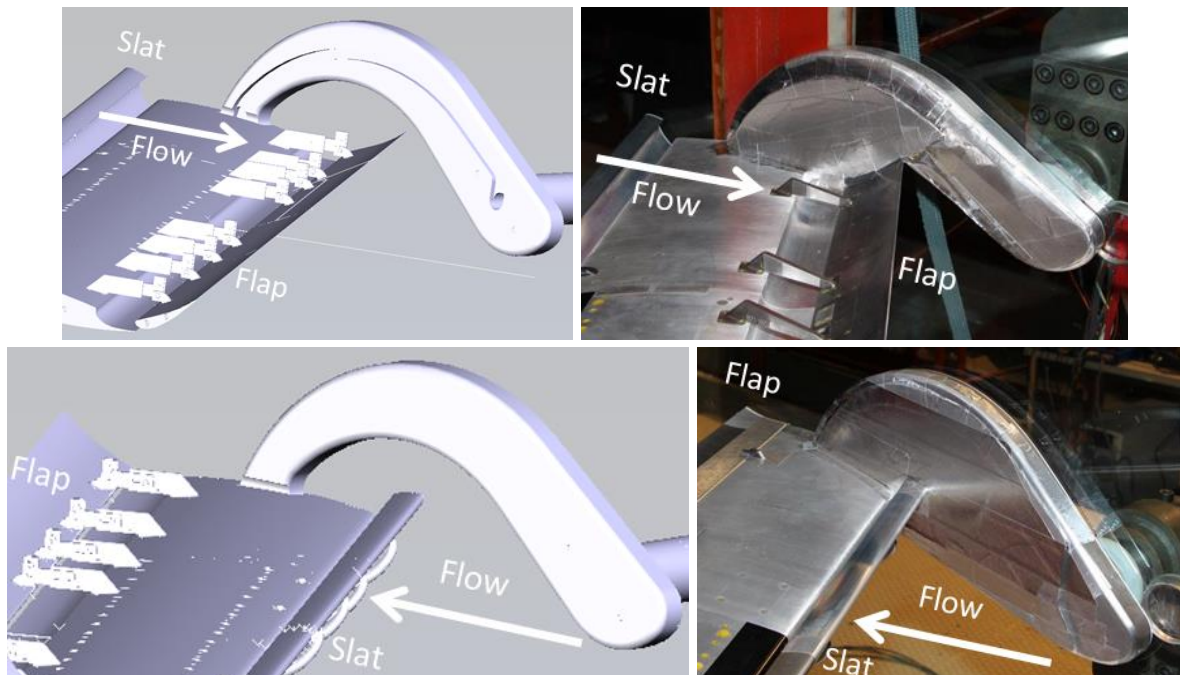


Figure 28: Original CAD of model arms (left) and improvised fairings (right)
 Top: upstream arm with cavity routing the vinyls and cables
 Bottom: downstream arm

4.1.8 Model arm fairings

During the SWAHILI tests the model side arms (that were specifically designed and manufactured to allow testing the F16 model with a 30° sweep angle) were suspected to add unwanted 3D aerodynamic effects and noise sources, so fairings were improvised by the windtunnel team, mainly based on adhesive tape (Figure 28).

Acoustic acquisitions with the 120-microphone array were achieved (i) with the bare arms and (ii) with the arms hidden with fairings. Figure 29 compares DAMAS noise maps in both situations for the full 2.5D configuration (no flap side-edge) at three frequencies 2.5-4.0-6.3 kHz, in a frequency range where the side arms looks noisiest. These maps are uneasy to compare because of their scale differences (dynamic of 15 dB but different min/max - noise spectra in the specific areas might be compared instead), but the maxima with the bare arms are always higher than those with the fairings

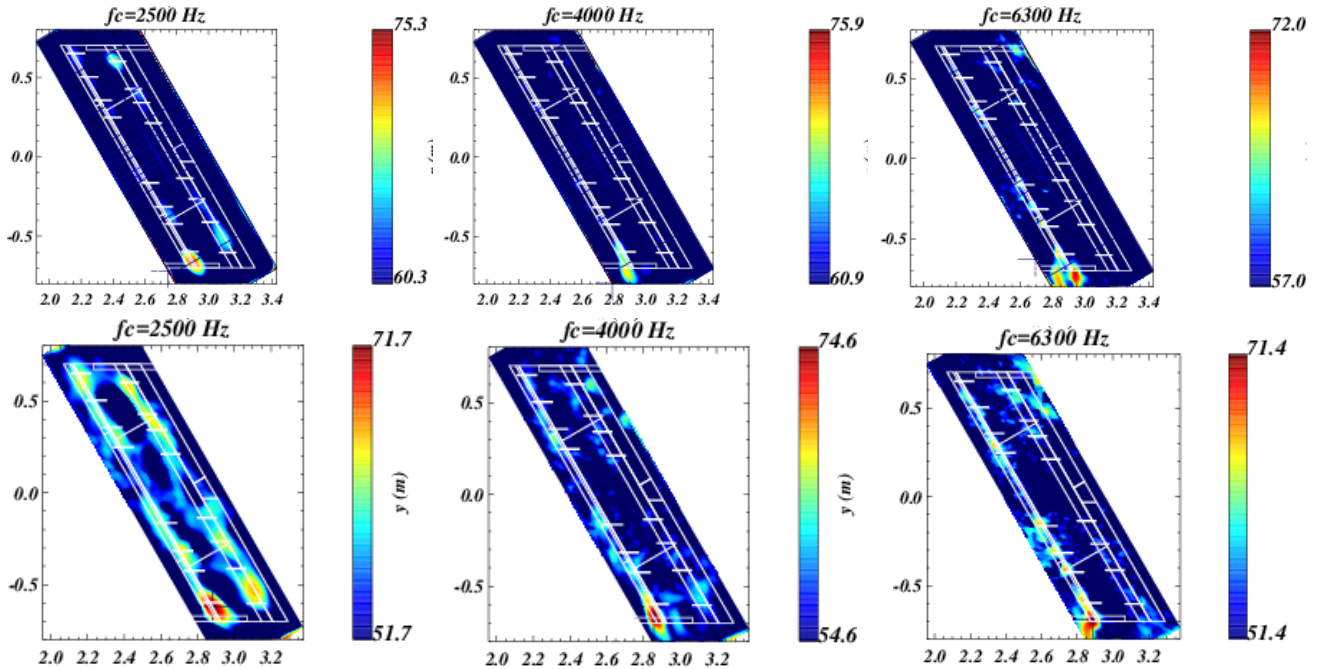


Figure 29: DAMAS noise maps with bare arms (top) and with arm fairings (bottom)

Figure 30 compares the influence of the bare arms versus the arms with fairings on noise spectra obtained by integrating the DAMAS noise maps in central slat and flap regions. It can be observed that the spectra are almost the same, which would tend to suggest that the bare arms are not a problem. This is for the full 2.5D configuration, but the results were very close when looking at the configurations with the flap side-edges.

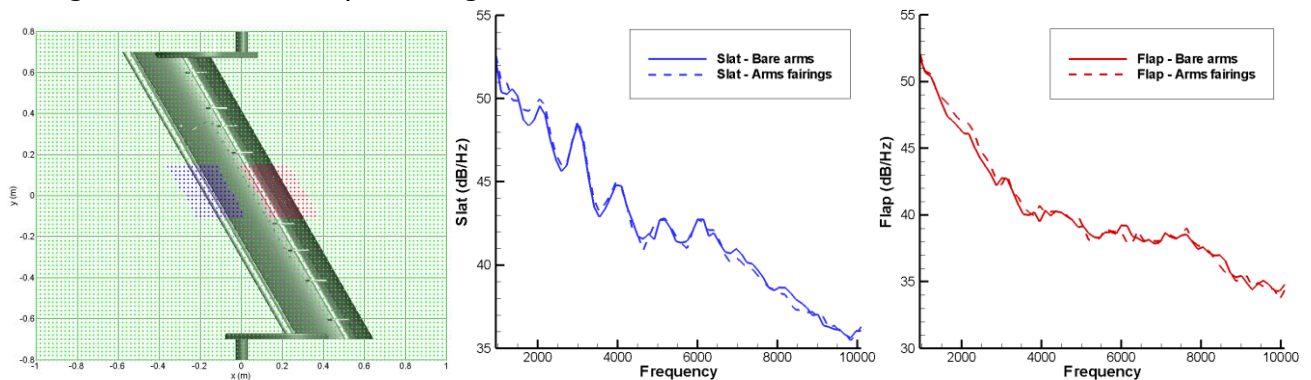


Figure 30: integrated noise spectra in slat and flap areas, with bare arms and with arm fairings (from SWAHILI).

In conclusion, the influence of these bare arms has perhaps been overestimated during the SWAHILI program. However, it looked wise to maintain the possibility of minimal fairings, especially for the arm located upstream the model. Consequently, ONERA provided simple elements (rigid/thin metallic sheets attached with adhesive tape) that facilitated the local fabrication of arm fairings, allowing several changes between the continuous slat and the slat side edges configurations.

4.1.9 Flow conditions

4.1.9.1 Model incidences

In the SWAHILI program, the pressure acquisitions (on-board pressure taps and Kulites, microphone arrays) were achieved on a large range of global model incidences, whereas extended PIV and LDV measurements were achieved at the reference incidence 5.33° .

The C_p measured at F2 at this 5.33° incidence (and with a 30° sweep) with the full slat/wing/flap model were used to find the best match with the C_p observed on the flapless model in AWT@NLR also with a 30° sweep, leading to a reference of 21.3° .

Similarly, the C_p measured at F2 at a 6.15° incidence (and with a 0° sweep) with the full slat/wing/flap model in the LEISA2 program were used to find the best match with the C_p observed on the flapless model in AAWT@UBRI also with a 0° sweep, leading to measurements in the range 16° , 18° , 20° , 22° and 24° .

For the INVENTOR tests in F2, also with a 30° sweep, it is interesting to keep the same reference incidence of 5.33° (for cross check with the SWAHILI database), which is also close to the targeted incidence at approach (5°) in the deliverable D2.1, and add 2 more angles with plus and minus 2.3° , e.g. 3.0° and 7.6° .

4.1.9.2 Wind velocities

Most SWAHILI tests were conducted at a reference flow velocity of 71 m/s. All tests in AWT@NLR were also achieved at 71 m/s only. Tests in AAWT@UBRI were achieved at lower wind velocities (30 m/s and 37 m/s)

For the INVENTOR tests in F2, it is proposed that 71 m/s remains the reference velocity, which is also in close agreement with the general specification in deliverable D2.1. In a view of deriving some velocity power laws it is proposed to add 3 more velocities for all acoustic measurements, say 40, 50, 61.5 and 71 m/s. Note that higher velocities would be interesting, but beyond reasonable values of the model deformation under aerodynamic loads.

4.1.10 Microphone array

The microphone array was mounted in the windtunnel ceiling. The 120 $\frac{1}{4}$ " condenser microphones are flush-mounted on a rigid plate (PVC) of about 1 m x 1 m (Figure 18, left side) and this plate is mounted at about 4 mm beneath a wiremesh cloth which is flush-mounted with the windtunnel ceiling. The geometrical center of the array (Microphone #1) is located at exactly 2490 mm from the test-section entry.

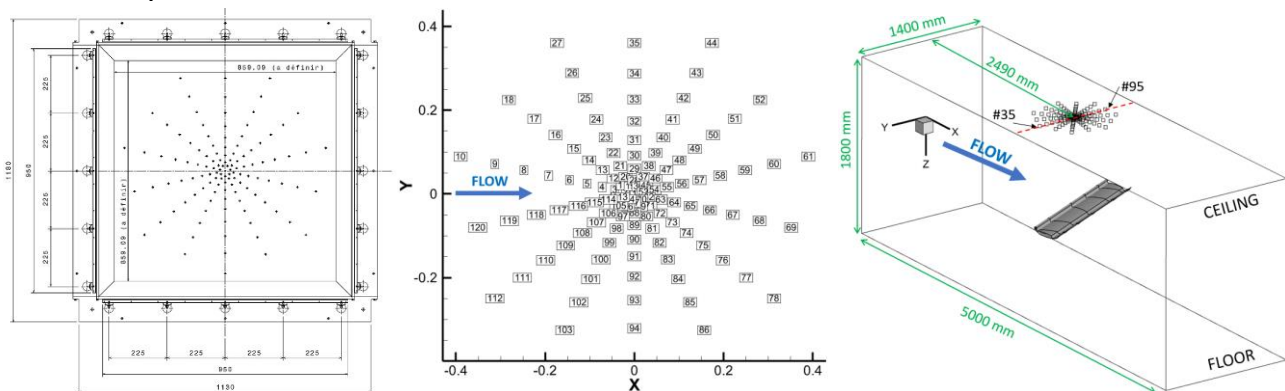


Figure 31: Microphone array mounted in the F2 windtunnel ceiling. Left side: array support. Middle: microphones numbering and coordinates in the array framework (origin at the central microphone #1). Right side: 3D view

The 120 microphones are distributed along 7 radial arms with 18 microphones each (the central microphone #1 is common to all arms). The angular step between two successive arms is about 25° . The radial distance between successive microphones on a given arm varies from 3 cm in the central region to 7 cm at the array periphery.

The (X, Y) coordinates in mm of all 120 microphones (relative to the central microphone #1) are given in Table 6.

#	X	Y	#	X	Y	#	X	Y	#	X	Y
1	0	0	31	0	129.2	61	390	89	91	0	-149.5
2	-20.3	4.6	32	0	173.4	62	32.3	-7.4	92	0	-197.4
3	-44.3	10.1	33	0	225.7	63	58.5	-13.3	93	0	-254
4	-72.7	16.6	34	0	287.5	64	89.4	-20.4	94	0	-321
5	-106.2	24.2	35	0	360.5	65	125.9	-28.7	95	0	-400
6	-145.7	33.3	36	9	18.8	66	169.1	-38.6	96	-14.4	-29.9
7	-192.5	43.9	37	19.7	40.9	67	220.1	-50.2	97	-26	-54
8	-247.7	56.5	38	32.3	67.1	68	280.3	-64	98	-39.8	-82.6
9	-312.9	71.4	39	47.2	98.1	69	351.4	-80.2	99	-56	-116.4
10	-390	89	40	64.9	134.7	70	16.3	-13	100	-75.3	-156.3
11	-25.9	20.7	41	85.7	177.9	71	35.5	-28.3	101	-97.9	-203.4
12	-46.9	37.4	42	110.2	228.9	72	58.3	-46.5	102	-124.7	-259
13	-71.7	57.2	43	139.3	289.2	73	85.1	-67.9	103	-156.4	-324.8
14	-101	80.5	44	173.6	360.4	74	116.9	-93.2	104	-16.3	-13
15	-135.6	108.1	45	25.9	20.7	75	154.3	-123.1	105	-35.5	-28.3
16	-176.5	140.7	46	46.9	37.4	76	198.6	-158.4	106	-58.3	-46.5
17	-224.8	179.3	47	71.7	57.2	77	250.9	-200.1	107	-85.1	-67.9
18	-281.8	224.8	48	101	80.5	78	312.7	-249.4	108	-116.9	-93.2
19	-9	18.8	49	135.6	108.1	79	14.4	-29.9	109	-154.3	-123.1
20	-19.7	40.9	50	176.5	140.7	80	26	-54	110	-198.6	-158.4
21	-32.3	67.1	51	224.8	179.3	81	39.8	-82.6	111	-250.9	-200.1
22	-47.2	98.1	52	281.8	224.8	82	56	-116.4	112	-312.7	-249.4
23	-64.9	134.7	53	20.3	4.6	83	75.3	-156.3	113	-32.3	-7.4
24	-85.7	177.9	54	44.3	10.1	84	97.9	-203.4	114	-58.5	-13.3
25	-110.2	228.9	55	72.7	16.6	85	124.7	-259	115	-89.4	-20.4
26	-139.3	289.2	56	106.2	24.2	86	156.4	-324.8	116	-125.9	-28.7
27	-173.6	360.4	57	145.7	33.3	87	0	-20.8	117	-169.1	-38.6
28	0	33.1	58	192.5	43.9	88	0	-45.5	118	-220.1	-50.2
29	0	60	59	247.7	56.5	89	0	-74.5	119	-280.3	-64
30	0	91.7	60	312.9	71.4	90	0	-108.9	120	-351.4	-80.2

Table 6: (X, Y) Coordinates (X, Y) in mm of all 120 microphones (relative to the central microphone #1)

4.1.11 Slat tracks

4.1.11.1 Slat tracks designs

In AWT@NLR, 14 slat tracks (6 proposed by DAV, 4 by NLR and 4 by Airbus/DLR) have been tested on the "VALIANT-like" flapless F16 model with 30° sweep, only based on acoustic measurements, and only with the continuous 2.5D slat. The same 14 slat tracks have been tested in F2 on the 3-element F16 model, also with the 30° sweep. The main characteristics of these 14 slat tracks are given here after.

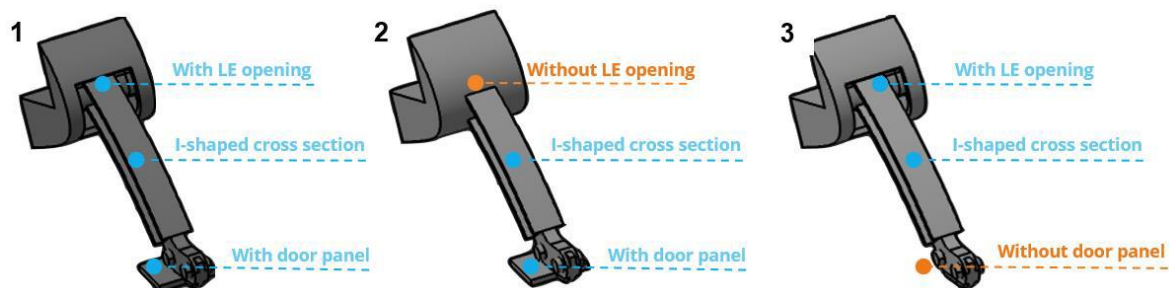


Figure 32: Baseline slat track

Figure 32 shows baseline or generic slat tracks #1 #2 and 3 proposed by DAV, which objective was to investigate the influence of the door panel and the opening cavity in the wing leading edge.

Figure 33 shows low-noise slat tracks proposed by DAV. The leading edge cavity is omitted since previous studies showed that this is the dominating slat track noise source, which has been confirmed by NLR. The slat tracks #4, #5 and #6 are equipped with upstream/downstream fairings which aim at avoiding separation and consequently reduce the noise.



Figure 33: Low-noise slat track designs with upstream and or downstream fairing

Finally, Figure 34 shows a set of low-noise slat tracks which were designed by NLR using RANS computations, which showed two noise generating mechanisms. The first and dominating mechanism is the separated flow located close to the connection between the slat track and main wing. To reduce the noise created by this source a tilted fairing (#7 and #8) was designed, where the tilt angle is the same as the one found from the RANS simulations. The second noise generating mechanism is caused by the cross-flow separating in a region close to the connection between the slat and slat track. To reduce the noise created by this source, an open slat track design is designed (#8 and #9) such that the cross-flow will not be obstructed by the slat track. Finally, the slat track is #10 is tentatively aligned with the flow direction, whereas all slat tracks #1 to #9 are in the direction of the airfoil chord or normal to the airfoil leading edge.

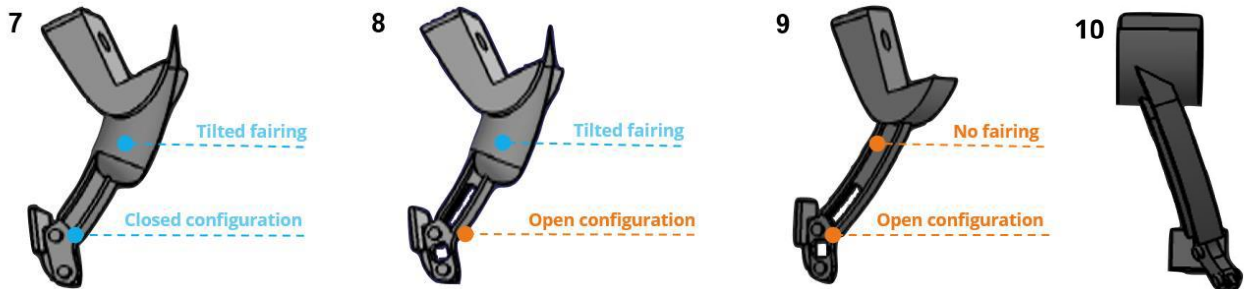


Figure 34: Low-noise slat track designs with a tilted fairing (#7 & #8) and/or opening (#8 & #9) and flow-aligned (#10)
One last set of slat tracks #11 to #14, proposed by Airbus and DLR is presented on

Figure 35 shows the slat track set proposed by DLR, based on an Airbus geometry proposed and used in the German INTONE project. Note that these designs are not representative of "real life" slat tracks, the main focus of this set is an investigation of small differences in the thickness exposed to the transverse or spanwise velocity component in the slat cove.

Note that these 4 slat tracks were not designed to fit the new 3 slat track pockets implemented in the wing leading edge, they are simply equipped with a foot that reproduces the shape of the wing LE and had to be attached simply using adhesive tape.



Figure 35: Slat tracks provided by DLR, based on an Airbus design (INTONE project)

4.1.11.2 Slat tracks implementation

3 slat track pockets have been manufactured on the central wing element, providing 3 possible slat track positions (see Figure 25 and Figure 26), located respectively at LY = -104, -138 and -172 mm from the mid span of the wing element. Note that slat tracks are only attached to the wing, not to the slat. Figure 36 shows the baseline slat track #1 installed in the pocket #2 (2.5D slat, left), in the pocket #3 (inboard slat side edge, center) and in the pocket #1 (outboard slat side edge, right).

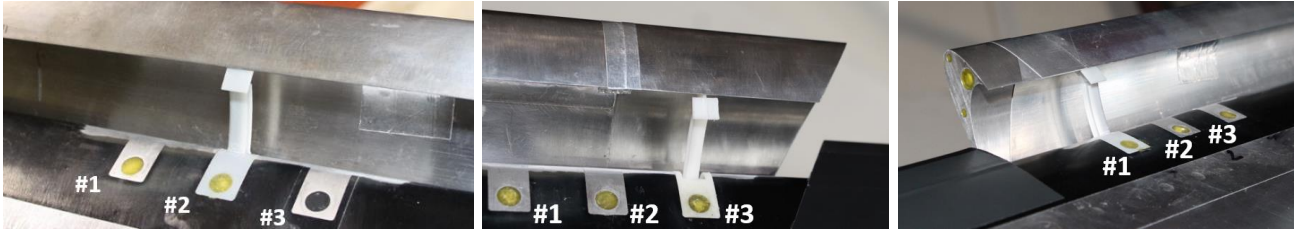


Figure 36: Slat track #1 installed in pocket #2 (2.5D slat, left), pocket #3 (inboard SSE, center) and pocket #1 (outboard SSE, right)

4.1.12 Slat porous inserts

4.1.12.1 Synthesis of tested porous inserts

Table 7 provides information about all the slat porous inserts that have been tested on the F16 model in AAWT (UoB, no flap, no sweep) and F2 (ONERA, 3-element, 30° sweep).

Tests in Bristol (see section 3.4.2,) involved slat porous inserts installed at the bottom of the slat cavity. 5 different concepts were tested: (i) a metallic foam beneath a wiremesh, proposed by DLR, (ii) three inserts based on the "Diamond Cell" structure of various dimensions (3.5, 4.5, 6.36 mm), designed by TUDelft and 3D printed by TCDublin, and (iii) one concept based on a fine "Kelvin Cell", designed and 3D printed by TCDublin. These tests used a special slat element labeled "J" of span 800 mm (visible on Figure 14 and Figure 37) equipped with two insert cavities of span 300 mm each (see also next section), with a non-treated span of 40 mm between them.

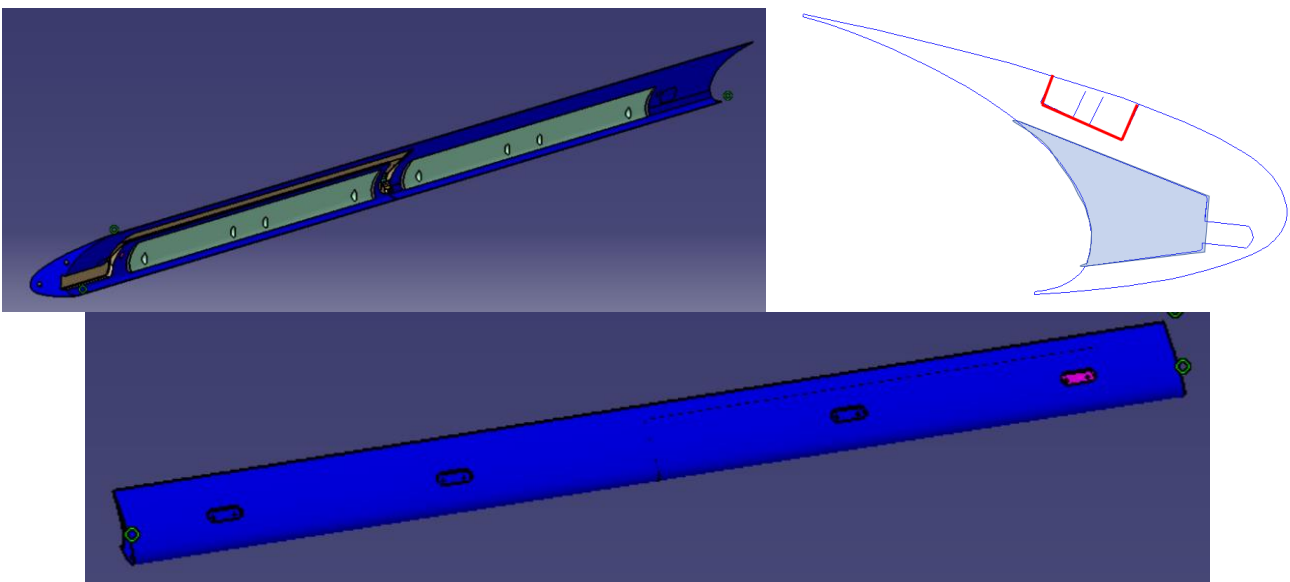


Figure 37: Slat central element "J" (span 800 mm) for porous inserts installed at the bottom of the slat cavity

Most of the porous inserts were 3D printed, with maximum dimensions limited by the printer, so each cavity received two inserts of length 150 mm. As explained in section 3.4.2 (and detailed in [5]), these inserts installed at the bottom of the slat cavity mainly worked as nearfield sound absorbers, with modest benefits on the farfield noise. Following this analysis, the tests to be achieved in F2 were slightly reoriented.








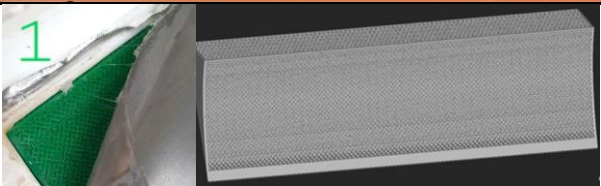
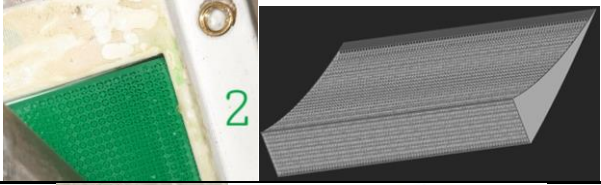
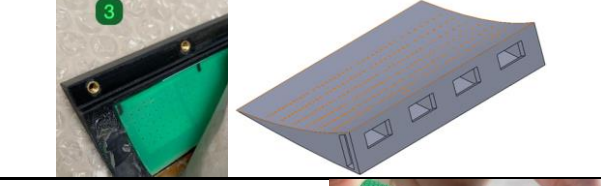



Material name concept, provider	Position	Pictures	Tested in		
			UoB	F2	AWB
Metallic foam beneath a wiremesh (DLR)	Slat cover		Yes	Yes	
Diamond Cell – TUD Large 6.36 mm	Slat cover		Yes	No	
Diamond Cell – TUD Large 4.5 mm	Slat cover		Yes	Yes	
Diamond Cell – TUD Large 3.5 mm	Slat cover		Yes	Yes	
Kelvin Cell -TCD "TCD fabric"	Slat cover		Yes	No	
Kelvin Cell -TCD "TCD very fine"	Slat cover		No	Yes	
TCD - MPPA	Slat cover		No	Yes	
TE#1 (Onera name) TCD Kelvin 2 (DLR) Solid ends/tips <i>Received "ready-to-test" by ONERA</i>	Slat TE		No	Yes	
TE#2 (Onera name) TCD Kelvin 1 (DLR) Solid ends/tips <i>Received "ready-to-test" by ONERA</i>	Slat TE		No	Yes	
TE#3 (Onera name) MPPA Lattice (DLR/TCD) <i>Received "ready-to-test" by ONERA</i>	Slat TE		No	Yes	
TE#4 (Onera name) TUD Diamond Lattice <i>Assembled on-site by ONERA (Diamond lattice confirmed)</i>	Slat TE		No	Yes	
TE#5 (Onera name) Material: ? <i>Assembled on-site by ONERA : felt and wiremesh</i> According to DLR : felt	Slat TE		No	Yes	
TE#6 (DLR name) Felt and wire mesh	Slat TE		No	No	
TE#7 (DLR name) Metallic foam and wire mesh	Slat TE		No	No	

Table 7: Synthesis of all slat porous inserts tested in UoB (AAWT), ONERA (F2) and DLR (AWB)

- Despite the modest acoustic outcome from the Bristol campaign, it was decided to test again the same inserts in F2, this time with the additional influence of the sweep angle, except 1/ the

largest Diamond Cell insert (6.36 mm) which showed no significant benefit, and 2/ the "Kelvin Cell" from TCDublin, which very fine structure unfortunately tent to shrink with time, with permanent damages.

- TCDublin decided to design and 3D print two more inserts installed in the same position, with different and more promising structure, (i) another very fine "Kelvin Cell lattice" structure with better mechanical resistance and a (ii) new material named MPPA.
- Since the insert position at the bottom of the slat cavity was assumed to bring little acoustic benefits, it was decided to test the same materials, but this time installed close to the slat trailing edge and the position of the stagnation point of the slat cove shear layer, with the objective of damping the interaction of this shear layer with the slat suction side, and thus mitigate the noise generated by this interaction. For this purpose, another slat element of span 800 mm was used (here after labeled "N") equipped with interchangeable trailing edges in which shallow cavities were filled with porous materials and covered with a glued wiremesh. 3 different ready-to-test trailing edges (TE#1, TE#2 and TE#3) were sent "ready-to-test" by DLR to ONERA, and 2 more (TE#4 and TE#5) were sent with porous materials just 3D-printed by TCDublin, to be assembled on-site by the F2 team.

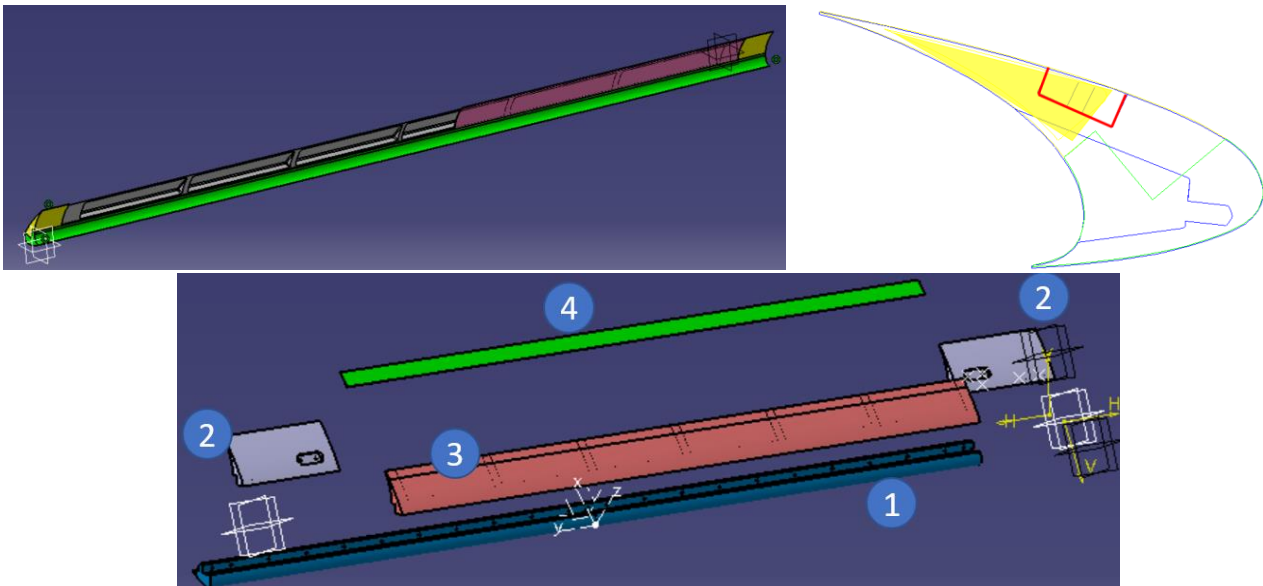


Figure 38: Slat central element "N" (span 800 mm) for porous inserts installed at the slat trailing edge (yellow zone). Leading edge and cusp (1), left/right hand upper slat parts slat brackets footprints (2), slat main body with cavities on the rear side (3), slat trailing edge (4)

Note that after these two campaigns, additional measurements have been achieved by DLR in AWB on the same model configuration as in F2, with 2 additional "TE" inserts (TE#6 and TE#7).

4.1.12.2 Adjustment of central slat elements "J" and "N"

Slat elements "J" (see Figure 37) and "N" (see Figure 38) have been used by DLR in past projects for tests of slat porous inserts of the F16 model of span 800 mm (e.g. in AWB@DLR and AAWT@UOB), but they had never been tested with the specific slat extensions built for F2 (named "D" and "F" on Figure 22), and the mechanical compatibility between all elements could not be checked before the INVENTOR tests. Unfortunately, as shown on Figure 39, a slight misalignment of the slat cusp (about 1.6 mm) and trailing edge (about 2.9 mm) was discovered in F2, which resulted in a significant difference of 3° between the slat angle of the elements "J" and "N" (about 24.8°) and the extensions "D" and "F" (27.8°, see Table 1).

For the acoustic tests these misalignments were smoothed using adhesive metallic tape and were not found to generate identified spurious noise.

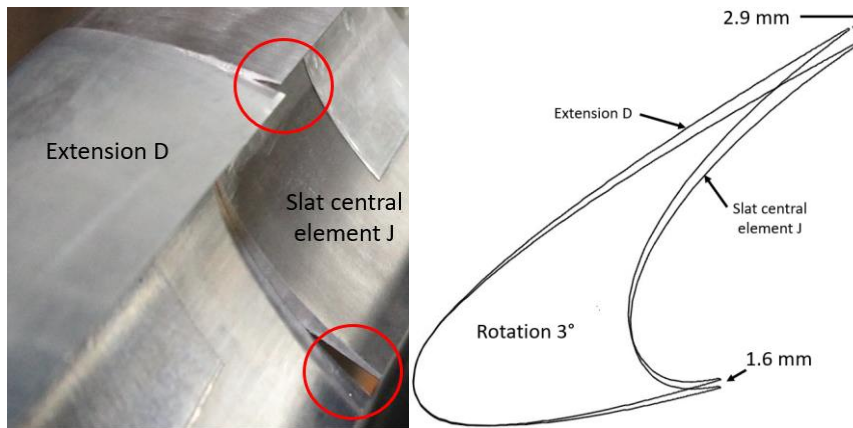


Figure 39: Misalignment between central elements J - N (used for porous inserts tests) with slat extensions D and F

4.1.13 Combination of slat track / slat side edges and slat porous insert

Porous inserts have been tested in priority on the 2.5D continuous slat (for comparison to UBRI with additional influence of sweep).

There was of course an interest to test these inserts with inboard/outboard slat side-edge(s), to investigate a possible noise mitigation. Since porous inserts were only compatible with the inboard slat side-edge configuration (Figure 25) none of them was tested with porous inserts.

However, there was definitely an agreed interest in simultaneously testing a slat track and a porous insert to investigate a possible mitigation of slat track noise by the porous insert. This was achieved with the generic slat track #1 in position (pocket) #2 with the "DLR metallic foam" and TUD Diamond Cell fine and medium inserts, and only for acoustics (no aerodynamic measurements)

4.2 Model deformation under aerodynamic loads

During the LEISA2 test campaign, it was observed that the mechanical assembly of the "old" central element and the new lateral extensions was somewhat flexible, leading to a vertical translation of several millimeters of the model under aerodynamic loads. This translation was calibrated with the LDV system for several velocities and incidences, then used to correct the position of the model in the PIV maps (LDV measurements were unaffected, because the LDV reference point is always chosen under aerodynamic loads).

In the SWAHILI test campaign, the sweep angle increased the model span (1.6 m instead of 1.4 m), and thus its flexibility. In that case, an original method was developed by the F2 team, derived from the classic PIV statistical process, which was also used in INVENTOR. It is based on the fact that the airfoil surface is typically clearly visible on PIV images, as it strongly reflects the laser light. For flow measurements, we tentatively suppress or mitigate these reflections because they tend to spoil the measurements. In this case they are very useful: applying the classic PIV image processing to two PIV images, one taken at velocity 0 m/s and one at the operating windtunnel velocity, and considering a "fake" time interval of 1 second between both, provides evaluation of "fake" velocity components (in m/s) that are directly read as of the displacements, in meters, then in millimeters. Figure 40 shows a typical example of PIV maps measured in a (LX, Z) plane, colored by the "fake velocity" components (U, W), directly read as displacements (dX, dZ) in the LX (chord) and Z (vertical) directions.

The left side map on Figure 40 shows that the displacement dX in the chord direction is rather small, typically of the order of 1 mm, which was considered as an averaged value for the full model, whatever the (LX, LY) position and the slat configuration.

The right side map on Figure 40 shows that the vertical dZ displacement is much larger (order of 10 mm) and typically depends on the LX position on the slat and the main wing. Such PIV measurements have been achieved at several LY positions by moving the PIV laser sheet over a total spanwise distance of about 200 mm. From the plot of dZ function of LX and LY, a linear law $dZ = a LX + b LY + c$ can be easily derived via a linear regression algorithm.

This process was repeated for the 3 slat configurations (continuous and inboard/outboard slat side edges) with different results due to different aerodynamic loads and different mechanical flexibility of the slat elements.

Th results will be mainly used to correctly position the flow velocity maps measured by PIV with respect to the model.

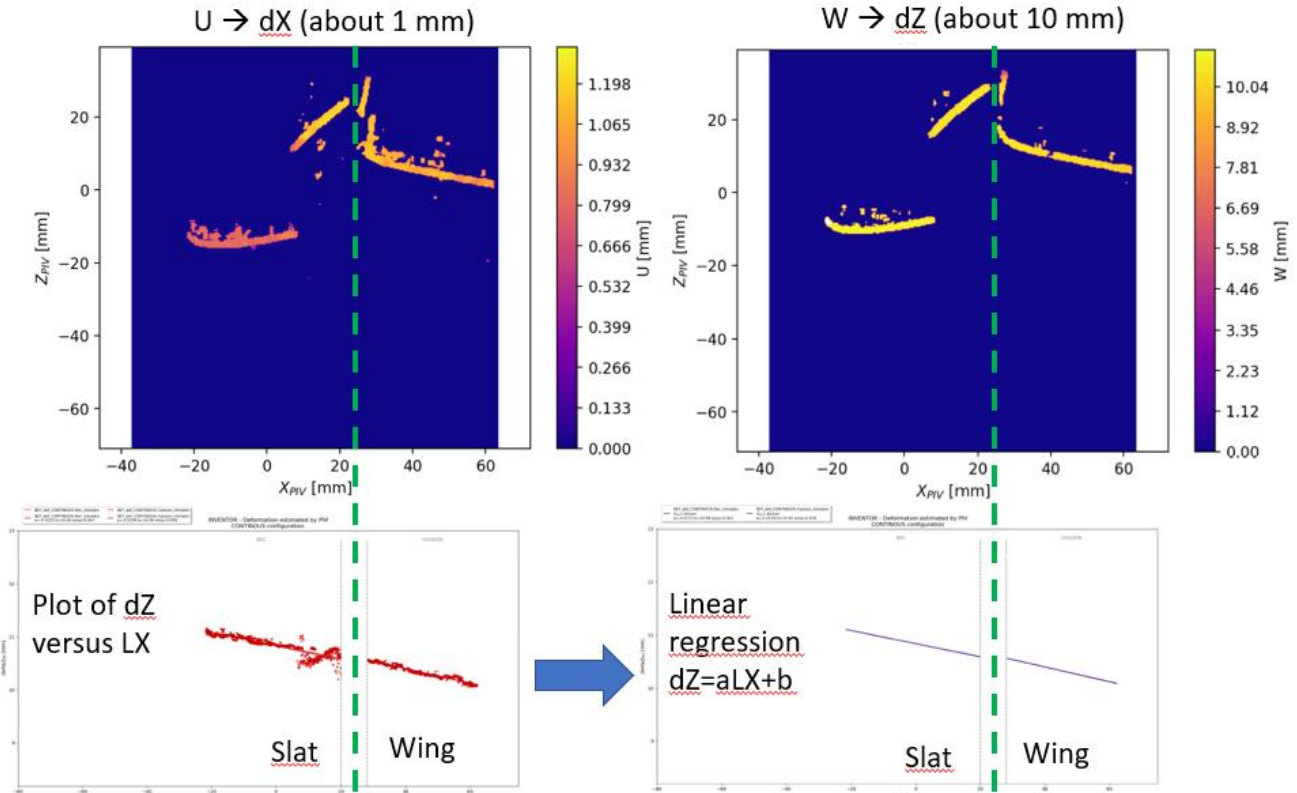


Figure 40: Measurement of model deformation using PIV

4.3 Wall pressure measurements

4.3.1 Introduction and test matrix

This section 4.3 covers the achievement and exploitation of all acoustic and wall pressure measurements achieved with the static pressure taps and Kulite sensors implemented on the model and the 120-microphone array located at the windtunnel ceiling.

The INVENTOR tests began with these acoustic and wall pressure acquisitions for all possible configurations, then the tests continued with aerodynamic measurements based on PIV and LDV. This task order, already used in LEISA2 and SWAHILI, was suggested by several reasons:

- These pressure sensors are generally not compatible with the seeding of particles (typically olive oil smoke) used for PIV and LDV in F2, which makes risky to operate both simultaneously.
- For the configurations considered in INVENTOR, the PIV measurements were achieved with the laser emission located on the WT ceiling, with the laser sheet crossing a glass window. This instrumentation is not compatible with the implementation of the microphone array, also in the WT ceiling.
- Moreover, the pressure taps are typically necessary for the initial incidence calibration, and also acoustic measurements are generally a selection criterion for further aerodynamic measurements, this is why the campaigns typically started with these pressure measurements.

In terms of test matrix, each model configuration (combination of slat side edge type, slat track and/or slat porous insert) was tested at 4 windtunnel velocities (40, 50, 60 and 71 m/s) and 3 model angle-of-attacks 3.0°, 5.3° and 7.6°, which means 12 acquisitions. Moreover, measurements were

achieved with the empty test section for background noise evaluations at 10, 20, 30, 40, 50, 60, 71, 80, 90 and 100 m/s.

- The 3 slat configurations (continuous 2.5D, inboard/outboard slat side edge) were tested without any slat track nor slat porous inserts (baseline).
- In the continuous (2.5D) slat configuration, all 14 slat tracks were tested in the median position #2, and all slat porous inserts listed in Table 7 were also tested. Moreover, three porous inserts ("DLR" metallic foam and "TUD Diamond lattice" fine (4.5 mm) and very fine (3.5 mm) were tested with the generic slat track #1 in position #2.
- In the outboard (respectively inboard) slat side edge configuration, the influence of the distance between the slat side edge and the slat track was measured with slat tracks #1 and #2 in positions #1, #2 and #3 at all 12 velocity/incidence combinations. Then all slat tracks #1 to #11 were tested in position #1 (respectively position #3) which is the closest to the slat side edge, but only at 6 velocity/incidence combinations (4 velocities at 5.3° and 3 incidences at 71 m/s).

4.3.2 Wall static pressure measurements

This section provides basic results of static pressure measurements from the model section equipped with pressure taps, described in section 4.1.6.1 and on Figure 23.

Figure 41 (left side) is a reproducibility test between the SWAHILI measurements achieved in 2016 and the INVENTOR results obtained with same model configuration (71 m/s and 5.3° , continuous slat). As reminded in section 4.1.6.1, the SWAHILI measurements at the wing leading edge were achieved with Kulite sensors operated in DC mode, whereas INVENTOR used additional static pressure taps at these positions, so this result is an *a posteriori* validation of the technique using Kulite sensors.

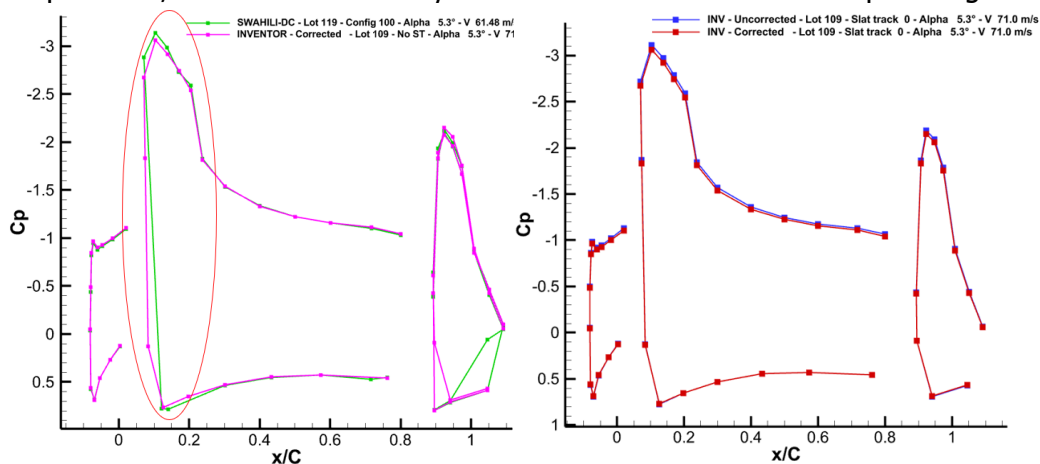


Figure 41: Static pressure on the model, continuous slat, no slat tracks, no porous inserts. Left: reproducibility with SWAHILI. Right: influence of blockage correction

Figure 41 (right side) compares the C_p corrected from the confinement/blockage effect in the F2 closed test section, using the static pressure measurements along 2 axial lines of 30 static pressure taps on the floor and the ceiling of the windtunnel. Uncorrected values are for comparison with CFD computations taking into account the windtunnel test set-up, whereas corrected values are for the comparison with CFD computations in free field. Note that the effect is weak.

Figure 42 shows typical influence of incidence at 71 m/s (left) and velocity at 5.3° (right), for the configuration with the continuous slat, no slat tracks, no porous inserts. The velocity has almost no influence since pressure coefficients are normalized by the dynamic pressure, whereas increasing the airfoil angle of attack typically generates higher flow velocities on the suction side of the slat and the wing leading edge.

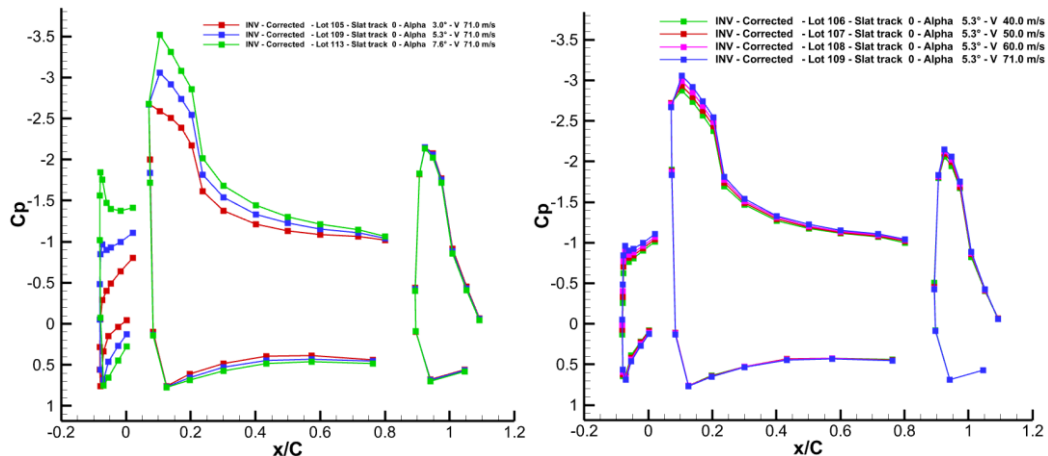


Figure 42: Static pressure on the model, continuous slat, no slat tracks, no porous inserts. Influence of incidence at 71 m/s (left) and velocity at 5.3° (right)

Finally, Figure 43 shows C_p measured with all 14 different slat tracks at velocity 71 m/s and incidence 5.3°. There is no significant effect, as expected considering the distance of about 96 mm between the slat track and the static pressure taps. For all other model configurations tested in INVENTOR (inboard/outboard slat side edge with/without slat tracks and all slat porous inserts, the slat elements had no static pressure taps, so the C_p can be only provided on the main element and the flap, which is not of significant interest and not presented here.

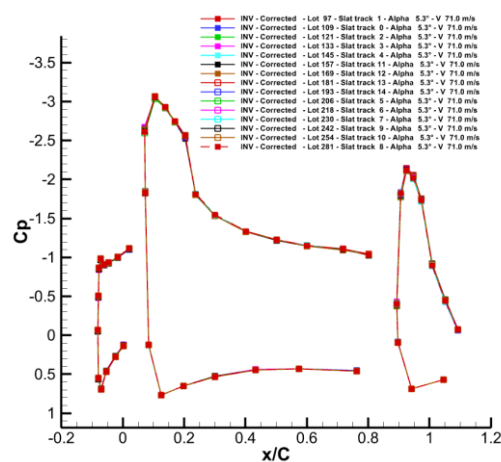


Figure 43: Static pressure on the model, continuous slat, no porous inserts. Influence of the slat track in position #2

4.3.3 Wall unsteady pressure measurements

This section presents a selection of results obtained with the Kulite sensors implemented on the leading edge of the main element (see the implementation and coordinates on Figure 24 / Table 4.

4.3.3.1 Influence of slat track

Figure 44 shows the power spectral densities of the pressure fluctuations measured by the Kulite sensor #11 (top left) without slat track (black line) and with all DAV/NLR slat track designs #1 to #10 (colored lines) installed in the pocket #2. This pocket #2 is located at $LY = -138$ mm from the midspan section of the main wing, whereas Kulite #11 is at $LY = -120$ mm, which means that the sensor is only 18 mm "downstream" (with respect to the spanwise flow generated by the sweep) of the slat track (see Figure 24). Consequently, this sensor is assumed to capture the hydrodynamic pressure fluctuations convected in the wake of the slat track: indeed, all PSDs measured with slat tracks are above the PSD without slat track, which makes sense. However, the hierarchy of the 10 slat track designs in terms of these local PSD levels is surprisingly different than what is observed in terms of radiated noise, see for example Figure 50 which displays, with the same color legend, the noise radiated by a small region including the slat track, measured by the microphone array. This is especially clear for slat tracks #1 and #3, which are found to be the noisiest in the farfield, mainly due to the open cavity at the wing leading edge, but which appear to generate the weakest local hydrodynamic pressure fluctuations. This is difficult to interpret/analyze, because local pressure sensors measure very energetic small structures whereas farfield microphone measure acoustic waves with low amplitude and large wavelengths, and the local source of this sound radiation might be

hidden by other energetic mechanisms with different characteristic frequencies but less radiative effect. On the same Figure 44 (top right), Kulite #9, located at LY = -30 mm, shows similar hierarchy between the slat tracks, but with less differences in amplitude, because of the larger distance (108 mm) to the slat track position #2. Finally, Figure 44 (bottom left) also displays measurements by Kulite #8 which is located at LY = 0, close to the main wing stagnation point at the pressure side. At this position the slat track design has apparently little influence on the PSD of surface pressure. However, we tentatively computed the OASPL integrated in the frequency band [7-18] kHz and normalized them with the OASPL of the configuration without slat track. These normalized OASPL are displayed on Figure 44 (bottom right), function of the slat track number, #1 to #10 for the DAV/NLR designs and #11 to #14 for the DLR/AI designs. This result shows a ranking between the slat tracks that is, at least qualitatively, close to the acoustic ranking derived from the OASPL of farfield noise presented on Figure 52 and Figure 54, except that the maximum deltas between slat tracks is about 1.5 dB in nearfield compared to 12 dB in farfield. This might be explained by the fact this Kulite sensor #8 is dominated by local hydrodynamic fluctuations which do not depend on the slat track design, but also captures much weaker acoustic radiations which are specific of each slat track design.

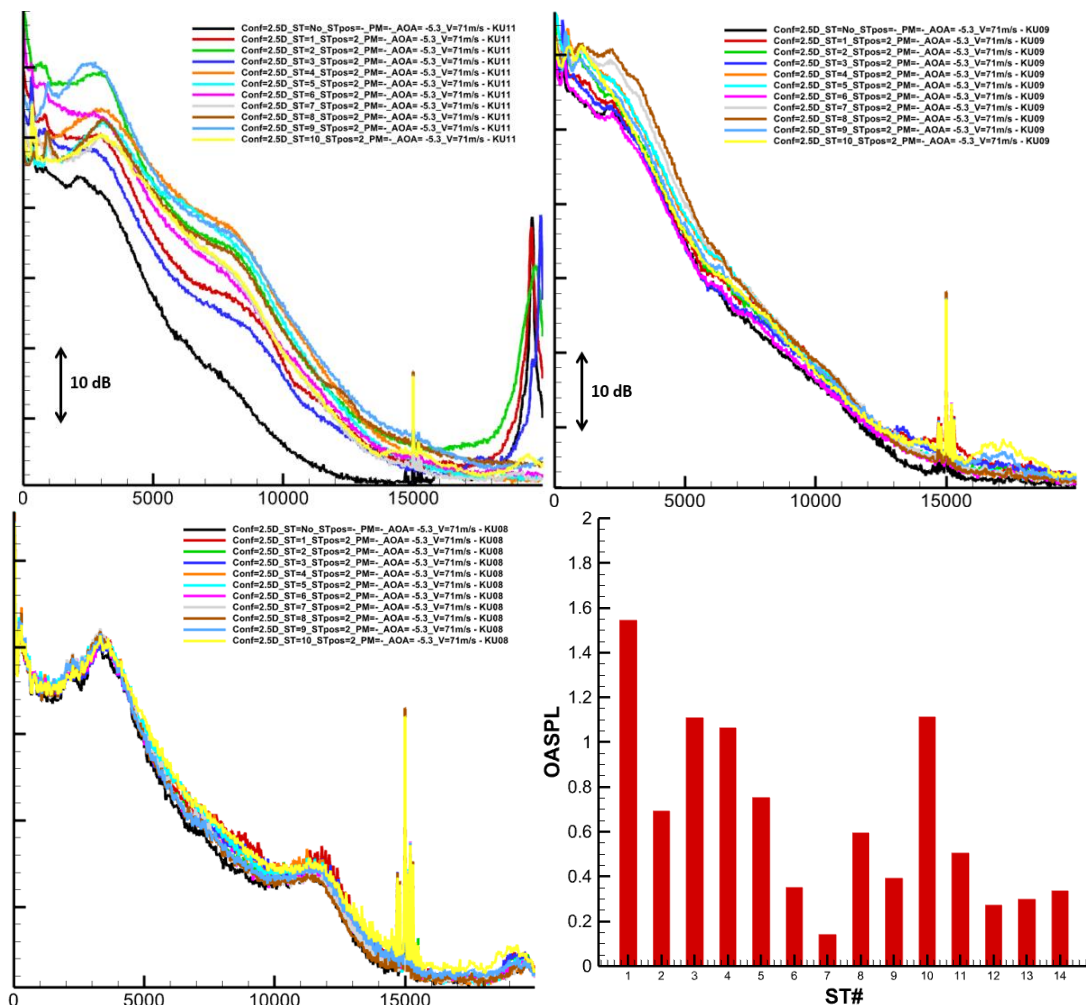


Figure 44: PSD of the pressure fluctuations measured by Kulite sensor #11 (top left) #9 (top right) and #8 (bottom left) for all DAV/NLR slat tracks (#1 to #10) in position #2 (71 m/s and 5.3°). Bottom right: OASPL [7-18] kHz measured by Kulite sensor #8 at 60 m/s and 5.3° for all slat tracks.

4.3.3.2 Influence of slat porous insert

On the slat special element "J" (Figure 37), two porous inserts of length 300 mm could be installed at the bottom of the slat cove, with a central non-treated zone of length 40 mm in between. Due to the span shift of -42.2 mm of the slat with respect to the main wing, the "upstream" porous insert is located in the range $-362.2 < LY < -62.2$ mm, so only Kulite sensors #11 and #12, respectively located

at LY=-120 mm and -240 mm are positioned in front of this porous insert, and might detect an influence of these inserts on the local pressure fluctuations.

In this respect, Figure 45 (top) shows the PSD of the pressure fluctuations measured by Kulites #11 (left) and #12 (right) with the porous inserts installed on the slat element "J" at the bottom of the slat cove ("Bristol type"). The black line corresponds to the case of hard inserts, which is considered as the reference without treatment. An interesting (but confusing) result is that these porous inserts do not actually damp the local pressure fluctuations measured by the Kulites on the main wing: on the contrary, most porous inserts apparently increase these fluctuations, except the TCD-MPPA and the TCD-Lattice. This does not mean that such porous materials are not efficient in reducing noise, as it will be observed on Figure 63 in terms of noise radiated in farfield.

Figure 45 (bottom) shows similar results for the porous inserts installed on the slat element "N" close to the slat trailing edge. We suppose that Kulite sensors "11 and #12 are also located in front of these inserts, which are typically designed to damp the local pressure fluctuations in the slat cove, which is actually observed, especially on the spectra measured by Kulite #11 (bottom left), but with tones also observed in far field (Figure 64), that are still unexplained.

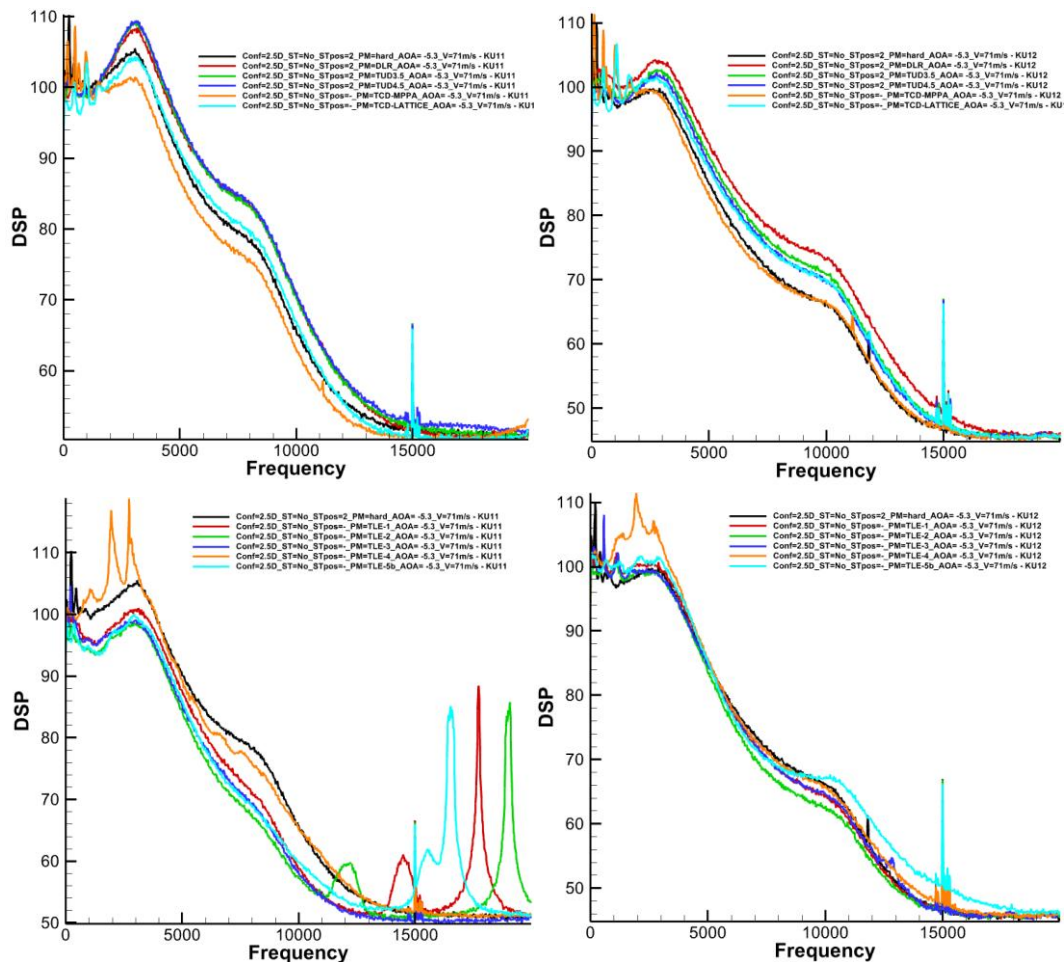


Figure 45: PSD of the pressure fluctuations measured by Kulite #11 (left) and #12 (right) at 71 m/s and 5.3° with:
Top: porous inserts installed on the slat element "J" at the bottom of the slat cove
Bottom: porous inserts installed on the slat element "N" at the slat trailing edge.
Black line: hard inserts on slat element "J" (reference).

4.4 Acoustic measurement

4.4.1 Introduction and test matrix

Acoustic measurements were achieved with the 120-microphone array described in section 4.1.10 and Figure 31, located at the windtunnel ceiling beneath a flush-mounted wiremesh cloth (see Figure 7). The same array has been used in the LEISA2, SWAHILI and INVENTOR programs.

4.4.2 Signal processing description

The array processing methods used by ONERA are derived from the well-known DAMAS [8] and DAMAS-C [9] microphone array techniques. Whatever the methodology is, the task consists in finding the optimal representation of noise sources reproducing the acoustic measurements, in particular the microphone cross-spectral matrix, as closely as possible. Different sources description could be considered, depending on the nature of the aeroacoustic source. To reproduce the directive acoustic pattern radiated by a jet, correlated sources distribution are generally privileged. Due to the large amount of variables to be identified, i.e. cross-spectra between numerous source terms, the problem is however poorly conditioned. To improve its stability, additional constraints, ideally based on physical requirements, need to be introduced, and the resolution could be very time consuming. For slat noise study addressed in this paper, a source model based on a distribution of uncorrelated monopoles is more convenient. It goes back to determine the diagonal of the source cross spectral matrix. Due to the reduced number of unknowns, the problem is better posed and could be solved in our case without regularization technique.

The task is to determine source parameters P , for instance the amplitude of the monopoles that optimally reproduce the microphone array measurements, specifically the microphone Cross-Spectral Matrix (CSM) Γ :

$$P = \arg \min \|\Gamma - \Gamma^{\text{model}}(P)\| \quad (\text{Equation 1})$$

where Γ^{model} is a model CSM. The acoustic pressure p_m generated from a set of N_s monopoles at the position of the m^{th} microphone is given by

$$p_m = \sum_{i=1}^{N_s} \alpha_i G_{i,m} \quad (\text{Equation 2})$$

where α_i is the amplitude of the i^{th} monopole and $G_{i,m}$ is the Green's function between i and m . Equation 2 is defined for a given frequency f . Thus, for uncorrelated monopoles, the model CSM is

$$\Gamma_{m,n}^{\text{model}}(C) = \sum_i G_{i,m} G_{i,n}^* s_i \quad (\text{Equation 3})$$

where s_i are the source auto-powers (for the frequency f).

In the present study, the propagation model used is the conventional free-field Green's function in uniform flow. The cross-spectral matrix of the microphone signals is computed with 2048-samples, non-overlapped and Hanning-windowed data blocks. With a sampling frequency of 131,072 Hz and an averaging over 1920 blocks, the resulting frequency resolution is equal to 64 Hz. The cross-spectral matrix is calibrated to correct the acoustic effects due to the microphone mounting [10][11].

The reverberation issue is addressed through the focusing performance of beamforming, that enables to spatially separate real acoustic sources within the test section from their images located outside the test section. The acoustic level is then determined with a deconvolution technique, by integrating the level of the real sources in the test section only. In this way, dereverberation depends on the spatial resolution of beamforming, so on the acoustic wave length, the size of the microphone array, the source-microphone distance. It also depends on the position and the intensity of the image sources, so on the geometry of the facility, the position of the model in the facility and the directivity pattern of the real noise sources.

For this purpose, the source distribution located in the airfoil plane at $Z = 0$ is extended in order to include the first image source by the lateral walls ($|Y| > 0.7$ m) and by the floor, as presented in Figure 46. Note that the floor is located 0.9 m below the airfoil, so the zone source extension is located 1.8 m below the airfoil.

The noise source spectra are calculated for a given zone by simply summing up all of the deconvolved source levels S_i over the zone area:

$$DSP_{\Omega}(f) = \sum_{i \in \Omega(f)}^{N_S} S_i(f) \quad (\text{Equation 4})$$

Figure 47 shows the different zones defined to extract the different components of interest for this study. The slat region is covered by (i) a central (yellow) zone including the 3 slat track positions and the inner/outer slat side edges, and (ii) a wider (green) zone including the full central slat element possibly equipped with slat porous inserts. The flap region is covered by only one (blue) region including about 70 % of the airfoil span. The regions where the airfoil intersects the walls are covered by specific (cyan and purple) zones.

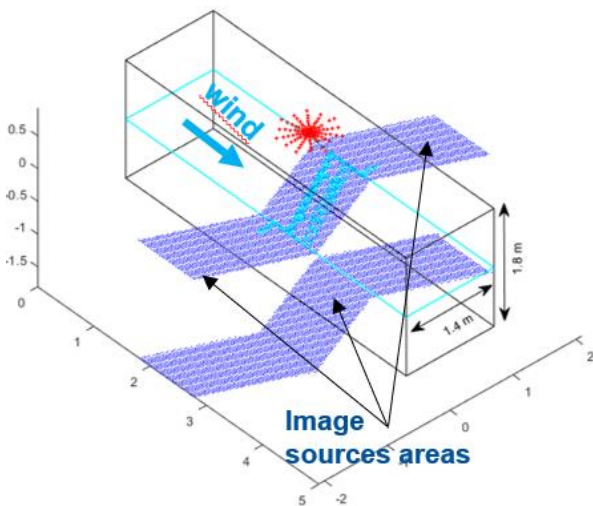


Figure 46: Scheme of the source distribution areas including image source zones

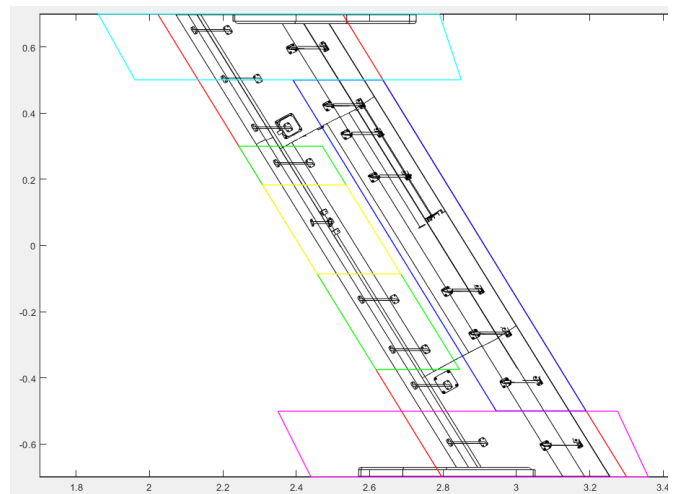


Figure 47: Description of the sources areas on the model pressure side silhouette. The airfoil is observed from the WT ceiling and microphone array. Flow is from left to right.

4.4.3 Slat track noise detection with the continuous slat

This analysis focused on the ability to extract the noise produced by a slat track from the global noise radiated inside the aerodynamic windtunnel closed test section, which is noisy and reverberant, thus typically not the best environment for acoustic measurements.

The raw results of the array processing exhibit very high level at the frontier of the point sources domain at low frequency of 2 kHz (Figure 48, left). This result is a consequence of the background noise of the wind tunnel mainly produced by the fan in the circuit. The interaction of the wall turbulent boundary layer with the airfoil produces also significant spurious noise. But, as these noise sources are well separated from the sources on the airfoil, they can be easily removed. At higher frequency (8 kHz) the signal to noise ratio is much better.

Figure 49 shows the ability of the array processing to detect the noise radiated by one slat track in this noisy and reverberant environment. These acoustics maps are obtained by focusing on the airfoil pressure side, comparing the results with and without a slat track implemented. We observe that the noise sources are the same for both maps excepted in the slat track area (yellow zone) where a strong source appears when the slat track is mounted. This result demonstrates the reproducibility of the method and its ability to isolate the noise generated by this small element.

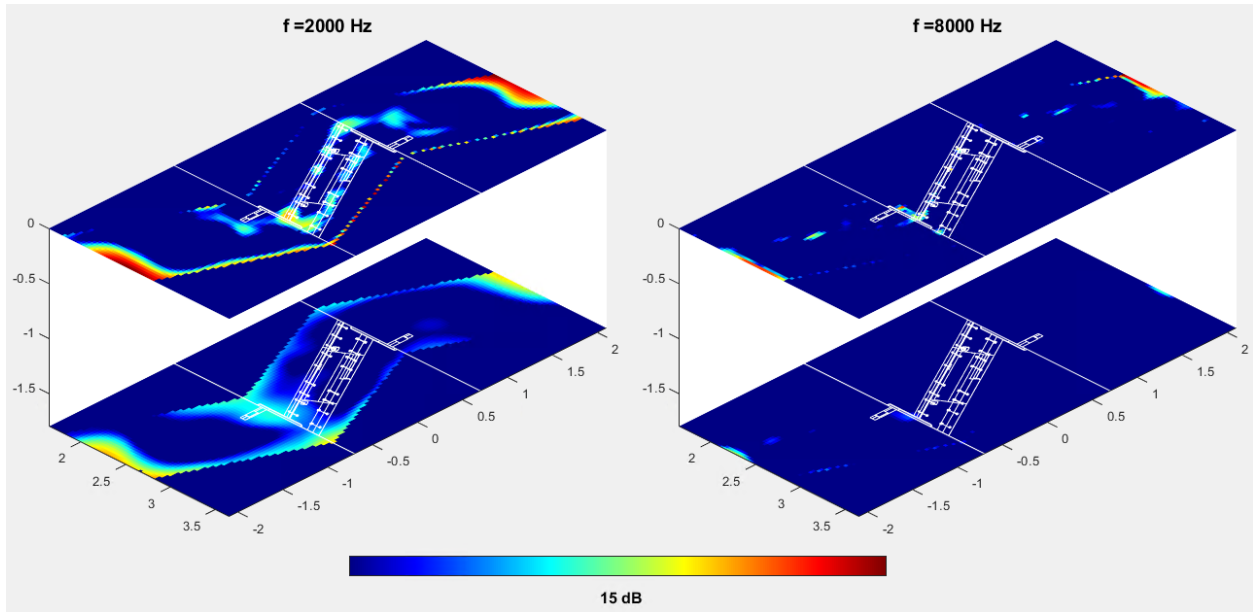


Figure 48: Raw third octave band noise source maps at 2 kHz (left) and 8 kHz (right). Continuous (2.5D) slat configuration with the baseline slat track #1

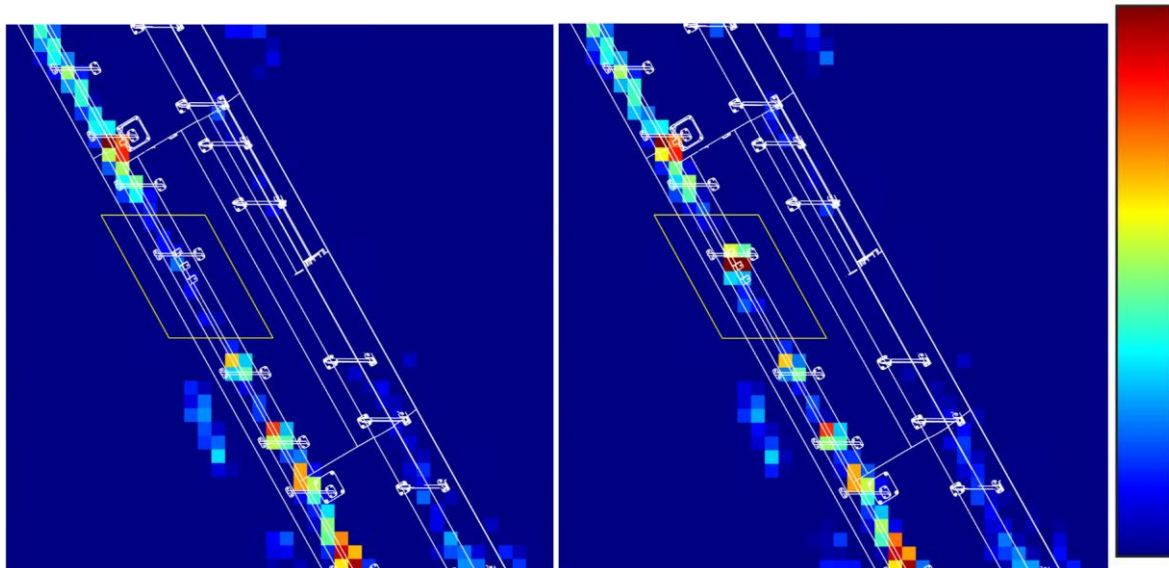


Figure 49: Third Octave Band acoustic map at 8 kHz. Left: without slat track, right: with baseline slat track ST #1.

4.4.4 Acoustic ranking of slat track designs with the continuous slat

The integration of noise sources in the slat track area (yellow trapezoid in Figure 47) of such noise map at any frequency of interest provides the slat track noise spectrum, which is qualitatively and quantitatively representative of the noise radiated by this specific area. This process has been applied for all tested slat track designs presented on Figure 32, Figure 33, Figure 34 and Figure 35.

The spectra corresponding to slat tracks with DAV/NLR designs (#1 to #10) are superimposed in Figure 50, along with the baseline where no slat track is installed. This result shows that the slat track noise (i) systematically emerges above the baseline (no slat tracks) over the whole frequency band of interest, (ii) and strongly depends on the slat track designs, especially above 7 kHz, and strong differences in noise levels (up to 15 dB) are observed, depending on the designs of the tested slat tracks.

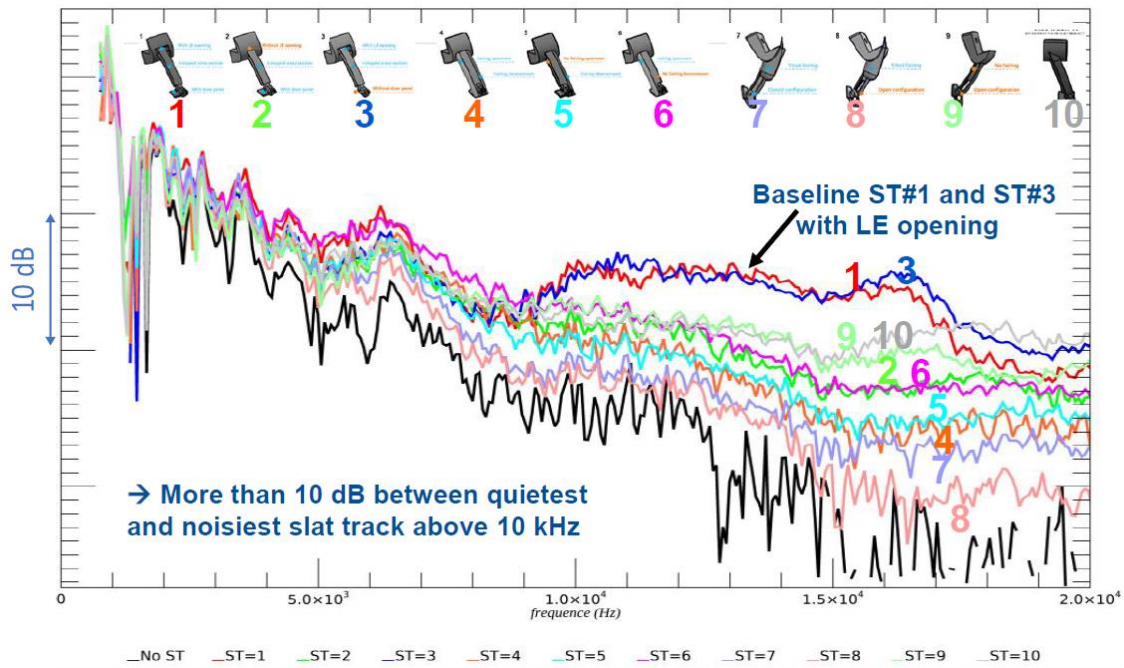


Figure 50: Comparison of integrated noise spectra for slat tracks designed by DAV/NLR #1 to #10 (60 m/s, 5.3°)

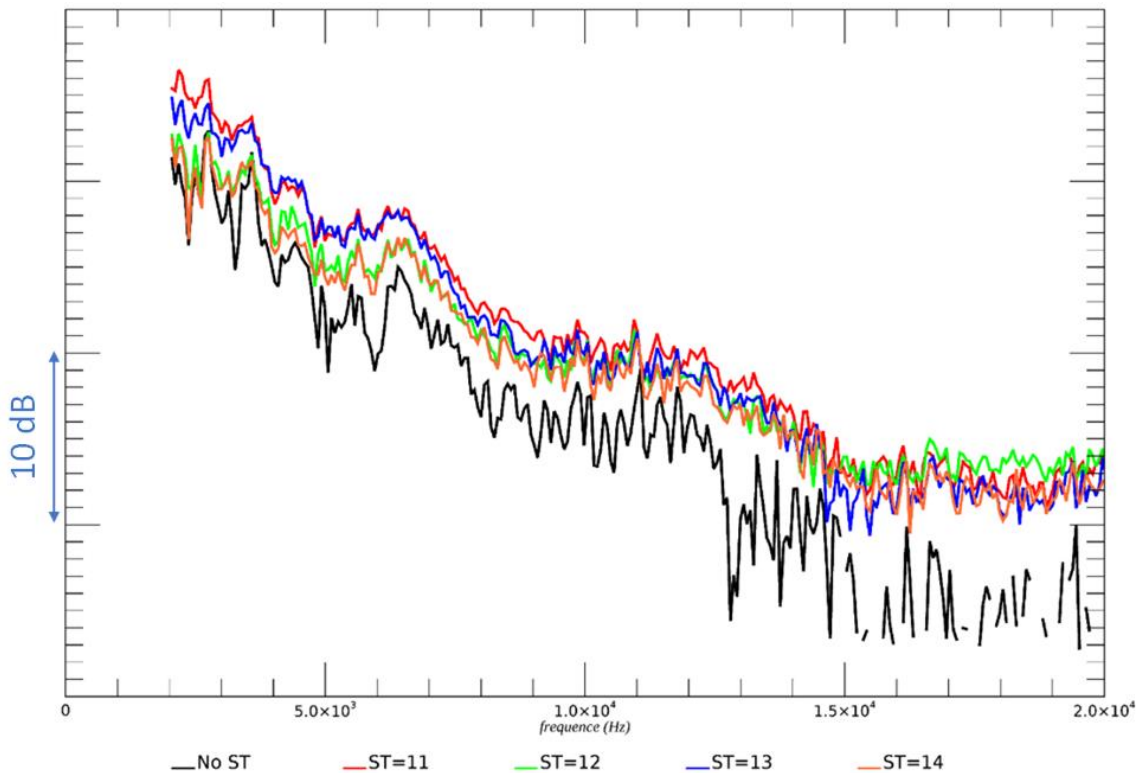


Figure 51: Comparison of integrated noise spectra for slat tracks designed by DLR #11 to #14 (60 m/s, 5.3°)

This comparison allows establishing an acoustic ranking between all slat track designs. The noisiest slat tracks are ST#1 and ST#3, which clearly results from the open cavity on the wing leading edge. Then the slat tracks with round leading/trailing edges are a good compromise, whereas the most silent slat tracks are the ST#7 and ST#8 with a tilted fairing, the best one (ST#8) with an opening. A similar comparison is presented on Figure 51 for the slat track designs proposed by DLR (ST#11 to ST#14, see Figure 35). Remember that these very simplified slat track geometries are not fully representative of “real life” slat tracks and were mainly aimed at assessing the effect of one specific geometrical parameter, the thickness.

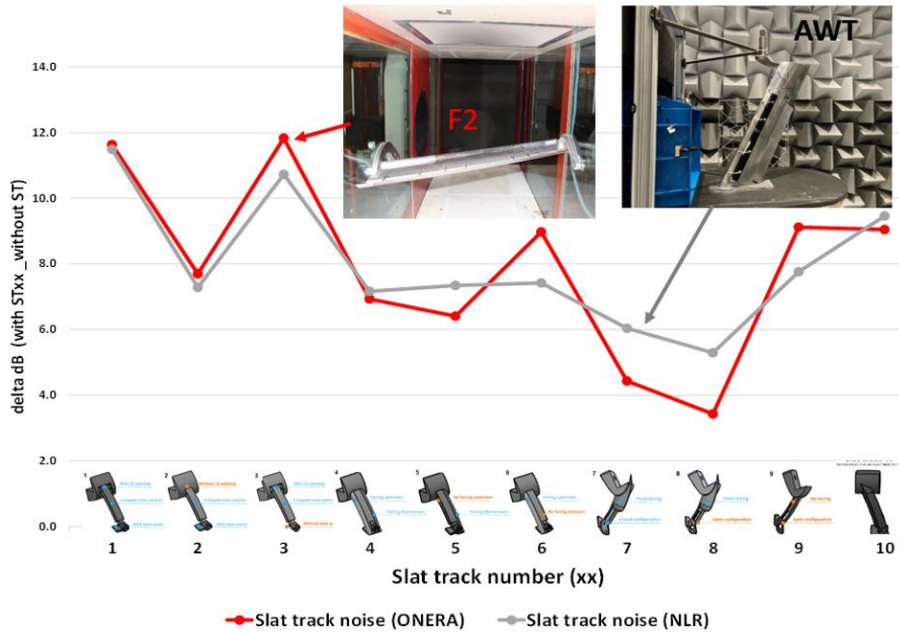


Figure 52: Comparison of the relative slat track noise results obtained in F2 and AWT at 60 m/s for the slat tracks designed by DAV/NLR ST#1 to ST#10. OASPL [7-18 kHz]

In order to assess the ability of these acoustic measurements in the aerodynamic wind tunnel F2, the results are compared on Figure 52 with those obtained through a similar test in the open anechoic wind tunnel AWT (NLR) [7], described in section 3.4.3 and on Figure 17 and Figure 18. The airfoil only differs by the absence of the flap and a modified main element trailing edge shape (red line on Figure 15) to reproduce the same static pressure distribution in the slat area. On Figure 52 the results obtained at 60 m/s in both wind tunnels, are compared in terms of overall sound pressure level integrated between 7 and 18 kHz, normalized with respect to the configurations without slat tracks in both facilities. Excepted for the slat track #6, a very good agreement is observed on the acoustic ranking of the different slat tracks obtained in both wind tunnel, which validates the capacity of this acoustic measurements in F2 for this purpose. To confirm the stability this acoustic ranking, Figure 53 shows similar results (F2 measurements only) at different model incidences, 3°, 5.3° and 7.6°.

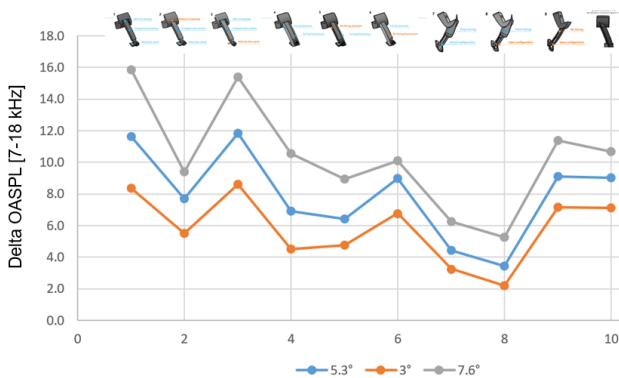


Figure 53: Comparison of the relative slat track noise results obtained in F2 at 60 m/s and AOAs 3°, 5.3° and 7.6° for the slat tracks designed by DAV/NLR #1 to #10

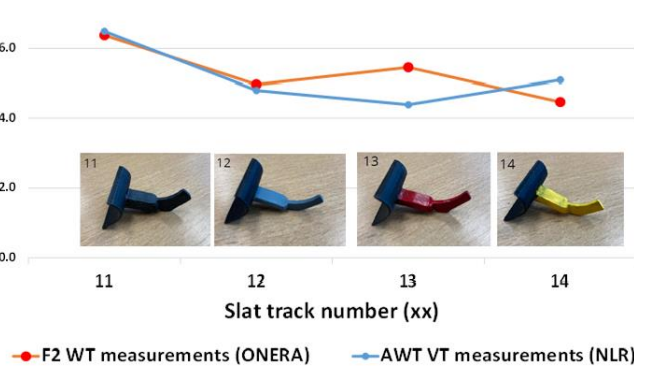


Figure 54 : Comparison of the relative slat track noise results obtained in F2 and AWT at 60 m/s for the slat tracks designed by DLR #11 to #14

Figure 54 presents the same comparison for the DLR/AI slat track designs and again underlines a good agreement between both windtunnel. Furthermore, it suggests that the noise slightly increases with the track thickness (thickest to thinnest: ST#11 > ST#14 > ST#13 > ST#12).

4.4.5 Slat side edge noise analysis (no slat track)

In the last paragraph, the acoustic assessment and ranking of the slat track designs were achieved with the continuous slat geometry.

In addition, two slat side edge configurations were also investigated, based on (i) an inboard slat side edge aligned with the flow (ISE, see section 4.1.7.2 and Figure 25) and (ii) an outboard slat side edge aligned with the airfoil chord (OSE, see section 4.1.7.3 and Figure 26).

In this section, we compare the noise generated by both side edge configurations ISE and OSE versus the continuous (or 2.5D) slat configuration, without any slat track installed.

The acoustic maps typically obtained at 1, 2, 4 and 8 kHz on the full airfoil via the array processing for the 3 slat configurations (2.5D, inboard/outboard slat side edge) are compared on Figure 55. Note that, for a fair quantitative comparison, at a given frequency, a common color scale is used for the 3 slat configurations. There is almost no noise source with the continuous 2.5D, which makes sense. On the contrary, the outboard slat side edge clearly displays stronger and more extended sources than the inboard SSE, at least at these frequencies below 8 kHz.

The trapezoidal yellow integration zone shown on Figure 55, already used for the acoustic ranking of slat tracks, was designed to include the positions of (i) both inboard/outboard slat side edges and (ii) the 3 pockets used for slat track implementation. When looking at the integrated spectra for the 3 slat configurations on Figure 56, either in absolute levels (left) or in deltas with respect to the continuous slat (right), it is interesting to see that the OSE is actually noisier than the ISE below 10 kHz, but this tendency is inverted above this frequency. Moreover, ISE and OSE are always noisier than the continuous slat, whatever the frequency.

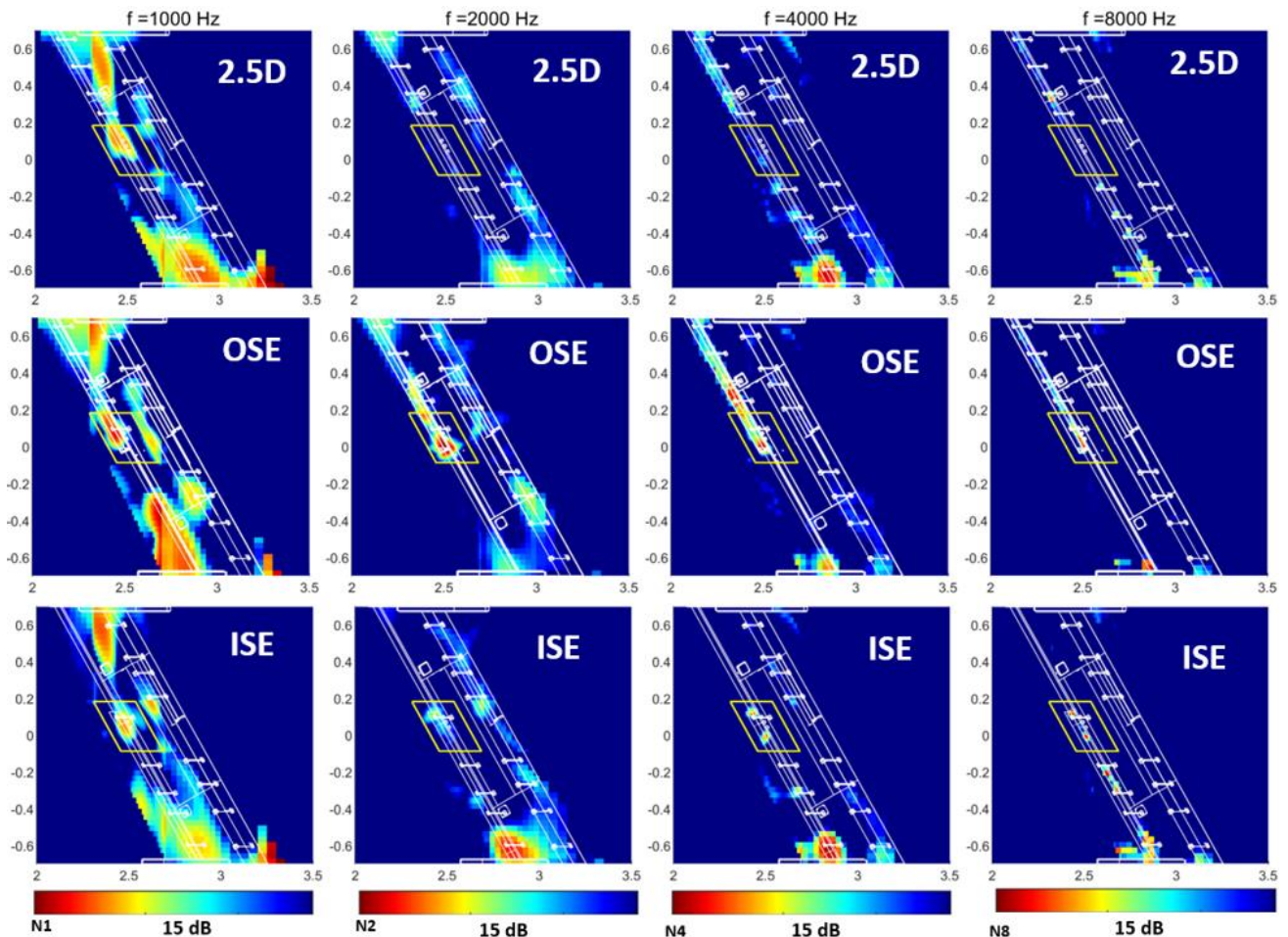


Figure 55: DMAS noise maps for the 3 slat configurations (2.5D: top, outboard SE: middle, inboard SSE: bottom) at 1, 2, 4 and 8 kHz

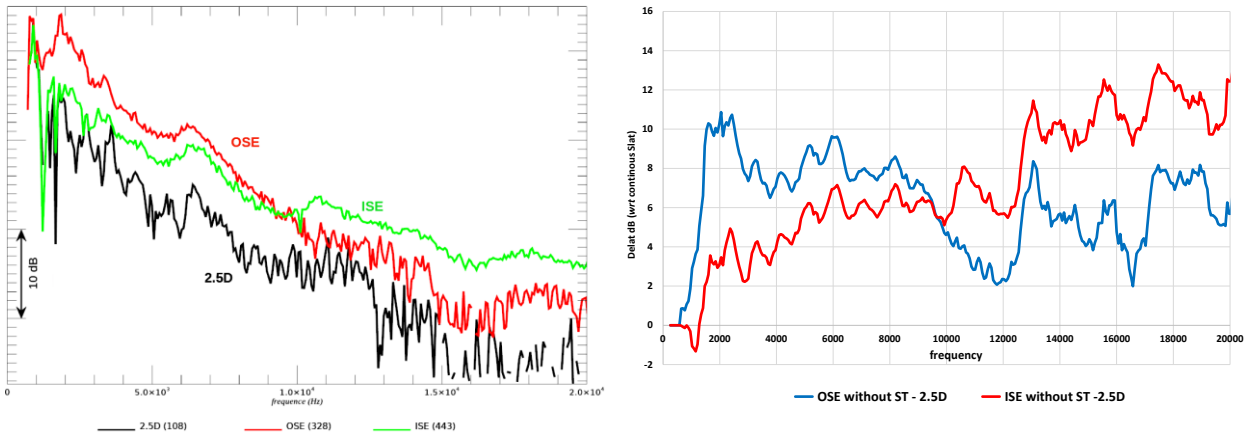


Figure 56: Slat side edge effect without slat track. Left: absolute levels. Right: deltas with respect to the continuous slat.

4.4.6 Influence of the slat side edge on slat track noise

In this section, we examine the influence of the slat side edge on the noise of a slat track installed at close distance of this side edge. Moreover, the influence of the distance between the slat side edge and the slat track is also investigated.

Figure 57 shows zooms of the noise maps at 8 kHz, in the region of the slat side edges and the slat tracks, for all 3 slat configurations 2.5D/ISE/OSE. Top maps are without slat track and bottom maps are for the generic slat track ST#1 installed (i) in Position #2 on the continuous slat, and at the closest position from the slat side edges, that is (ii) Position #1 for OSE and (iii) Position #3 for ISE. A common color scale is used for the six presented maps, in order to have a quantitative comparison.

Without slat track (top maps on Figure 57), as already seen in the last section, the OSE and ISE are clearly noisier than the 2.5D slat, which is not a surprise. The sources look more extended in the OSE configuration, where the side edge is not aligned with the flow (but aligned with the airfoil chord), than in the inboard SE configuration, where the side edge is aligned with the flow. At this specific frequency of 8 kHz, the OSE is noisier than the ISE, but Figure 56 showed that this tendency is inverted above 10 kHz.

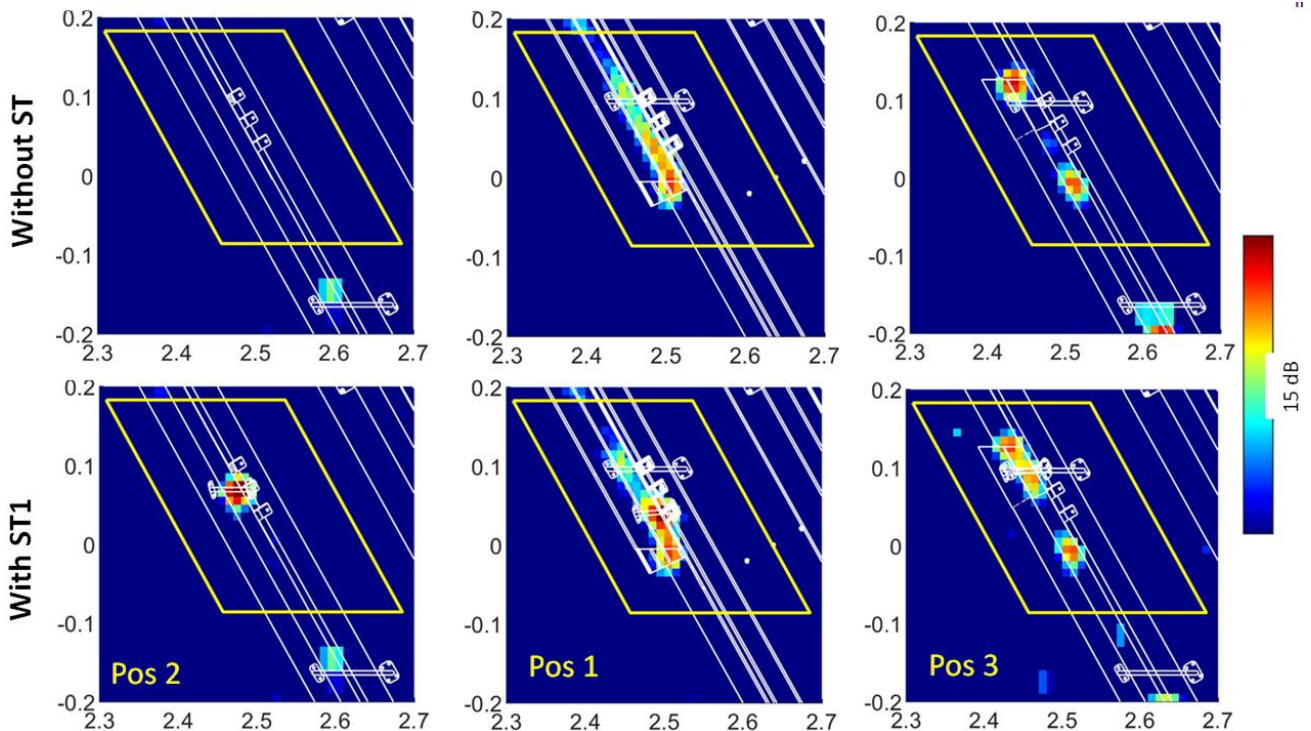


Figure 57: Comparison of the acoustic maps (octave band 8 kHz) in the slat side edge and slat track area (yellow zone) for the 3 slat configurations (2.5D, OSE, ISE) without (top) and with (bottom) baseline slat track #1

When the slat track ST#1 is installed (bottom maps on Figure 57), a corresponding noise source is clearly visible on the three maps.

Figure 58 compares the integrated noise spectra, radiated by the 2.5D slat (black line), the OSE (solid colored lines) and the ISE (dashed colored lines) when the noisiest slat track ST#1 is installed at the 3 positions #1 (blue lines), #2 (red lines) and #3 (green lines). Figure 59 shows the same results for the relatively quiet slat track ST#2.

In order to help in the interpretation of these integrated spectra, pictures of the slat configurations are displayed on Figure 58 and Figure 59 with the direction of the cross-flow velocity component (labeled V_t) generated by the sweep angle. For the same purpose, Figure 60 compares the 3 slat configurations (2.5D, ISE and OSE) with the slat track position #2 and the crossflow (or spanwise) velocity component labeled U_{span} .

First, we focus on the influence of the distance between the slat track and the slat side edge. The effect is globally weak, but there is a clear trend: whatever the side edge type, either ISE or OSE, the noise always increases when the slat track is at the shortest distance to the side edge, which makes sense since these side edges generates 3D flows which are more intense at close distance. This noise increase reaches several dBs for the noisiest slat track ST#1 above 12 kHz (Figure 58). With slat track #2 (Figure 59), which is intrinsically more silent, the effect is weaker: position #1 remains louder with the OSE, but with ISE all 3 positions are very close.

Second, we look at the influence of the slat side edge configuration on the slat track noise. With the quiet slat track ST#2 installed (Figure 59), the slat track self-noise is low and, consequently, does not affect significantly the noise radiated by the slat side edges: the OSE is slightly noisier than ISE below 10 kHz, and the ISE is about 5 dB noisier than the OSE above 10 kHz, just like without any slat track installed.

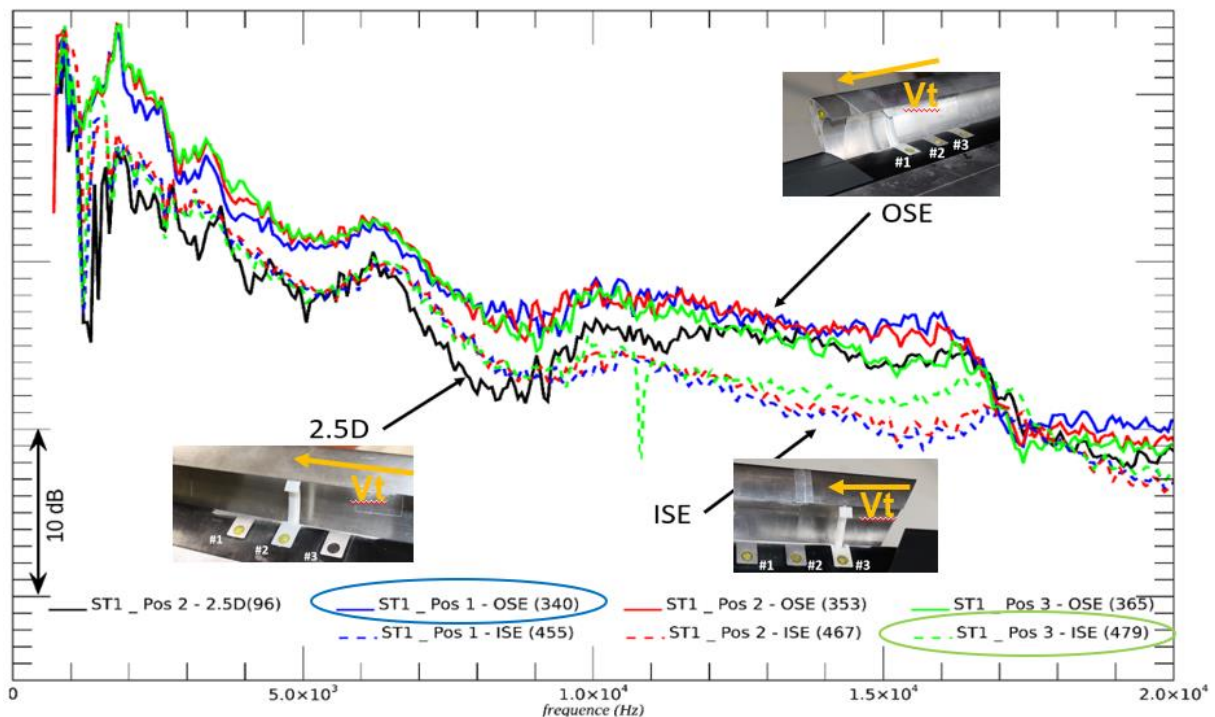


Figure 58: Influence of the position of slat track ST#1 with respect to de slat side edge

With the noisiest slat track ST#1 installed (top plot of Figure 59), the results are completely different: the OSE is the noisiest on the whole frequency band, with noise levels that are very comparable to those with the continuous slat (2.5D) above 12 kHz. This suggests that (i) the self-noise of this noisy slat track ST#1 dominates the self-noise of both slat side edges and (ii) in the OSE configuration, the slat track "ingests" approximately the same "upstream" mean flow (referring to the spanwise velocity component generated by the sweep angle) as in the 2.5D configuration, generated by the upstream

slat element, deployed along a span of about 0.8 m. In the ISE configuration the slat track is located at a short distance downstream the side edge, with probably a very limited spanwise velocity component, and thus weaker effect on the slat track self-noise.

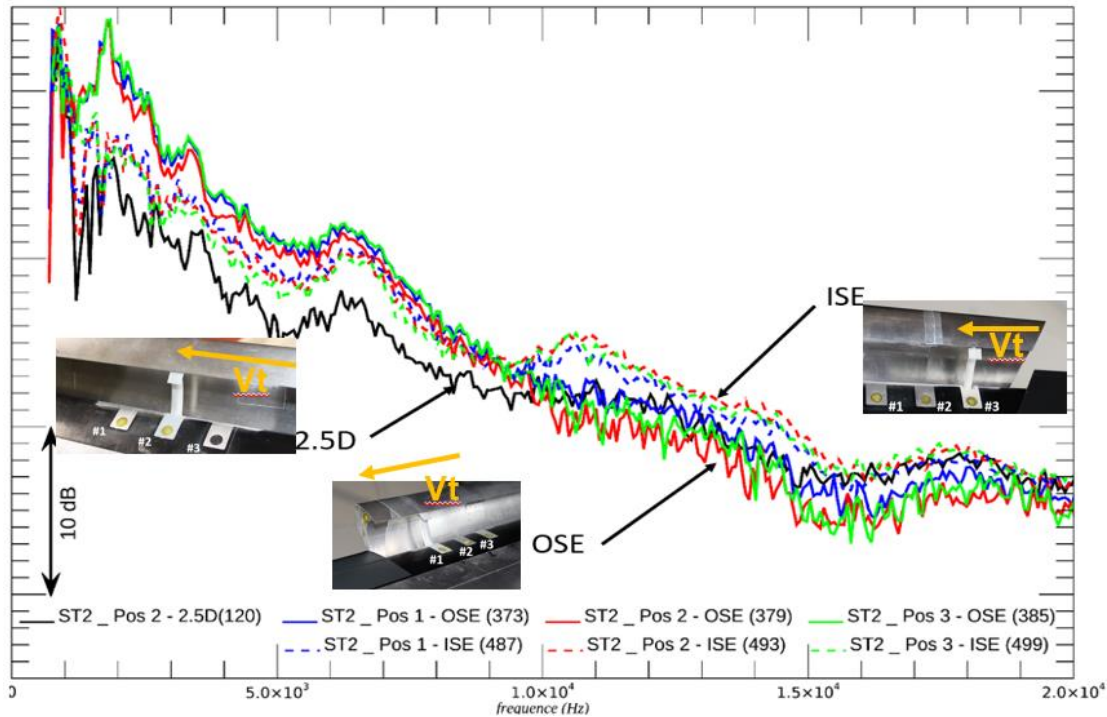


Figure 59: Influence of the position of slat track ST#2 with respect to de slat side edge

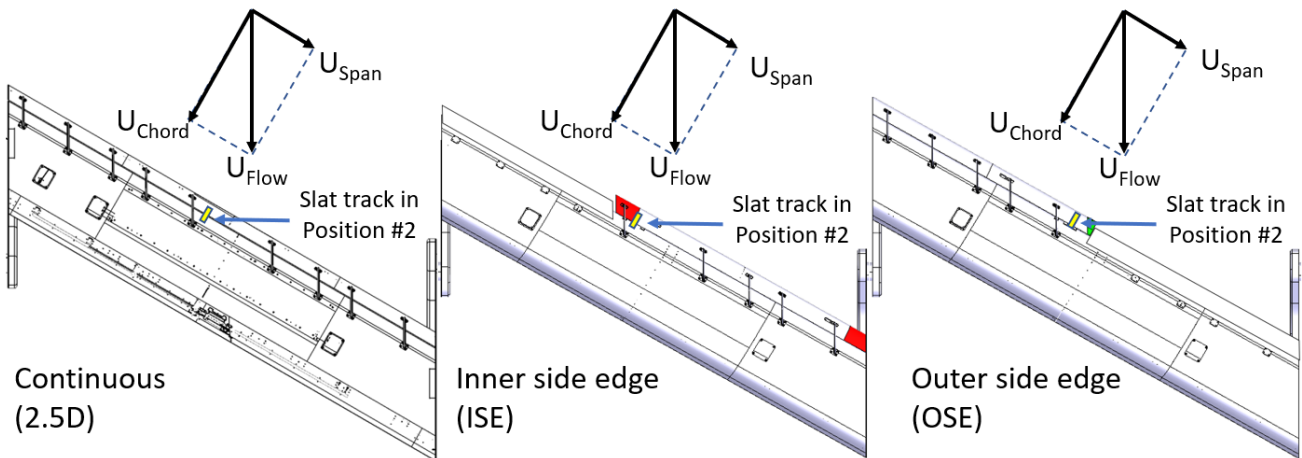


Figure 60: Comparison of the slat track position (#2) in the 3 slat configurations 2.5D, ISE and OSE

In order to better highlight these effects for each configuration, the delta between the noise radiated with and without the slat tracks ST#1 and ST#2 is plotted in Figure 61. Below 8 kHz, the self-noise of both slat tracks is small and consequently no significant noise increase is noticed for both inboard or outboard side edge. In this frequency domain, the slat track noise is only detected for the continuous slat. Above 8 kHz, the noise is much stronger in the OSE case than in the ISE case, with levels that are very comparable to the 2.5D case. With the quieter slat track #2 (dashed line), the contribution of the side edge noise dominates the slat track self-noise, which reduces the impact of the slat track.

Finally, these results suggest that:

- the noise of slat track ST#1, mostly generated by the open cavity at the wing leading edge, is significantly influenced by the crossflow (or transverse/spanwise) velocity component, as long

as the spanwise flow has been developed upstream the slat track along a significant length of deployed slat, similar in the OSE and 2.5D configurations and,

- the sweep apparently plays a role in slat track noise generation (at least for this ST#1 with a leading edge opening), a hypothesis that could be only verified via either (i) tests of the same slat tracks on the F16 model with 0° sweep, or (ii) numerical simulations of slat track noise without sweep.

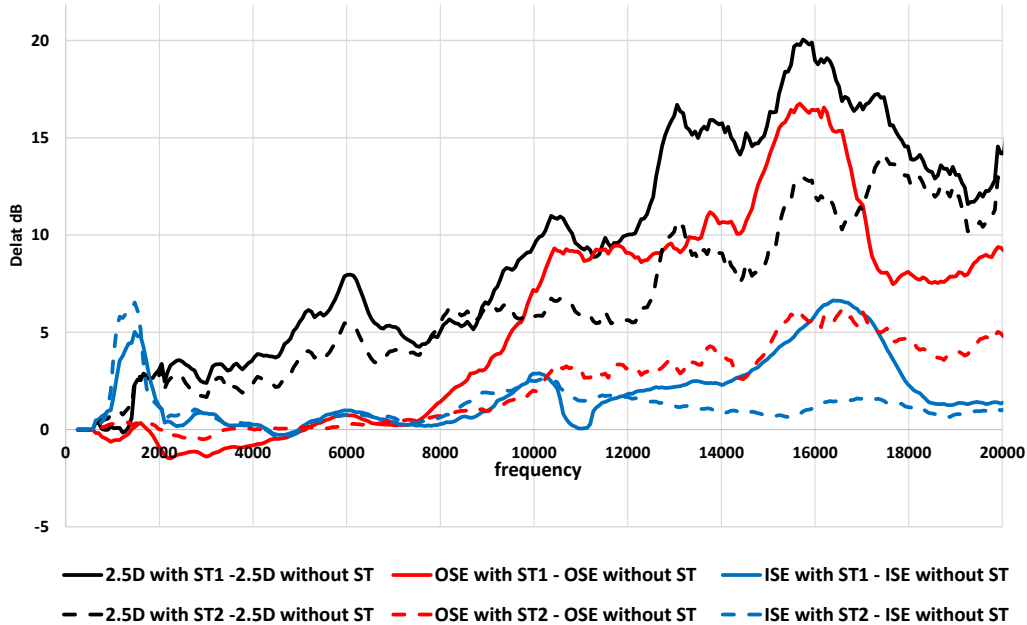


Figure 61: Influence of the slat track depending on the side edge configuration for both ST#1 and ST#2

Finally, Figure 62 synthesizes, in OASPL integrated in the [7-18 kHz] frequency band, all acoustic results concerning the slat configurations (2.5D, OSE and ISE) without and with the generic slat tracks ST#1 and ST#2. On the left plot, without slat track the ISE is slightly noisier than OSE only because the [7-18 kHz] is preferably in the high frequency band. When the (noisiest) slat track ST#1 is implemented, it dominates the noise and is much efficient with the 2.5D and OSE configurations. When the (quieter) ST#2 is implemented, it does not modify the ranking of the slat configurations: ISE > OSE > 2.5D. The right plots on Figure 62 show the influence of the distance between the slat track #1 (top) and #2 (bottom) and the side edge. With the noisiest ST#1, the noise is always higher when the slat tracks is at closest position of the side edge, namely Position #1 for the OSE and Position #3 for the ISE. With quieter slat track ST#2 the effect is not so clear.

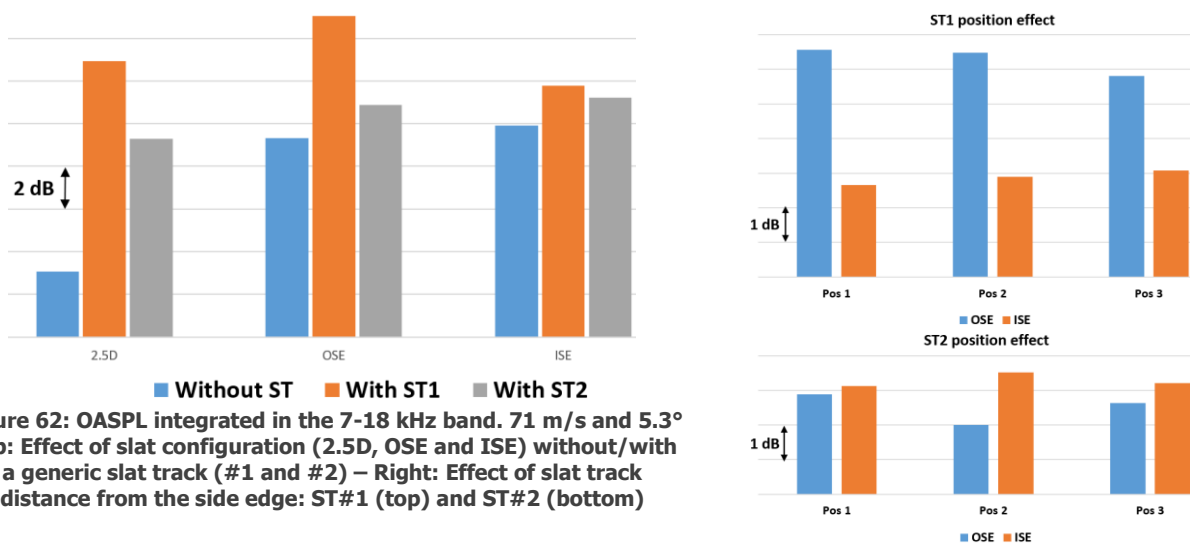


Figure 62: OASPL integrated in the 7-18 kHz band. 71 m/s and 5.3°
 Top: Effect of slat configuration (2.5D, OSE and ISE) without/with a generic slat track (#1 and #2) – Right: Effect of slat track distance from the side edge: ST#1 (top) and ST#2 (bottom)

4.4.7 Slat porous inserts acoustic analysis

4.4.7.1 F2 results

On Figure 63 we compare the acoustic spectra obtained with the porous inserts of "Bristol" type which were located at the bottom of the slat cove on the special slat central element "J" (see Table 7 and Figure 37). These spectra are integrated from the DAMAS noise maps but, this time, the integration includes the whole slat area (yellow and green zones on Figure 47), since these porous inserts were implemented on a large span extent (2 x 300 mm) of the slat central element "J". Figure 63 compares the DLR metallic foam, the TUD Diamond Lattice (fine 4.5 and very fine 3.5) and the materials that were specifically designed and 3D printed by TCD after the tests at the University of Bristol, namely the TCD-MPPA and the TCD-Lattice. The initial analysis focused on the "nominal" flow conditions of 71 m/s and 5.3°, but the corresponding data were considered to have poor reliability, showing unexpected strong tones in the 10-15 kHz frequency band. Note that one of the inserts was solid ("hard"), and was supposed to reproduce the baseline configuration or the continuous 2.5D slat with the nominal slat element "E". These solid inserts also generated the same tones, which suggested that they were not generated by the porous inserts themselves. As expected, the problem of misalignment of the slat element "J" (see section 4.1.12.2 and Figure 39) was immediately suspected, but the examination of the noise maps at the exact frequencies of these tones did not clearly reveal any suspicious noise source, neither at the junctions the central elements with the slat extensions, nor anywhere else.

These investigations led us to look at different angle of attacks, smaller 3° and larger 7.6°, firstly at the same windtunnel velocity of 71 m/s, then at a reduced velocity of 42.7 m/s, which corresponds to the highest flow velocity tested in UoB with a 0° sweep angle (37 m/s), considering the 30° sweep in F2 ($37/\cos(30)=42.7$).

Note that all presented spectra are in fine bandwidth and plotted against the frequency variable. When investigating slat self-noise, one more appropriate variable might be the Strouhal number St based on the slat chord C_s ($St = fC_s/U$), since typical slat noise models (see e.g. Guo's model [12]) displays maxima at about $St=1\approx 2$. In our case, with $C_s = 55.8$ mm (see Table 1), a value $St=1.5$ corresponds to a frequency of 1.9 kHz at 71 m/s and 1.2 kHz at 43 m/s.

The results presented on Figure 63 show that the tones only appear at 71 m/s and 5.3°, which might suggest some resonances only generated in very specific conditions.

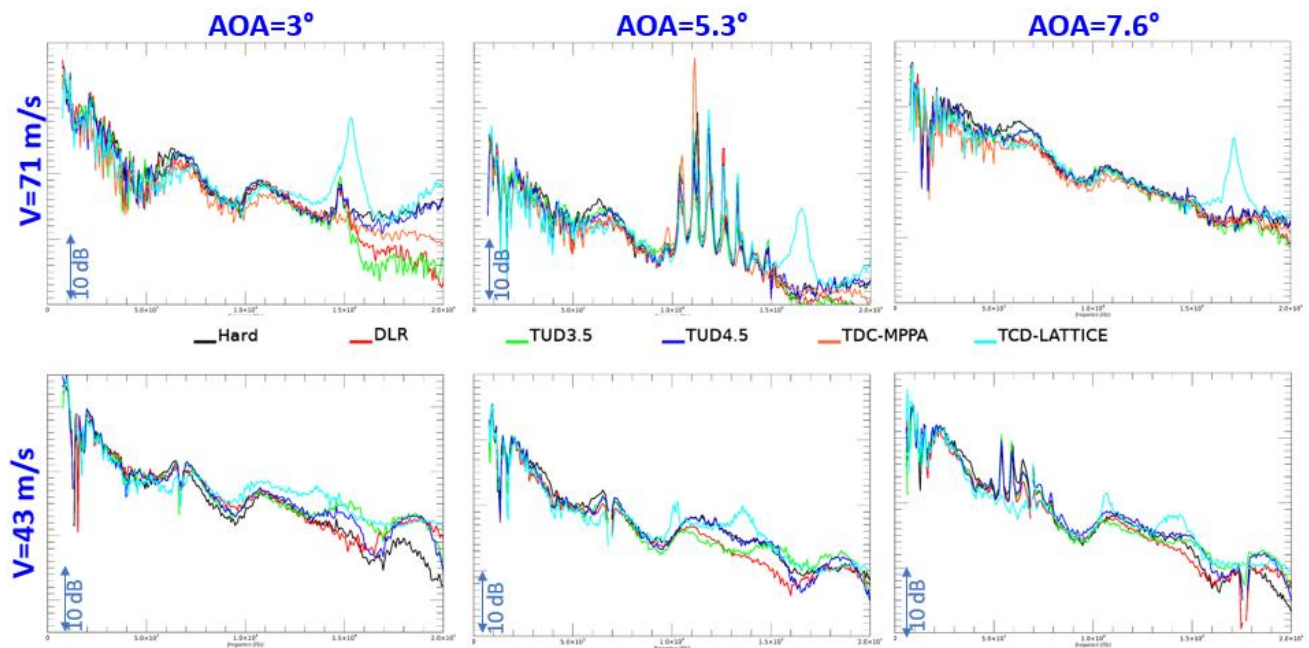


Figure 63: Integrated noise spectra (0-20 kHz) obtained for the "Bristol" type porous inserts.

However, when looking at these spectra below 10 kHz, one might observe tendencies close to, or similar as, those noticed during the tests at UoB. Indeed, between 3 kHz and about 6 or 7 kHz, all porous inserts provide slight noise reductions (of about 2-3 dB max) compared to the solid insert.

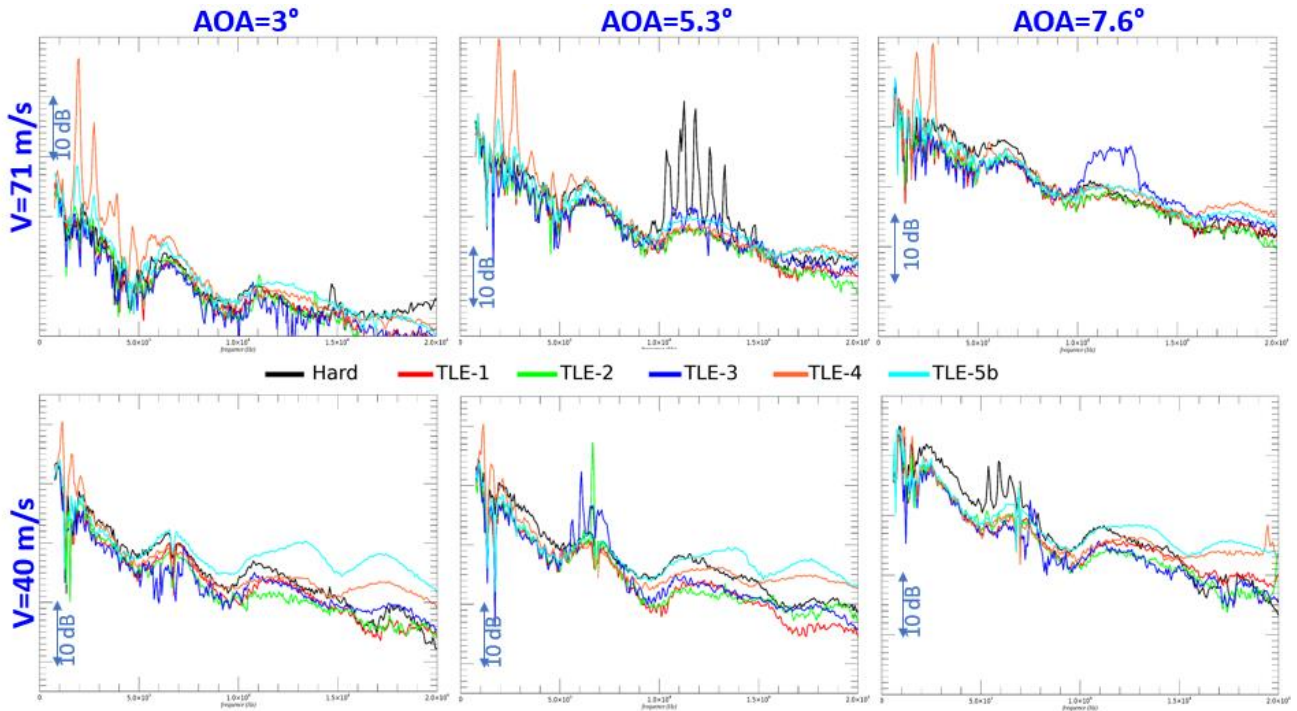


Figure 64: Integrated noise spectra obtained for the "trailing edge" type porous inserts.

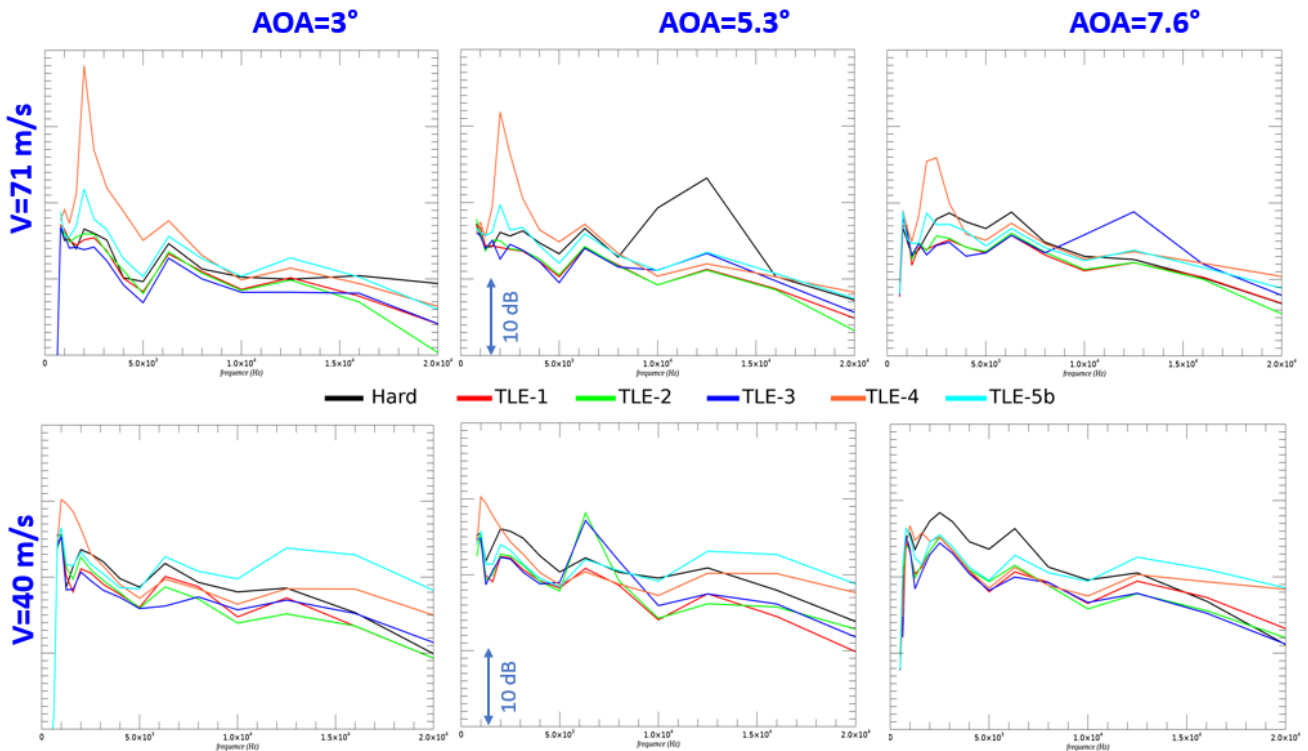


Figure 65: Same as Figure 64, but spectra in third octave bands (Integrated noise spectra obtained for the "trailing edge" type porous inserts).

Figure 64 shows similar results for the second set of porous inserts installed on the slat pressure side close to the slat trailing edge of another slat central element named "N" (see Table 7 and Figure 38). Note that the "Hard" configuration is the same as on Figure 63, based on solid inserts installed on the slat element "J". So, at first view, it looks like this "N" slat element does not generate tones, at

least in the presented conditions. Again, one can detect a significant frequency band [8-15 kHz] where all porous inserts are a few dB quieter than the baseline solid slat (except TLE-5b, which might result from an inadequate assembly of the wiremesh covering the porous element, due to difficulties met by the F2 team with the glue used for this assembly). For a more synthetic interpretation of this result, Figure 65 shows the same spectra, but this time in third octave bands. Again, when restricting the analysis to the lower velocity 43 m/s (and eliminating the TL-5b for the reasons already mentioned) a nice noise attenuation by all "trailing Edge" porous inserts is observed compared to the hard wall case.

Finally, the effects of all tested porous inserts are compared on Figure 66 in terms of OASPL integrated in the frequency band [2-14 kHz] for all angle of attacks (3°, 5.3° and 7.6°) and the two flow velocities 71 m/s and 43 m/s ("Bristol" type inserts) or 40 m/s ("trailing edge" type inserts).

Among the "Bristol" type inserts (Figure 66, left) the TCD-MPPA is clearly the best candidate, except at 71 m/s – 5.3° but, again, these flow conditions remain doubtful. The DLR foam and the TCD-Lattice are also providing noise reductions.

For the "trailing edge" type inserts (Figure 66, right), the acoustic ranking is less clear. One should not consider the flow conditions [71 m/s, 5.3°] and [40 m/s, 7.6°] where significant noise reduction provided by some inserts just result from the absence of tones for these inserts. Otherwise, the inserts bringing the best "averaged" results are the TLE-1, TLE-2 and TLE-3, which were actually the inserts that were received "ready-to-test" by the F2 wind tunnel.

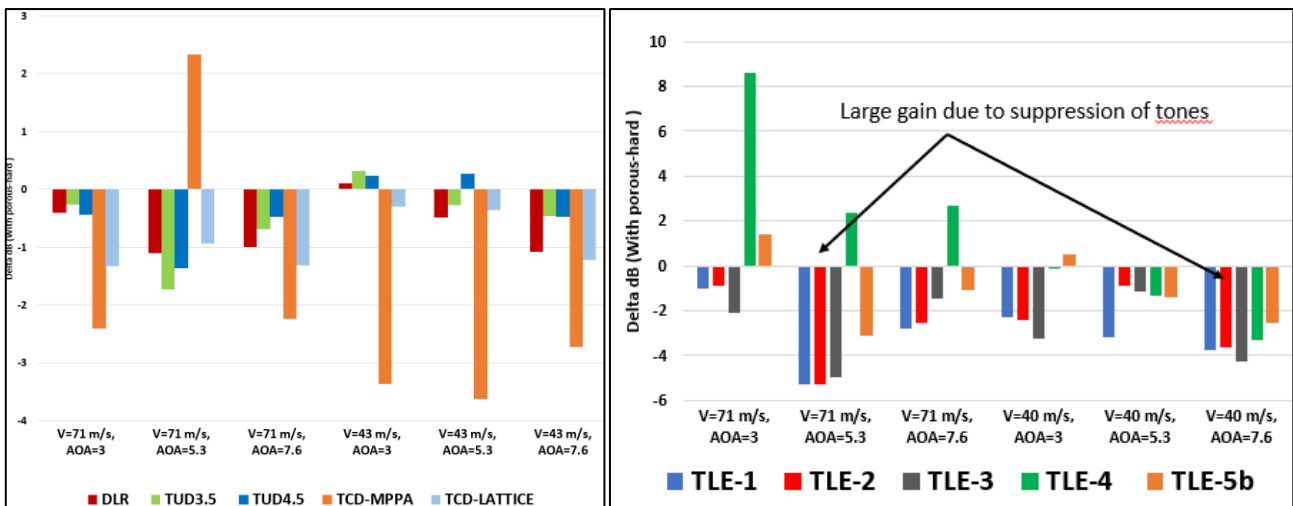


Figure 66: Effects of all tested porous inserts compared in terms of OASPL integrated in the frequency band [2-14 kHz] for all angle of attacks (3°, 5.3° and 7.6°) and the two flow velocities 71 m/s and 43/40 m/s
 Left: "Bristol" type inserts. Right: "Trailing edge" type inserts



Figure 67: Test-set up of the swept F16 model in AWB for additional tests of porous inserts. Noise map at 8 kHz

4.4.7.2 Additional tests in AWB

After the INVENTOR tests in F2, DLR has achieved additional experiments in AWB with the same F16 model with 30° sweep and an equivalent angle-of-attack of 14°. The objective was to test again the same porous inserts of both “families” (the “Bristol” type installed at the bottom of the slat cove, and (ii) the “Trailing Edge” type, installed on the slat pressure side close to the slat trailing edge) and tentatively draw useful conclusions on their respective capabilities in terms of slat noise mitigation. Note that, prior to these tests, the misalignment issue of slat parts J and N mentioned in section 4.1.12.2 (Figure 39) was fixed.

Figure 67 shows the set-up of the swept F16 model in AWB, including only the left side plate of the nozzle. Note that this set-up was mentioned in section 3.3.7 as the improved SWAHILI set-up.

The following inserts have been tested:

- “Bristol” type: solid, DLR-foam, TCD Lattice fine and very fine
- “Trailing Edge” type: TE-MPPA, TE-felt, TE-felt/mesh, TE-foam/mesh, all without/with a tape to reduce the chordwise extent of the porous media.

With all tested inserts (including the solid insert or baseline reference), a strong tone was observed at about 8 kHz (7.8 to 7.9 kHz) at 40 m/s, and the noise maps at this frequency identified a source located on the right hand side region of the central slat element (see the noise map on Figure 67), without any clear explanation of the origin of this source. However, this source was considered as not relevant for slat noise, because outside of the interesting frequency range.

On Figure 68, the “Bristol” type (left) and the “Trailing Edge” type (right) porous inserts are compared in terms of third octave band spectra in the [1-8 kHz] at a velocity of 61.5 m/s. An interesting observation is that all tested inserts provide some noise mitigation compared to the reference solid surface.

- Concerning the “Bristol” type (left) porous inserts, the TCD-Lattice and the MPPA show best noise reduction in the frequency band 2 – 4 kHz. Such inserts might be useful for near field attenuation of slat track noise, and DAV is especially a potential user of this property, to be tested in INVENTOR WP5 on the GB-A model.
- Concerning the “Trailing Edge” type (right), porous inserts, the TE-MPPA, TE-foam and TE-felt inserts show the best noise reduction, which is broadband in the range [1 kHz – 4 kHz]. Note that Airbus is a potential user for this type of porous insert.

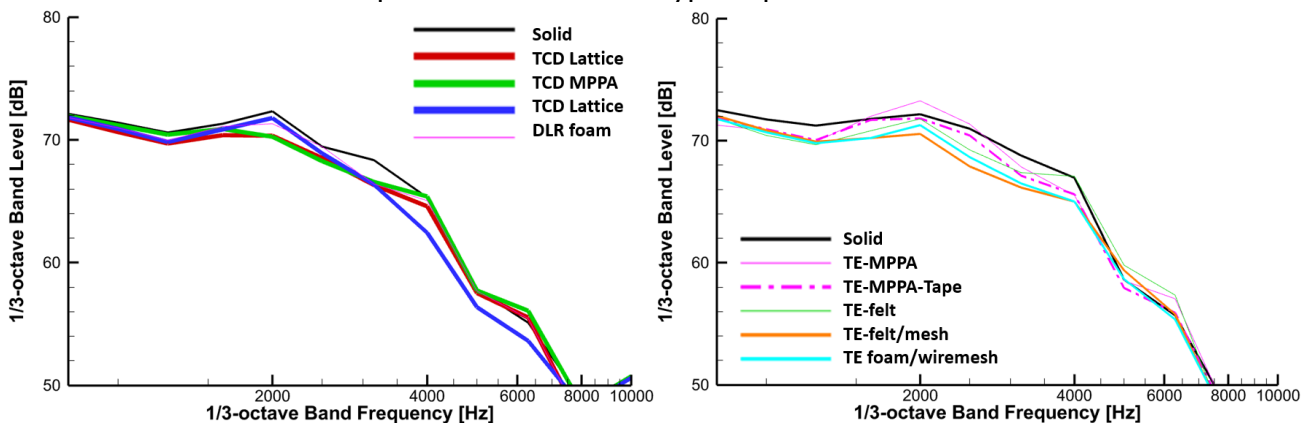


Figure 68: “Bristol” (left) and “Trailing Edge” (right) type porous inserts compared in 1/3 octave band spectra. 61.5 m/s
The variation of the chordwise extend of the porous TE insert was meant to provide a design guideline on the necessary size of such TE inserts. Based on the marginal effects of less than ± 1 dB this guideline could not be elaborated. Numerical simulations might be suitable and better means to perform design studies in the future.

4.4.8 Slat track noise mitigation using slat porous inserts

The last acoustic investigation in this section 4.4 concerns the possible mitigation of the slat track noise using slat porous inserts. For this purpose, the inserts of the "Bristol" family, installed at the bottom of the slat cove, are probably the most promising, as they are supposed to act as sound absorber. Actually 3 of them were tested, the DLR metallic foam and two TUD Diamond Lattice fine 4.5 and very fine 3.5 mm, with the generic (and noisiest) slat track #1. The results were obtained with the integration of noise maps in the slat track area (yellow zone on Figure 46).

Figure 69 shows these spectra, again at 3 angles of attack and 2 velocities. On these fine bandwidth plots it is clear that the effect of the porous inserts is rather weak, and it is obviously difficult to detect and quantify such small level differences. The same spectra are presented on Figure 70 in third octave bands, which slightly facilitates the interpretation, showing a weak noise reduction when using the DLR foam and the TUD 4.5 materials.

Finally, Figure 71 synthetize, with OASPL integrated in the [2-14 kHz] the mitigation (or possibly the reinforcement) of the slat track noise using the porous inserts. Again, these results tend to show that the DLR and the TUD 4.5 materials would be the best candidates.

4.4.9 Comparison with numerical simulations

For a fair and reliable validation of the CFD/CAA numerical simulations achieved by the partners involved in the Subtask 4.3.2, ONERA was in charge to apply the same array processing method to the virtual acoustic pressure signals generated from these numerical simulations at the positions of the 120 microphones of the array. This investigation has been achieved with the data provided by ONERA, DAV and NLR, and the results are presented at the end of their individual contributions in Section 5 of the present report.

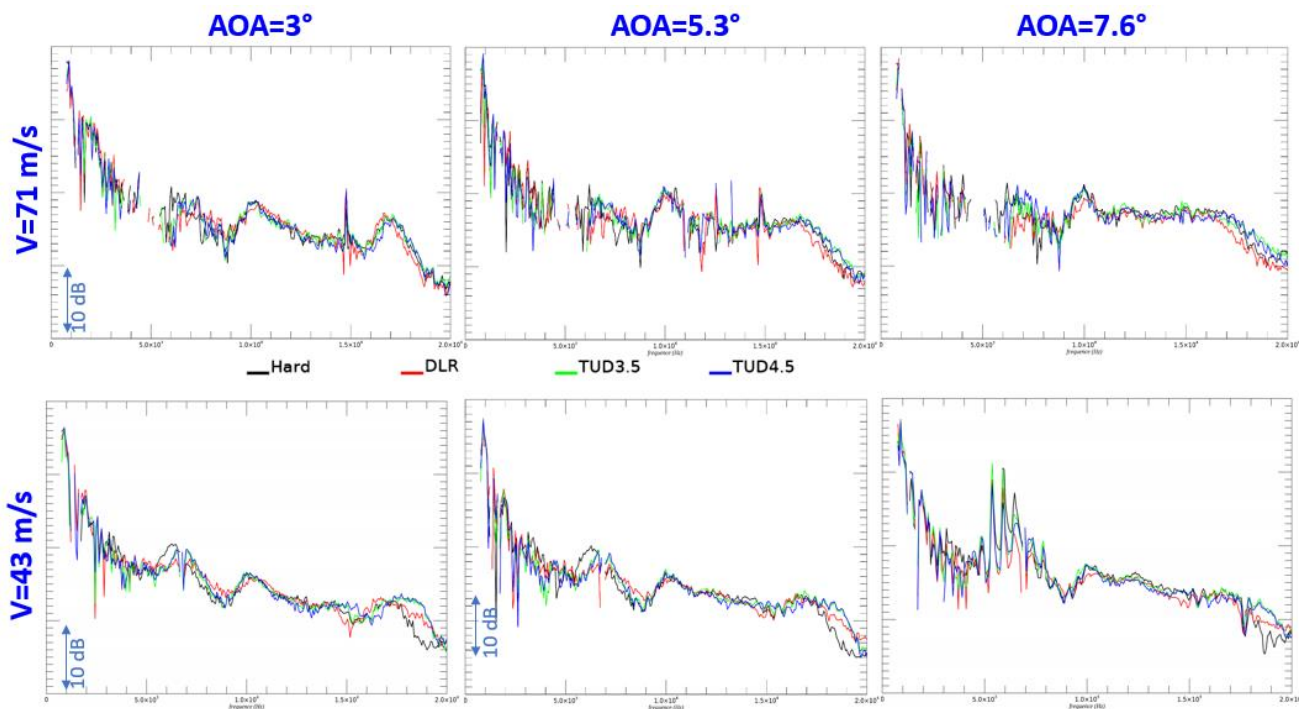


Figure 69: Slat track noise mitigation with 3 "Bristol" type porous inserts: integrated (in the slat track area) noise spectra obtained with the slat track #1 in position #2.

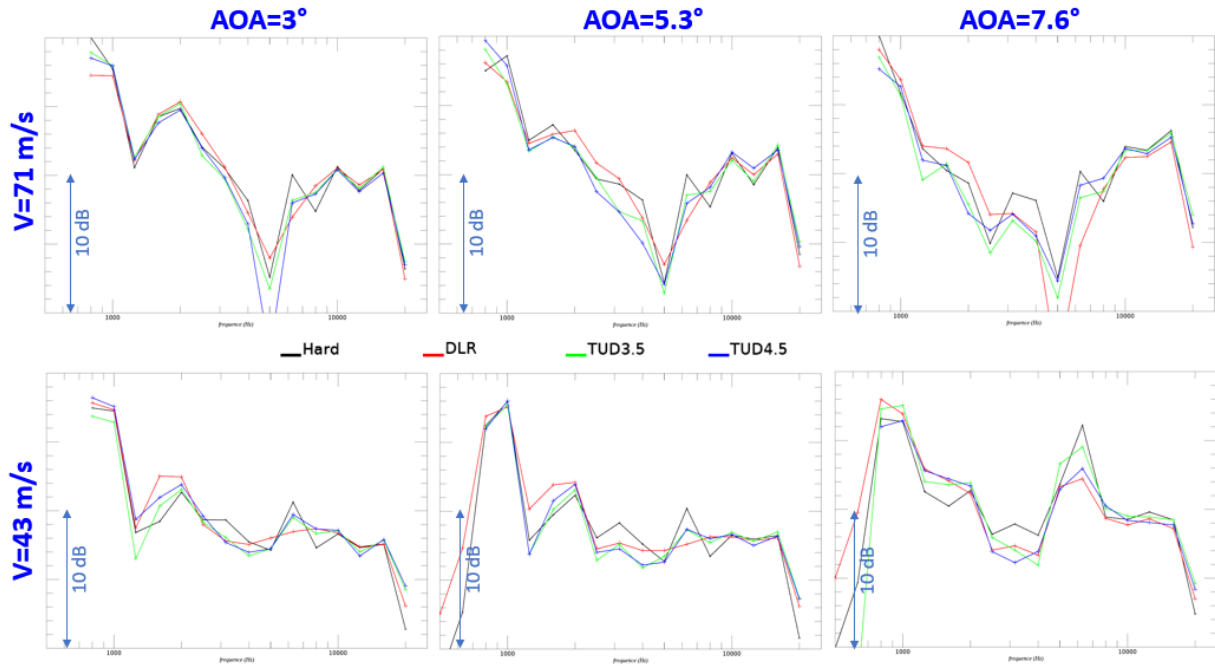


Figure 70: Same as Figure 69 but spectra in third octave bands. Slat track noise mitigation with 3 "Bristol" type porous inserts: integrated (in the slat track area) noise spectra obtained with the slat track #1 in position #2

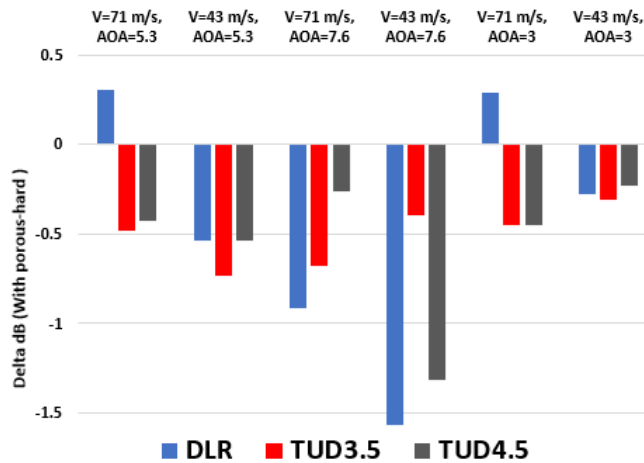


Figure 71: Slat track noise mitigation with 3 "Bristol" type porous inserts and the slat track #1 in position #2: OASPL integrated in the frequency band [2-14 kHz] for all angle of attacks (3°, 5.3° and 7.6°) and the two flow velocities 71 m/s and 43 m/s

4.5 Aerodynamic measurements using PIV

4.5.1 PIV set-up

PIV is an optical not intrusive method of flow visualization used to obtain local velocity measurements. The fluid is seeded with small tracer particles (oil droplets of averaged size 0.5 μm) assumed to faithfully follow the flow dynamics. The principle consists in recording images with a CCD camera of these particles crossing a bright plane (pulsed laser) at two successive moments with a time interval of about 10 μs). Typical images contain about 2048 x 2048 pixels, divided in a matrix of patches of 32 x 32 pixels each. Comparison between both successive images allows to calculate the averaged travel of particles of any given patch, which provides the displacement/velocity vector of this patch through a specific process, and a final map on about 64 x 64 patches. The combination of 2 maps from 2 cameras looking at the laser sheet with different angles allows to derive 3 instantaneous velocity components (3C-PIV). A typical mean flow measurement is based on time averaging 500 to 1000 maps recorded at a typical rate of 10 Hz.

In F2, the full PIV system (laser emission system and two CCD cameras) is set on the tables of the "Displacement Device Laser" (DDL), a massive frame which surrounds the test section (equipped with glass walls) and allows moving the system along the three orthogonal directions in ranges of 500 mm along X, 600 mm along Y, and 1000 mm along Z. A schematic of this DDL (without any optical device) is shown on Figure 72 (left). The same figure (right) shows a picture of the full 3C-PIV system, with the vertical laser sheet emitted from the ceiling through a glass window, and two cameras installed on both sides of the DDL. This set-up allows rapid traversing with successive PIV measurements without modifying the optical settings.

For the INVENTOR tests, the measurement plane (or the Laser sheet) was always vertical, or always contained the vertical axis Z. Two optical setups have been used (see Figure 73):

- Left: longitudinal or chordwise measurements, providing velocity maps in (LX, Z) planes at successive span positions LY,
- Right: transverse or spanwise measurements providing velocity maps in (LY, Z) planes at successive chord positions LX.

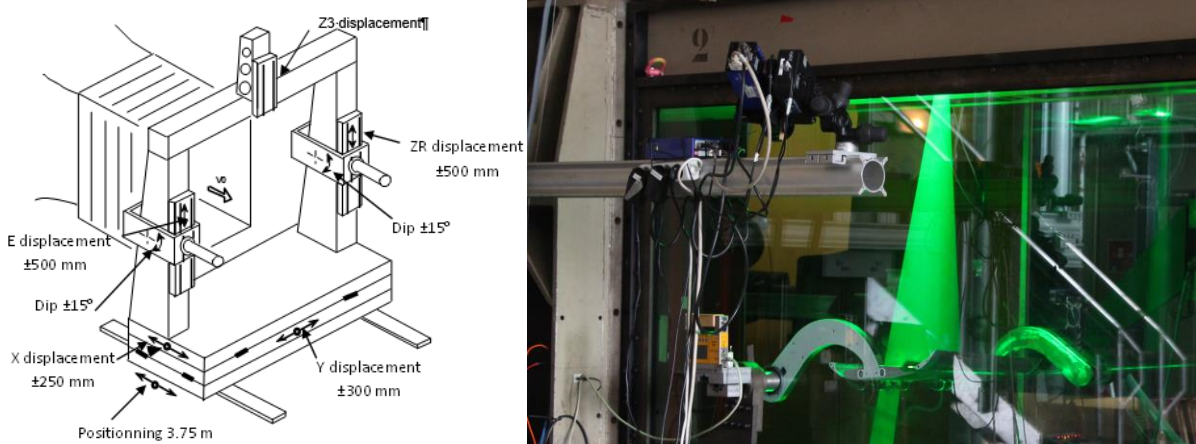


Figure 72: Left: DDL (Displacement Device Laser) diagram (PIV system not represented). Right: 3-component PIV system installed on the DDL, with the laser plane emitted from the ceiling.

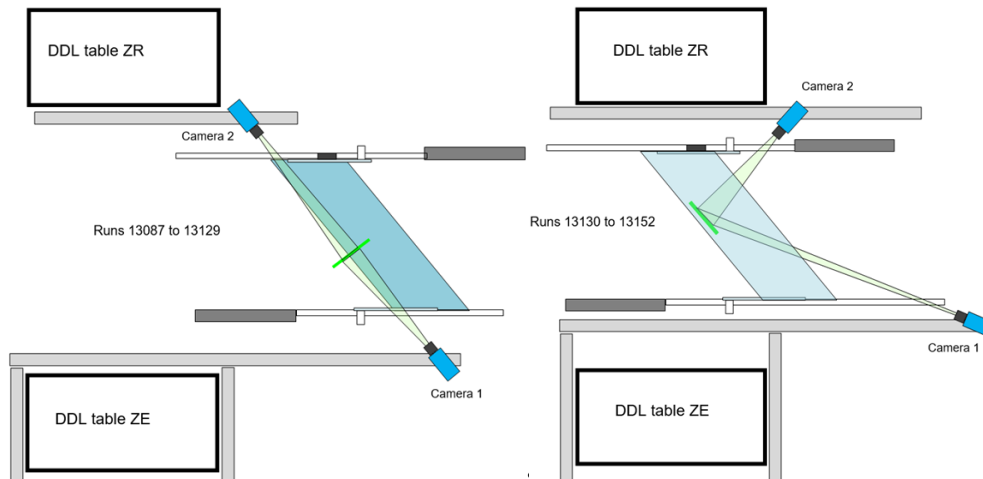


Figure 73: PIV optical set-ups. Left: longitudinal/chordwise (LX, Z) planes. Right: transverse/spanwise (LY, Z) planes

4.5.2 Velocity maps calibration

A major challenge of PIV measurements is to precisely position the PIV images (or velocity maps) with respect to the model in the flow. This is typically done without flow, using a physical reference grid (a black plate with a matrix of white dots) precisely positioned with respect to a well-known solid point on the model (Figure 74). In our case, this solid point B was chosen along the slat cusp (which is apparent since the model is installed upside down) at the spanwise position corresponding to the median slat track pocket #2. This calibration was achieved with the model at a global incidence of

0° , an arbitrary choice allowing further positioning of PIV maps for any other angle-of-attack of the model.

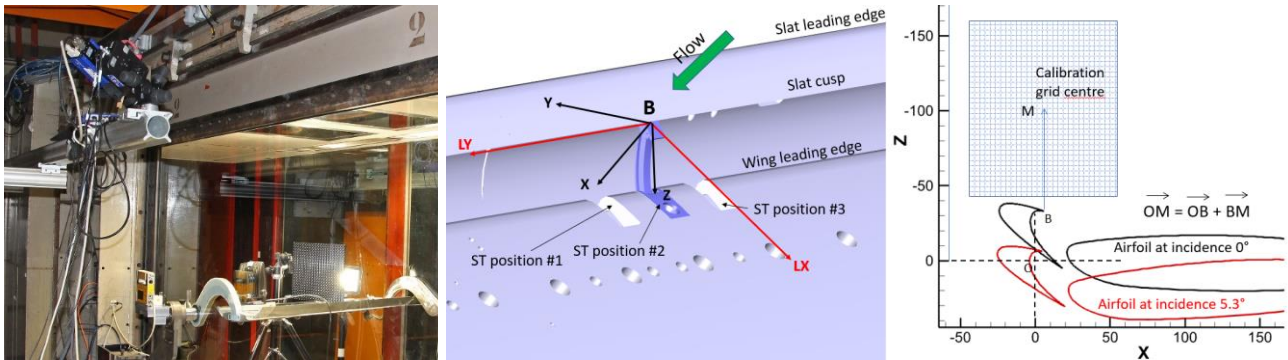


Figure 74: Geometrical calibration of the PIV system using a reference grid placed on the model at a global incidence 0° . (Note: the horizontal axis on the right side plot should read LX, not X)

The geometrical calibration was achieved in 2 steps:

- Denoting M the centre of the reference grid, the coordinates of \overline{BM} was manually measured with a ruler (precision about one half millimeter). Knowing the coordinates \overline{OB} of the cusp B in the airfoil axis framework AO (see Figure 19, origin O at the leading edge of the retracted slat), the maps were provided by the F2 team in this AO framework
- The final positioning of the velocity maps with respect to the model immersed in the flow must account for the deformation (dX , dY , dZ) due to the aerodynamic loads described in section 4.2 and Figure 40. For any slat configuration (2.5D or inboard/outboard slat side edge) and flow conditions (velocity and incidence) this deformation was measured using PIV and simplified as:
 - dX is considered as an average 1 mm everywhere,
 - dY is considered as 0 (no deformation in span direction),
 - dZ is derived with a 2D linear regression as $dZ = a LX + b LY + c$

So for all measured velocity maps, any point of coordinates (LX, LY, Z) is translated with a vector ($-dX$, $-dZ$) with $dX = 1$ mm, $dZ = a LX + b LY + c$ and :

- any chordwise map (LY = constant) is rotated by an angle $-\text{Arctg}(a)$ in its own plane (LX, Z) (\rightarrow rotation axis is LY), about its centre M
- any spanwise maps (LX = constant) is rotated by an angle $-\text{Arctg}(b)$ in its own plane (LY, Z) (\rightarrow rotation axis is LX), about its centre M.

4.5.3 Typical flow field explorations

Figure 75 shows typical chordwise (left) and spanwise (right) positions of the measured PIV maps for the continuous (2.5D) slat configurations, with one generic slat track installed in pocket #2. 15 chordwise maps were measured in the LY range $[-82, +82$ mm] and 6 transverse maps in the LX range $[-38, +25$ mm].

Finally, Figure 76 shows similar information for slat side edge configurations. The LX range for the transverse maps is the same $[-38, +25$ mm] as for the 2.5D slat, whereas the LY range is adapted to the position of the slat side edge, namely $[-140, +82$ mm] for the outboard SSE and $[-82, +110$ mm] for the inboard SSE.

The complete list of available PIV maps is detailed hereafter in Table 8.

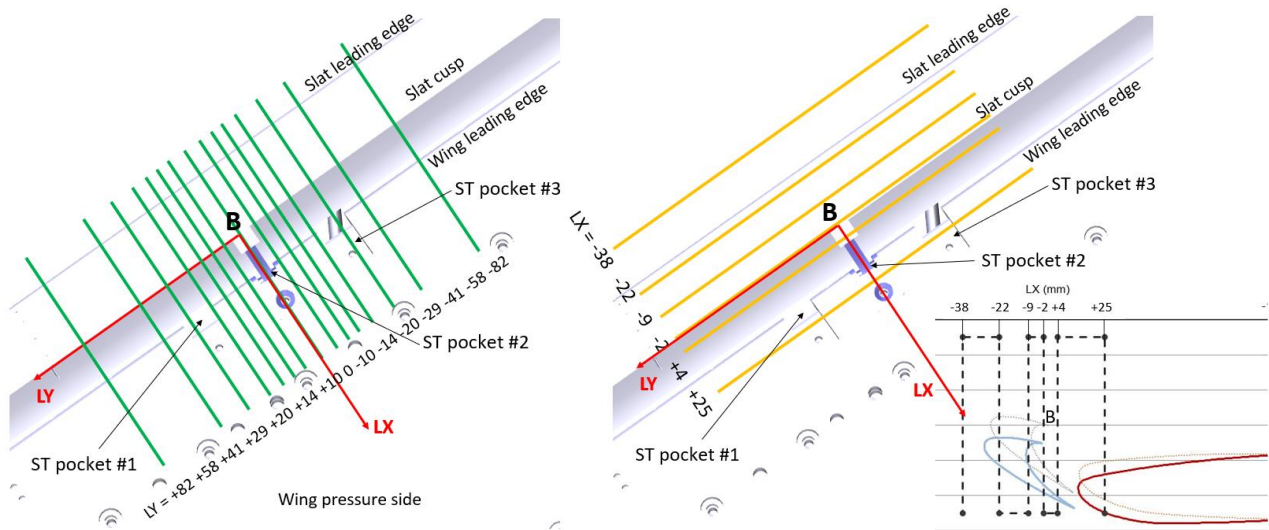


Figure 75: Typical chordwise (left) and spanwise (right) positions of the measured PIV maps, positioned with respect to the slat cusp in the LY location of the slat track pocket #2. (Note: LX and LY refer to the model at incidence 0°)

Slat	AoA	ST#	ST Pos#	Insert	Chordwise maps			Spanwise maps		
					Nb	LY (mm)	Lots	Nb	LX (mm)	Lots
2.5D	5.3°	1	2		15	-82 to 82	721 to 735	6	-27 to 36	1007 to 1012
2.5D	5.3°	2	2		15	-82 to 82	736 to 750	6	-27 to 36	1001 to 1006
2.5D	3°				3	-100, 0, 65	757-756-751	6	-27 to 36	1013 to 1018
2.5D	5.3°				3	-100, 0, 65	758-755-752			
2.5D	7.6°				3	-100, 0, 65	759-754-753			
2.5D	5.3°	11	2		16	-82 to 82	760 to 775			
2.5D	5.3°	13	2		15	-82 to 82	776 to 791			
2.5D	5.3°	5	2		15	-82 to 82	792 to 806			
2.5D	5.3°	7	2		15	-82 to 82	807 to 821			
2.5D	5.3°			Rigid	1	0	837			
2.5D	5.3°			DLR-Foam	1	0	838			
2.5D	5.3°			TUD 3.5	1	0	839			
2.5D	5.3°			TCD-Lattice	1	0	840	6	-27 to 36	1019 to 1026
2.5D	5.3°			TCD-MPPA	1	0	841	6	-27 to 36	1027 to 1032
2.5D	5.3°			BDF1	1	0	842			
2.5D	5.3°			BDF2	1	0	843			
2.5D	5.3°			BDF3	1	0	844			
Inner	5.3°				10	-140 to 82	846 to 855	6	-27 to 36	968 to 973
Inner	5.3°	1	2		18	-140 to 82	857 to 874	6	-27 to 36	982 to 987
Inner	5.3°	2	2		18	-140 to 82	875 to 892	6	-27 to 36	988 to 993
Outer	5.3°				9	-82 to 110	895 to 903	6	-27 to 36	962 to 967
Outer	5.3°	1	2		19	-82 to 110	907 to 925	6	-27 to 36	956 to 961
Outer	5.3°	2	2		19	-82 to 110	926 to 944	6	-27 to 36	950 to 955

Table 8: Full PIV test matrix.

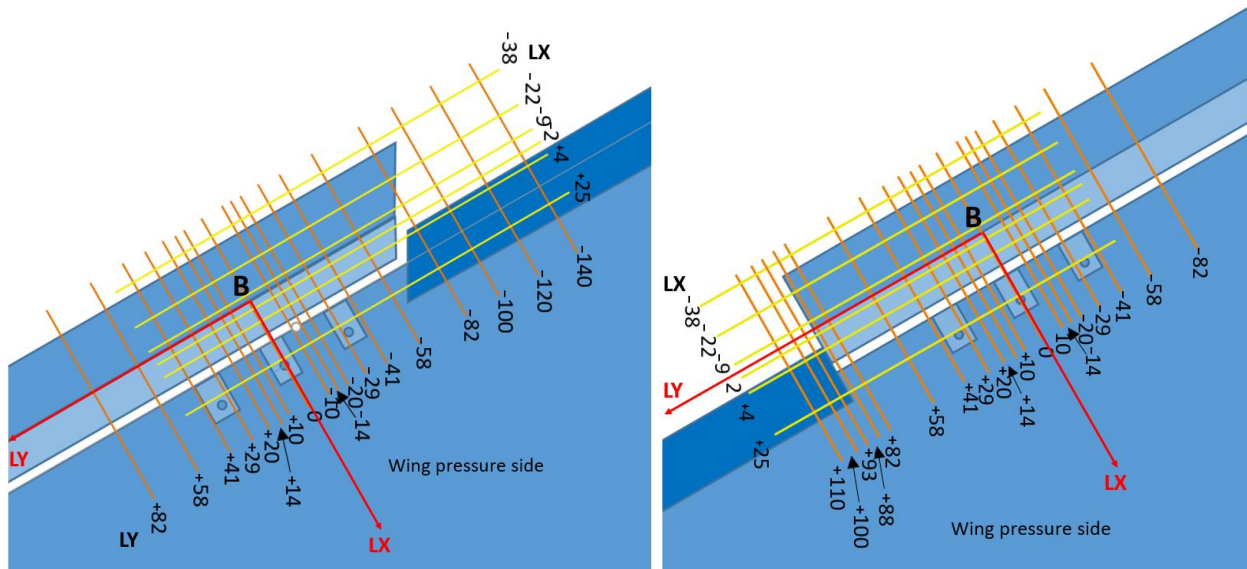


Figure 76: Same as Figure 75 for outboard (left) and inboard (right) slat side edge configurations. (Note: LX and LY refer to the model at incidence 0°)

4.5.4 Axis frameworks of the final PIV database

The PIV maps are provided in the final INVENTOR database in two different axis frameworks, for different use/applications, from simple flow visualization to validation of CFD computations. Note that these two axis systems are names "2D" and "2D" but both contain fully 3D information for both the spatial coordinates and the velocity components.

4.5.4.1 "2D" maps

"2D" maps are provided in the AO axis framework (LX, LY, Z) (see Figure 19) which origin O is the position of the retracted slat leading edge in the LY position of the slat track pocket #2, when the airfoil is at 0° incidence. Note that "2D" maps have typically a constant LX (transverse maps) or LY (chordwise maps) coordinate.

In these maps, the provided velocity components are (LU, LV, W) where LU (resp. LV) is oriented in the LX (resp. LY) directions.

Figure 77 shows an example of such map measured at LY=-82 mm with the continuous 2.5D slat, the model at an angle-of-attack of 5.3° and the flow velocity 71 m/s.

These "2D" maps are obviously interesting for the validation of CFD computations which were achieved with 3D grids built from the expansion in the span direction of the original CAD of the F16 model 2D section.

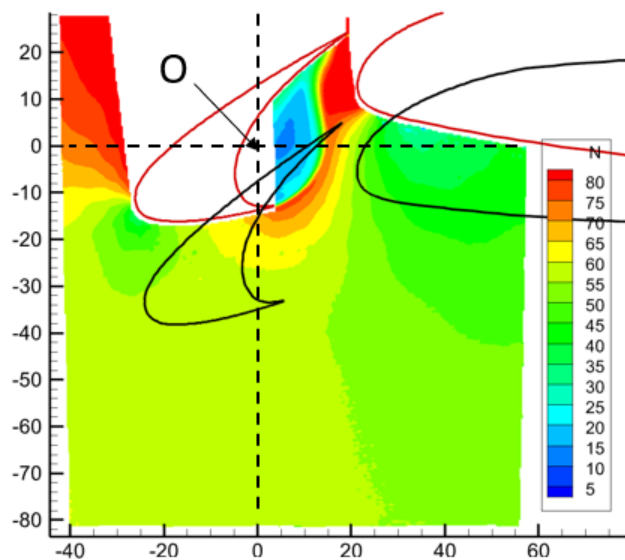


Figure 77: Definition of the axis framework (LX, LY, Z) for "2D" maps. The origin O is the position of the leading edge of the retracted slat, for the airfoil section located in the LY position of the slat track pocket #2, airfoil at 0° incidence

4.5.4.2 "3D" maps

The second set of PIV maps, named "3D" are given in a (X, Y, Z) axis framework linked to the windtunnel, with an origin attached to the F16 model but not dependent of its global configuration in terms of sweep and angle-of-attack. This point simply is chosen at the intersection of the vertical Z axis (used to adjust the sweep angle) and the horizontal Y axis (used to adjust the angle-of-attack) shown on Figure 20 and Figure 21.

Figure 78 shows 3 chordwise velocity maps plotted on the model in the continuous 2.5D slat with the generic slat track # 1 installed in the pocket #2. The model has an angle-of-attack of 5.3° and the flow velocity is 71 m/s. The 3 maps are located at $LY = -82, 0$ and $+82$ mm with respect to the spanwise position of the pocket #2.

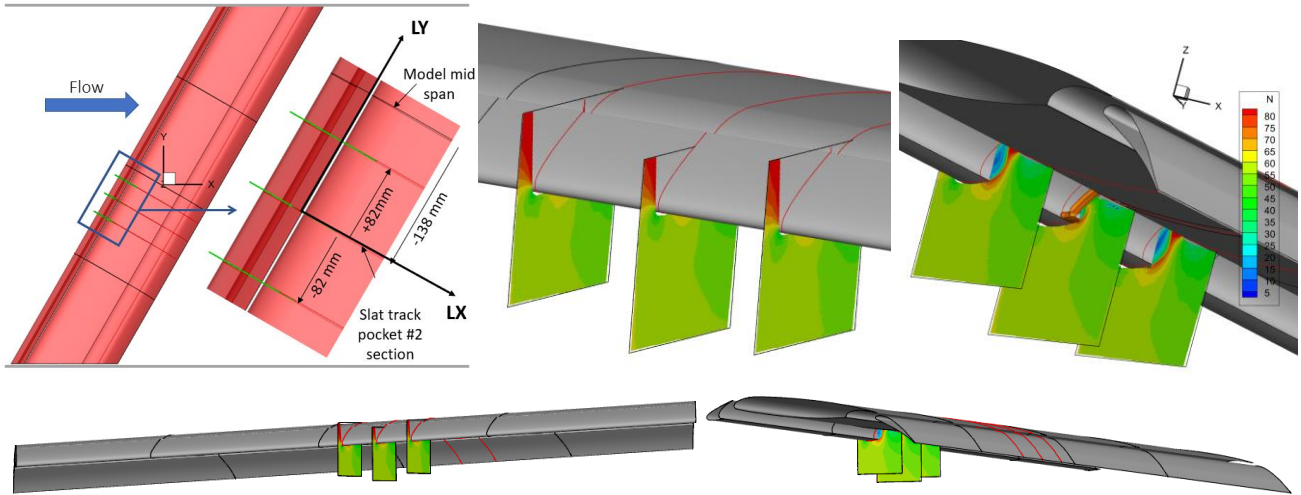


Figure 78: "3D" chordwise PIV maps. Continuous 2.5D slat. Generic slat track # 1 installed in pocket #2. Model incidence 5.3° and flow velocity 71 m/s. Maps located at $LY = -82, 0$ and $+82$ mm w.r.t. the spanwise position of the pocket #2

4.5.5 Early comparison PIV/CFDdatabase

An early cross-check of the validity of these PIV-3C maps was based on comparisons with a mean flow computation with the lattice Boltzmann solver ProLB. Figure 79 shows the ProLB computational set-up and the multi-resolution Cartesian grid with the F16 model installed in the F2 WT. Note that all solid surfaces (windtunnel walls and airfoil are implemented as virtual boundaries. Moreover the model is considered without any slat/flap brackets nor arm supports.

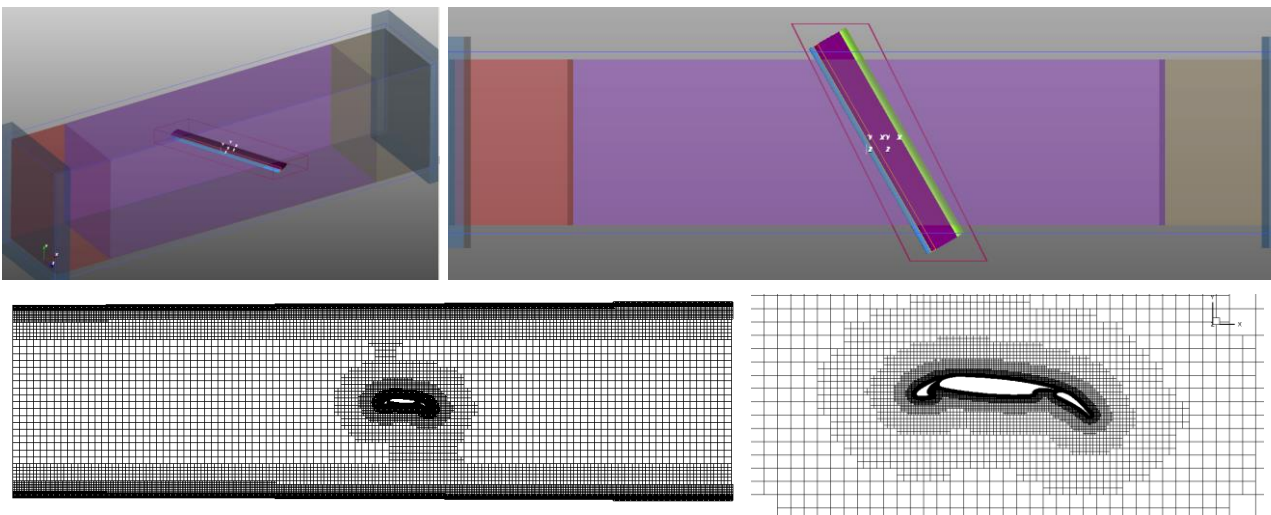


Figure 79: ProLB computational set-up and Cartesian grid

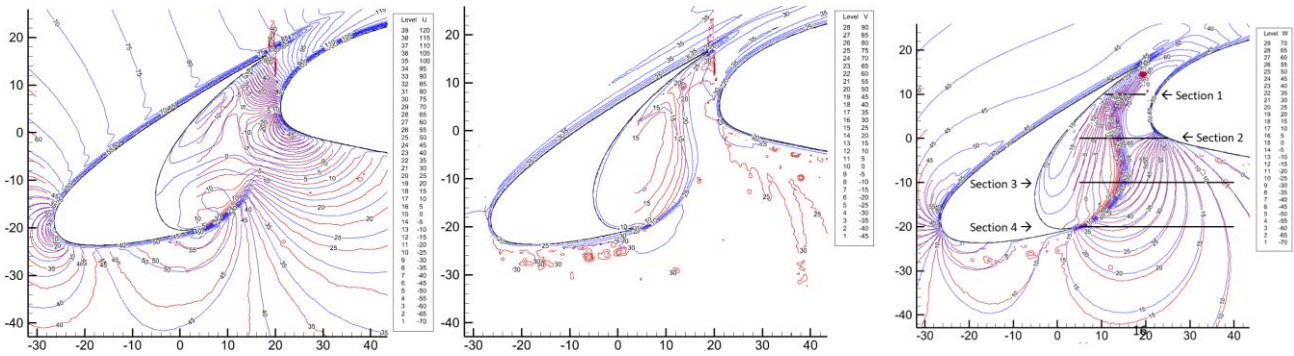


Figure 80: Comparison of PIV-3C and LBM on the mean flow velocity components (U, V and W) in the slat cove

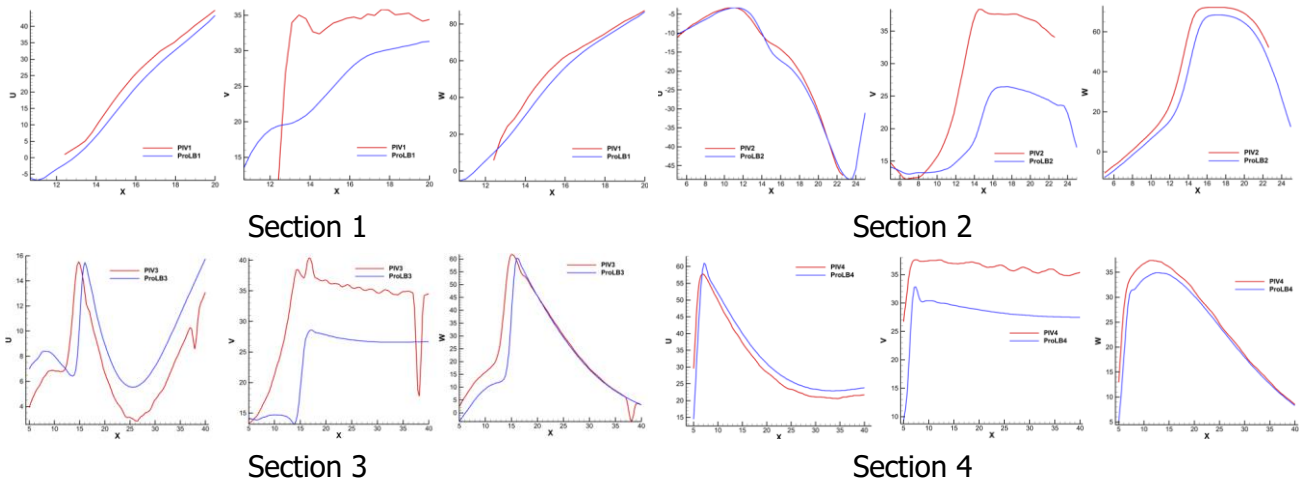


Figure 81: Same as Figure 80 (Sections 1 to 4 displayed on the W plot on Figure 80)

The computation is achieved for an airfoil angle-of-attack of 5.3° and a flow velocity of 71 m/s. A velocity map is extracted from the volume in a plane located at $LY = -56$ mm from the airfoil median section, which corresponds to $LY = +82$ mm with respect to the section of the slat track pocket #2 (see Figure 78, compared to the).

From this CFD computation Figure 80 shows iso-lines of the mean flow velocity components U, V and W in the slat cove directly compared to the PIV data.

Figure 81 shows the same result along 4 lines or sections displayed on the W plot on Figure 80. Globally we have a good agreement between PIV and CFD on the axial and vertical components U and W. The agreement is not so good for the transverse component V, which is often observed with PIV-3C when the flow velocity in the direction transverse to the laser sheet is significant.

4.5.6 Using PIV for flow analysis

In this section, PIV-3C is tentatively used to analyse characteristics of the flows.

One objective might be to detect flow differences at the vicinity of two different slat tracks, aiming at explaining different noise emissions. As an illustration,, Figure 82 compares 3 PIV-3C maps (velocity magnitude) close to the slat track #1 (left) and slat track #2 (right). On each case, 3 maps are plotted, one in the slat track section and 2 more maps at $LY = \pm 10$ mm. Both slat track designs mainly differ by the presence of an open cavity on the wing leading edge for slat track #1, which is closed for slat track #2, and was found to be a major noise source. The interpretation is not straightforward because these maps have limited coverage due to the multiple shadow zones generated by the slat track itself. However, it looks like the velocity magnitude downstream the slat track (the cross flow is from right to left) is globally higher for slat track #2.

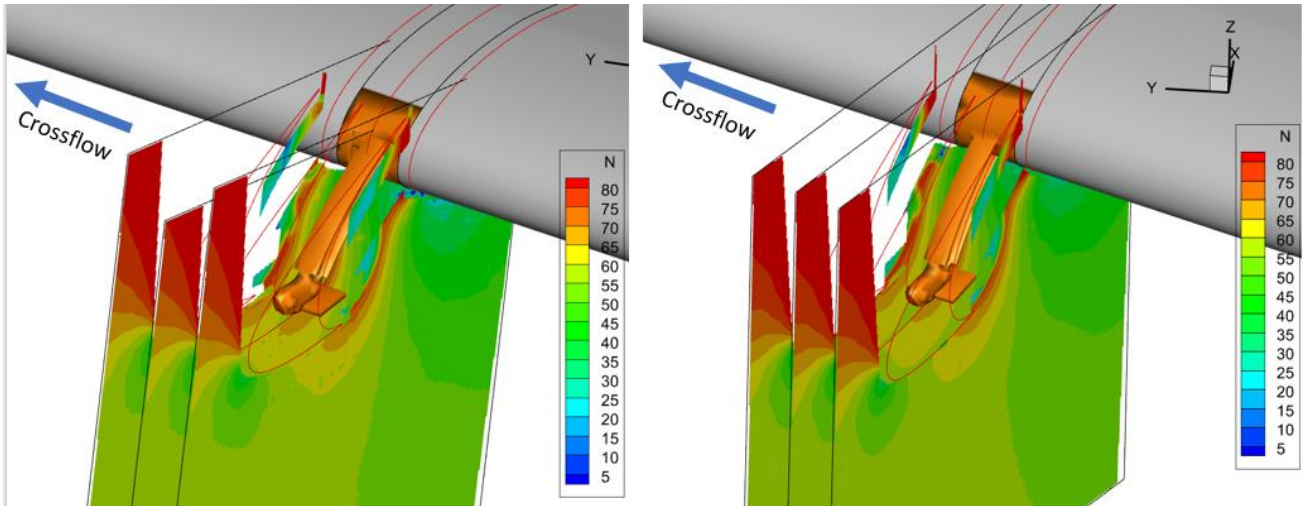


Figure 82: Comparison of 3 PIV-3C maps (velocity magnitude) close to the slat track #1 (left) and the slat track #2 (right). Only the slat sections are represented.

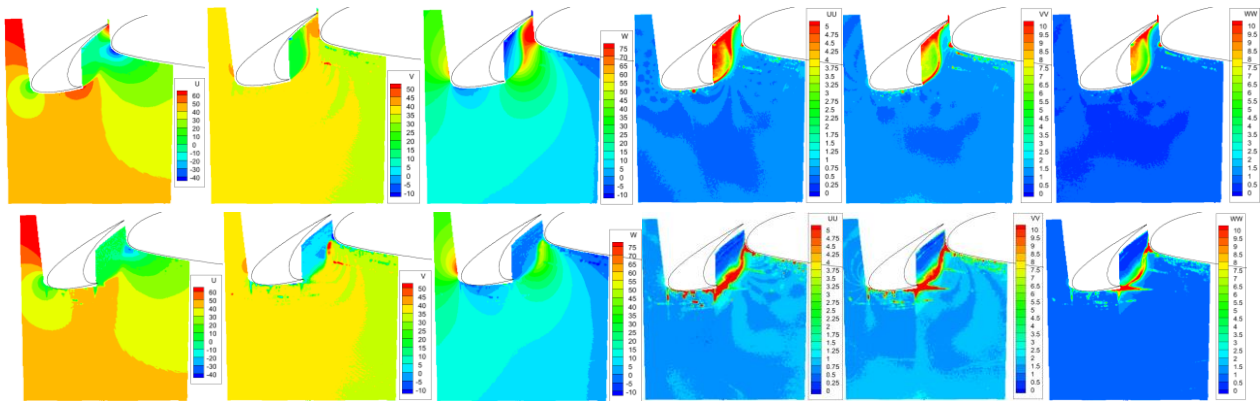


Figure 83: Tentative physical analysis of the mean flow without (top) and with (bottom) a porous insert (TE #3) installed at the slat trailing edge. From left to right: average (U, V, W) and RMS (UU, VV, WW) mean flow components

Figure 83 is a tentative to compare the mean average (U, V, W) and RMS (UU, VV, WW) components of the mean flow in the slat cove without (top) and with (bottom) a porous insert (TE #3) installed at the slat trailing edge. Note that these porous inserts is assumed to damp the unsteadiness of the flow at the position where the shear layer impacts the slat pressure side close to the slat trailing edge. The comparison of PIV maps actually shows a strong influence of the porous insert, especially with much lower levels of the 3 RMS components on the slat pressure side near the trailing edge. However the effects is also significant on the average velocity components, which is unexpected.

4.6 Aerodynamic measurements using LDV2D

4.6.1 Set-up

LDV is also an optical not intrusive method of flow characterization, based on fluid seeding, used to obtain instantaneous and time-averaged velocity measurements. The principle consists in generating a fringe system in a small volume at the intersection of two coherent Laser beams. Any particle passing the fringe system will generate a pulsed light detected with a telescope, at a frequency proportional to the velocity component normal to the fringes. By using up to 3 pairs of Laser beams of different colors, it is possible to access 3 components of the local velocity.

In INVENTOR, for reasons of limitations of the optical access to the slat cove area, only two colinear pairs of Laser beams have been used (LDV2D), aligned with the model leading edge and routed through the slat cove, with the telescope installed in the opposite side of the test section, providing only 2 velocity components, perpendicular to the beams. When the model angle-of-attack is set to 0° , the Laser beams are horizontal and the measured velocity components are exactly LU (chorwise) and W (vertical). When a non-zero incidence is applied, the laser beams are not horizontal anymore,

and approximations of LU and W are provided thanks to a correction process allowing to include the influence of the (unknown) chordwise V component.

LDV is a time-resolved measurement, meaning that each velocity acquisition is associated with a time marker, allowing to recording temporal fluctuations of the velocity, possibly providing spectral analysis on a frequency bandwidth directly linked with the density of particles generated by the seeding system.

In INVENTOR, a combination of stationary and unsteady velocity measurements have been achieved at a given number of positions in the areas already explored via PIV measurements. Note that the presence of a slat track in the slat cove obviously adds a difficulty as a new obstacle generating shadow zones, either for the laser beams or for the telescope.

The full LDV2 system is installed on the DDL system for rapid displacements in any direction and successive acquisitions in several points (Figure 84).

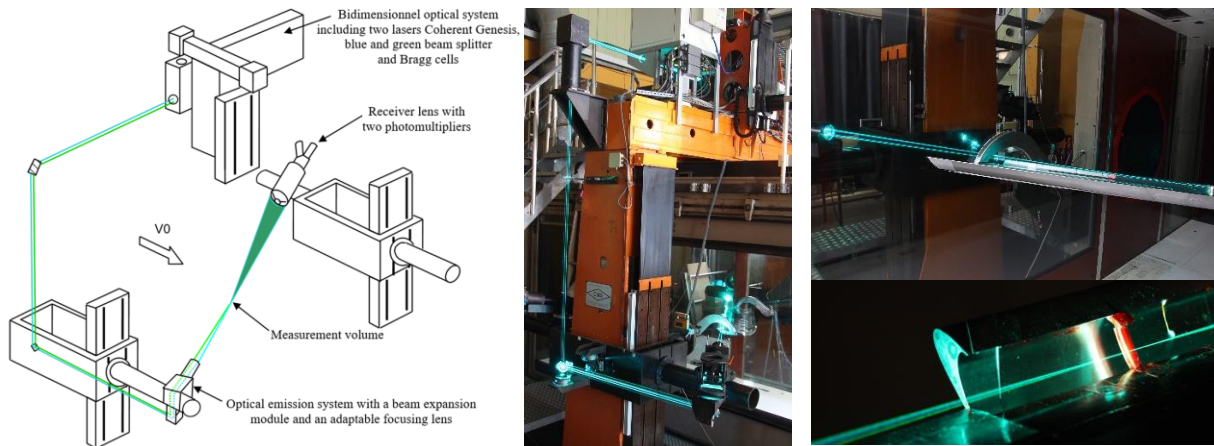


Figure 84: INVENTOR LDV2D set-up, diagram and pictures

4.6.2 LDV2D geometrical calibration

In contrast to PIV, the positioning of the LDV spot with respect to the model can be achieved with the flow, which means that the deformations of the model due to aerodynamic loads are automatically taken into account, as long as the flow velocity and the model incidence are not changed, which has been the case throughout the full LDV campaign (5.3° and 71 m/s only). A typical calibration consists in “manually” positioning the LDV spot at the reference position (same point as for the PIV: point B on the slat cusp at the spanwise position of the slat track pocket #2) and take this point as the zero position for all further displacements. Of course, this calibration must be repeated each time the slat configuration ($2.5D$ and inboard/outboard slat side edge) is changed.

4.6.3 LDV2D framework axis

4.6.3.1 Coordinates

All LDV positions have been provided by the F2 team in the F2 axis frameworks (X_{F2} , Y_{F2} , Z_{F2}) and (LX_{F2} , LY_{F2} , Z_{F2}), with the same origin B located on the slat cusp at the spanwise position of the slat track pocket #2 (model at incidence 5.3° and wind velocity 71 m/s).

These F2 axis differ from the PIV axis frameworks used to provide the « 2D » and « 3D » PIV maps, namely (LX , LY , Z) [same origin B] and (X , Y , Z) [origin at the intersection of the sweep/incidence rotation axis].

- X_{F2} : [opposite to X] horizontal, parallel to the windtunnel axis (opposite to flow direction)
- Y_{F2} : [opposite to Y] horizontal, transverse (rotation axis for global incidence)
- Z_{F2} : [same as Z] vertical, from ceiling to floor (on the airfoil: from pressure to suction side)
- LX_{F2} : [opposite to LX] horizontal, chord direction (opposite to flow direction)
- LY_{F2} : [opposite to LY] horizontal, span direction.

Finally, all coordinates are provided in the 4 axis framework (X_{F2}, Y_{F2}, Z_{F2}) , $(LX_{F2}, LY_{F2}, Z_{F2})$, (X, Y, Z) and (LX, LY, Z) . Note that, in the provided files, (X, Y, Z) and (LX, LY, Z) are respectively renamed $(LX_{2D}, LY_{2D}, Z_{2D})$ and (X_{3D}, Y_{3D}, Z_{3D}) .

4.6.3.2 Velocity components

In contrast with spatial coordinates, LDV2D velocity components are provided in only one axis framework (LU, W):

- LU: horizontal, chord direction in the flow direction,
- W: vertical, from ceiling to floor (on the airfoil: from pressure to suction side).

4.6.4 LDV2D test matrix

LDV measurements are time consuming, so they were achieved for only a limited number of configurations, all of them only at the windtunnel velocity of 71 m/s and the model incidence of 5.3°. For all configurations, short and long temporal acquisitions were mixed. Short time acquisitions contain approximately 50000 samples for mean velocity evaluation only. Long time acquisitions are about 8 time longer and contain approximately 400000 samples for unsteady and velocity evaluation only

Slat track		No	No	#1	#2
Insert		No	« TE #1 »	No	No
Slat 2.5D	Survey in LXF2 direction at LYF2 = 0 and several ZF2	<ul style="list-style-type: none"> • 24 unsteady points at ZF2 = 2.5, 5, 7.5, 10, 12.5, 15, 17.5, 20 • 142 steady points at ZF2 = 5, 10, 15, 20 	<ul style="list-style-type: none"> • 23 unsteady points at ZF2 = 2.5, 5, 7.5, 10, 12.5, 15, 17.5, 20 • 146 steady points at ZF2 = 5, 10, 15, 20 	<ul style="list-style-type: none"> • 18 unsteady points at ZF2 = 0.5, 2.5, 5, 7.5, 10, 12.5, 15, 17.5, 20 	<ul style="list-style-type: none"> • 18 unsteady points at ZF2 = 2, 2.5, 5, 7.5, 10, 12.5, 15, 17.5, 20
	Survey in LYF2 direction at several (LXF2, ZF2) positions			<ul style="list-style-type: none"> • (LXF2, ZF2) = (-8, 6), (-10.75, 10), (-13.5, 15), (-7.5, 20), (-3.5, 16), (0, 12.5), (-16, 17) • 11 unsteady points each 	<ul style="list-style-type: none"> • (LXF2, ZF2) = (-8.5, 6), (-10.75, 10), (-14, 15), (-7.5, 20), (-3.5, 16), (0, 12.5), (-16, 17) • 11 unsteady points each
Out-board slat side edge	Survey in LYF2 direction at several (LXF2, ZF2) positions	<ul style="list-style-type: none"> • (LXF2, ZF2) = (-8, 6), (-10.75, 10), (-13, 13), (-10, 17), (-1, 15) • 9 unsteady points each 		<ul style="list-style-type: none"> • (LXF2, ZF2) = (-8, 6), (-10.75, 10), (-13, 13), (-10, 17), (-1, 15) • 9 unsteady points each 	<ul style="list-style-type: none"> • (LXF2, ZF2) = (-8, 6), (-10.75, 10), (-13, 13), (-10, 17), (-1, 15) • 21 steady points each • 6 unsteady points each
In-board slat side edge	Survey in LYF2 direction at several (LXF2, ZF2) positions	<ul style="list-style-type: none"> • (LXF2, ZF2) = (-8, 6), (-10.75, 10), (-13, 13), (-10, 17), (-1, 15) • 9 unsteady points each 		<ul style="list-style-type: none"> • (LXF2, ZF2) = (-8, 6), (-10.75, 10), (-13, 13), (-10, 17), (-1, 15) • 9 points unsteady each 	<ul style="list-style-type: none"> • (LXF2, ZF2) = (-8, 6), (-10.75, 10), (-13, 13), (-10, 17), (-1, 15) • 21 steady points each • 6 unsteady points each

Table 9: LDV2 test matrix (steady and unsteady points)

For all 3 slat configurations (continuous 2.5D slat and inboard/outboard slat side edge) the tests included (i) the baseline (no slat track nor porous insert) and (ii) the slat tracks #1 and #2 in position

#2 only. Moreover, one slat porous insert (TE #3) was also tested on the continuous 2.5D slat, without slat track.

A detailed test matrix is given on Table 9. Note that "unsteady points" where long acquisition (400000 samples) were achieved, also provided mean velocity information.

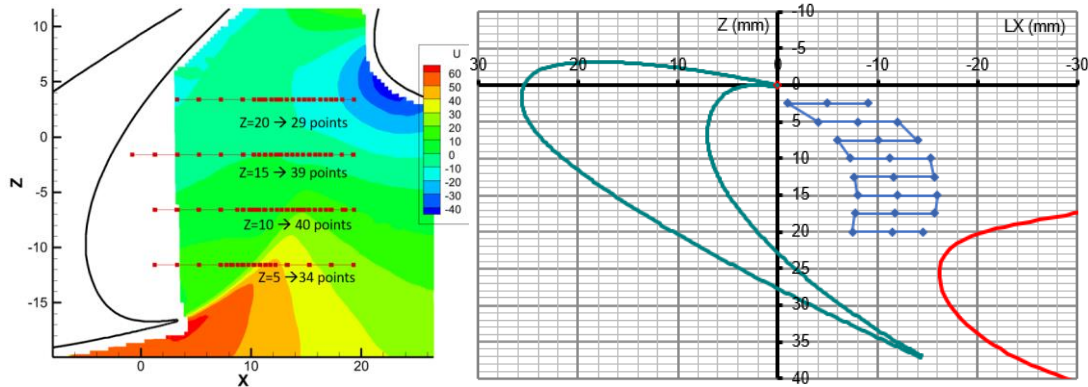


Figure 85: Location of LDV2D measurements with the continuous slat and no slat track. Left: 142 "steady points". Right: 24 "unsteady points"

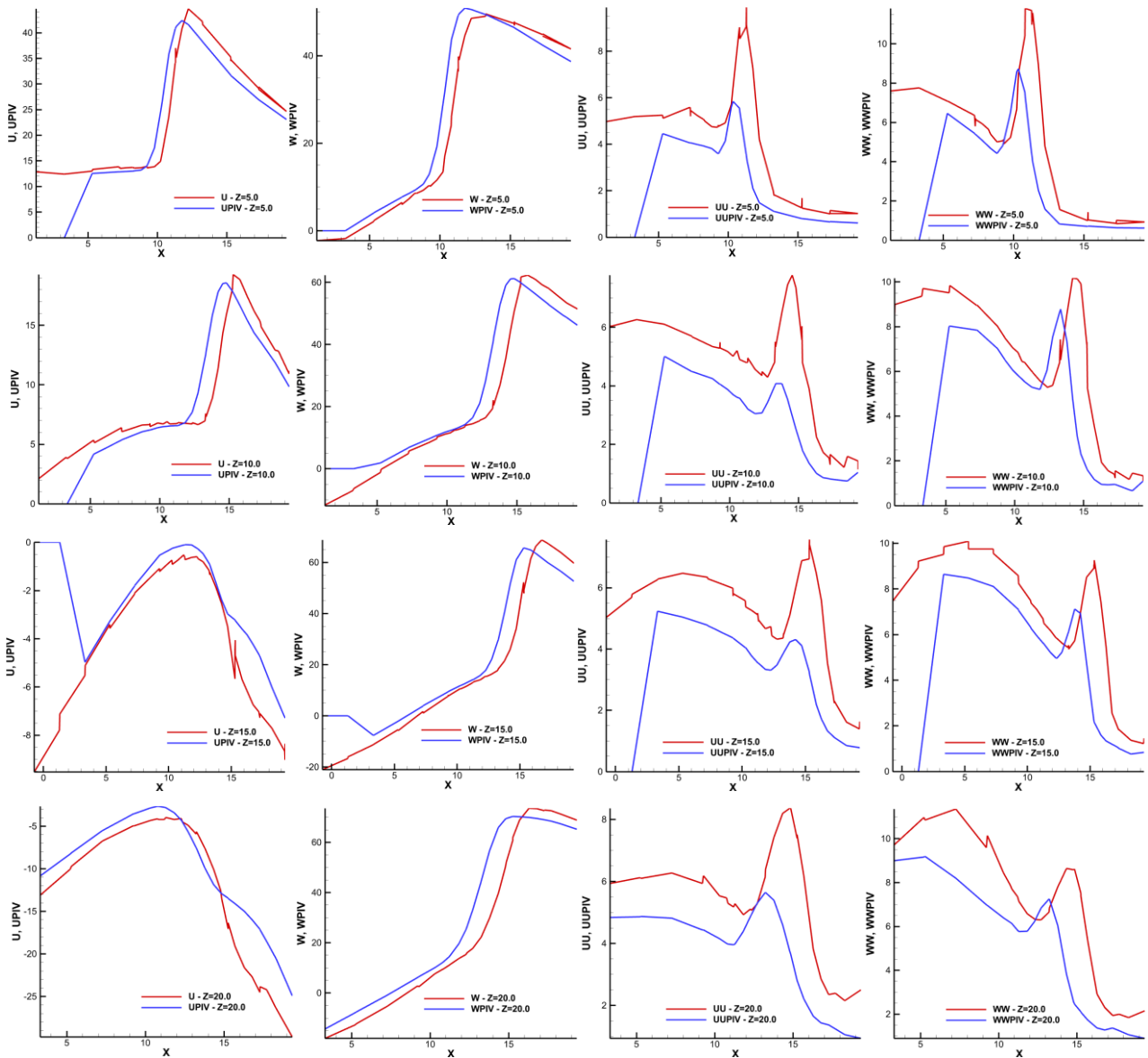


Figure 86: Comparison of LDV2D (red) and PIV (blue) measurements of LU, W, LU_{RMS}, W_{RMS} (from left to right) along 4 horizontal lines (see Figure 85) at Z = 5, 10, 15, 20 (from top to bottom). Continuous 2.5D slat, no slat track

4.6.5 Selection of LDV2D results and comparison with PIV

4.6.5.1 *Continuous (2.5D) slat without slat track*

Figure 85 shows the location of LDV2D measurements on the continuous 2.5D slat without slat track, including 24 "unsteady points" (right) and 142 "steady points" located on 4 horizontal lines at $Z = 5, 10, 15, 20$. The points are plotted on a PIV map, and Figure 86 presents detailed comparisons of the LU and W averaged velocity components (V is not available with LDV2D) and RMS components LU_{RMS} , W_{RMS} measured by LDV2D and PIV along these 4 lines.

The LU and W components are in very good agreement, despite a slight shift of about 1 mm in the LX direction, most probably a systematic error due to the uncertainty of the position of the PIV maps with respect to the airfoil. This shift is also observed on the RMS components LU_{RMS} , W_{RMS} , but the most visible tendency is a systematic underestimation of these components with PIV. This result is not a surprise and has been observed in many occasions. It is generally explained by the strong differences of spatial and temporal averaging process of LDV and PIV.

4.6.5.2 *Continuous (2.5D) slat with slat tracks #1 and #2*

Figure 87 shows the location of LDV2D measurements (unsteady points) on the continuous 2.5D slat with the slat track #1 or #2 installed in the pocket #2. These two generic slat tracks mainly differ from the presence of an open (resp. closed) cavity at the junction of slat track #1 (resp. #2) with the wing leading edge, a cavity known to be a strong noise source. Typical measurements are achieved along explorations in the LY direction and at several points in the plane $LY = 0$ which contains the slat track.

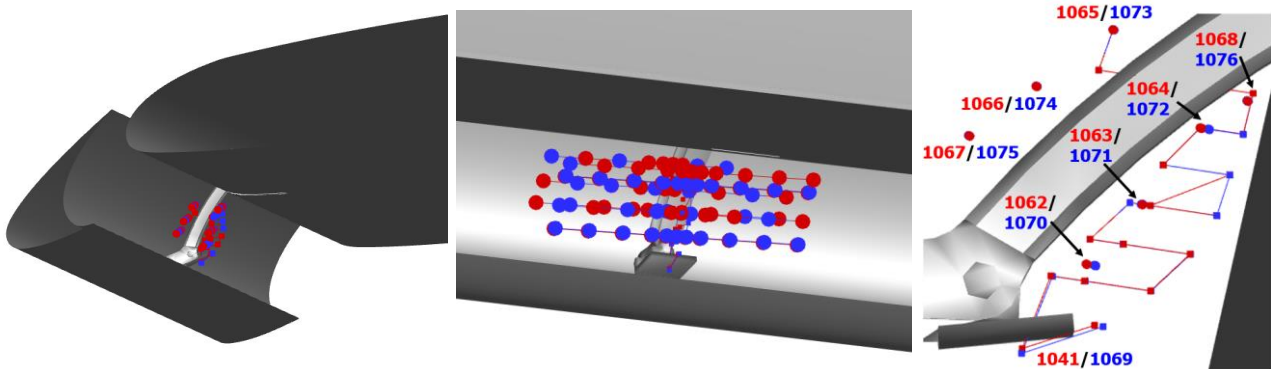


Figure 87: Location of LDV2D measurements with the continuous slat and slat track #1 (red) or slat track #2 (blue). 11 explorations in the LY direction and 18 points in the $LY=0$ plane of the slat track.

Figure 88 compares the components LU, W, LU_{RMS} , W_{RMS} (left to right) measured with LDV2D with slat track #1 (red) and #2 (blue) installed on the continuous 2.5D slat. The figure shows 3 explorations in the LY direction at positions 1065/1073 (top), 1068/1076 (middle) and 1062/1070 (bottom) (see Figure 87). The main observation is that both slat track do not show significant differences, even on the 2 first explorations 1065/1073 and 1068/1076 which are very close to the cavity in the wing leading edge. Consequently, these velocity comparisons are apparently not sufficient to explain the noise generated by the slat track opening.

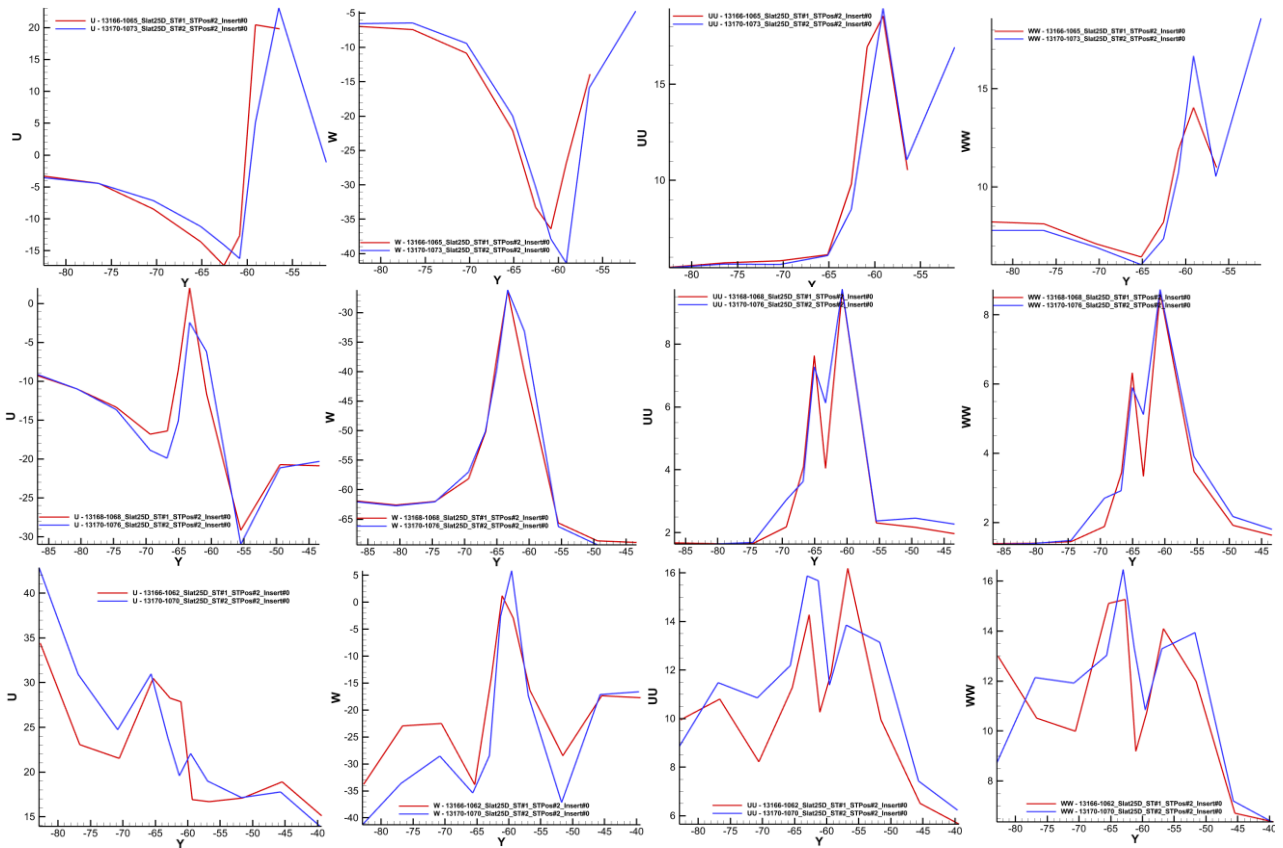


Figure 88: LU, W, LU_{RMS}, W_{RMS} (left to right) with slat track #1 (red) and #2 (blue). Continuous 2.5D slat. 3 explorations in the LY direction at positions 1065/1073 (top), 1068/1076 (middle) and 1062/1070 (bottom) (see Figure 87).

5 Slat tracks flow/noise numerical simulations

5.1 Context and objectives

This section 5 is related to the subtask 4.3.3 (Numerical simulations) in which DAV and ONERA were assumed to achieve CFD/CAA computations of selected tested configurations of slat tracks installed on the continuous 2.5D slat, with the objective to recover the trends observed in the experiments.

NLR initially proposed to achieve such numerical simulation in the Task 4.1, based on the flapless "VALIANT-like" configuration tested in its windtunnel AWT, but finally chose to stick to the more aerodynamically realistic F2 configuration, so this activity is also reported in the present deliverable.

DLR's numerical activities are also reported here, although they are not directly connected with experimental activities in F2. They concern numerical simulations of slat track noise mitigation based on active blowing close to the slat track. These computations were based on the slat track ST#11 and the continuous 2.5D slat installed on the F16 model in F2. However, the investigation is only numerical, since no blowing device was available for the tests in F2.

Last but not least, the numerical activities presented in this section 5 only concern slat track noise, whereas the trends concerning the slat porous inserts are tentatively recovered through numerical simulations on the basis of the tests in AAWT@UBRI with the unswept configuration. These numerical simulations were achieved by RWTH and are presented in section 6.

In the next sections, each involved partner details his own numerical approaches and results.

5.2 Numerical simulations by Dassault-Aviation

5.2.1 Objectives

DAV's objectives were to study the slat tracks #1 and #2 using a DES approach (Detached Eddy Simulation) with its in-house finite-element solver AETHER. For simplicity, only the continuous, rigid slat configuration has been considered (no slat side edge, no porous material). The results are compared to experimental data (pressure spectra on the skin of the model, PIV and LDV data, and far-field acoustic measurements) for validation purpose.

5.2.2 Geometry

Three configurations have been simulated by DAV:

- track ST1 (or GB_STRef_TI1_TH1_LEO_D1) in position 2,
- track ST2 (or GB_STRef_TI1_LEONo_D1) in position 2,
- no track,

see Figure 89 and Deliverable D2.3. The wing is the F16 airfoil of DLR at 30° sweep angle with continuous slat. For simplicity, neither the structural slat brackets on the pressure side, nor the flap brackets (on the pressure side too) are accounted for in the simulation. The airfoil elements (slat, main wing and flap) result from simple extrusions of 2D curves in the spanwise direction at $\alpha=5.3^\circ$ incidence. The walls of the test section are also defined from the extrusion of a 1.4 m x 1.8 m boundary in the flow direction, x.

The wind-tunnel frame (x, y, z) and a so-called *airfoil frame* ($Lx_\alpha, Ly_\alpha, Lz_\alpha$) are also presented Figure 89 (here $\alpha = 0^\circ$). The component Ly_α is in the wing spanwise direction (from the upstream to the downstream directions) and Lx_α is in the chordwise direction (downward). In the remainder, the components of the mean velocity are referred to as (U, V, W) in the wind-tunnel frame and ($LU_\alpha, LV_\alpha, LW_\alpha$) in the airfoil frame, and the root mean square of the components of velocity as (u', v', w') and ($Lu'_\alpha, Lv'_\alpha, Lw'_\alpha$) respectively.

For simplicity during the wind-tunnel tests, the aerodynamic measurements were specified at 0° incidence, in spite of the 5.3° of the airfoil. Note then that measurements at constant Lx_0 or Ly_0 do not follow perfectly the spanwise or chord-wise directions (respectively) of the airfoil actually at 5.3°

incidence. For scientific purpose, velocity components in the airfoil frame are given in the airfoil directions at 5.3° incidence though.

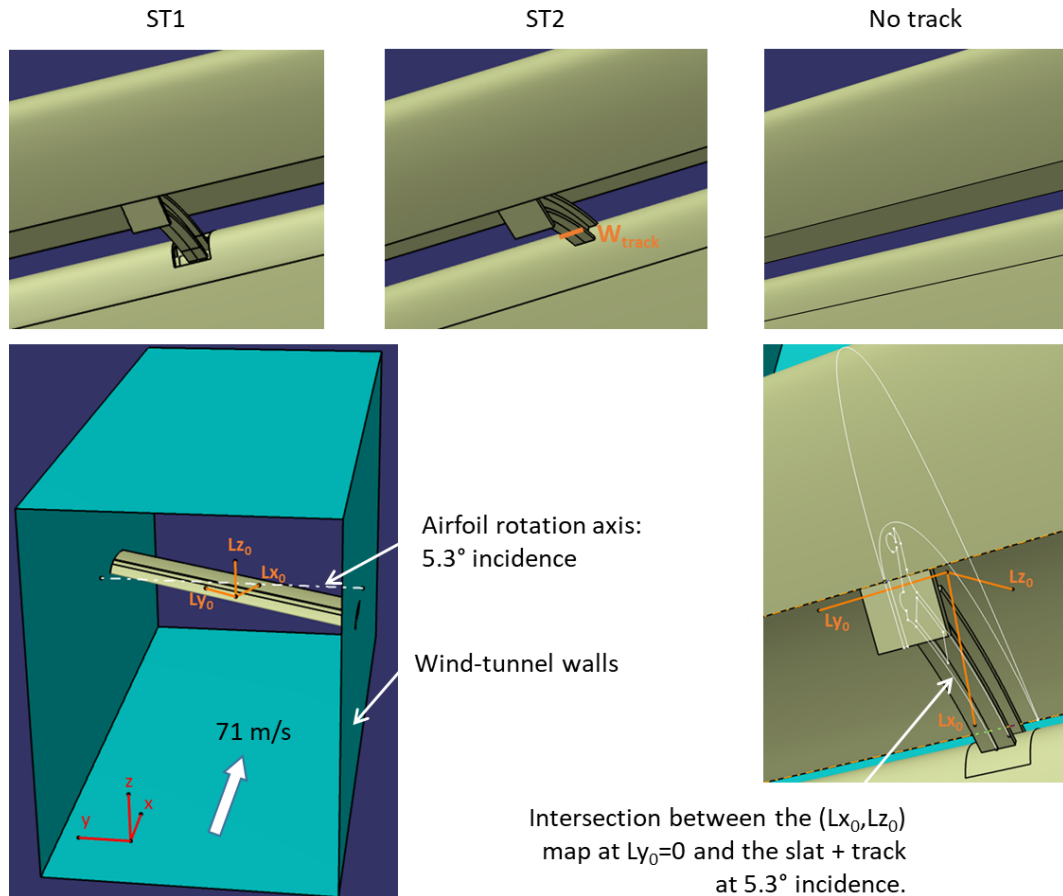


Figure 89: Geometry: (top) tracks ST1 and ST2, and no-track; (bottom) wind-tunnel frame (x, y, z) and airfoil frame at 0° incidence (Lx_0, Ly_0, Lz_0) . Note that the (Lx_0, Lz_0) map at $Ly_0=0$ (0° incidence) is not exactly in the middle plan of the track at 5.3° incidence.

5.2.3 Numerical strategy

As for the GB-TA-MLG1 noise simulations (see deliverable D3.7), the computational approach is carried-out in 2 steps: first, the flow fluctuations are computed by DES using the DAV's in-house solver AETHER; then, the acoustic field is determined by the Curle's acoustic analogy by using the time-domain fluctuations of pressure over the geometry. Further details of the CFD approach can be found in the deliverable D3.7, Sec. 4.

A no-slip condition is applied on the airfoil (including the track) and a slipping condition is set on the walls of wind-tunnel.

The 3D mesh comprises several areas:

- a boundary-layer like mesh around the geometry,
- two uniform, isotropic and refined areas in the vicinity of the track, see Figure 90. The resolution of the finest mesh is $200 \mu\text{m}$.
- a coarser, isotropic area elsewhere, up to the wind-tunnel walls, filled by a Voronoi approach.

A total of 79.2 million points are then defined.

For the acoustic computations, the input pressure data over the geometry are limited to 200 mm distance from the slat track (≈ 3.6 slat chord, *i.e.* 55.8 mm) in order to avoid spurious contributions from coarse areas.

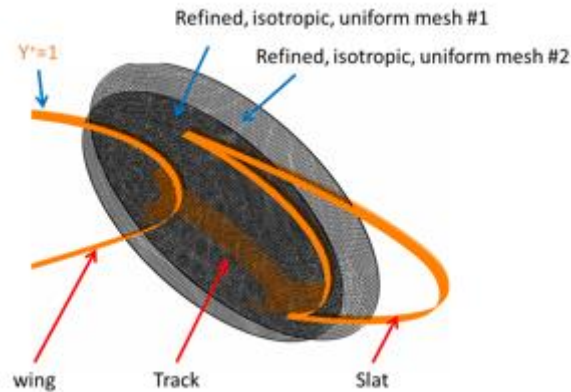


Figure 90: Mesh in the vicinity of the slat track.

5.2.4 Results

5.2.4.1 Mean aerodynamic data

Mean velocity data in the slat cove are presented Figure 91, without track. These results illustrate the fair agreement between the simulation and the measurements (PIV). To quantitatively assess the simulation results, velocity profiles are plotted Figure 92 against the Lx_0 direction in $Lz_0 = -13, 0$ and 8 mm ($Ly_0 = 0$ mm). A reasonable agreement is found for each velocity component U, V, W (in the wind-tunnel frame). In particular, the velocity profile through the shear-layer separating the recirculation domain and the high-speed area in the slat cove ($Lx_0 > 0$) is correctly captured.

The spanwise velocity field $LV_{5,3}$ is shown Figure 93 (no track). It is interesting to note the uniformity of $LV_{5,3}$ outside of the recirculation domain. In this area, $LV_{5,3}$ is approximately equal to the projection of the wind-tunnel velocity onto the spanwise direction, $LV_{5,3} \approx U_{inf} \cos(30^\circ)$, showing the weak modification of this component by the airfoil and thus the 2D behavior of the velocity field (or 2.5D), as expected. In the recirculation area, the $LV_{5,3}$ component is between 0 and $U_{inf} \cos(30^\circ)$ and roughly uniform too.

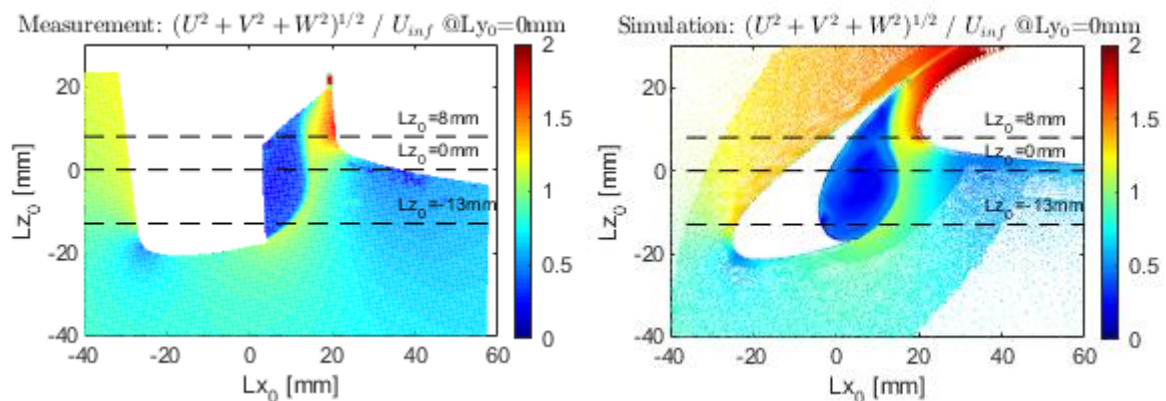


Figure 91: Mean velocity in $Ly_0 = 0$: no track. Left: PIV data. Right: simulation.

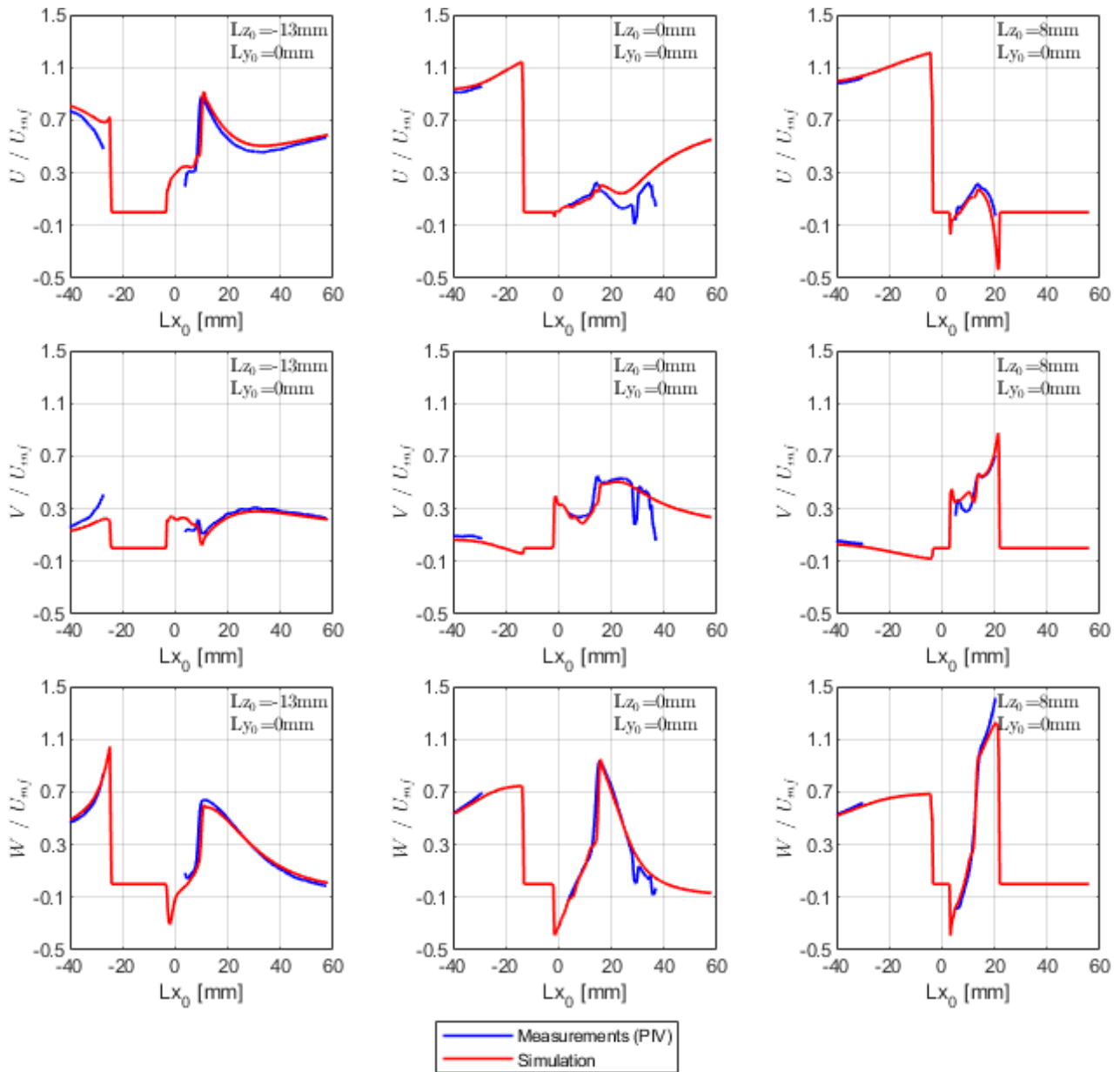


Figure 92: Mean velocity components U , V , W in the Lx_0 direction at $Lz_0 = -13, 0$ and 8 mm ($Ly_0 = 0$): no track.

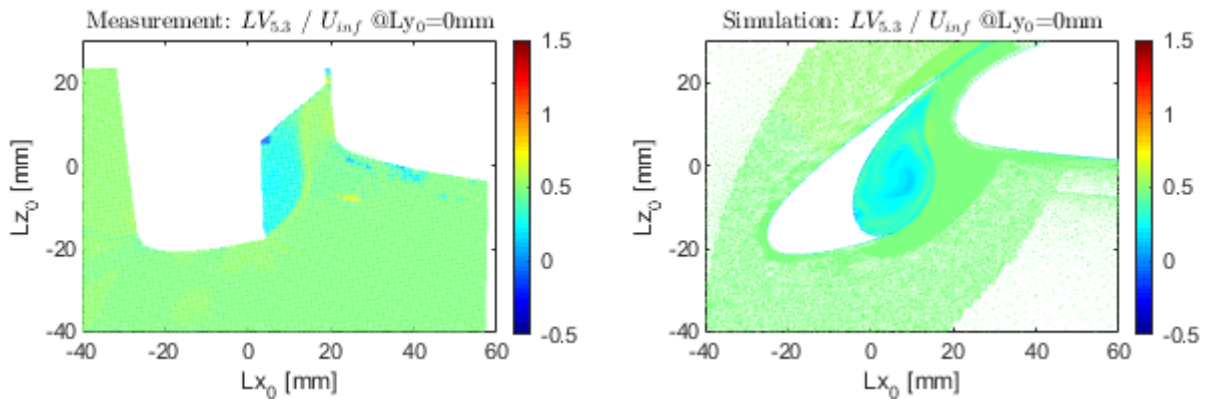


Figure 93: Mean spanwise velocity $LV_{5.3}$ in $Ly_0 = 0$: no track. Left: PIV data. Right: simulation.

Mean velocity maps are shown Figure 94 regarding the slat track ST1. Three positions are considered: $Ly_0 = -10$ mm $\approx -1,7L_{\text{track}}$ (upstream/inboard side, without intersection through the track), 0 mm

(through the slot track, see Figure 89), $10 \text{ mm} \approx 2.1W_{\text{track}}$ (downstream/outboard side, without intersection through the track), where $W_{\text{track}} = 4.8 \text{ mm}$ is the characteristic track width, see Figure 89. The impact of the track on the downstream flow is weak, even downstream at $L_{y_0} = 10 \text{ mm}$. Between the upstream side and the downstream side ($L_{y_0} = \pm 10 \text{ mm}$), the mean velocity seems to differ in the recirculation bubble only, near the upper slot boundary. Quantitative comparisons are presented Figure 95 showing again a fair agreement between the measurements and the simulations regarding the ST1 track (plain lines). Measurement and simulation data without track are superimposed to quantitatively confirm the weak impact of the track on the mean velocity at $L_{y_0} = \pm 10 \text{ mm}$, which is besides actually limited to the recirculation area.

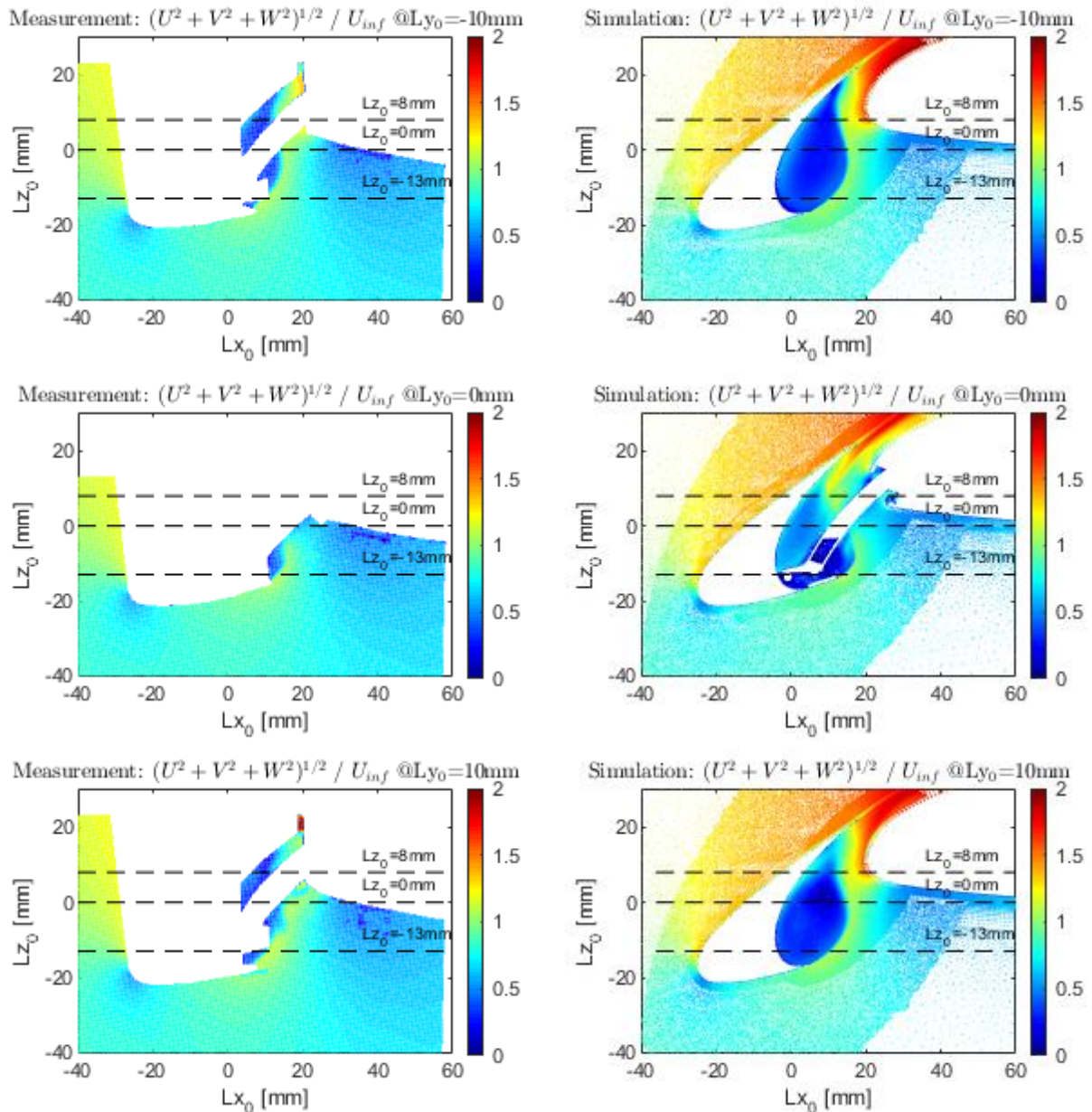


Figure 94: Mean velocity in $L_{y_0} = -10 \text{ mm}$ (upstream/inboard side, without intersection through the track), 0 mm (through the track) and 10 mm (downstream/outboard side, without intersection through the track): track ST1. Left: PIV data. Right: simulation.

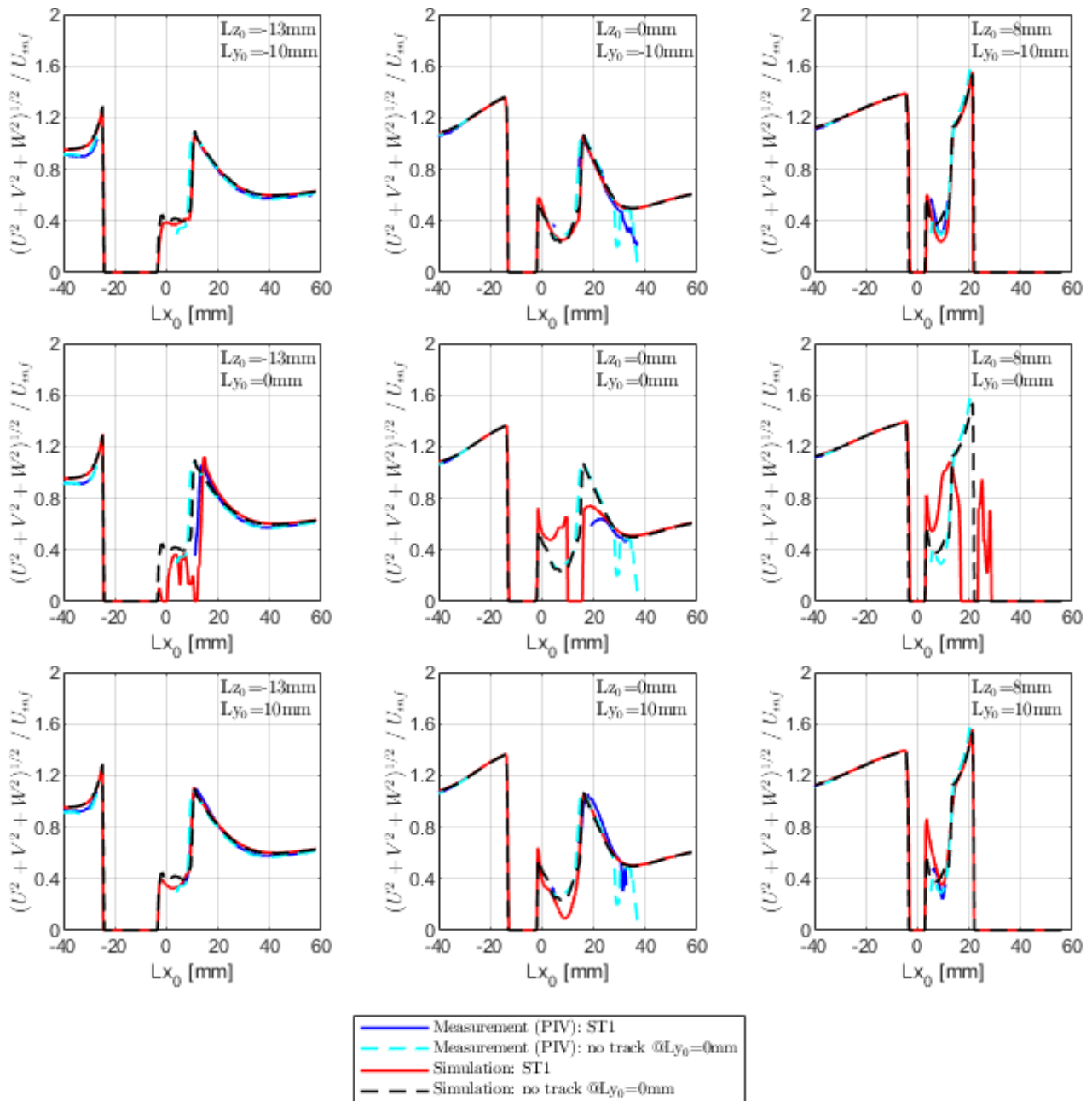


Figure 95: Mean velocity in the Lx_0 direction at $Ly_0 = -10, 0, 10$ mm and $Lz_0 = -13, 0$ and 8 mm: track ST1 (plain lines) and no track at $Ly_0 = 0$ mm (dashed lines).

5.2.4.2 Fluctuations of velocity

The aerodynamic field of the turbulence rate in the slat cove without track is presented Figure 96 and Figure 97. The simulated levels are notably weaker than the measurements. In particular the high levels measured in the initial shear-layer from the pressure side of the slat trailing edge (more than 25%) are not reproduced by simulation (less than 5%). The turbulence rate is consequently underestimated through the whole shear-layer down to its interaction on the slat cove. The location of the maximum level of turbulence in the slat shear-layer is well captured though (in the chord-wise direction Lx_0). The amplitude of the turbulence in the recirculation area is also underestimated.

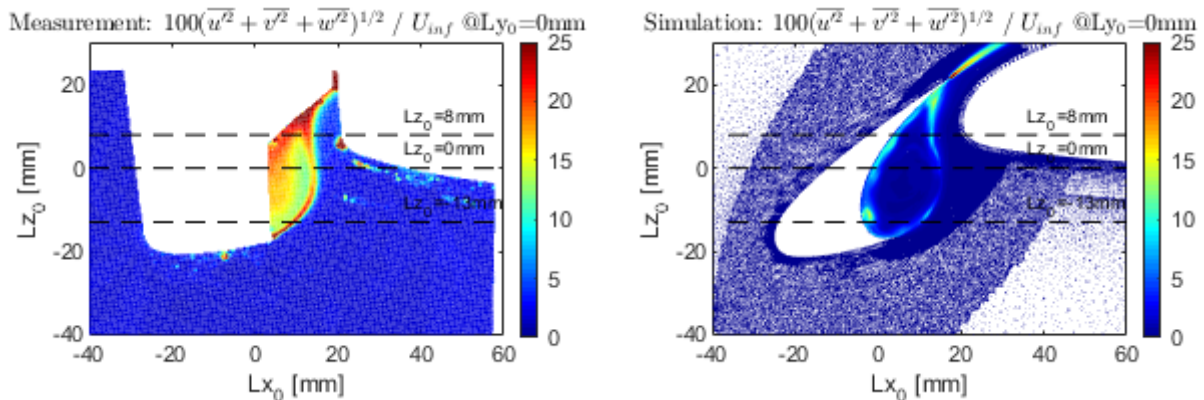


Figure 96: Turbulence rate of velocity in $L_{y_0}=0$: no track. Left: PIV data. Right: simulation.

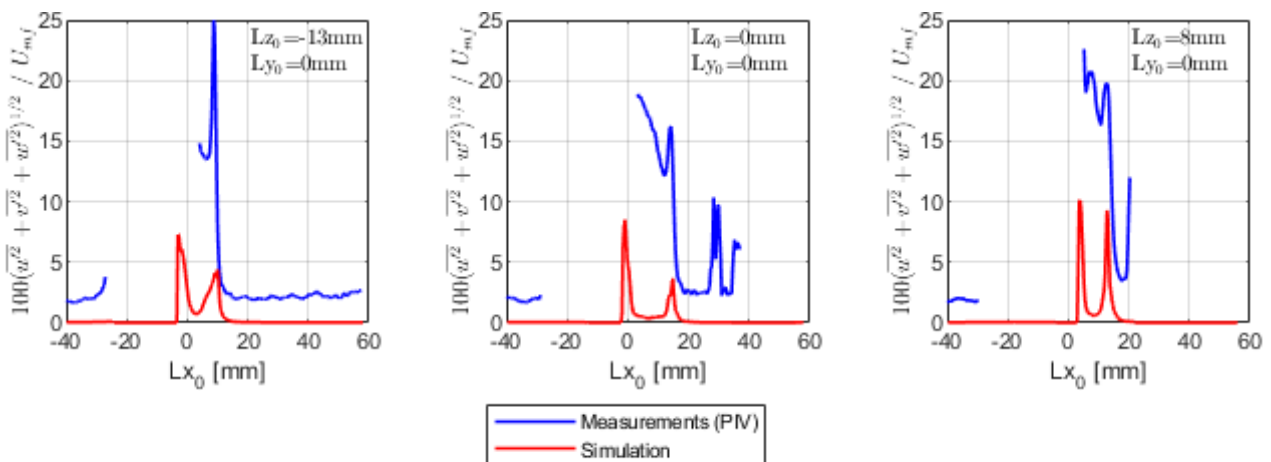


Figure 97: Turbulence rate of the velocity in the L_{x_0} direction at $L_{y_0}=0$ mm and $L_{z_0}=-13, 0$ and 8 mm: no track.

Figure 98, the 3 components of the total turbulent velocity are represented in the airfoil frame. To highlight the characteristics of the turbulence in the slat cove, the experimental data and the simulation are drawn with specific ranges, 20% and 10% respectively. The measurements show that the turbulent velocity is strongly anisotropic from the initial development of the slat shear-layer. In particular, the $Lv'_{5,3}$ component is noticeably higher than the other ones. The intensity of $Lu'_{5,3}$ in the slat cove area is also clearly weaker than $Lv'_{5,3}$ and $Lw'_{5,3}$ (measurements). Near the area of interaction of the shear-layer on the slat, $Lv'_{5,3}$ and $Lw'_{5,3}$ have conversely similar intensities. These characteristics of the turbulence are not fully captured by simulation yet. Besides, areas of maximal turbulence are observed in the slat shear-layer by simulation, while turbulence seems to continuously develop experimentally. These results tend to show an erroneously laminar development of the initial slat shear-layer computed by simulation.

Cross-velocity terms are additionally plotted Figure 99. Similar disagreements are noticed between the measurements and the simulation (no track): weaker simulated levels; incorrect characteristics of isotropy; wavy *vs.* monotonic distribution of the turbulence in the shear-layer.

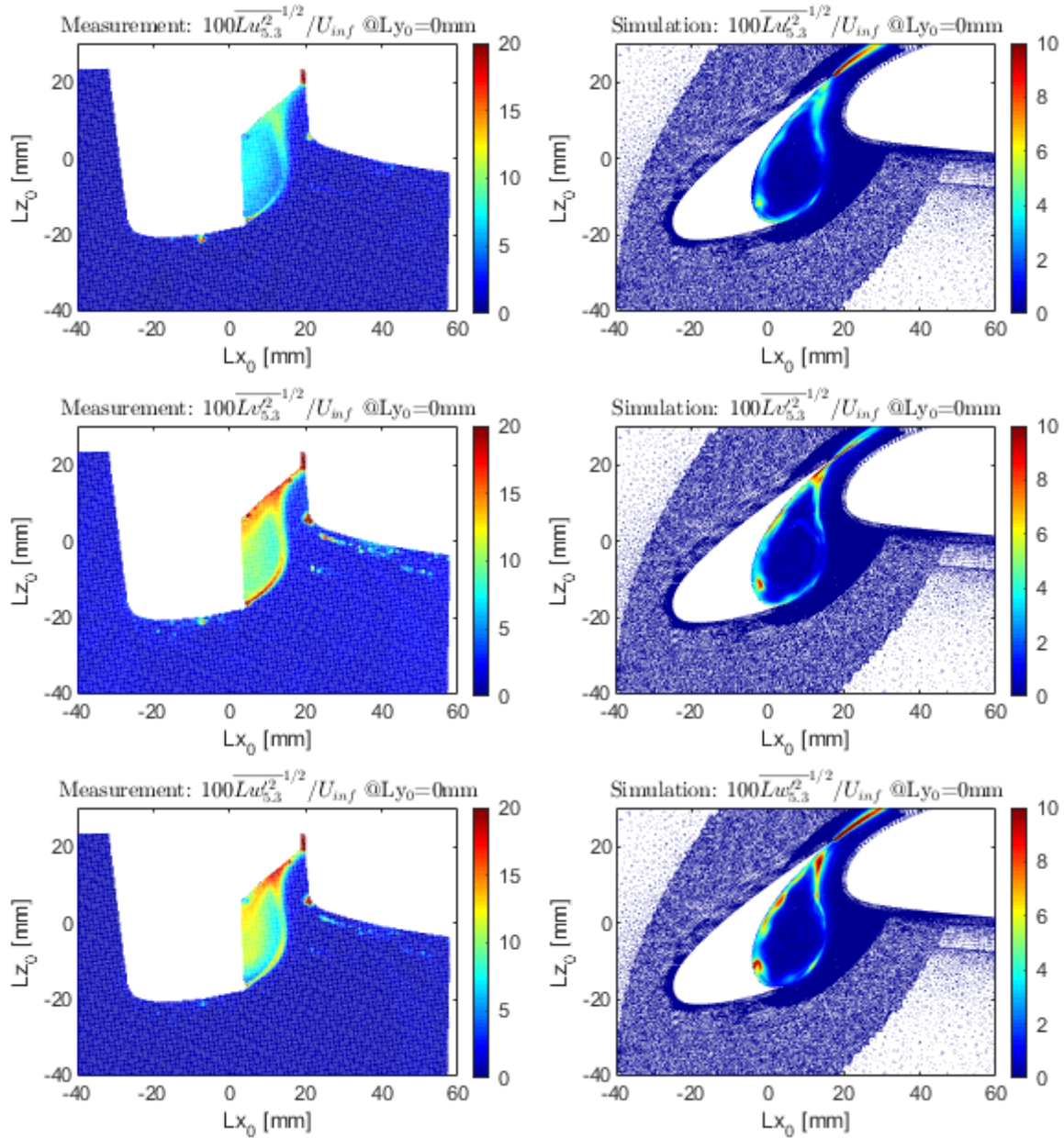


Figure 98: Root mean square of the $Lu'_{s,3}$, $Lv'_{s,3}$ and $Lw'_{s,3}$ velocity components in $Ly_0 = 0$: no track. Left: PIV data. Right: simulation.

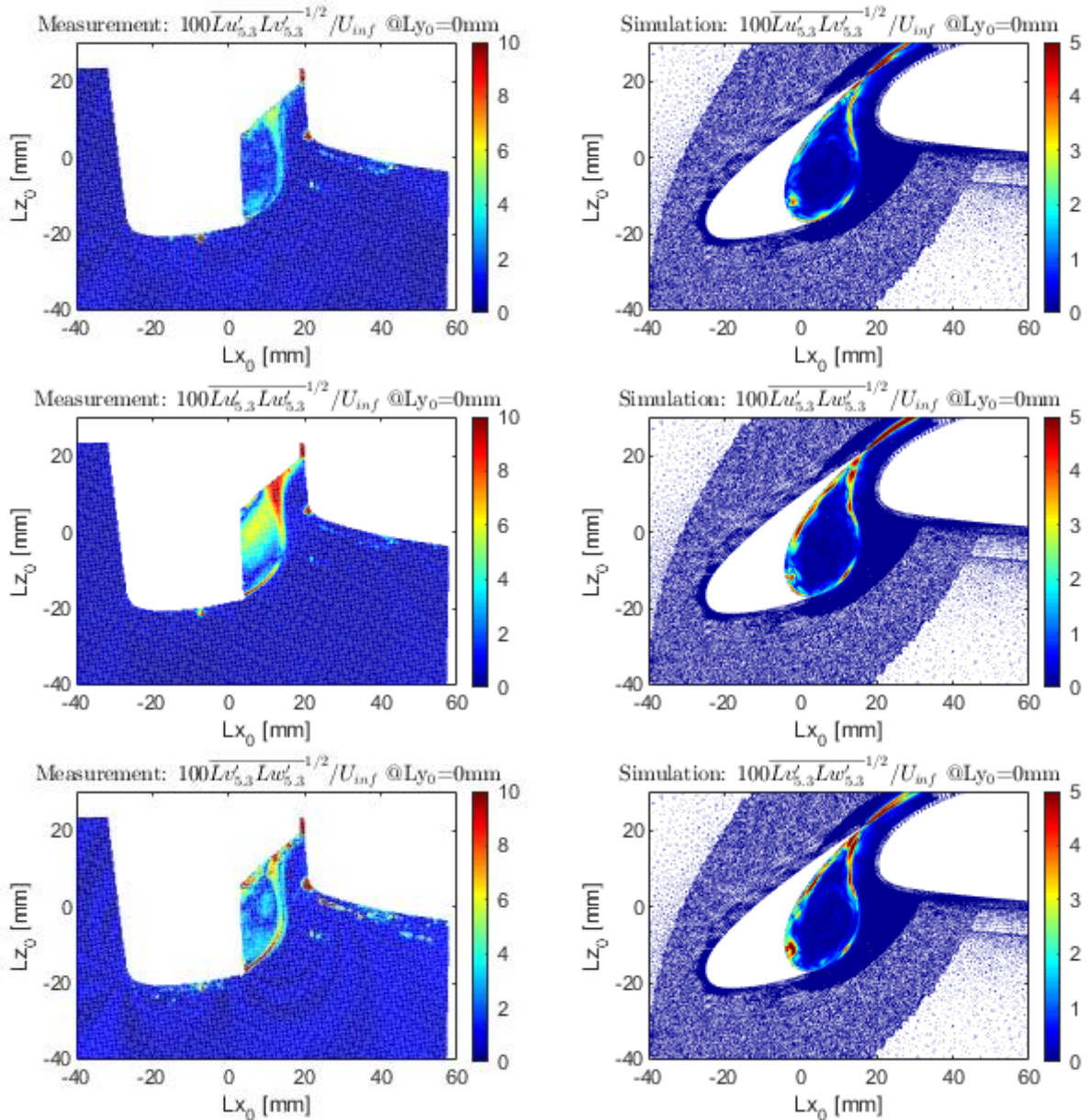


Figure 99: Root mean of the cross velocity components $Lu'_{5.3}Lv'_{5.3}$ (top), $Lu'_{5.3}Lw'_{5.3}$ (middle) and $Lv'_{5.3}Lw'_{5.3}$ (bottom) in $Ly_0=0$: no track. Left: PIV data. Right: simulation.

The distribution of turbulence with the slat track ST1 is displayed Figure 100. As expected, intense levels are observed in the $Ly_0=0$ mm map, in particular on the suction side of the track, including the wing cavity. On the downstream side $Ly_0=+10$ mm, strong perturbations are also noticed on the suction side of the wing. Quantitative comparisons of the simulation and the measurements are shown Figure 101 (upstream, $Ly_0<0$), Figure 102 ($Ly_0=0$ mm) and Figure 103 (downstream, $Ly_0>0$). Results without track are superimposed for comparison (dotted lines). The experimental results show that the impact by the track is limited to $Ly_0 = 0$ mm and to ($Ly_0 = 10$ mm, $Lz_0 \geq 0$ mm). The conclusion from the simulation noticeably differ though (wi/wo track). Indeed, higher turbulence levels are obtained with track almost everywhere. In this case (with track), the results are in better agreement with the measurements.

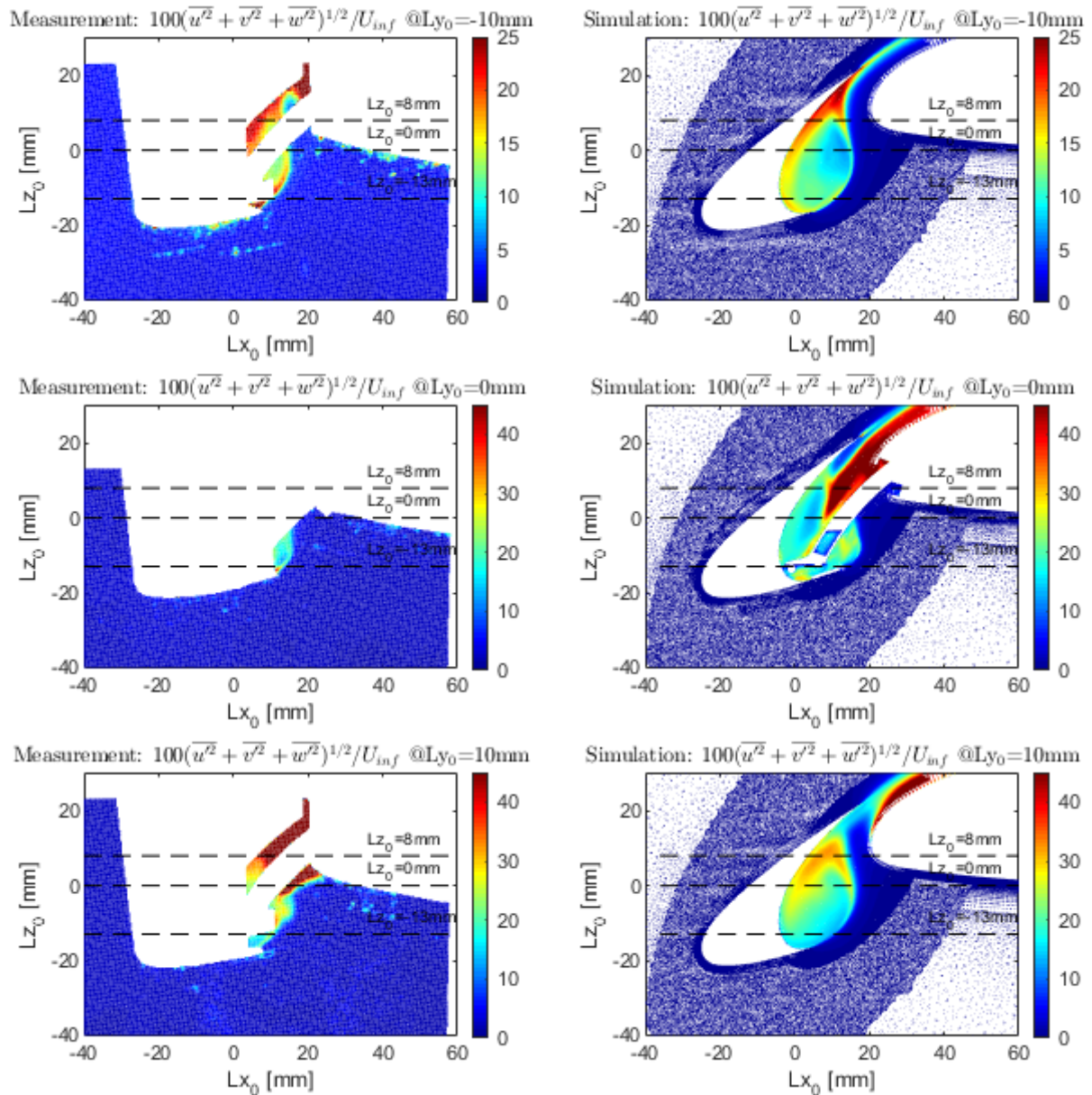


Figure 100: Turbulence rate of velocity in $L_{y_0}=-10, 0$ and 10 mm: track_ST1. Note the specific color range used for $L_{y_0}=-10$ mm. Left: PIV data. Right: simulation.

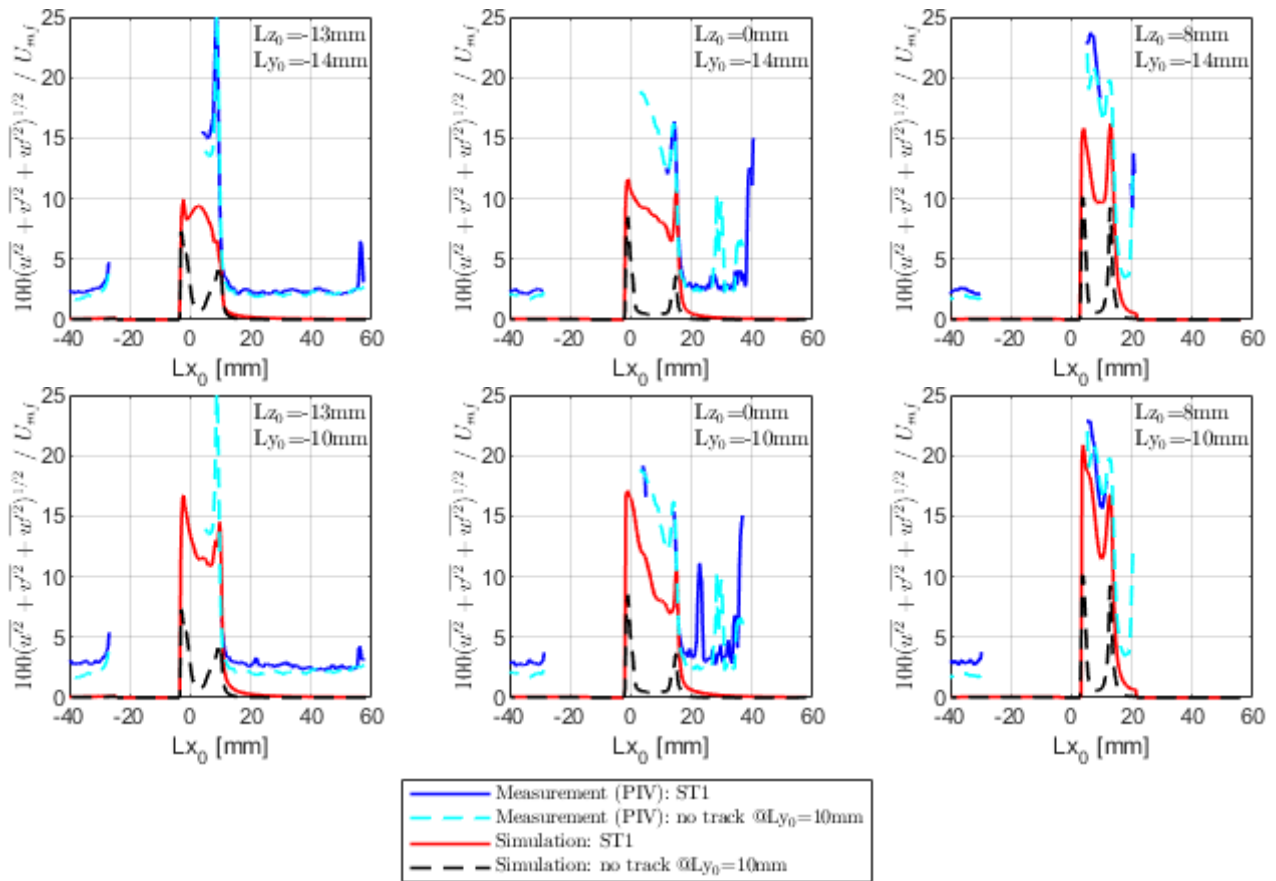


Figure 101: Turbulence rate of velocity in the Lx_0 direction at $Ly_0 = -14$ and -10 mm (upstream), and $Lz_0 = -13, 0$ and 8 mm: track ST1.

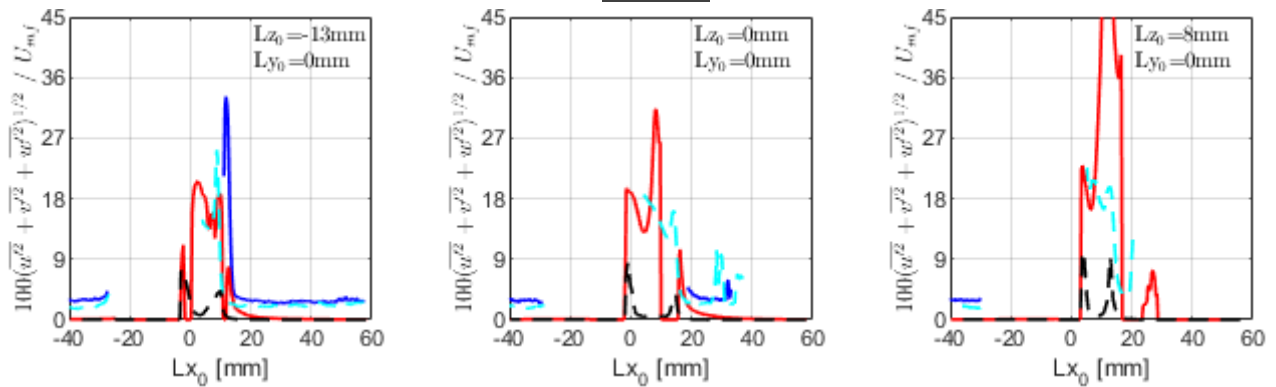
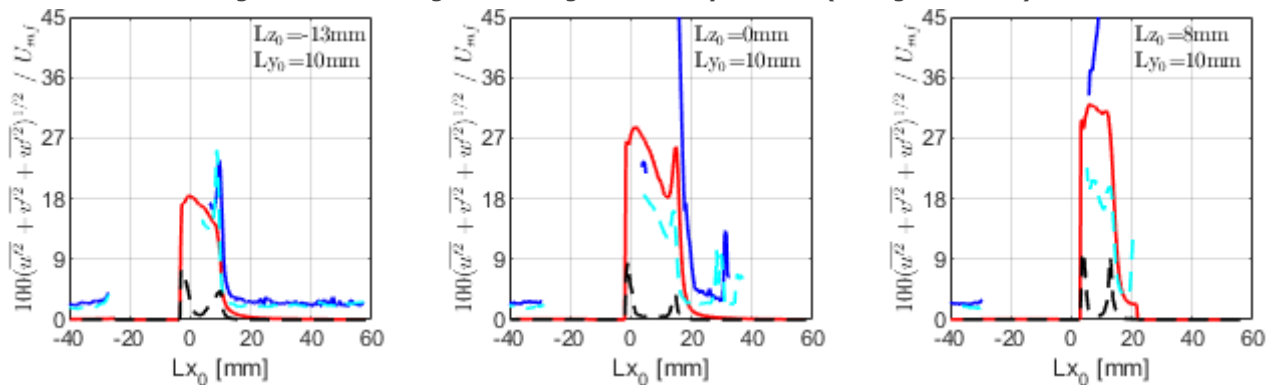


Figure 102: Same legend as in Figure 101 at $Ly_0 = 0$ mm (through the track).



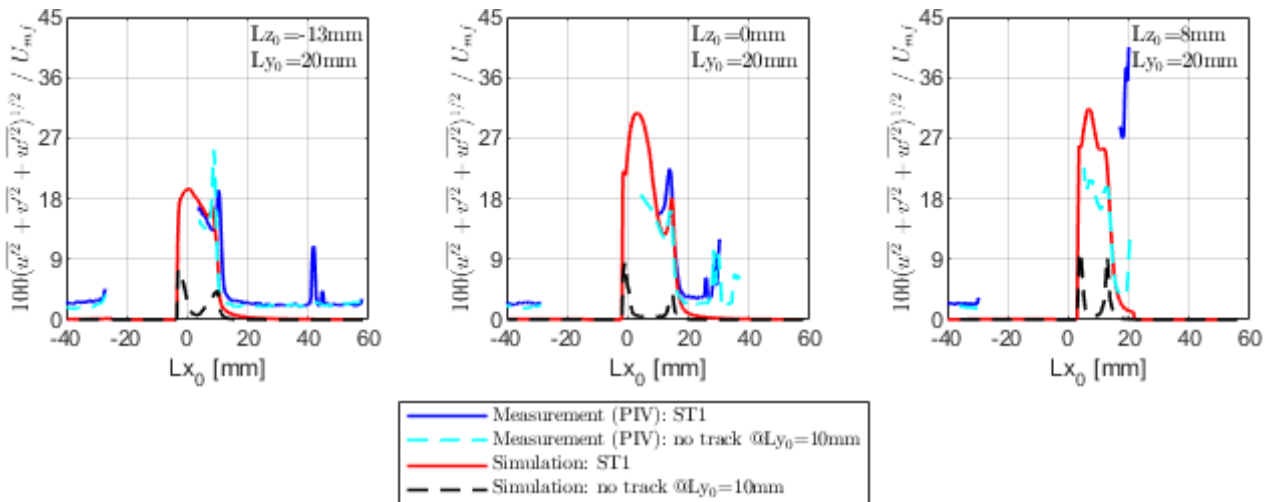


Figure 103: Same legend as Figure 101 at $L_{y_0} = 10$ and 20 mm (downstream).

5.2.4.3 Fluctuations of pressure

Measurements by 4 Kulite sensors on the wing leading edge, KU9 to KU12 (see their positions on Figure 104), are compared to simulation data in Figure 105. Three configurations are studied: without track, track ST1 and track ST2. The data without track in KU11 are used as reference and are superimposed over each figure for comparison. Without track, the experimental spectra are close, for all the Kulite, as expected. Analogously, the simulation data in KU9, KU10 and KU11 are close too, but notably lower than the measurements (between 5 and 10 dB up to 2 kHz), which is compliant with the weak turbulence levels observed previously without track. The very low levels simulated at KU12 are due to the poorly refined mesh in this area. No impact of the slat tracks (ST1 or ST2) is observed experimentally upstream (KU12). Downstream, the impact reduces with the distance to the track increasing as expected (from KU11 to KU9). In KU9, the measured pressure spectra, with/without track, are even similar. The hierarchy of the experimental pressure spectra with track is not explained downstream though. Higher levels were indeed expected for ST1 (presence of a wing leading edge cavity) with respect to ST2 (closed cavity), while the opposite is obtained. Simulation data don't reveal noticeably different levels of pressure spectra yet (ST1 *wt.* ST2). The results of the ST2 track are in fair agreement with the measurements downstream (KU9-KU11) up to 3 kHz.

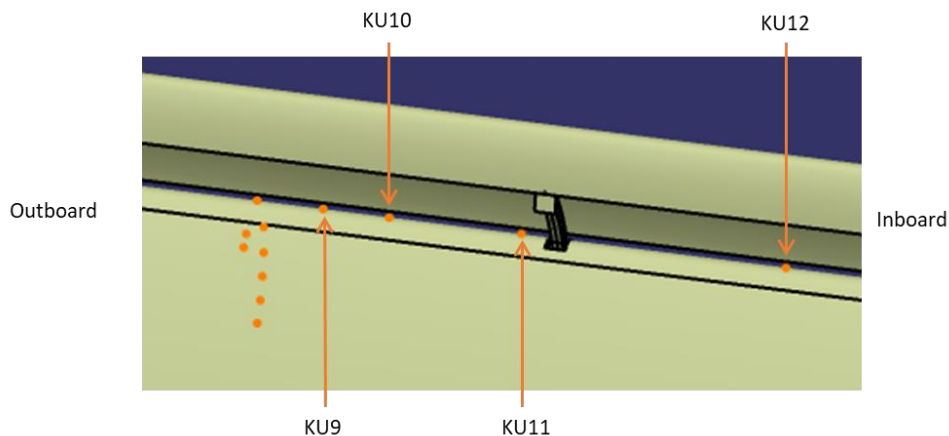


Figure 104: Location of the Kulite KU9 to KU12 on the wing leading edge.

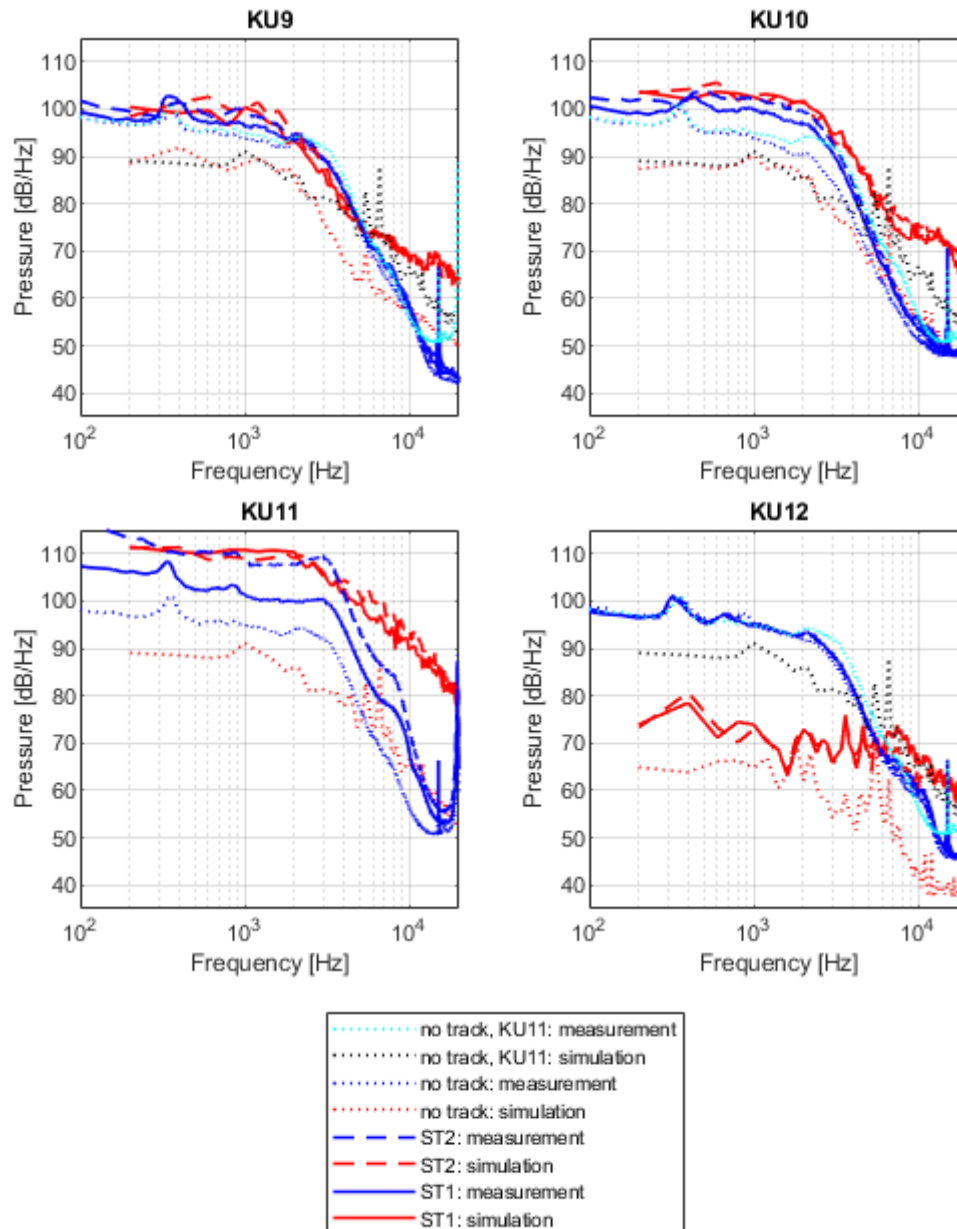


Figure 105: Pressure spectra to the position of the Kulite on the wing leading edge KU9 to KU12.

5.2.4.4 Acoustics via virtual beamforming

The acoustic pressure was propagated up to the position of each microphone of the 120-microphone array in F2 using an integral method based on the Curle's analogy. For illustration, Figure 106 compares the noise spectra computed at the position of the central microphone AW1 of the 120-microphone array in F2, for the baseline (no slat track) and for the slat tracks #1 and #2.

From these time signals, DAV computed the cross spectra matrix between all the 120 microphones using the periodogram method based on 58 data blocks, 500 time samples per block, 100 kHz sampling frequency and rectangular windows, without overlapping. The resulting cross spectral matrix was provided by DAV to ONERA. The same array processing was applied to the simulation data numerical signal as to the experimental data. Figure 107 shows DAMAS noise maps at 1, 2, 4 and 8 kHz computed from the simulation data without slat track (top), with slat track #1 (middle) and #2 (bottom). The origin of the noise sources detected on the slat and the flap without slat track is not obvious but when a slat track is installed (#1 or #2), the corresponding noise source clearly dominates the maps at all considered frequencies.

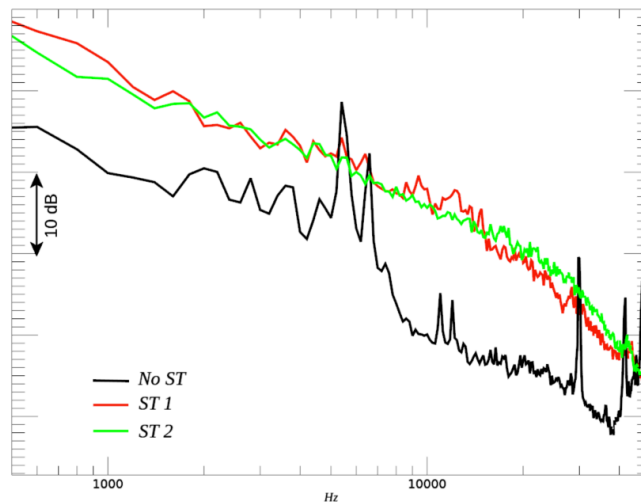


Figure 106: Noise spectra computed by DAV at the position of the central microphone of the 120-microphone array in F2, without slat track with the slat tracks #1 and #2

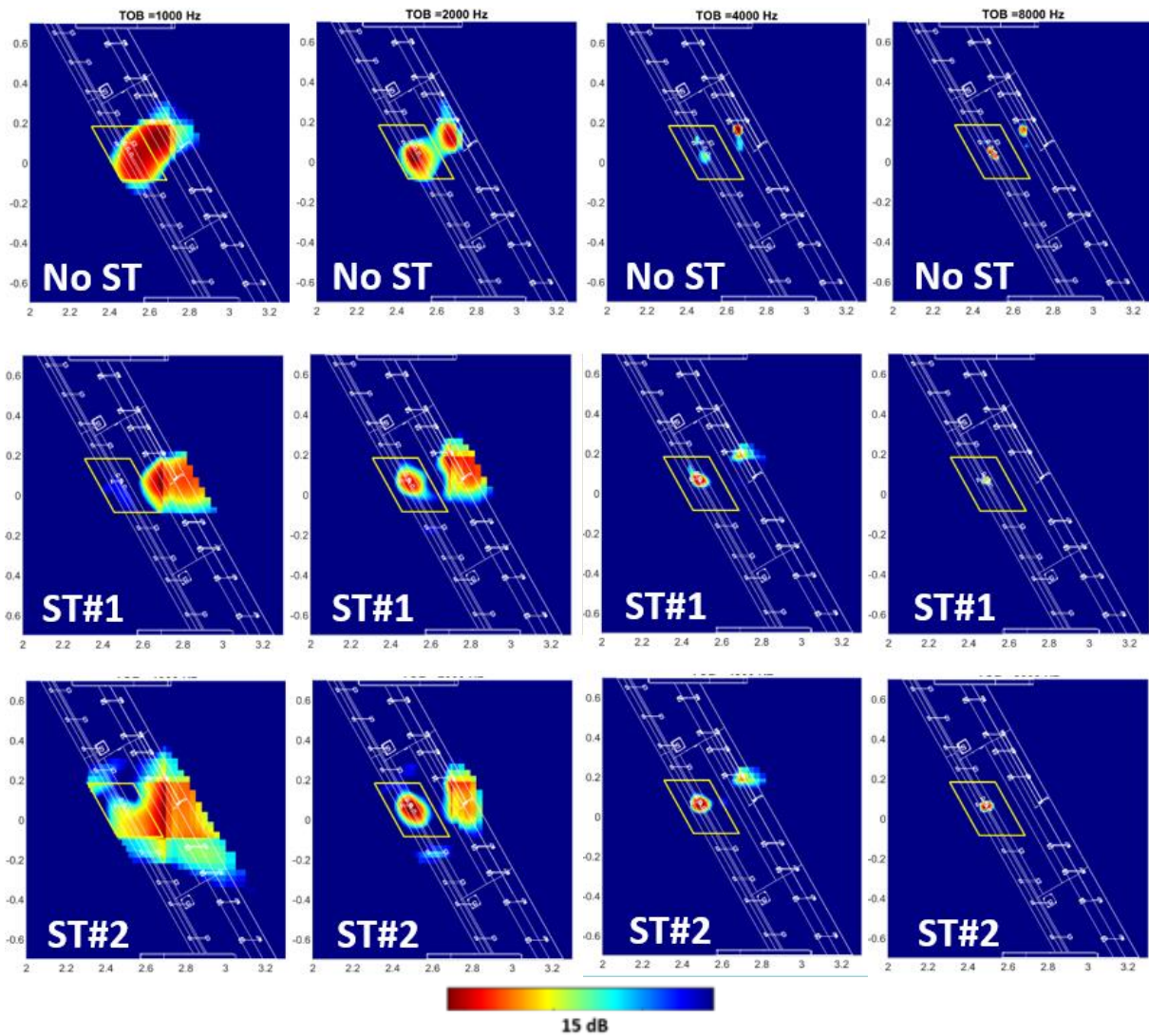


Figure 107: DAMAS noise maps at 1, 2, 4 and 8 kHz computed from the virtual acoustic signals computed by DAV on the positions of the 120 microphones without slat track (top) and with slat track #1 (middle) and #2 (bottom)

These noise maps were integrated over the same area (yellow zone on Figure 96) and the results (integrated spectra) are compared on Figure 108 with similar experimental data. Without track, a large deviation is noticed. Spectral arches are observed below 10 kHz for both the experimental and simulation datasets though. With tracks, the simulation data are in better agreement with the measurements. While still significantly underestimated for low-frequencies (< 4 kHz), the measurements are deemed to be fairly well reproduced at high-frequency.

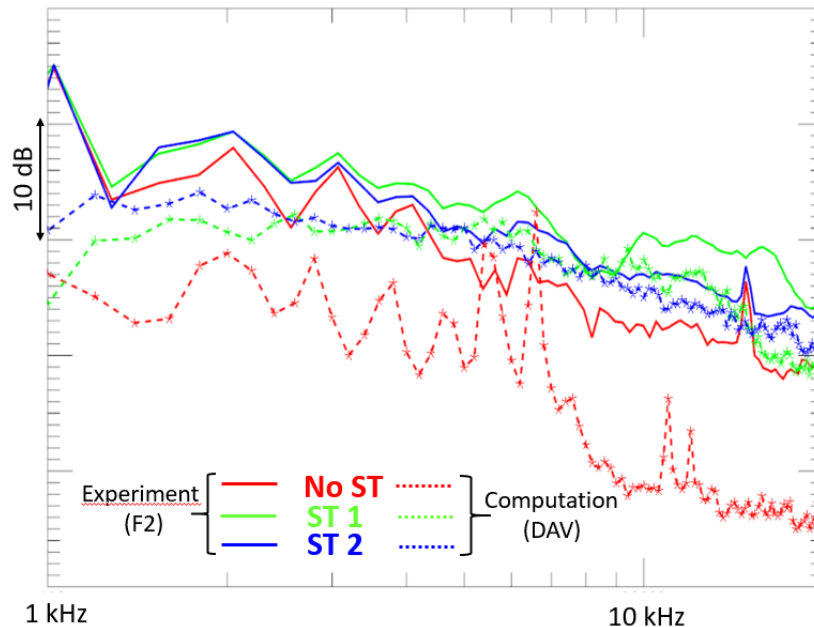


Figure 108: Noise spectra from the DAMAS noise maps integrated in the slat track area (yellow zone on Figure 107). Experimental results (solid) and numerical simulation (dashed) by DAV, without slat track and with slat tracks #1 - #2

5.2.4.5 Additional acoustic analysis

Additional acoustic results are shown in this present section. They concern the identification of slat track noise sources. The sources are identified by conventional beamforming over the 3D slat track geometry from acoustic signals generated to about 3000 points uniformly distributed on a 500-mm diameter sphere (i.e about 9 slat chord length) centered to the slat track. This virtual microphone array is illustrated Figure 109.

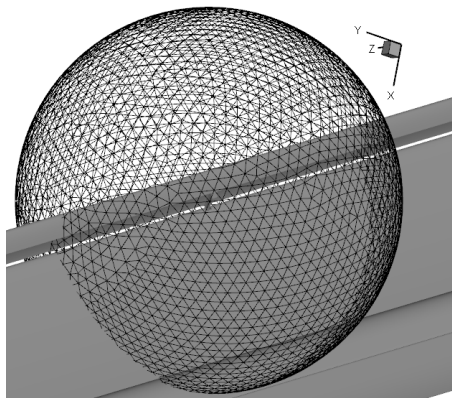


Figure 109: Spherical microphone array.

Results are presented Figure 110. As expected, the track and the wing-leading edge are identified. The slat cove seems to be part of the source at 8 kHz too. Besides, unexpected contributions are additionally observed. These spurious sources are attributed to conventional side-lobes from the beamforming technique. They could be attenuated by using a deconvolution technique such as

DAMAS or Clean-SC for instance. The directivity effects of the noise source and are consciously left out in the present analysis and further investigations would be necessary to improve the results.

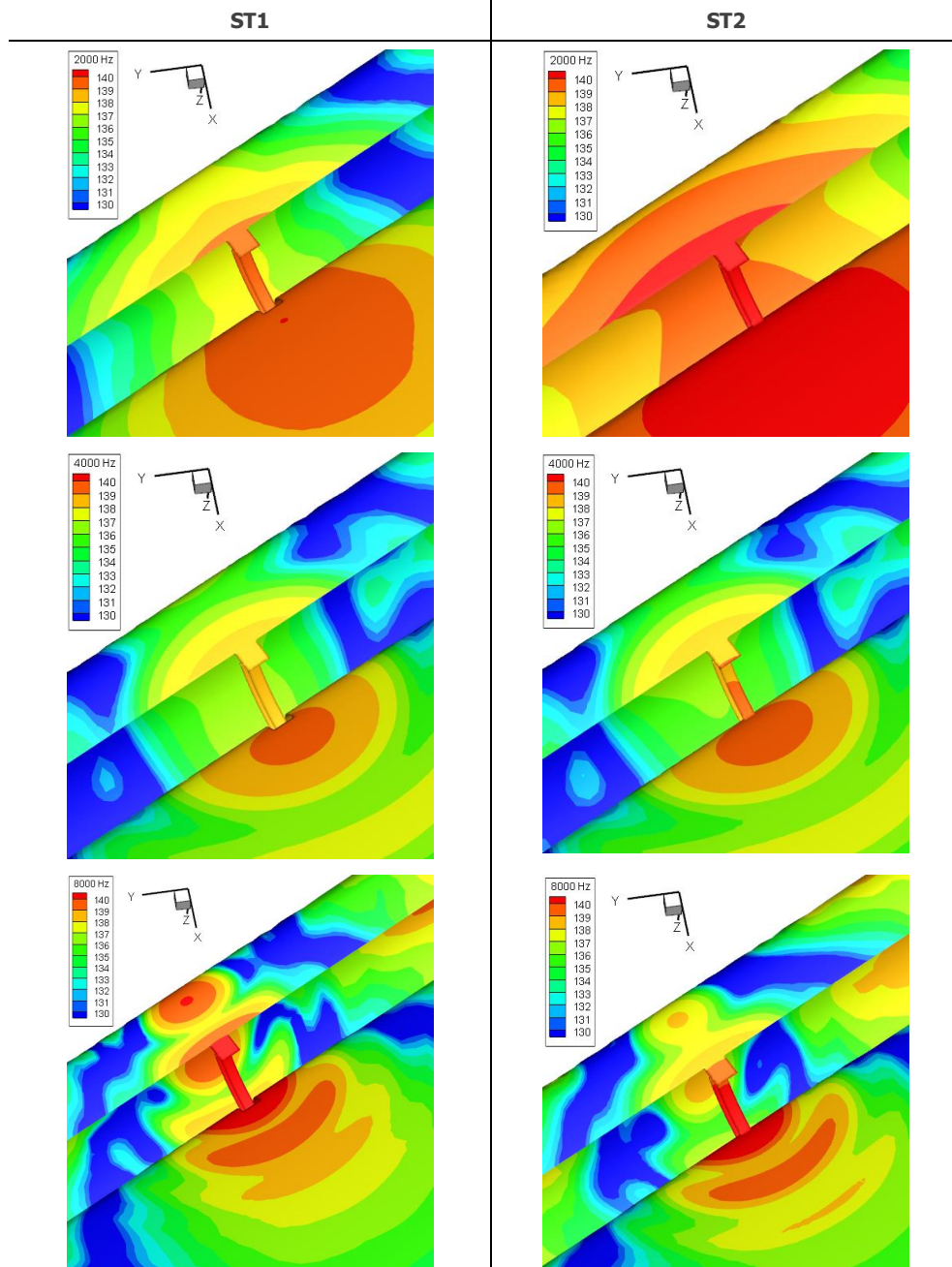


Figure 110: 3D beamforming maps of the ST1 (left) and ST2 (right) configurations at 2000 Hz (top), 4000 Hz (middle) and 8000 Hz (bottom) (third octave-band levels, dB, ref. $4 \cdot 10^{-10} \text{ Pa}^2$).

As explained in Section 5.2.3, the acoustic signals were synthesized by using the time-domain Curle's analogy. Curle's source terms are represented Figure 111 to Figure 113 at 2 kHz, 4 kHz and 8 kHz respectively (third-octave band levels). Here, the source term $S(\vec{y}, \theta, f)$ is computed to the location of the central microphone of the Onera's microphone array (corresponding roughly to the flyover direction at 90° with respect to the track):

$$S(\vec{y}, \theta, f) = \frac{f^2}{4} \cos^2 \theta \overline{|\hat{p}(\vec{y}, f)|^2} \quad (1)$$

where f is the frequency, \vec{y} is a point over the geometry, θ is the angle between the normal to the geometry in \vec{y} and the direction to the microphone, and \hat{p} is the Fourier transform of the pressure signal. The results clearly show an acoustic contribution

- 1) by the track, in particular from the outboard side close to the wing leading edge,
- 2) by the slat cove, in particular on the outboard side of the track,
- 3) by the wing leading edge on the pressure side. Note the two-lobe distribution of the source levels.

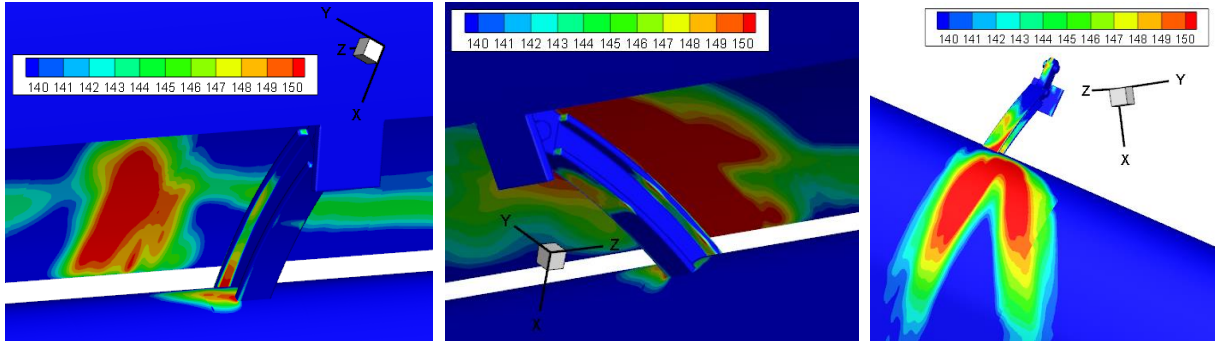


Figure 111. Amplitude of the Curle's source term at 2 kHz toward the central microphone of Onera's microphone array (third octave band levels, dB, ref. $4 \cdot 10^{-10} \text{ Pa}^2\text{m}^{-2}$). Slat track ST2. Left: outboard view, pressure side. Middle: inboard view, pressure side. Right: pressure side view without slat.

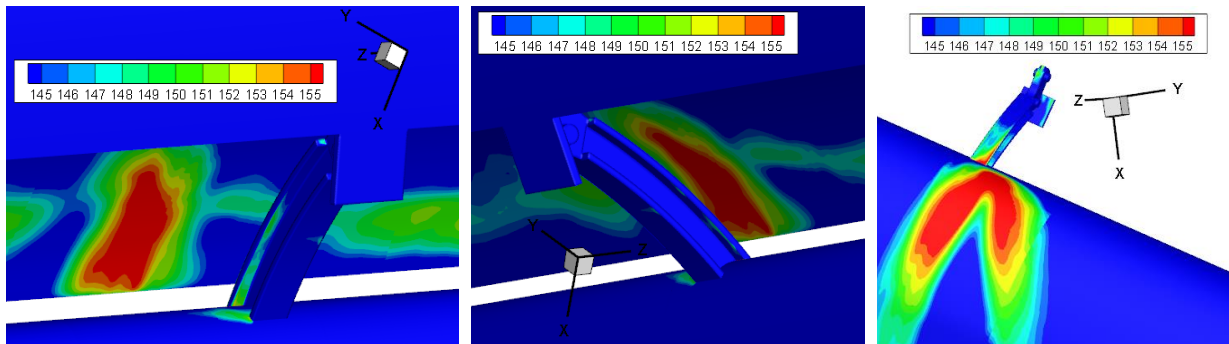


Figure 112. Same legend as Figure 111 at 4 kHz.

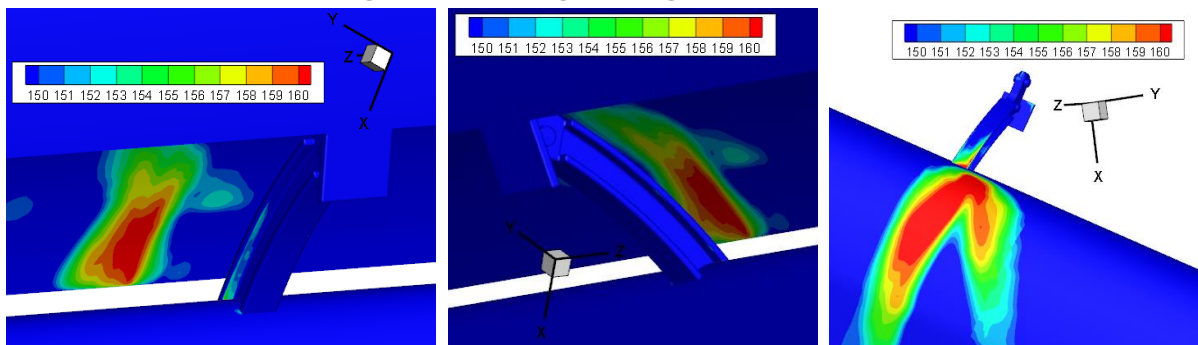


Figure 113. Same legend as Figure 111 at 8 kHz.

The observation of the areas covered by the highest source levels shows that the relevance of these 3 contributions increases from 1) to 3).

To understand the origin of these noise sources, iso-vorticity surfaces are computed to highlight the development of shear-flows. In particular, vorticity is computed following the axes of the airfoil geometrical frame ($Lx_{5,3}, Ly_{5,3}, Lz_{5,3}$). Surfaces of iso-vorticity in the $Lx_{5,3}$ and $Lz_{5,3}$ directions, 'LX53 Vorticity' and 'LZ53 Vorticity' respectively, are shown Figure 114 to Figure 116 for different view angles with respect to the track ST1. These results show the development of

- positive- $Lx_{5,3}$ and positive- $Lz_{5,3}$ vortex structures generated from the outboard, bottom edge of the track, 'impacting' the slat cove and going through the slat gap to the wing suction side then;

- negative- $Lx_{5,3}$ and negative- $Lz_{5,3}$ vortex structures generated from the inboard, top side of the track and going through the slat gap to the wing suction side then.

The presence of these structures is clearly correlated with the areas of high source terms previously identified on the slat cove and on the pressure side of the wing leading edge. In particular, the two lobes noticed on the wing leading edge are related to each of the vortex structures, from the inboard and outboard sides of the track separately. The topology of the vortex structures is sketched on Figure 117.

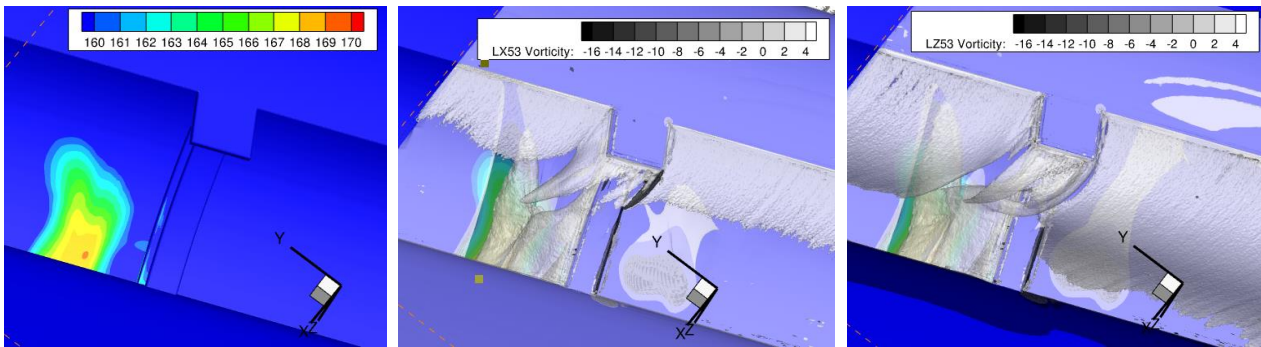


Figure 114: Pressure side views from the outboard side. Slat track ST1. Left: RMS contour levels of the Curle's source term at $\theta = 90^\circ$ for each point \vec{y} , see Eq. (1) (dB, ref. $4 \cdot 10^{-10} \text{ Pa}^2\text{m}^{-2}$). Middle: Vorticity in the $Lx_{5,3}$ direction (s^{-1}). Right: Vorticity in the $Lz_{5,3}$ direction (s^{-1}). -16 s^{-1} and $+4 \text{ s}^{-1}$ iso-vorticity surfaces are superimposed (transparent) to the Curle's source term.

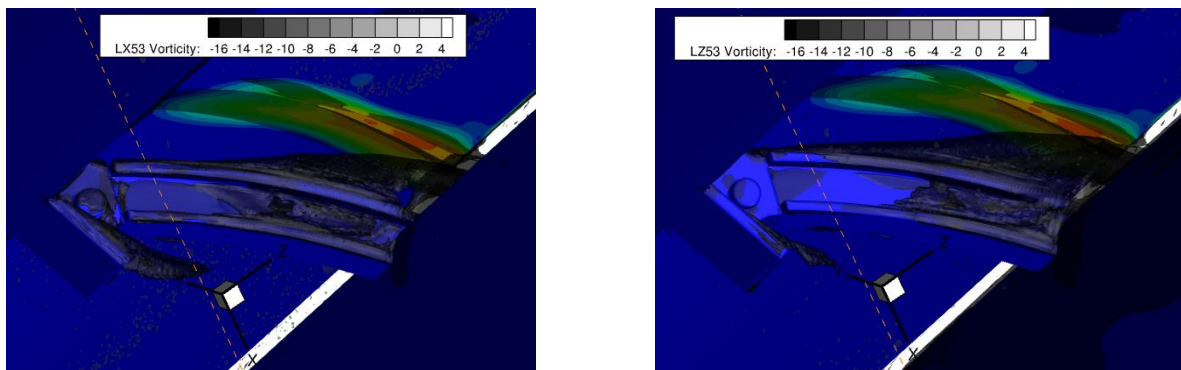


Figure 115: Pressure side views from the inboard side. Slat track ST1. Left: Vorticity in the $Lx_{5,3}$ direction (s^{-1}). Right: Vorticity in the $Lz_{5,3}$ direction (s^{-1}). The -16 s^{-1} iso-vorticity surface is superimposed (transparent) to the Curle's source term.

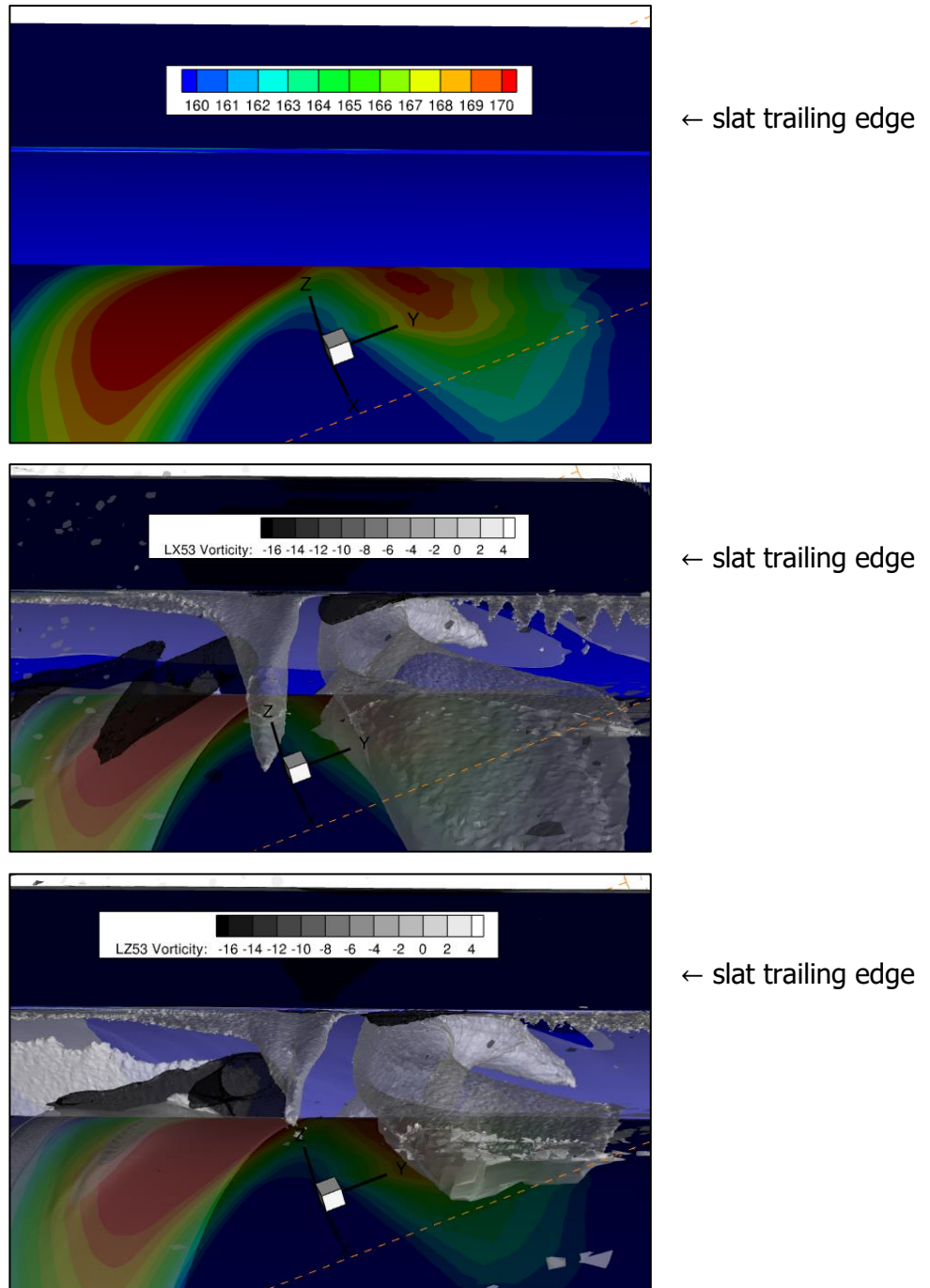


Figure 116: Suction side views. Slat track ST1. Top: RMS contour levels of the Curle's source term at $\theta = 90^\circ$ for each point \vec{y} , see Eq. (1) (dB, ref. $4 \cdot 10^{-10} \text{ Pa}^2 \text{ m}^{-2}$). Middle: -16 s^{-1} and $+4 \text{ s}^{-1}$ iso-vorticity surfaces in the $L_{x_{5,3}}$ direction (transparent) and Curle's source levels. Bottom: -16 s^{-1} and $+4 \text{ s}^{-1}$ iso-vorticity surfaces in the $L_{z_{5,3}}$ direction (transparent) and Curle's source levels.

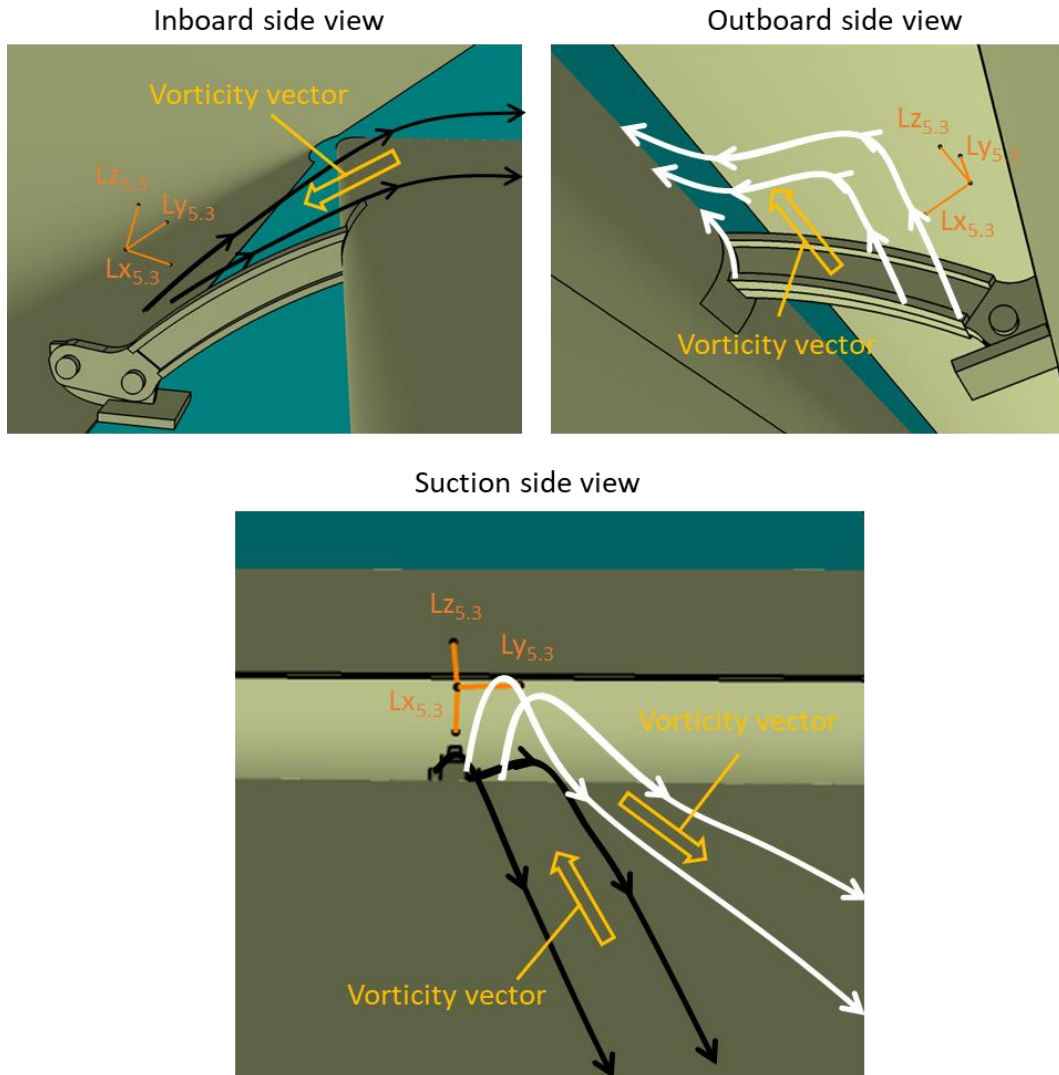


Figure 117: Illustration of the development of vortex structures.

5.3 Numerical simulations by ONERA

5.3.1 Context and objectives

ONERA has performed unsteady Zonal DES computations of the 2.5D swept configuration without and with a slat track, combining a body-fitted approach for the wing elements and an immersed boundary method for the slat track. The simulations consider the baseline (no slat track), and the slat track #2. The results are compared to the measurements to assess the simulations. Then, a finer analysis of the flow is performed, in order to identify the specific flow modifications responsible for noise reduction.

The aim of these simulations is twofold:

1. Assess the capability of the proposed numerical approach based on a zonal use of a high-fidelity turbulent flow resolution, with respect to the reference measurements carried out at F2. Indeed, the simulation of the whole configuration, including the swept airfoil in the $1.8 \times 1.4 \text{ m}^2$ F2 wind tunnel section is very challenging. For that reason, we made use of the ZDES approach, with the scale-resolving approach only applied in a limited refined grid area around the slat track, while the overall configuration is treated in RANS with a coarser grid resolution. Moreover, the slat track is accounted for in the simulation thanks to a zonal use of an immersed boundary condition (IBC) approach.

- Investigate the flow mechanisms responsible for the additional noise sources when the slat track is present.

5.3.2 Configuration and computational grid

The baseline no-track configuration is the one presented in detail in the experimental part. We consider the F16 airfoil with deployed slat and flap and a 30° sweep angle, at an angle of attack of 5.3° . The whole F2 wind tunnel section is considered in the simulations, with slip wall conditions applied on the side walls, floor and ceiling and classical no-slip wall conditions on the airfoil. For the simulations, we will consider the inflow velocity $U_\infty=71$ m/s.

A three-dimensional multi-block structured grid has been generated around the configuration, with noticeable grid refinement applied in the slat cove region and in the boundary layers. Special care was taken in order to refine the location of the slat track, to anticipate its inclusion thanks to an immersed boundary method. Figure 118 presents several views of the computational domain and grid topology. As already mentioned, one of the big challenges of the simulations is to properly simulate the specific flow features due to the inclusion of the slat track, while considering a very large configuration with many complex flow phenomena (e.g. slat cove shear layer, slat wake, turbulent boundary layer on the main wing, flap cove shear layer, flap wake...).

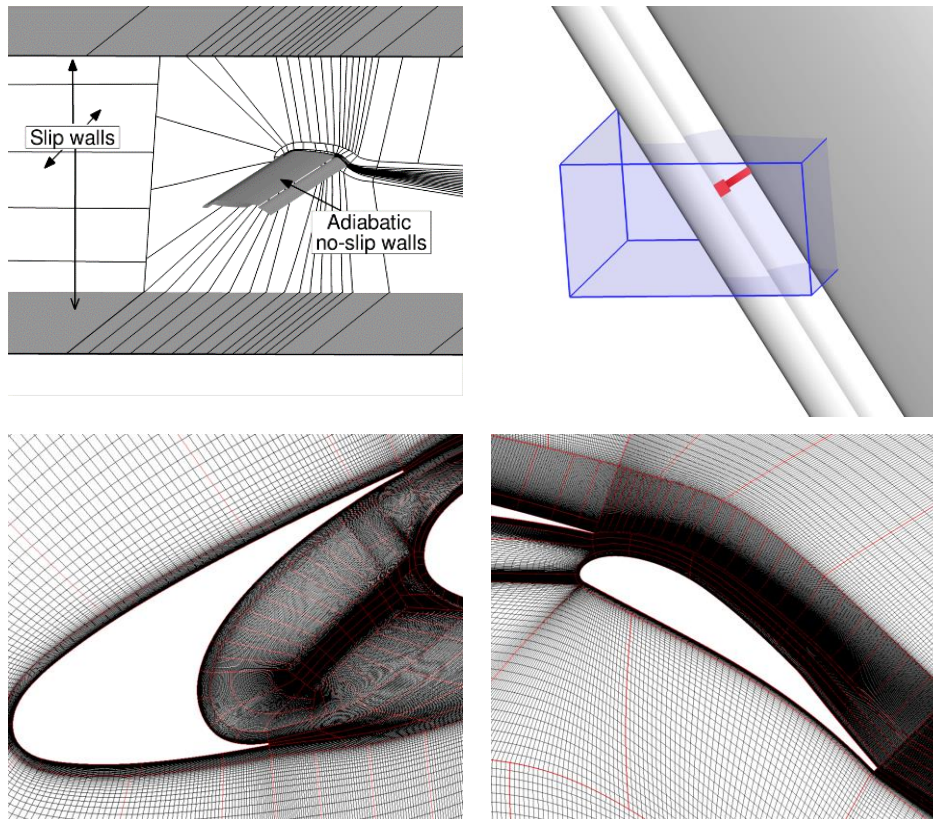


Figure 118: Computational domain and details of the structured grid in the mid-span x - z plane. The blue box in the top right picture indicates the limited region of interest resolved using the ZDES mode 2 (2020) approach, where the grid density is significantly increased in the span direction.

The high-fidelity simulation of all these flow mechanisms on a span of 1.4 m would require several billions of points, which was not considered as relevant for the present study. For that reason, it has been decided to focus the computational effort on the slat cove flow in its central area in span, close to the slat track. This is done in practice by refining the grid only in a limited region clustered around the slat track, as highlighted by the blue box in Figure 118. This refined region covers a span of 80 mm around the slat track, with a uniform spanwise grid resolution. Grid coarsening in span is then applied gradually up to the side walls. As it will be detailed in the next sub-section, this area will be

resolved using the ZDES mode 2 (2020) approach, while the overall configuration will be treated in RANS. This strategy makes it possible to limit the overall number of grid points to about 145 million for the whole configuration. It is worth noting that the use of a similar grid resolution along the full span would have led to a grid point count of more than 2 billion, which was not acceptable for the present study. Two configurations have been studied:

- The nominal “no-track” configuration.
- A configuration with a slat track installed. Among the various slat track geometries studied in INVENTOR, it was chosen to first focus on the Track #2 configuration. This track was provided by DaV, under the reference GB_STRef_TI1_LEONo_D1. Figure 119 presents the geometry of this slat track and the surface grid used to include it in the simulation as an immersed boundary condition.

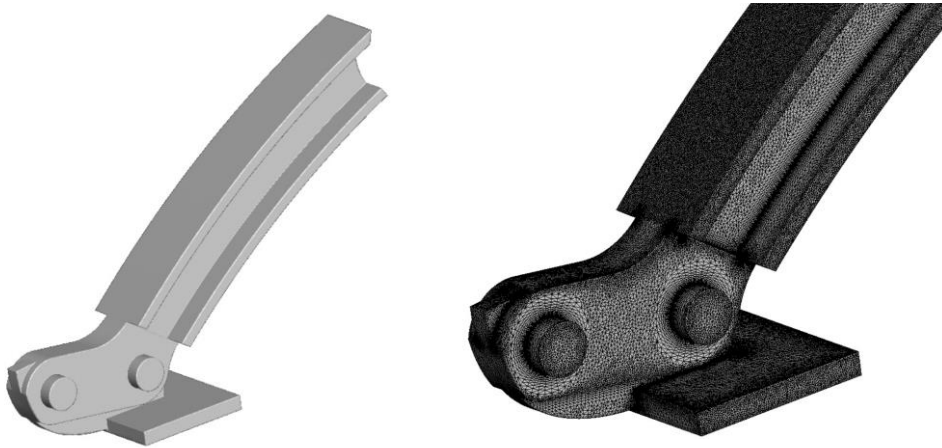


Figure 119: Geometry of the slat track #2 (left) and details of the surface grid used for the IBC pre-processing (right).

5.3.3 Numerical strategy

Scale-resolving ZDES numerical simulations of the flow have been carried out, for both the baseline (clean) airfoil and for the airfoil equipped with a slat track. In order to minimize, as much as possible, the overall number of grid points, we take full advantage of the zonal capabilities of the ZDES approach. Therefore, the whole configuration, including the full-span swept airfoil and the wind tunnel walls, is computed in RANS mode, while only a reduced region located in the center part of the slat cove is computed using the ZDES mode 2 (2020) approach [13], on a locally refined grid. Using this mode, the solver switches automatically from a RANS behavior in the attached boundary layers (whatever the grid resolution) to a LES behavior in the separated areas such as the slat cove main shear layer, or the slat track wake.

As shown in the previous sub-section, the computational grid is a standard body-fitted grid, built around the clean airfoil configuration. In order to take into account the presence of a slat track, we use a hybrid numerical strategy, where an immersed boundary condition technique is applied locally on the body-fitted grid, for the slat track geometry only. This avoids the constraint of building a body-fitted grid around the complex slat track shape, while taking full benefit of the body-fitted grid for an accurate resolution of the boundary layers developing around the airfoil.

The simulations have been carried out using ONERA’s in-house finite-volume solver FUNK, with a low-dissipative second-order accurate spatial scheme (AUSM+P with wiggle detector [14]) and a second-order implicit time integration, with a time step of $0.2 \mu\text{s}$. This very small time step is the consequence of the use of a fine grid resolution in the wall-normal direction close to the walls (*i.e.* $\Delta y^+ \sim 1$)

As a preliminary assessment of the simulations, Figure 120 displays the computed mean wall pressure coefficient at mid-span, compared to the F2 measurements. An overall fair agreement is observed with the experiment, although the suction peak magnitude on the main wing element is underestimated. This under-estimation of the suction peak is most probably due to a small separation occurring on the flap suction side, evidenced by a small plateau on the C_p distribution, which seems

to be absent from the experiment. Nevertheless, we can notice a perfect agreement with the measurements on the slat surface, which is the main region of interest of the present study.

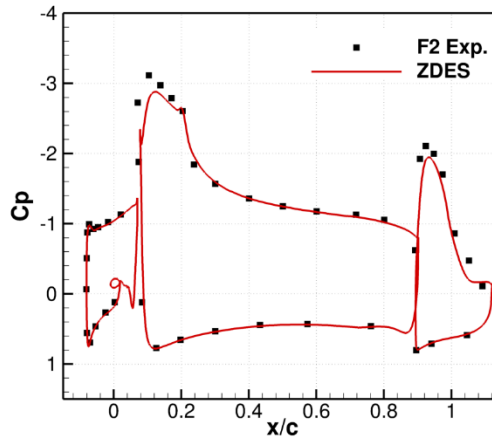


Figure 120: Mean wall pressure coefficient distribution for the reference no-track case.

5.3.4 Physical analysis of the flow

5.3.4.1 No-track configuration

Before going further into the results' analysis, it is worth noting that a grey area issue has been observed in the simulations. This issue, generally observed with the DDES approach, is generally due to an excessive shielding in RANS mode in separated flow regions. The ZDES mode 2 formulation however proposes several improvements to get rid of this delay in the formation of instabilities (e.g. choice of the subgrid length scale and specific threshold for the RANS-to-LES switch). In the present case, the method is efficient in the sense that the switch from RANS to LES occurs rapidly in the shear layer originating from the cusp. However, we observe the persistence of typical RANS values for the turbulent viscosity in the core region of the slat cove recirculation bubble. As evidenced by Figure 121 (left), this is mostly due to the swept flow that develops in the core region of the slat cove, where turbulent viscosity is convected from the pure RANS area "upstream" (in the sweep direction) of the ZDES region. It was found that the destruction term of the SA transport equation is not able to compensate this convection effect in the core region of the slat cove. Indeed, in the core region of the slat cove, the mean velocity in the spanwise direction reaches about 30% of the inflow velocity, which yields significant convection effects in the sweep direction. Two modifications of the model have been tested in order to minimize this grey area issue:

- The imposed value of the destruction function f_w in the grey area has been increased to 10000 (its original value is 100 [13]), in order to boost the effect of the destruction term.
- The rotational correction of the SA model [15] has been implemented and applied in the slat cove region. Indeed, this correction reduces the eddy viscosity in regions where vorticity exceeds strain rate, such as in vortex core regions where pure rotation should not produce turbulence.

It was found that these two modifications help a bit to reduce the level of turbulent viscosity in the slat cove (see Figure 121, right). However, for the no-track case, there is still a persistence of high turbulent viscosity levels in the first half of the core region of the slat cove.

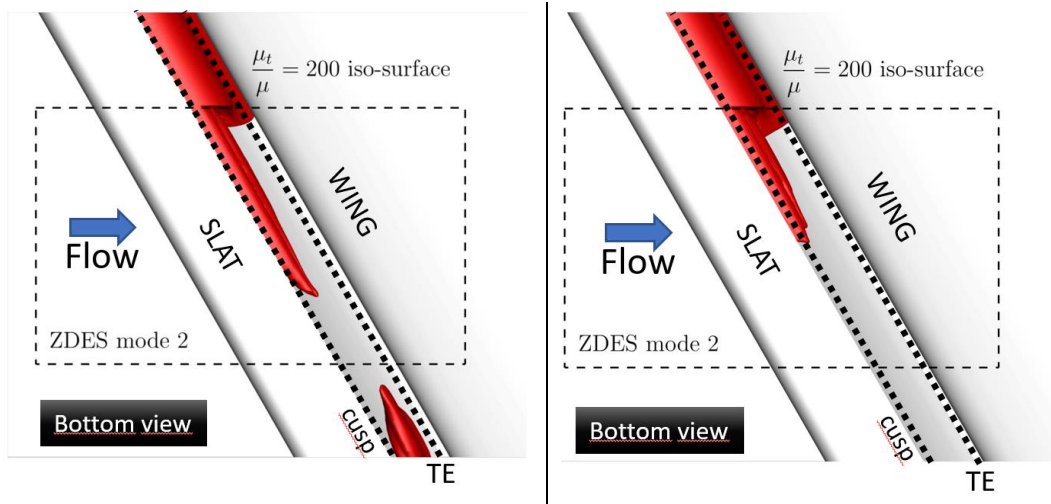


Figure 121: Iso-surface of "RANS-level" turbulent viscosity in the slat cove for the no-track configuration (view from bottom). Left: original ZDES 2020 formulation. Right: ZDES with $f_v=10000$ and SA-R formulation applied in the slat cove.

Figure 122 shows instantaneous flow visualizations in the slat cove region, using the Q criterion. The usual slat cove flow features are well recovered: a turbulent shear layer develops downstream of the slat cusp and impinges on the slat cove upper surface. There, the flow is strongly accelerated through the gap, leading to the formation of elongated streamwise vortices downstream of the impingement point. The effect of the sweep is slightly noticeable on the development of the main shear layer, where the initial Kelvin-Helmholtz vortices appear to be sensitive to the mean swept flow and to the persistent high turbulent viscosity levels. However, it is observed that almost no turbulent structures are visible in the central core region of the recirculation bubble, which is of course due to the aforementioned grey area issue in this region. Indeed, the resolved turbulent structures seem to remain clustered around the main recirculation bubble, with no turbulent mixing in the core region.

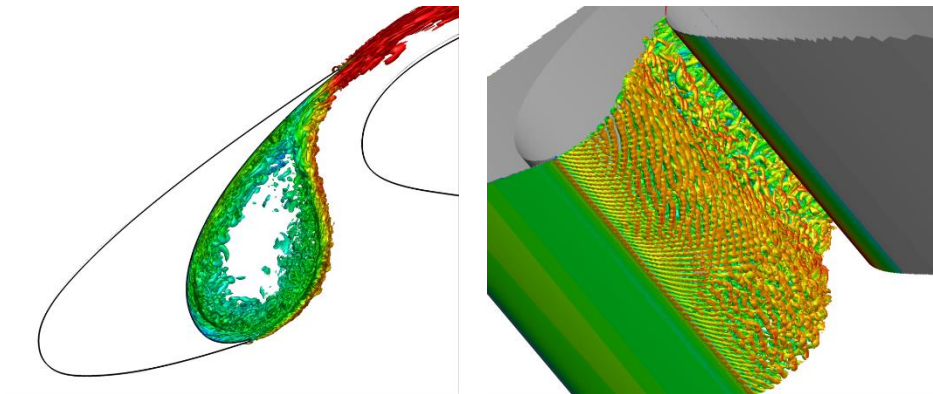


Figure 122: No-track configuration: iso-surface of the Q criterion in the slat cove area ($\frac{Qc^2}{U_\infty^2} = 1000$), coloured by the velocity magnitude (blanking is applied outside of the refined grid area).

5.3.4.2 Track #2 configuration

For this configuration, the grey area issue appears to be significantly less present. Indeed, Figure 123 shows that several large-scale vortices develop around the slat track, leading to a fully turbulent wake "downstream" of it (in the sweep direction). Surprisingly, some of the turbulent structures present in the wake seem to be re-ingested upstream of the track when the wake impinges on the upper slat cove surface. This leads naturally to an appropriate behavior of the ZDES model, where the turbulence model switches in LES mode almost everywhere in the slat cove.

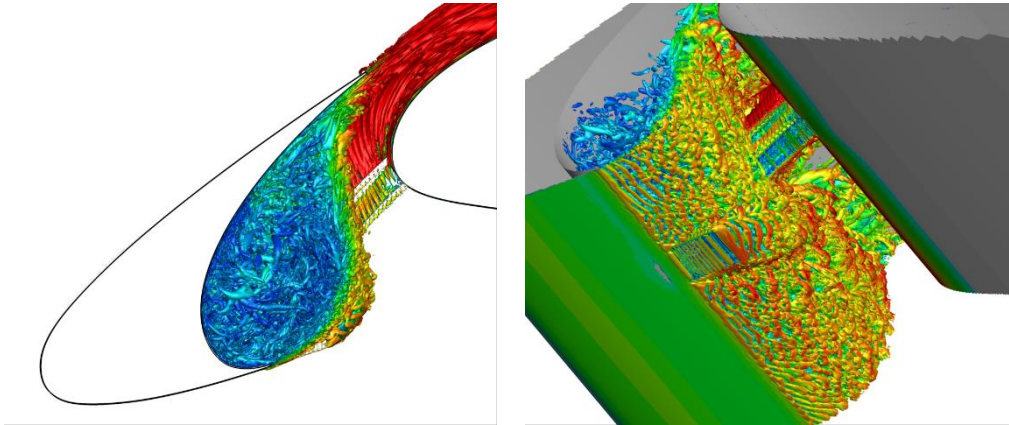


Figure 123: Track #2 configuration: iso-surface of the Q criterion in the slat cove area ($\frac{Qc^2}{U_\infty^2} = 1000$), coloured by the velocity magnitude (blanking is applied outside of the refined grid area).

A more detailed analysis can be carried out from Figure 124, where a higher value of the iso-Q surface is considered. There, at least two potential noise generation mechanisms can be identified:

- A. A turbulent wake develops from the slat track's lower panel, with initial two-dimensional Kelvin-Helmholtz vortices formed at the panel's trailing edges. This wake quickly transitions to fully-developed turbulence and is ingested in the slat cove swept flow, before impinging on the upper slat cove surface. This impingement is most probably responsible for a broadband noise source.
- B. Two large vortices are also formed on the sides of the track and are strongly accelerated through the gap. These two vortices impinge on the upper main wing leading edge, which may constitute an important source of noise, due to the high velocity encountered in this specific area.

The impact of these two flow features on the possible noise generation is confirmed by looking at the distribution of the RMS wall pressure fluctuations, displayed in Figure 125. The footprint of the two aforementioned phenomena is clearly visible at the wall. It also appears that the large side vortices "B" also significantly interact with the slat inner surface and trailing edge, as an additional potential noise source.

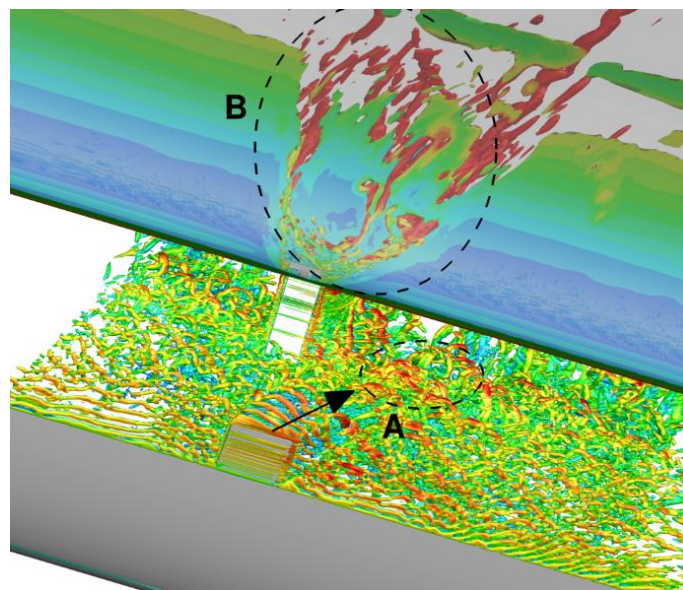


Figure 124: Potential noise sources for the track #2 configuration. (Iso-surface of the Q criterion in the slat cove area ($\frac{Qc^2}{U_\infty^2} = 10000$), coloured by the velocity magnitude).

In the light of these findings, it could be interesting to investigate the use of flow control strategies in the specific flow regions identified as possible noise sources, such as for instance the use of a porous insert close to the slat track at the leading edge of the wing.

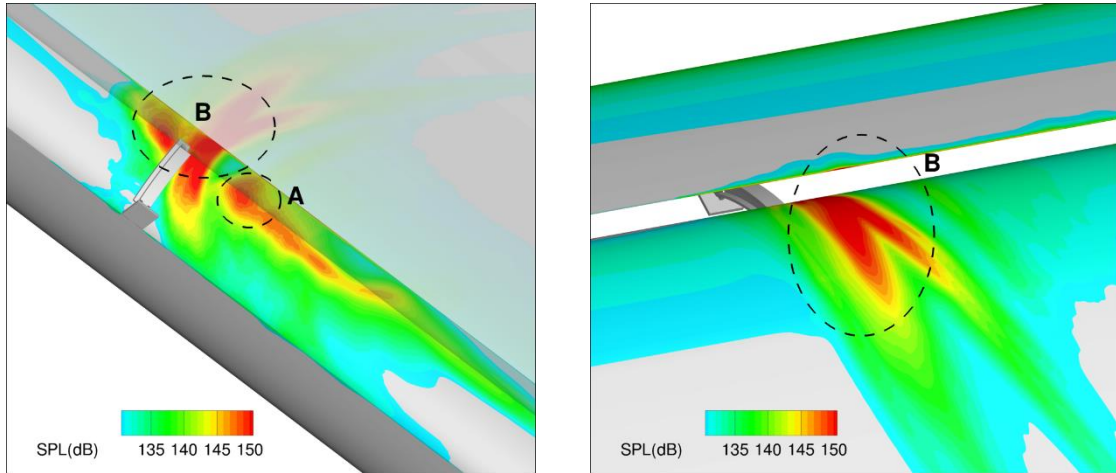


Figure 125: RMS pressure fluctuation at the wall for the track#2 configuration.

5.3.5 Mean flow statistics

This section presents a comparison of the flow statistics (mean velocity and resolved turbulent kinetic energy) at several constant L_y planes, where (L_x, L_y, L_z) denotes the airfoil frame, with its origin located at the slat cusp, at the center of the track. Several of these planes were measured with PIV in F2 and will be used as reference.

5.3.5.1 No-track configuration

Figure 126 presents the mean velocity and resolved turbulent kinetic energy obtained for the no-track case, in the plane $L_y=0$. First of all, the mean velocity distribution and overall shape of the slat cover recirculation bubble appear in good agreement with the PIV measurements.

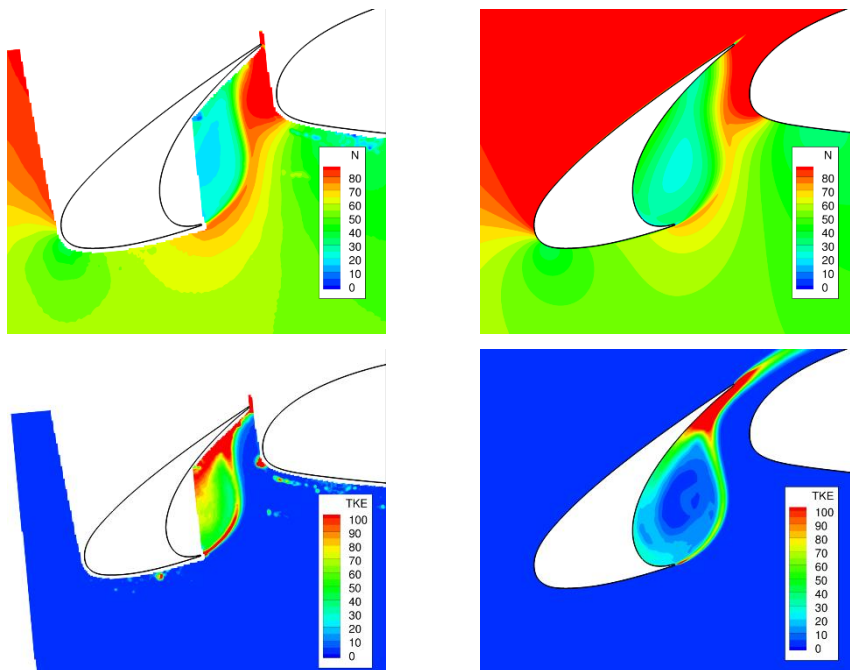


Figure 126: Mean velocity magnitude (m/s, top) and resolved turbulent kinetic energy (m^2/s^2 , bottom) maps in the plane $L_y=0$ for the no-track case. Left: PIV; Right: simulation.

However, there is an important lack of resolved turbulent fluctuations in the core region of the slat cove. This is of course directly related to the grey area issue already pointed out in Section 5.3.4. Nevertheless, the level of resolved turbulent kinetic energy near the impingement of the cusp shear layer appears correctly predicted.

In order to provide a more quantitative comparison between the PIV measurements and the ZDES simulation, several rakes have been extracted from the $Ly=0$ plane. The precise location of these rakes is shown in Figure 127.

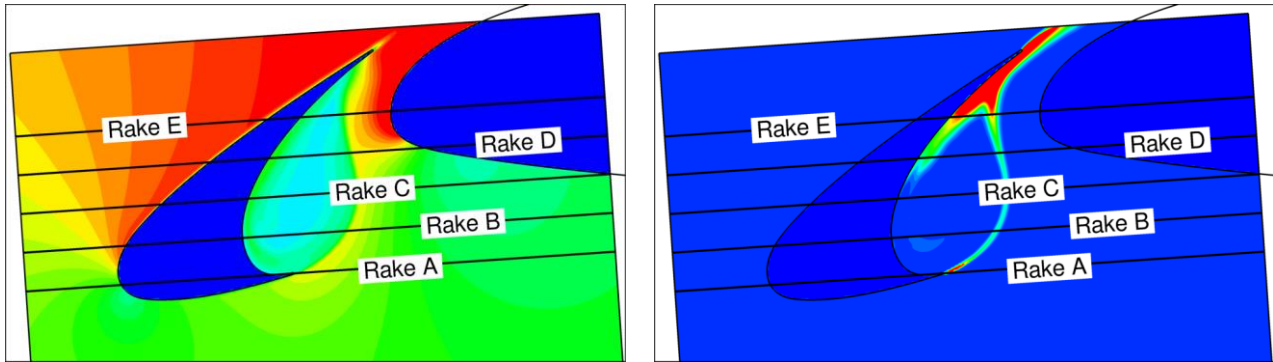


Figure 127: Extraction rakes for the no-track case.

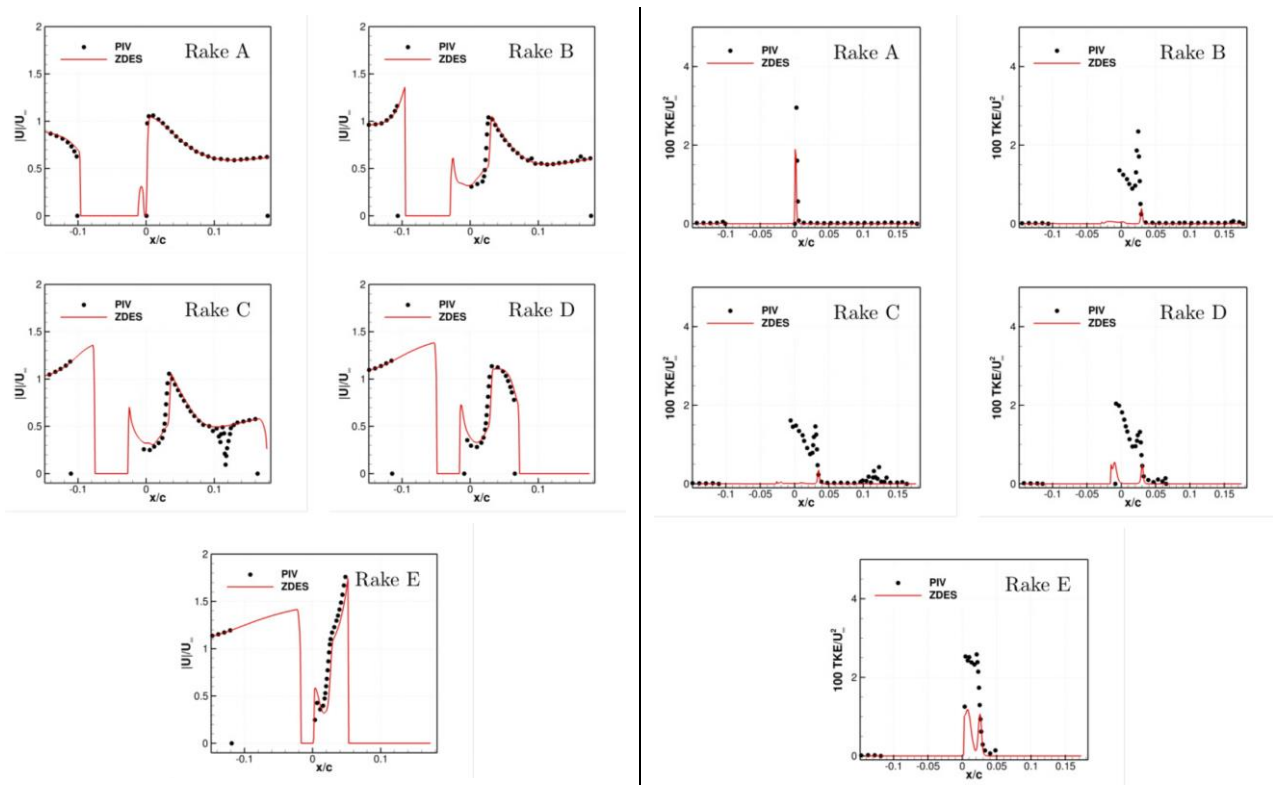


Figure 128: Mean velocity magnitude (left) and resolved turbulent kinetic energy (right) along the extracted rakes A to E (see Figure 127) for the no-track configuration.

Figure 128 displays the mean velocity and resolved turbulent kinetic energy profiles obtained along these rakes, for the ZDES simulation and the PIV measurements. The mean velocity profiles predicted by the simulation exhibit an overall very satisfactory quantitative agreement with the measurements. Both the location of the slat cusp shear layer and the acceleration of the flow through the gap are well reproduced. However, as already noticed, the turbulent kinetic energy levels are significantly under-predicted, for all rakes. Although the peak of TKE linked to the slat cusp shear layer is visible, the magnitude of TKE is dramatically lower in the simulation than in the PIV, especially in the core

region of the slat cove. This is obviously due to the delayed switch to LES of the turbulence model in this specific area, as already discussed. Closer to the impingement point of the shear layer (rake E), the discrepancy between the simulation and the experiment is a bit less pronounced (although still not acceptable) and the simulation is able to reproduce the double-peak distribution of TKE.

5.3.5.2 Track #2 configuration

Figure 129 and Figure 130 present the mean velocity and resolved turbulent kinetic energy obtained for the track #2 case, in the respective planes $L_y=0$ and $L_y=20$ mm (*i.e.* “downstream” of the slat track with respect to the sweep). Unfortunately, due to the blanking effect of the slat track on the optical access, only few data are available in the slat cove in the measurements. For the two planes, the overall distribution of the mean velocity magnitude is in fair agreement with the available PIV distributions. It appears however difficult to draw reliable conclusions on the resolved TKE distribution, as most of the high-level TKE regions are blanked in the experiments. The simulations exhibit several spots of high TKE levels, which correspond to the impingement of the various vortices generated around the slat track on the slat cove upper surface or on the main wing leading edge.

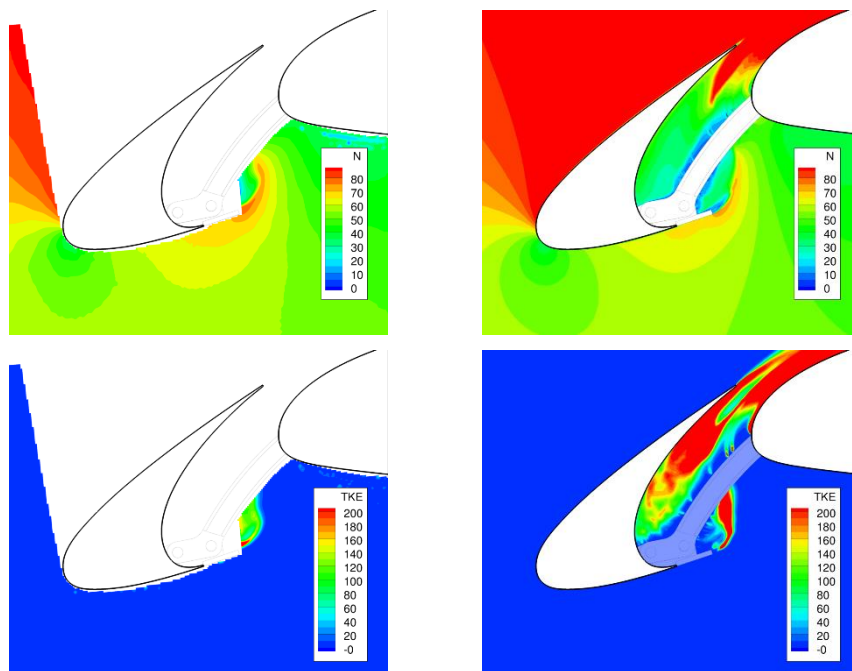


Figure 129: Mean velocity magnitude (m/s, top) and resolved turbulent kinetic energy (m^2/s^2 , bottom) maps in the plane $L_y=0$ for the track #2 case. Left: PIV; Right: simulation.

Similarly to what was done for the no-track case, several rakes have been considered in each L_y plane to get a more quantitative comparison between the simulation results and the measurements. These rakes, referred to as A to D are shown in Figure 131.

Figure 132 to Figure 135 display the profiles of mean velocity magnitude and resolved TKE in the respective successive planes $L_y=0$, $L_y=10$ mm, $L_y=14$ mm and $L_y=20$ mm. Again, we observe a very good agreement between the mean velocity distributions predicted by the simulations and the PIV measurements. The overall location of the slat cusp shear layer and acceleration mechanism through the gap are very well predicted. Again, it is a bit difficult to analyze in detail the TKE distributions, as measurements are only available in low-level TKE regions. However, the analysis of several rakes located close to the slat cusp seem to indicate that the development of resolved turbulence occurs in a more satisfactory way in this simulation, compared to the no-track configuration. It is worth noting that very high levels of resolved TKE are observed near the upper slat cove surface, especially for the plane $L_y=14$ mm. This is consistent with the observations from Section 5.3.4.2 (Figure 124 and Figure 125).

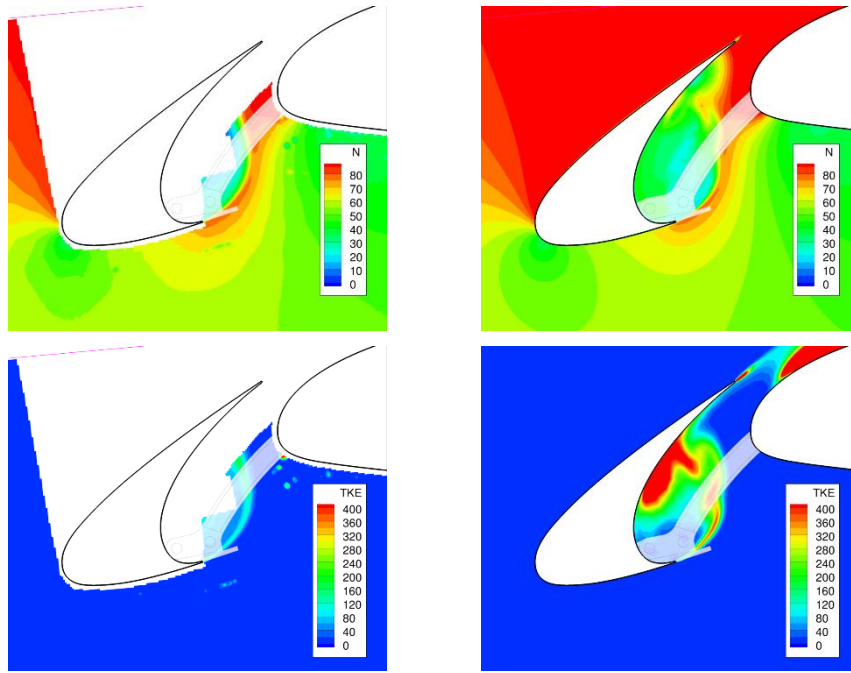


Figure 130: Mean velocity magnitude (m/s, top) and resolved turbulent kinetic energy (m^2/s^2 , bottom) maps in the plane $L_y=20\text{ mm}$ for the track #2 case. Left: PIV; Right: simulation.

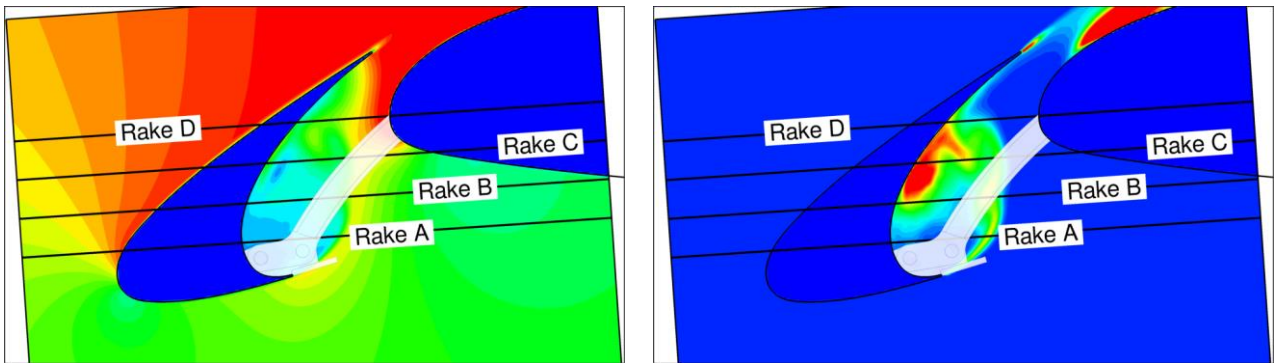


Figure 131: Extraction rakes for the track #2 case.

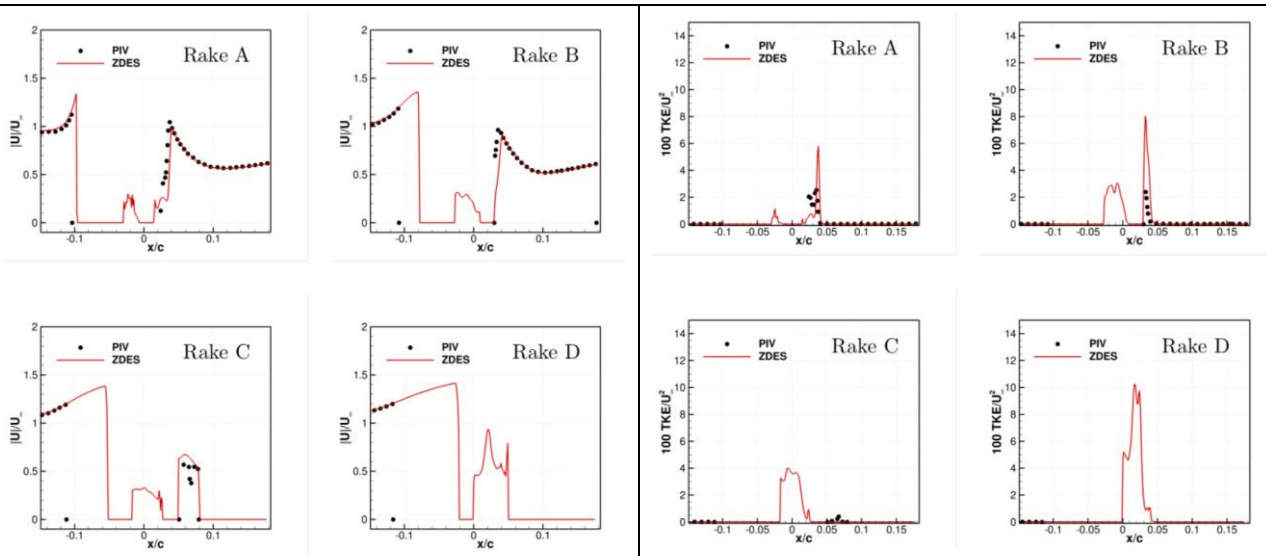


Figure 132: Mean velocity magnitude (left) and resolved turbulent kinetic energy (right) along the extracted rakes A to D (see Figure 127) for the track #2 configuration, at $L_y=0$.

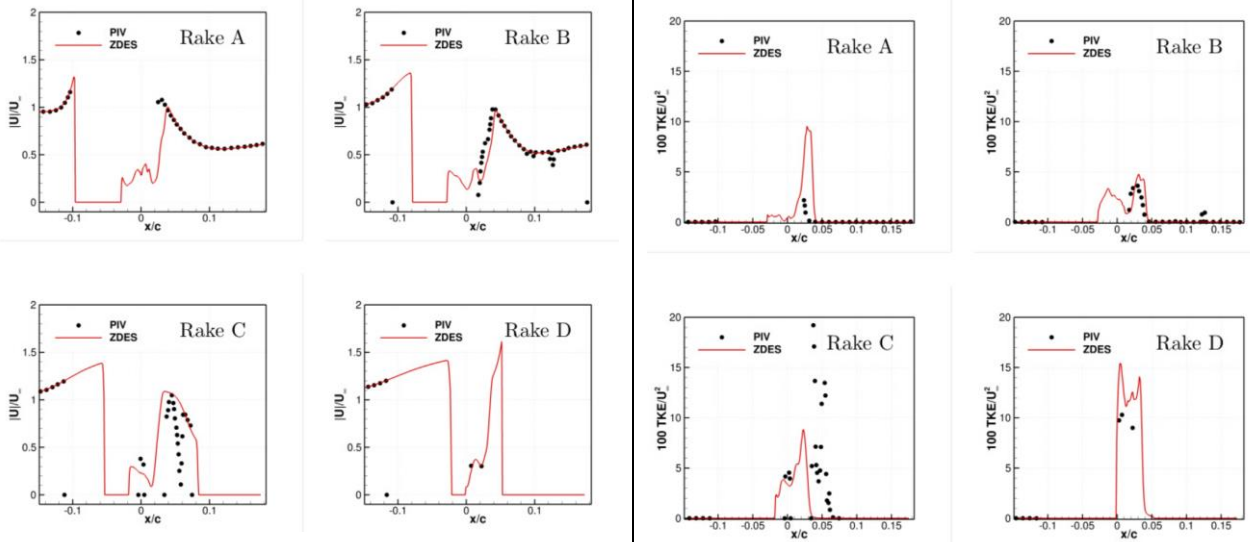


Figure 133: Mean velocity magnitude (left) and resolved turbulent kinetic energy (right) along the extracted rakes A to D (see Figure 127) for the track #2 configuration, at $L_y=10$ mm.

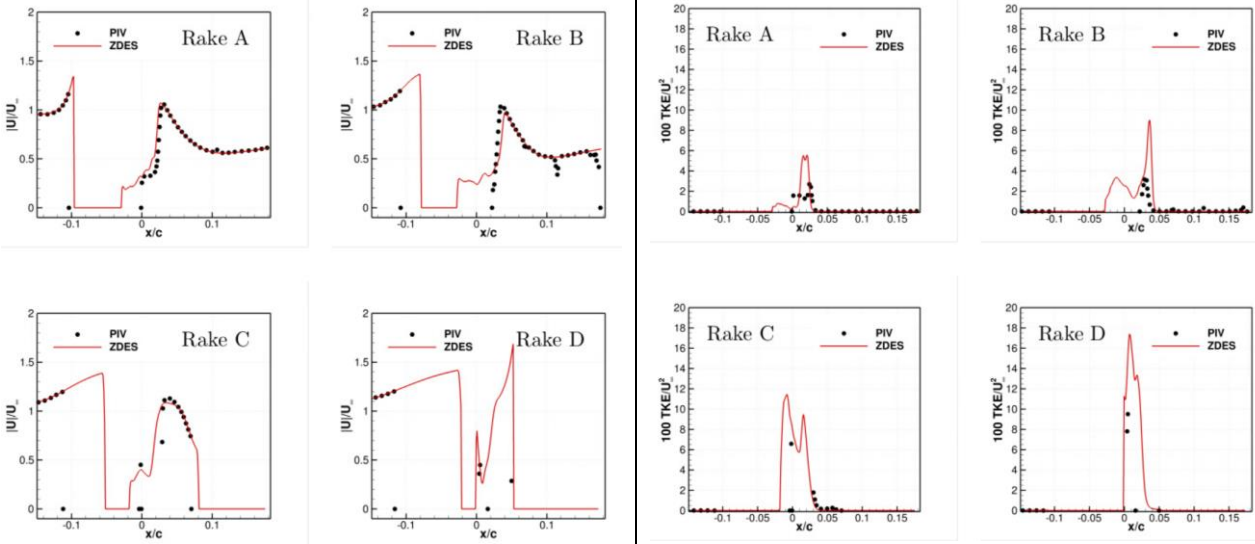


Figure 134: Mean velocity magnitude (left) and resolved turbulent kinetic energy (right) along the extracted rakes A to D (see Figure 127) for the track #2 configuration, at $L_y=14$ mm.

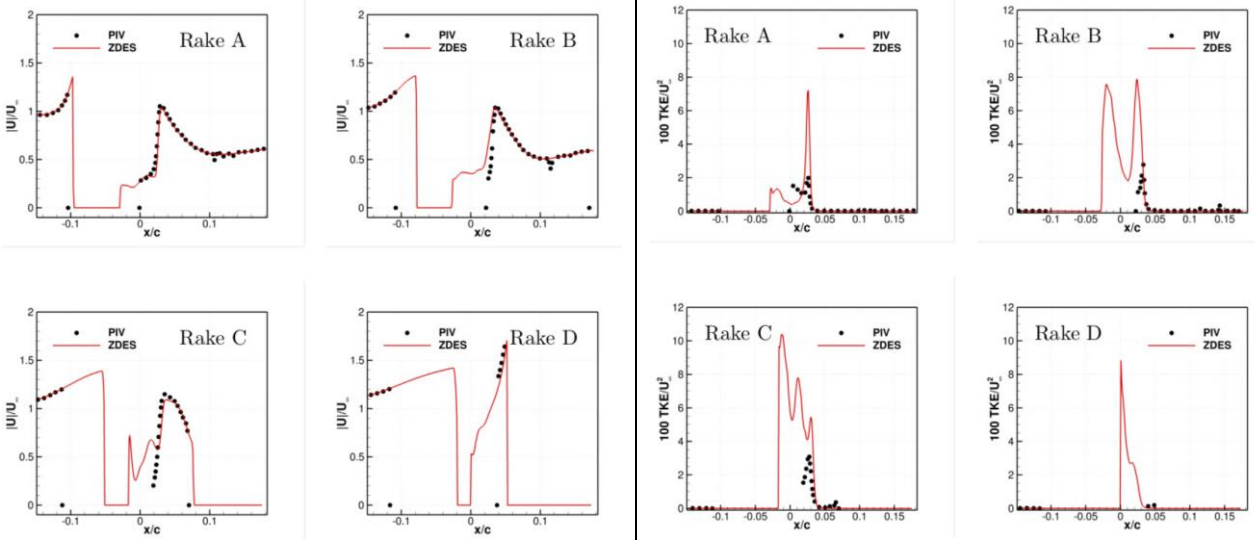


Figure 135: Mean velocity magnitude (left) and resolved turbulent kinetic energy (right) along the extracted rakes A to D (see Figure 127) for the track #2 configuration, at $L_y=20$ mm.

5.3.6 Wall pressure power spectral densities

Several measurements with Kulite probes are also available from the experimental campaign, in order to provide wall pressure Power Spectral Densities (PSD) near the leading edge of the main wing. Unfortunately, most of these sensors are located away from the slat track. In the present numerical study, it was chosen to cluster the computational effort to the vicinity of the slat track, in order to keep the computational cost of the simulation at an acceptable level. Therefore, only few sensors are located in the refined grid area treated in ZDES, as illustrated by Figure 136. According to this figure, only the probe KU11 lies in this refined area. The probe KU10 is also located very close to the refined zone. Finally, the probe KU09 might also be exploitable, as it remains close to the refined grid area and is located "downstream" of the slat track. It can then be reasonably expected that the turbulent fluctuations and acoustic waves in this area are still fairly resolved.

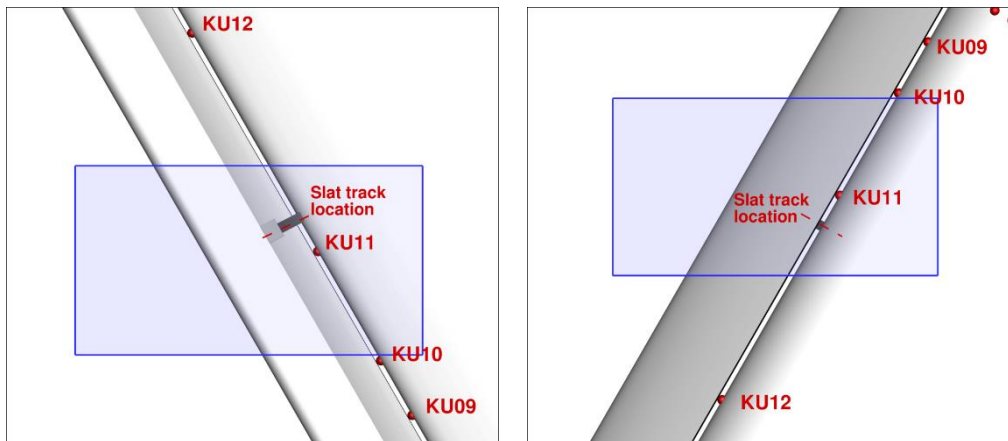


Figure 136: Kulite probes locations. The blue box indicates the refined grid area, resolved in ZDES mode. Left: view from the bottom; Right: view from the top.

Figure 137 presents the wall pressure PSD obtained at each of these three probes, compared to the Kulite probes measurements. The data sampling used in the simulation covers a total time of 28ms. The pressure spectra have been computed with a frequency resolution of 100 Hz.

For the no-track case, an overall under-estimation of the wall pressure PSD is observed with respect to the measurements. This is again probably the consequence of the delay in the formation of turbulent fluctuations in the core region of the slat cove. The agreement is slightly better for probes KU10 and KU9, because they are located in some regions where the grey area issue is less present.

For the track #2 configuration, we observe a huge under-prediction of the wall pressure PSD compared to the measurements at probe KU11, although the slope of the spectrum is correctly predicted up to 3 kHz, where the measured PSD suddenly drops. At this location, it is striking that the overall level of the measured PSD is significantly higher than at the other probes. It is worth noting that probe KU11 appears to be located close to the impingement point of the slat track side edge vortices on the main wing (see Figure 124 and Figure 125), which might certainly explain such high levels. Therefore, the overall under-estimation at this specific location can be due to a slight shift of these side edge vortices in the simulation, compared to the experiment. Again, the agreement with the measurements is better for the probes KU10 and especially KU09, where the wall pressure fluctuations are almost perfectly predicted.

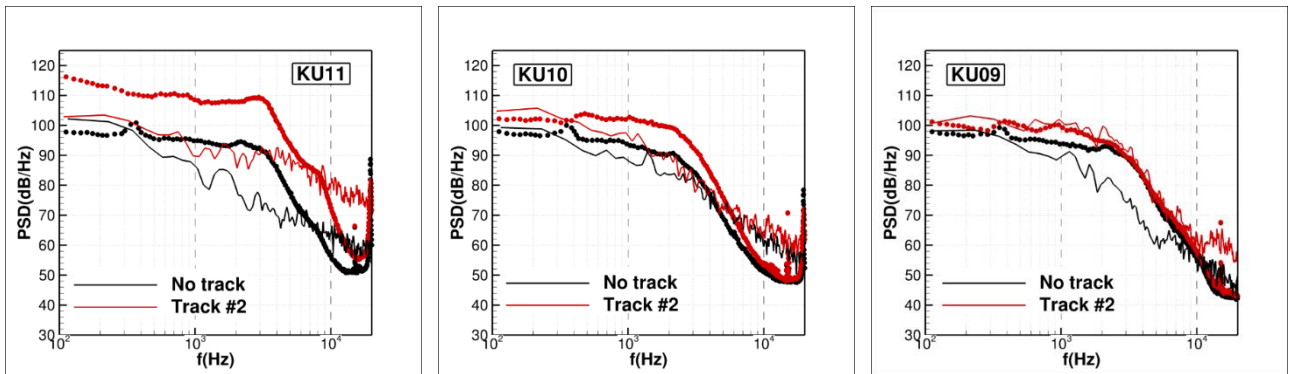


Figure 137: Wall pressure power spectral densities at the Kulite probes locations KU11, KU10 and KU9 (see Figure 136). Symbols: F2 measurements; Lines: Simulation.

5.3.7 Acoustics

5.3.7.1 Local noise source

This section briefly presents the acoustic results obtained from our simulations. A first illustration of the modifications of the acoustic field by the inclusion of the slat track is provided by Figure 138, displaying the instantaneous dilatation field close to the slat. It appears clearly that the magnitude of the acoustic waves is higher for the slat track #2 configuration. It also seems that additional directivity patterns are present in this case.

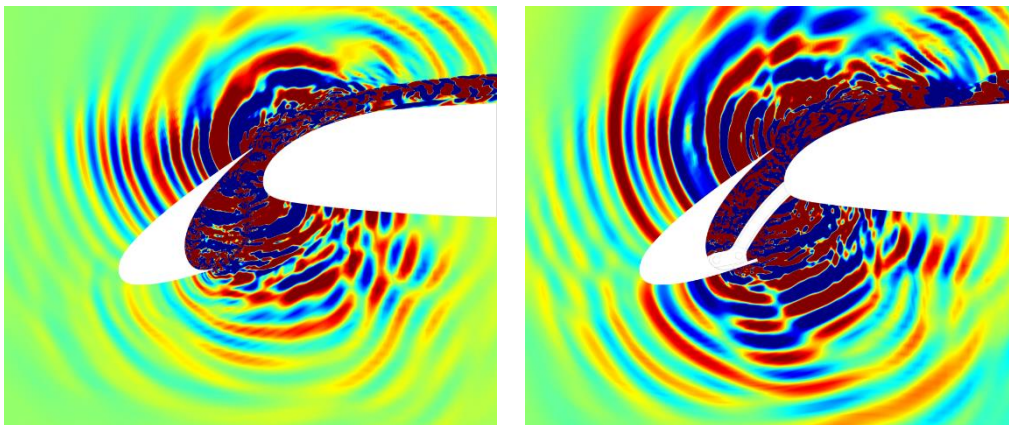


Figure 138: Iso-contours of the dilatation field in the slat area. Left: no-track configuration. Right: track #2 configuration. Levels shown between $-0.02\rho_\infty U_\infty/c$ and $0.02\rho_\infty U_\infty/c$.

5.3.7.2 Farfield noise using a Ffowcs Williams-Hawkings solver

In addition to these first observations, the radiated acoustic field has been investigated. For that purpose, the ONERA in-house code KIM has been used to compute the acoustic far-field at 120 observer points, corresponding to each microphone from the acoustic antenna. We consider the permeable formulation of the Ffowcs Williams-Hawkings (FW-H) equation, which requires the unsteady sampling of the aerodynamic field on a permeable surface close to the airfoil. Figure 139 shows the permeable surface used for the FW-H method. It was carefully designed such that no turbulent structures cross this surface, while being located close enough from the noise sources to avoid the artificial damping of the acoustic waves due to grid stretching and numerical dissipation (see Figure 138).

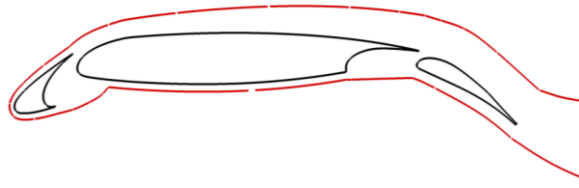


Figure 139: Permeable surface (red) used for the FW-H method.

A total sampling time of 24 ms is available on the FW-H surface, providing 20.7 ms of pressure signal at the locations of the microphones after the FW-H integration. These signals have been transferred to R. Davy from ONERA, for a beamforming analysis (see next section).

Figure 140 (left) presents the narrow-band acoustic PSD computed at the central microphone of the acoustic antenna (Mic#1) for the no-track and slat track #2 configurations. As expected, the airfoil equipped with track #2 is noisier than the no-track configuration over a wide range of frequencies, by about 5 to 14 dB (see Figure 140, right), with an average increase of about 7 dB in the range between 5 to 20 kHz, fully consistent with experimental observations.

In both cases, it is worth noting that two high-frequency broadband peaks are present in the pressure spectra, at about 25 kHz and 45 kHz, with similar magnitudes. These two peaks can be related to the vortex shedding occurring respectively at the slat trailing-edge and at the slat cusp and correspond to the circular wave patterns observed in Figure 138.

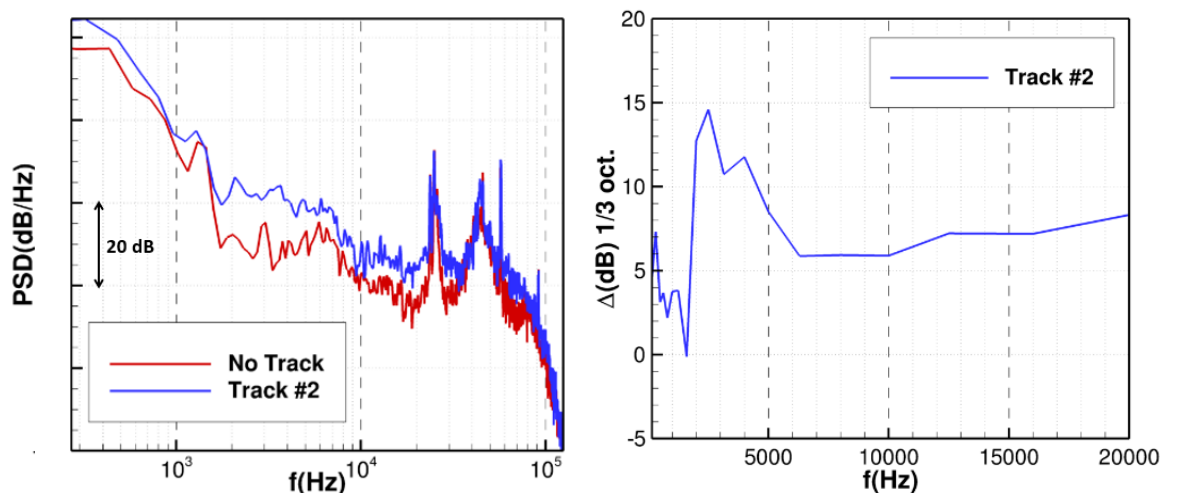


Figure 140: Left: Acoustic power spectral density computed at the central microphone of the acoustic antenna (in dB, $p_{ref} = 2 \times 10^{-5} \text{Pa}$). Right: Sound pressure level difference with respect to the no-track configuration (third-octave band dB, $p_{ref} = 2 \times 10^{-5} \text{Pa}$).

5.3.7.3 Virtual beamforming

The ZDES computation includes the whole test-section of the F2 wind tunnel and the complete airfoil in RANS mode, but the refined aeroacoustic mesh is only adapted to simulate the slat track noise. In order to properly compare the simulation with the measurements, the same microphone array processing was applied to the numerical signals computed at the positions of the microphone as to the corresponding experimental data. Obviously the cross-spectra are calculated with much less time averages due to the short duration of the calculated time signals.

In a first step, the deconvolved maps are calculated for each narrow band frequency. For a synthesized comparison, these maps are integrated in octave band. The comparison between the acoustic maps from the experiments and from the numerical simulation are compared for both configurations without slat track (Figure 141) and with the slat track ST#2 (Figure 142) in the octave band 2, 4 and 8 kHz.

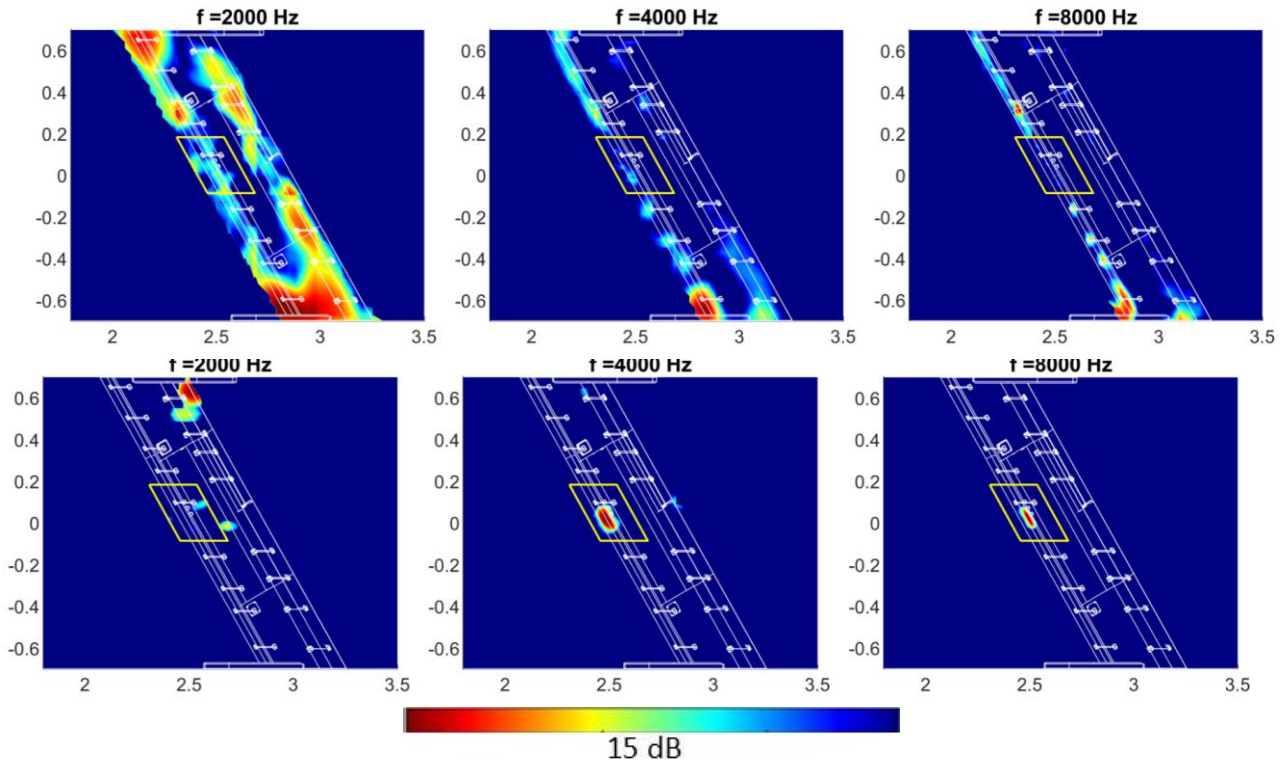


Figure 141: Comparison of the experimental (top) and numerical simulation (bottom) deconvolved acoustic maps for the configurations without slat track.

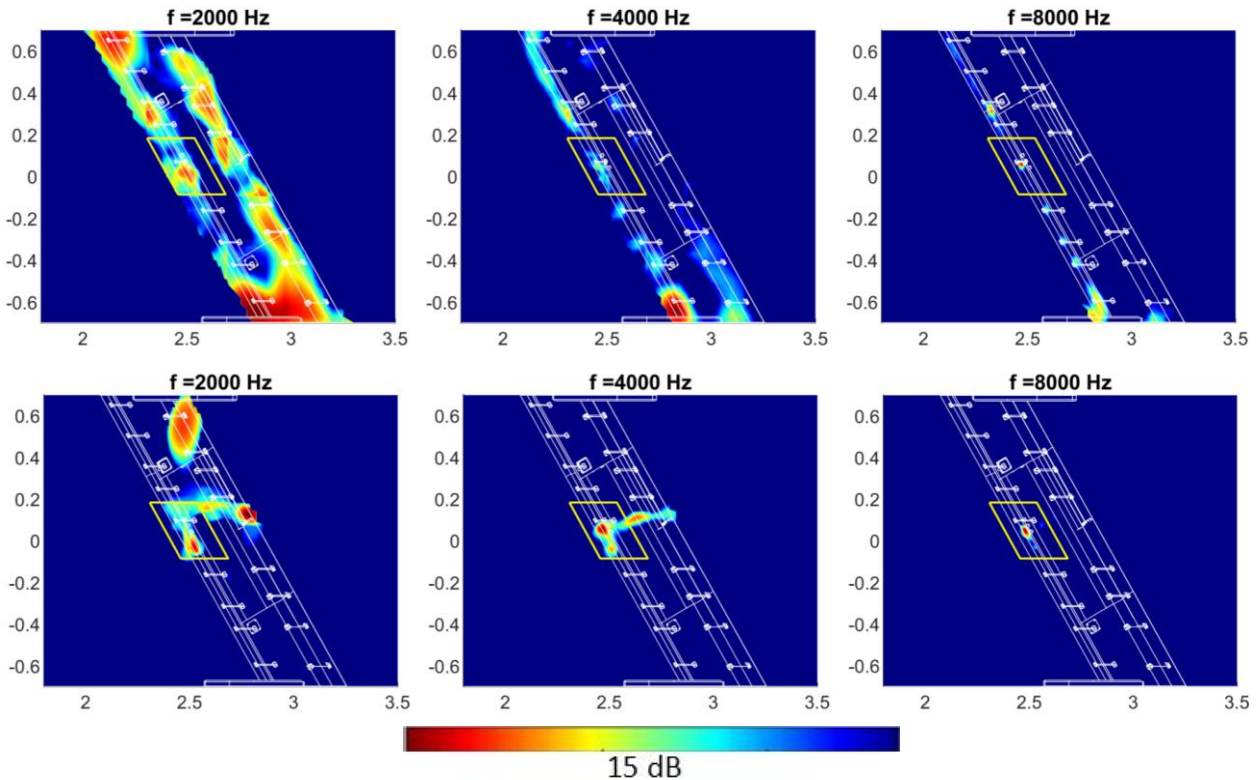


Figure 142: Comparison of the experimental (top) and numerical simulation (bottom) deconvolved acoustic maps for the configurations with slat track ST#2.

Even if the mesh is refined only on 80 mm in the spanwise direction, the source localization process was done on the whole airfoil in order to check potential spurious noise in the simulation. Indeed, we can observe that at 2 kHz, a strong source emerges at the junction between the flap and the right wall of the wind tunnel, which is not expected in the simulation. In contrast, experimentally, it is difficult to avoid a spurious noise due to the mounting devices at the wall, that ensures the attachment

and the incidence adjustment of the whole airfoil. At higher frequency, the maps clearly show an extended source in the ZDES resolved area without slat track, and a more compact source on the slat track when the latter is present. At 4 kHz, the numerical results exhibit a source on the flap (Figure 143), which is probably due to the interaction between the large-scale vortices emanating from the slat track and the flap trailing edge. As those vortices are no longer resolved in LES mode at the suction side of the main wing, their mixing with the turbulent boundary layer is probably not well predicted by the RANS model, leading to too strong large-scale coherent structures in the flap region.

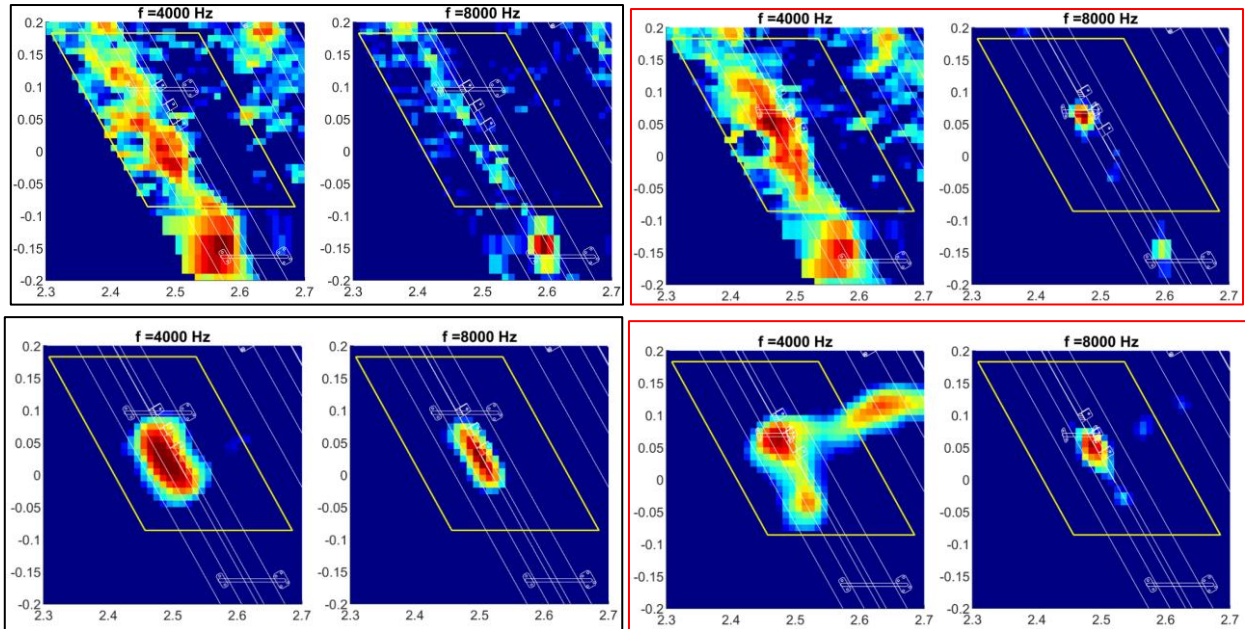


Figure 143: Zoom in the slat track area - Comparison of the experimental (top) and numerical simulation (bottom) deconvolved acoustic maps. Left (black frame): no slat track. Right (red frame): with slat track ST#2 (Note that scales differ between maps)

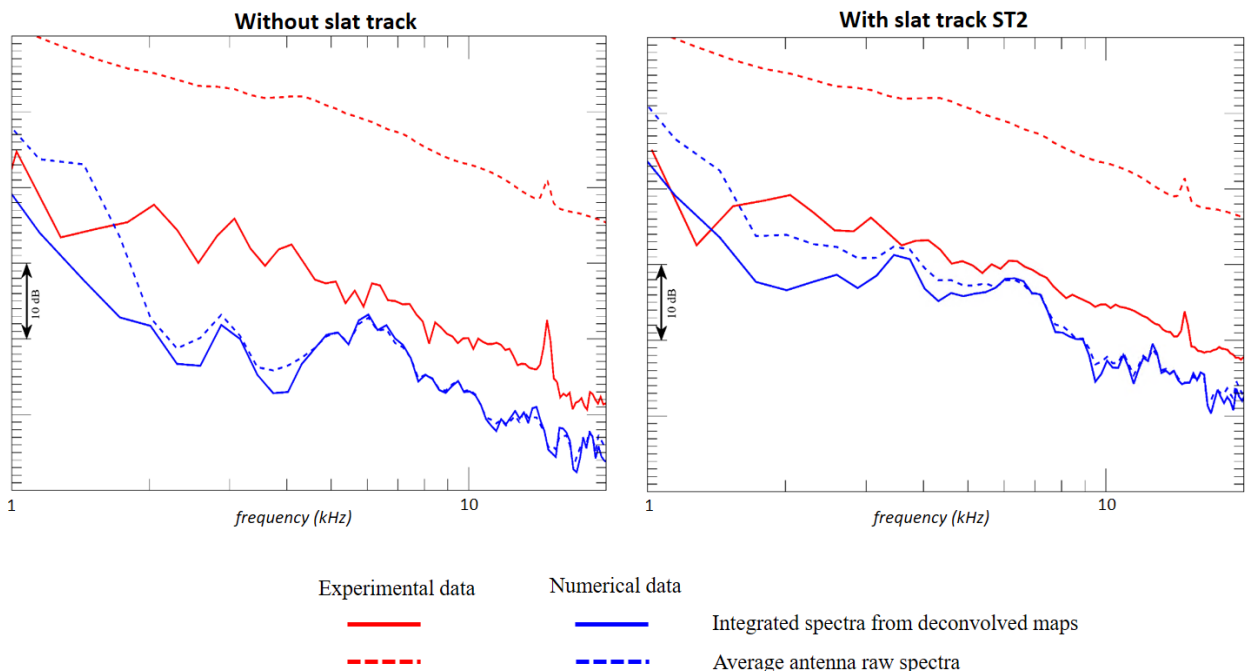


Figure 144: Comparison of numerical simulation with experimental data. Left: without slat track - Right: with slat track ST#2

Finally, the acoustic source spectra could be calculated by integration of the noise maps over different area. Obviously to compare here the numerical simulation with the experimental data, the noise maps were integrated in the yellow trapezoidal zone plotted in Figure 143. In order to exhibit the effect of

the array processing, the raw spectra measured in F2 or directly calculated by the FW-H method are superimposed in Figure 144 with the spectra obtained by integration of the deconvolved acoustic maps. Firstly, it shows that the slat track noise is about 15 dB below the total noise measured by the microphones of the antenna. In contrast with the numerical data, both spectra (direct FW-H and calculated from deconvolved maps) are close, and differ only in the low frequency range where the maps exhibit sources outside the slat track region. Secondly, the comparison of the spectra calculated in the slat track area via the array processing shows that the spectral shape is globally well reproduced for both configurations, but the simulation underestimates the experimental amplitude. Nevertheless, with the slat track mounted, the noise computation is in quite good agreement above 4 kHz with the experimental measurement despite this slat track is one of the quietest.

5.4 Numerical simulations by NLR

5.4.1 Context and objectives

NLR has performed hybrid RANS–LES simulations with its in-house flow solver ENSOLV, validated with the F2 measurements. The 2.5D configuration has been set-up, with periodic boundary conditions in the span direction and including one single slat track. The nominal flow conditions of the experiment have been used (velocity 71 m/s, angle of attack 5.33°). Considering the relative simplicity of their geometric shape, the slat tracks of DLR (based on an Airbus design) appeared to be the most suitable for validation purposes and the slat track #11 has been chosen.

5.4.2 Geometry and flow conditions

The baseline geometry consists of the DLR F16 3-element airfoil with a chord of $c = 300$ mm and a sweep angle of $\Lambda = 30^\circ$ as installed in the ONERA F2 tunnel. A single slat track is included, in particular, the DLR's baseline slat track as shown in Figure 145. It has a maximum thickness in span of about 7.5 mm and a similar height. There is an offset at its foot where it is attached to the wing. As reference, also the wing without slat track is considered.

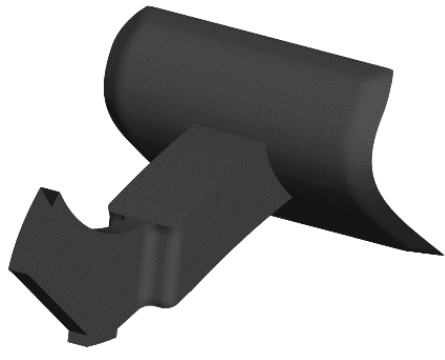


Figure 145: DLR's baseline slat track #11

Computations have been performed at the wind-tunnel conditions, consisting of a free-stream velocity $U_\infty = 71$ m/s at standard atmosphere and an angle of attack of $\alpha = 5.33^\circ$, implying a Mach number $M_\infty = 0.2$ and a Reynolds number $Re_c = 1.46 \cdot 10^6$. The tunnel walls have also been included in the set-up (modelled with a slip boundary condition).

5.4.3 Grid set-up

A multi-block structured grid of 26.4 million cells has been generated. The overset grid technique is used with separate, overlapping grids for the slat track (10.4 million cells), the main wing (9.6 million), the slat (3.6 million), and the flap (2.5 million). An impression of the grid is shown in Figure 146.

The slat track domain has a span width of 65 mm. In this domain, a target cell width was used of 0.2 mm in order to resolve a good portion of the turbulence structures in the separated flow around the slat track.

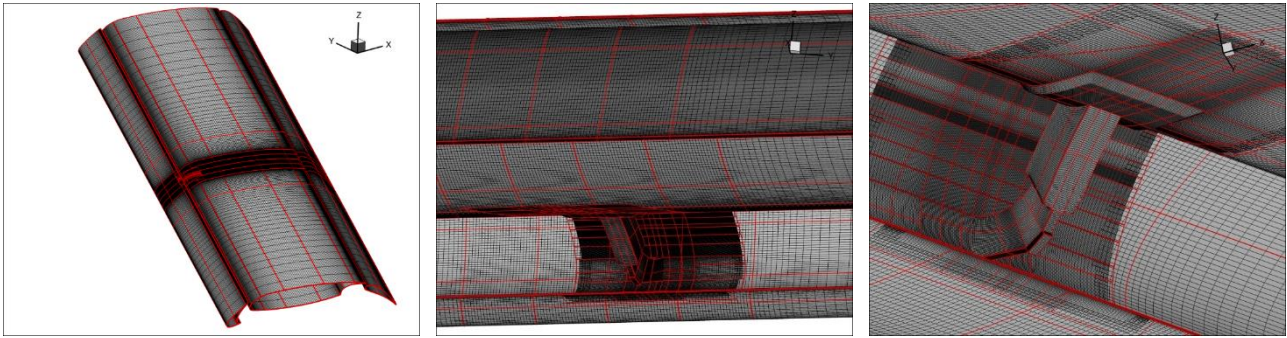


Figure 146: Impression of overset multi-block grid

5.4.4 Steady RANS result

First, a steady RANS computation (using the TNT $k-\omega$ model) has been performed to check the general set-up and assess the 2D extent of the flow. Figure 147 shows that there is a significant pressure gradient on the slat and the leading edge of the wing in the spanwise direction. For this reason, the complete wing as well as the tunnel walls have also been included in the hybrid RANS–LES computation rather than using only a limited spanwise extent with periodic boundary conditions. The chord-wise pressure distribution at the centre of the wing shows some discrepancies with the measured data. In particular, the suction peaks of the main wing and the slat are underpredicted. On the other hand, the pressure distribution around the slat, which is the main region of interest, is consistent with the experiment.

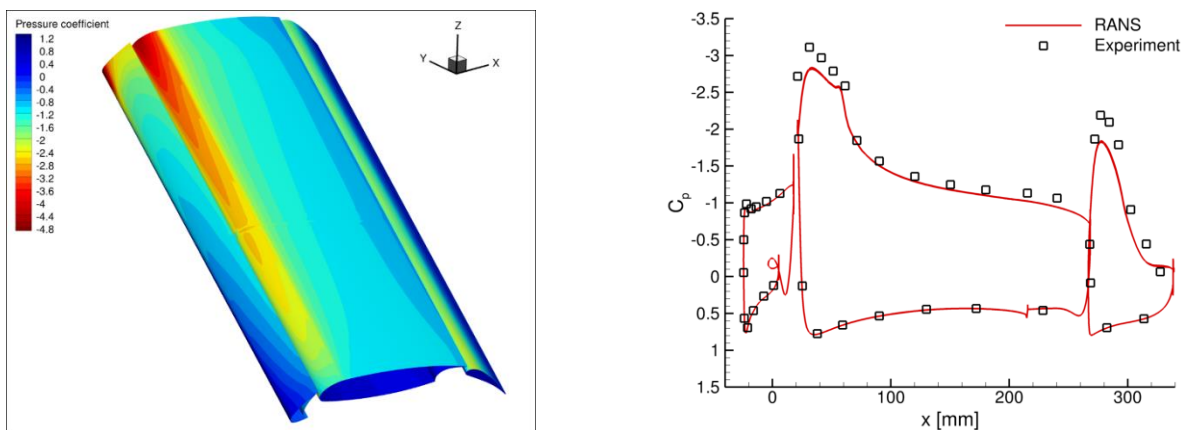


Figure 147: Steady pressure distribution (left: complete wing; right: section at the centre of the wing)

5.4.5 Hybrid RANS–LES set-up

The hybrid RANS–LES computations have been performed with NLR’s in-house flow solver ENSOLV using the X-LES method, which is a DES-type method based on the TNT $k-\omega$ model. It includes two approaches for mitigating the so-called grey-area problem common to hybrid RANS–LES methods: a high-pass filtered SGS model and a stochastic backscatter model [16]. This ensures a rapid development of resolved turbulence in separating shear layers. In the current case, this applies in particular to the shear layer within the slat cove.

As the focus lies on the sound generated by the slat track, a zonal approach is used in which the X-LES model is only activated inside the slat track domain. In the other three domains (wing, slat, flap), the unsteady RANS equations are solved. Within the slat track domain, RANS zones are also enforced on the pressure side of the slat (upstream of its trailing edges) as well as on the pressure side of the main wing. An illustration of the effective RANS and LES regions is shown in Figure 148.

In order to be able to determine the effect of the slat track on the flow and acoustic fields, a computation without slat track should be performed with as much as possible the same set-up. Thus, the grids around the wing, flap, and slat are kept the same in that case, while the slat track domain

is replaced by a domain of the same size and with a similar grid resolution, but without the slat track. Again, X-LES is only activated in this 'no slat track' domain.

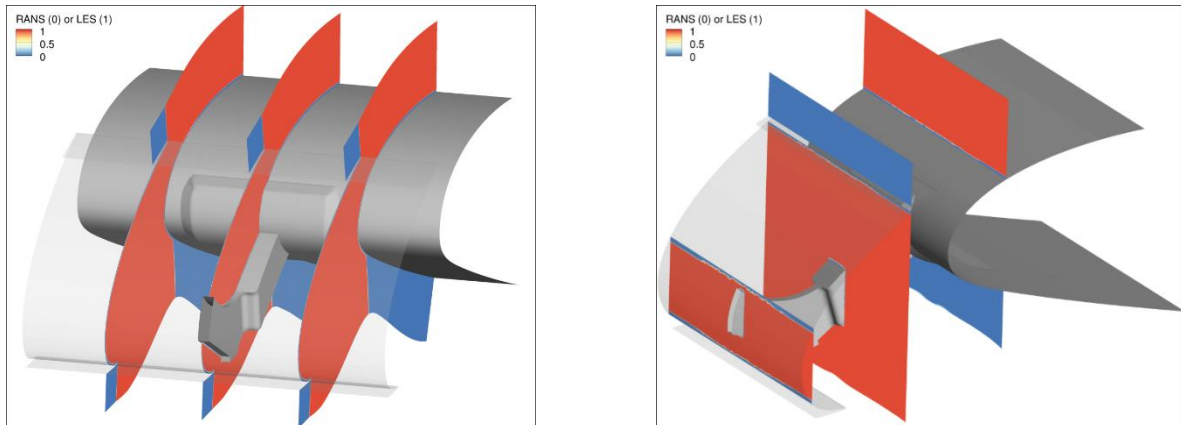


Figure 148: Impression of RANS (blue) and LES (red) regions in slat-track domain

In order to capture both turbulent vortices and acoustic waves accurately, a fourth-order finite-volume method with low numerical dispersion and dissipation is used for the convective terms [17]. A standard second-order discretization is used for the diffusive terms. Also, the standard second-order backward scheme is used to integrate the equations in time. In order to balance the time-discretization errors with the high-order spatial accuracy, a small convective CFL number is required in the order of $CFL \approx 1/8$. This resulted in a time step size of $8 \cdot 10^{-5}$ CTU ($= 3.4 \cdot 10^{-7}$ s), with the convective time unit defined as $CTU = c/U_\infty$. A total of 61,000 time steps were computed, giving a total time interval of 4.88 CTU ($= 20.6$ ms). Flow statistics were determined over the last 55,000 time steps (4.4 CTU).

The initial solution, after 0.5 CTU, is shown in Figure 149. On the left, the turbulent structures are visualized using the iso-surfaces of the Q criterion (coloured with the vorticity magnitude). It shows that the shear layers become unstable closely after the slat trailing edges and full 3D turbulence quickly develops. Note that the mean flow has a strong upward direction close to the wing leading edge, whereas, due to the wing sweep, it is mainly directed in spanwise direction (positive y direction) inside the slat cove further away from the wing leading edge. Thus, the flow separation induced by the slat track is mainly located above and to the left (positive y) of the track. In this separated-flow region, fine-scale turbulence structures are resolved. A limitation of the current set-up, however, is that the turbulence in the slat cove itself is not fully resolved. In particular, the sweep induced velocity in positive y-direction feeds flow from the slat domain, captured by RANS and therefore lacking resolved turbulence, into the slat-track domain where little resolved turbulence develops until the slat track is encountered and the flow separates.

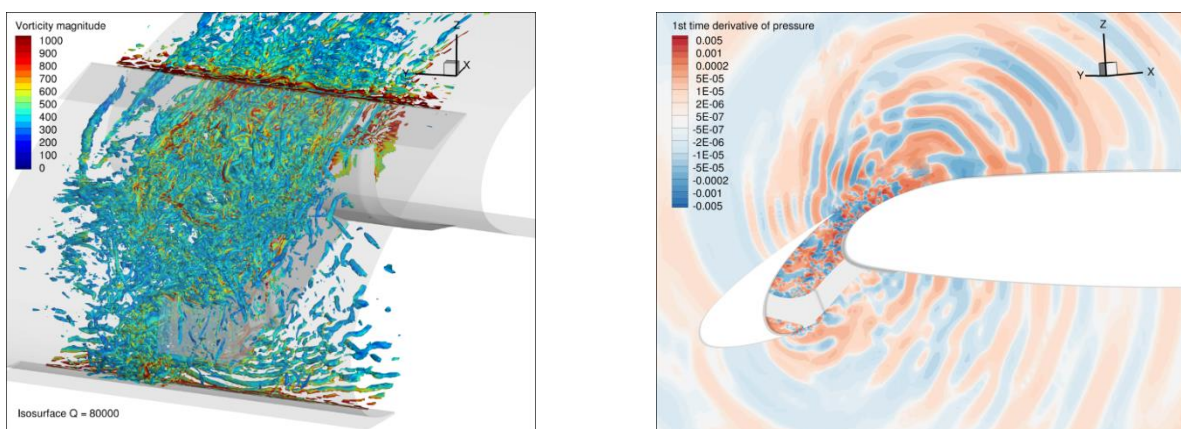


Figure 149: Initial solution after 0.5 CTU (left: iso-surfaces of Q-criterion; right: first time derivative of pressure)

The right picture of Figure 149 shows the first time derivative of the pressure in a plane normal to the wing leading edge (approximately the symmetry plane of the slat track). As taking the derivative is equivalent to multiplying with the frequency in the Fourier domain, it accentuates higher frequency components relative to lower ones. Clearly, acoustic waves are captured in a significant region around the slat and wing leading edge.

5.4.6 Validation with PIV measurements

The computed velocity field is compared to the PIV data from the F2 tunnel in Figure 150 to Figure 155. For clarity, the comparison is limited to the magnitude of the mean velocity $|U|$ and the magnitude of velocity fluctuations $|u'| = \sqrt{(u_x'^2 + u_y'^2 + u_z'^2)}$, with u_x' , u_y' , and u_z' , the root-mean-square values of the velocity components minus their average.

First, Figure 150 shows the velocity for the case without slat track in a 2D plane normal to the leading edge at the centre of the turbulence-resolving 'no slat track' domain (span-wise coordinate $LY = 0$). The computed mean velocity closely matches the PIV data. The stagnation points, both on the slat and on the main wing, are consistent. Also, the location and the shape of the shear layer inside the slat cove are very similar, although there is a slight shift in x direction. The computed velocity fluctuations confirm that resolved turbulence develops quickly inside the shear layer just after the lower slat trailing edge, giving similar levels as in the PIV data. The highest levels of fluctuations occur at the location where the shear layer hits the slat, as expected (and which is generally considered to play an important role in slat noise). The main difference with the PIV data is that in the computations there is a significantly lower level of fluctuations in the centre of the recirculating flow region inside the slat cove. This is related to the limitation of the current set-up as explained above, with flow lacking resolved turbulence entering the LES domain from the side.

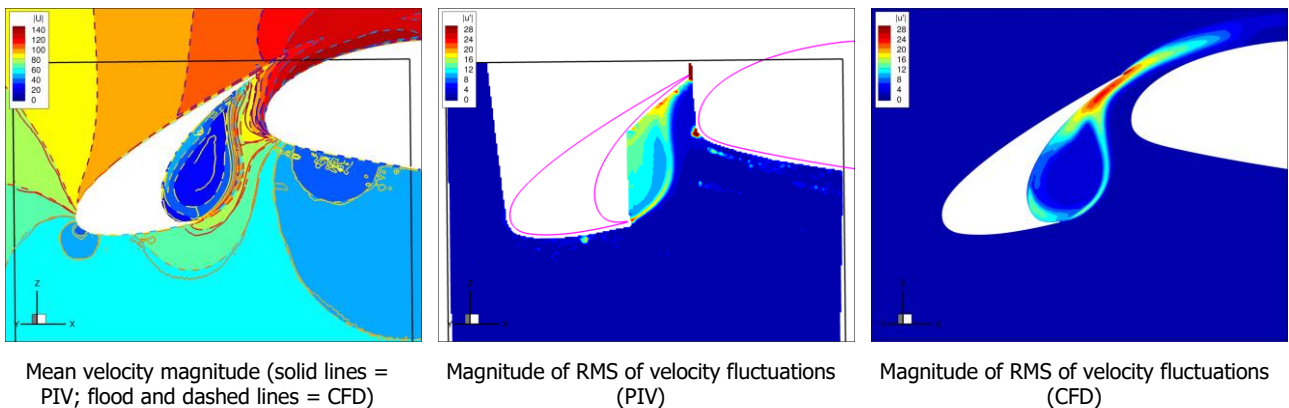


Figure 150: No slat track: Comparison of mean and RMS velocity with PIV data at $LY = 0$

A more quantitative comparison is made at a number of selected 1D lines in Figure 151. Three horizontal grid lines have been selected from the PIV grid and the CFD solution has been interpolated to these PIV grid lines. Again the mean velocities closely match, especially upstream of the slat and to the right of the shear layer, where there are high velocities as the flow is sucked through the gap between the slat and the main wing. The largest differences are seen in the recirculating flow region with low velocity magnitudes inside the cove. For the velocity fluctuations, the computed peak level is somewhat lower than the PIV data in the initial shear layer (line $i = 221$), but gradually seems to catch up as the shear develops. At the top line ($i = 281$), the peak level in the shear layer is the same. To the left of the shear layer, there is a second peak due to the shear layer hitting the slat after which fluctuations are transported along the slat wall to the left. The level of this peak is also consistent, but the CFD shows a much lower level in between the two peaks. This is also seen at the middle line (241), where the CFD gives a much lower level in the recirculation region as also noted above. Note that the PIV data shows a background level in the fluctuations of about 1 to 2 m/s (a turbulent intensity of about 0.8 to 1.6%), which, by nature, is not present in the computations (in RANS mode). Also, the PIV data shows some anomalies with disturbances in both the mean velocity and the

fluctuations where they are not expected (for line $i = 241$ around $x = -160$ mm and -140 mm and for line $i = 281$ at $x = -165$ mm).

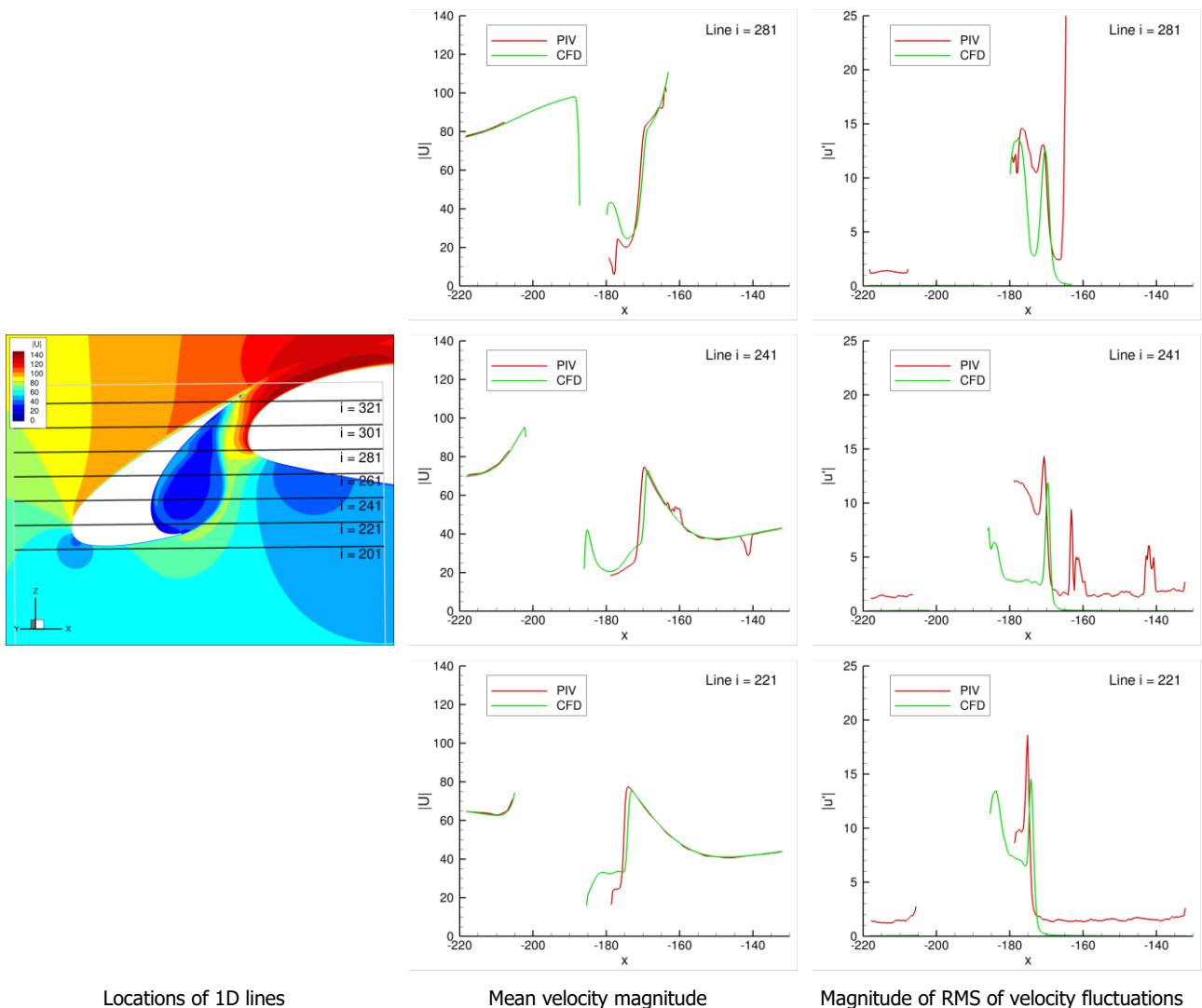
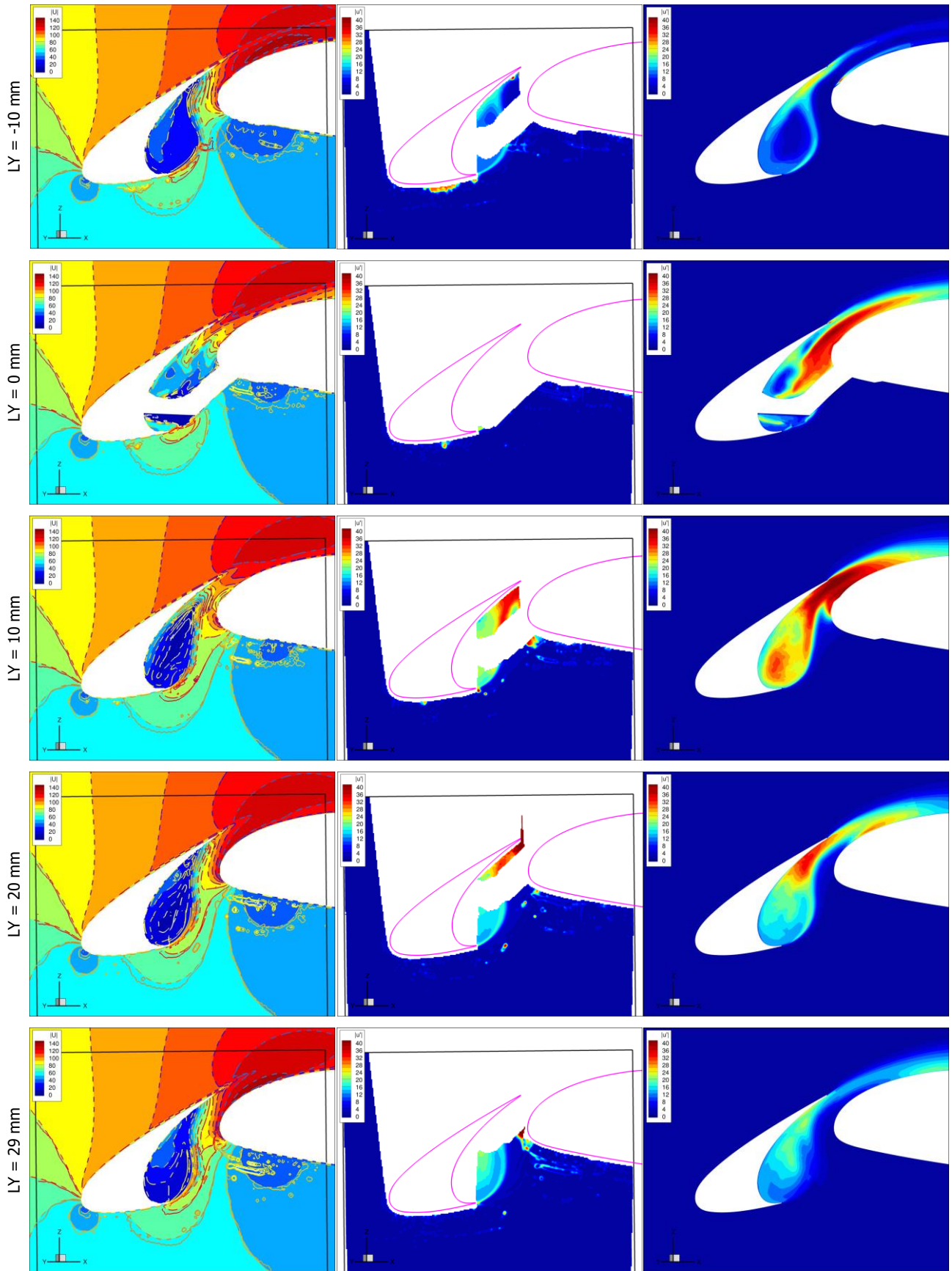


Figure 151: No slat track: Comparison of mean and RMS velocity with PIV data at selected 1D lines at LY = 0

For the computation with slat track, the velocity is shown in several planes in Figure 152, including one upstream plane (with respect to the sweep-induced spanwise flow) at $LY = -10$ mm, one plane through the slat track at $LY = 0$, and three downstream planes ($LY = 10$ mm, 20 mm, and 29 mm). Generally, similar flow patterns are observed in the CFD and PIV results. Upstream of the slat track, the flow is very similar to the case without slat track (note that a different scale is used for the fluctuations). There is a small separation visible here induced by the offset on the wing leading edge. High levels of fluctuations are seen above the slat track close to the wing in the planes through the track ($LY = 0$) and just downstream ($LY = 10$ mm) due to the flow separating from the track. These high fluctuations are transported through the gap between the wing and the slat without hitting the slat at $LY = 0$, but they do hit the slat at $LY = 10$ mm. Further downstream at $LY = 20$ mm, the levels are reduced, but still higher than the case without slat track. Inside the slat cove, the flow separation is located mainly to the side of the track (instead of above), leading to strongly increased levels in the recirculating flow region inside the cove. As a result, similar levels are now seen in the CFD and PIV results in the recirculation region in the downstream planes ($LY = 20$ mm and 29 mm), with the flow in the CFD now being fed with resolved turbulence from the flow separation.



Mean velocity magnitude (solid lines = PIV; flood and dashed lines = CFD) Magnitude of RMS of velocity fluctuations (PIV) Magnitude of RMS of velocity fluctuations (CFD)

Figure 152: With slat track: Comparison of mean and RMS velocity with PIV data

The last plane (LY = 29 mm) is close to the boundary between the slat-track (LES) and slat (RANS) domains, where interpolation between the domains occurs. As a consequence, the turbulence is no longer fully resolved here, in particular leading to a low level of velocity fluctuations in the shear layer at this plane.

Again, for a more quantitative comparison, plots are shown at selected 1D lines in Figure 153 to Figure 155 at the plane LY = -10 mm, 10 mm, and 20 mm. Both the mean velocity and the velocity fluctuations mostly correlate very well, ignoring some apparent anomalies in the PIV data (in particular at line $i = 213$ around $x = -170$ mm and -155 mm). There is hardly any shift in the location of the shear layer. The peak velocity to the right of the shear layer is the same and also the level of velocity fluctuations in the shear layer is very close. Additionally, the level in the recirculation region at LY = 20 mm is now also much closer than upstream, as far as it is available in the PIV data.

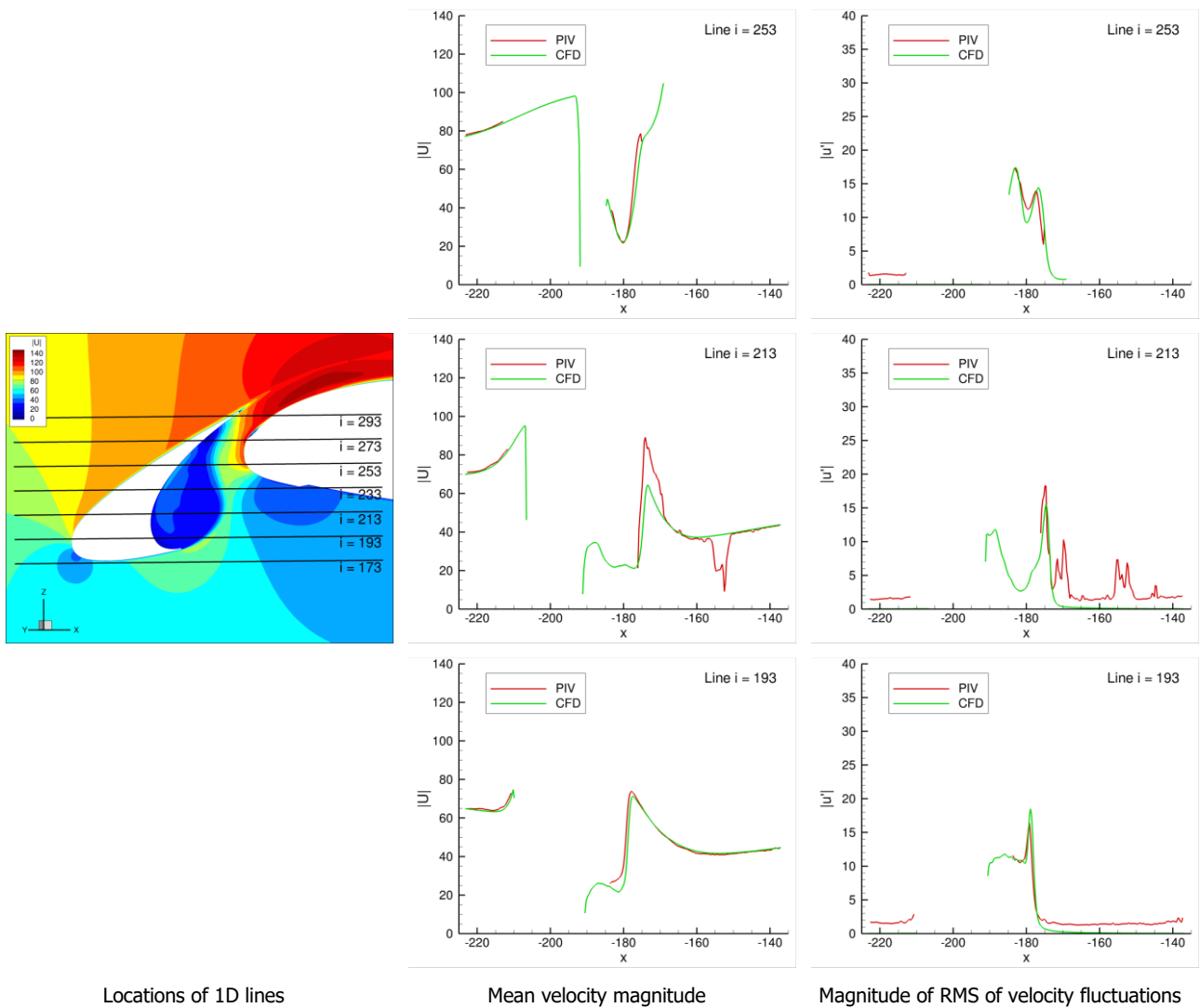
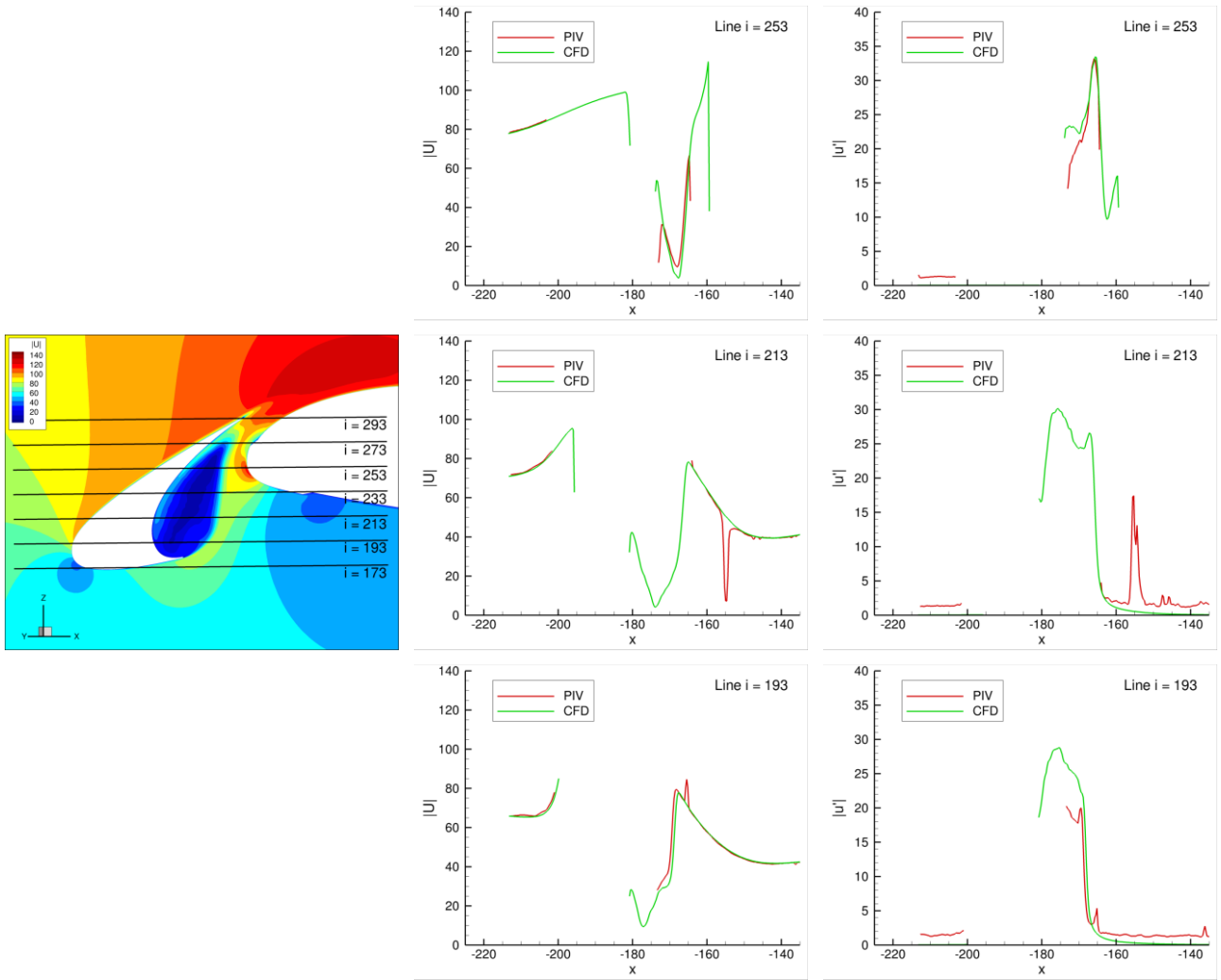


Figure 153 With slat track: Comparison of mean and RMS velocity with PIV data at LY = -10 mm (upstream of track)



Locations of 1D lines

Mean velocity magnitude

Magnitude of RMS of velocity fluctuations

Figure 154 With slat track: Comparison of mean and RMS velocity with PIV data at LY = 10 mm (downstream of track)

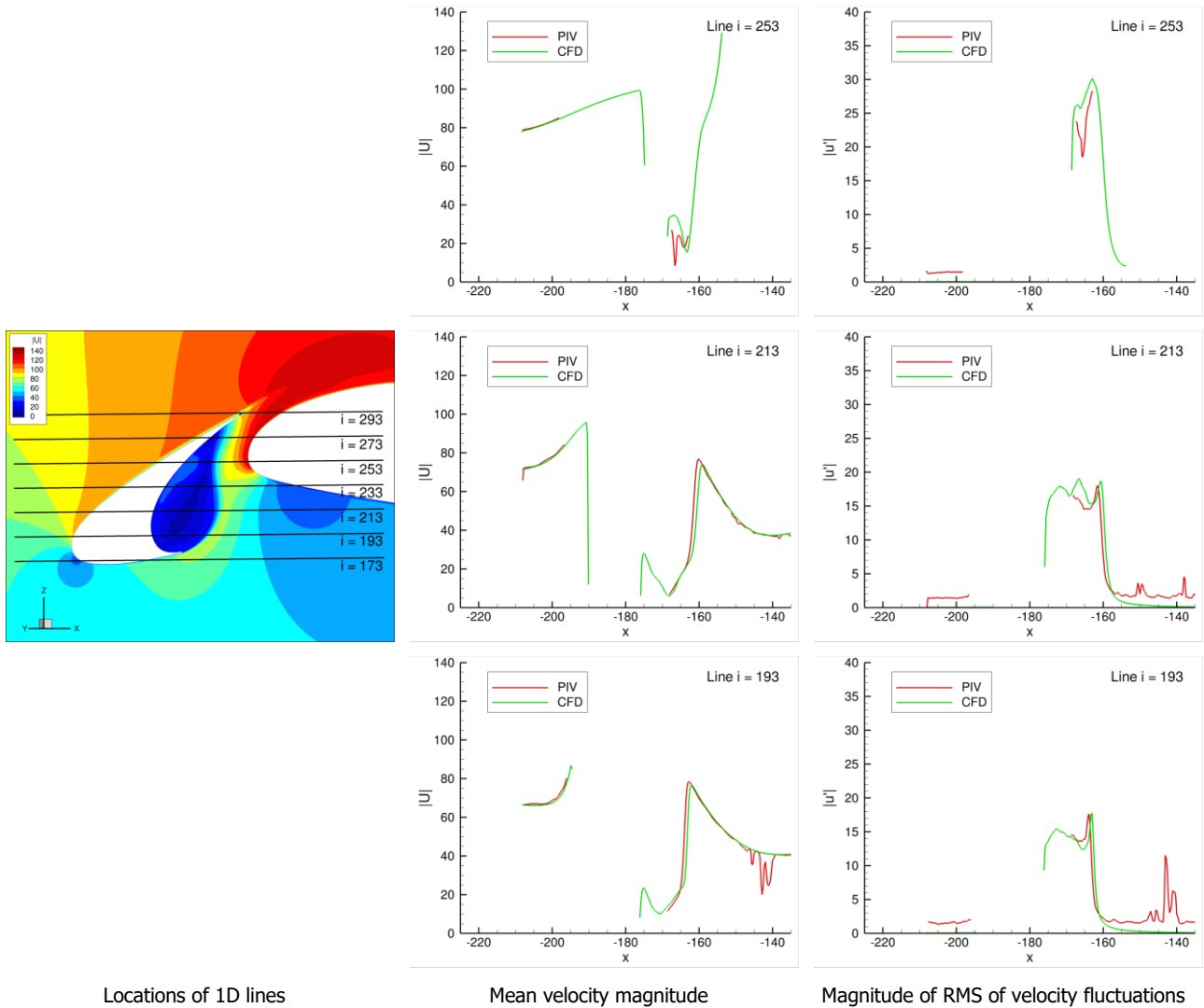
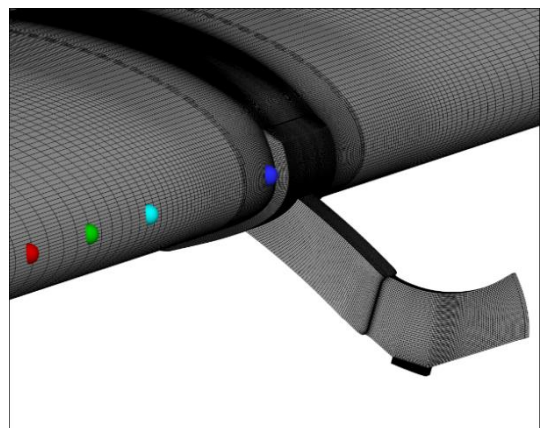


Figure 155 With slat track: Comparison of mean and RMS velocity with PIV data at LY = 20 mm (downstream of track)

5.4.7 Validation with Kulite data

As a first assessment of the noise generated by the slat track, the pressure spectrum is determined at the locations of four Kulites along the wing leading edge as shown in Figure 156. The computed pressure spectra are compared to the measured ones in Figure 157, considering both cases with and without slat track. One Kulite is positioned close to the slat-track offset (KU11) and is located inside the slat-track domain where the turbulence is resolved. The other three Kulites are positioned further away downstream where the RANS equations are solved. It should be stressed that the computations only capture a limited part of the sound generation, as turbulence is only resolved near the slat track. Thus, slat noise itself is only generated in this region (extending only 65 mm in span), but is missing along the remaining part of the slat.



KU6 KU9 KU10 KU11
Figure 156: Locations of Kulites

Additionally, the time interval used for the computations (about 20 ms) is much smaller than the one used in the experiments and is probably too small to fully capture the lower frequency range. Furthermore, the experimental pressure levels show some variation between the Kulites for the case without slat track (for example, the peak level at KU6 is about 5 dB lower) for which the reason is not clear. All these considerations combined imply that a direct comparison of the absolute pressure levels is of limited value, especially at the downstream Kulites.

Focussing on the difference in pressure levels with and without slat track, a qualitative similarity is seen between the computations and measurements. There is a strong increase at KU11 close to the slat track in the order of 15 to 25 dB (up to about 10 kHz) related to the highly turbulent, separated flow from the slat track which passes the wing leading edge there. At the other Kulites, there is a much weaker increase roughly in the order of 5 dB for the low frequency range (up to about 3 or 4 kHz), which may be attributed to acoustic waves originating from the slat track. The computations also show an increase of pressure levels at higher frequencies, contrary to the measurements. This can be explained partly by the presence of slat noise itself in the measurements, which may dominate over the slat-track noise at higher frequencies at the downstream Kulites, but is lacking in the computations in the RANS region. Finally, the computations show much higher pressure levels than the measurements for the highest frequencies (above 10 kHz) in particular at KU11 and KU10, which may be suspected of being numerical rather than physical noise. High frequency numerical noise could be generated, for example, when flow with a high level of resolved turbulence leaves the slat-track LES domain and enters the wing RANS domain (on the suction side) where this resolved turbulence is dissipated.

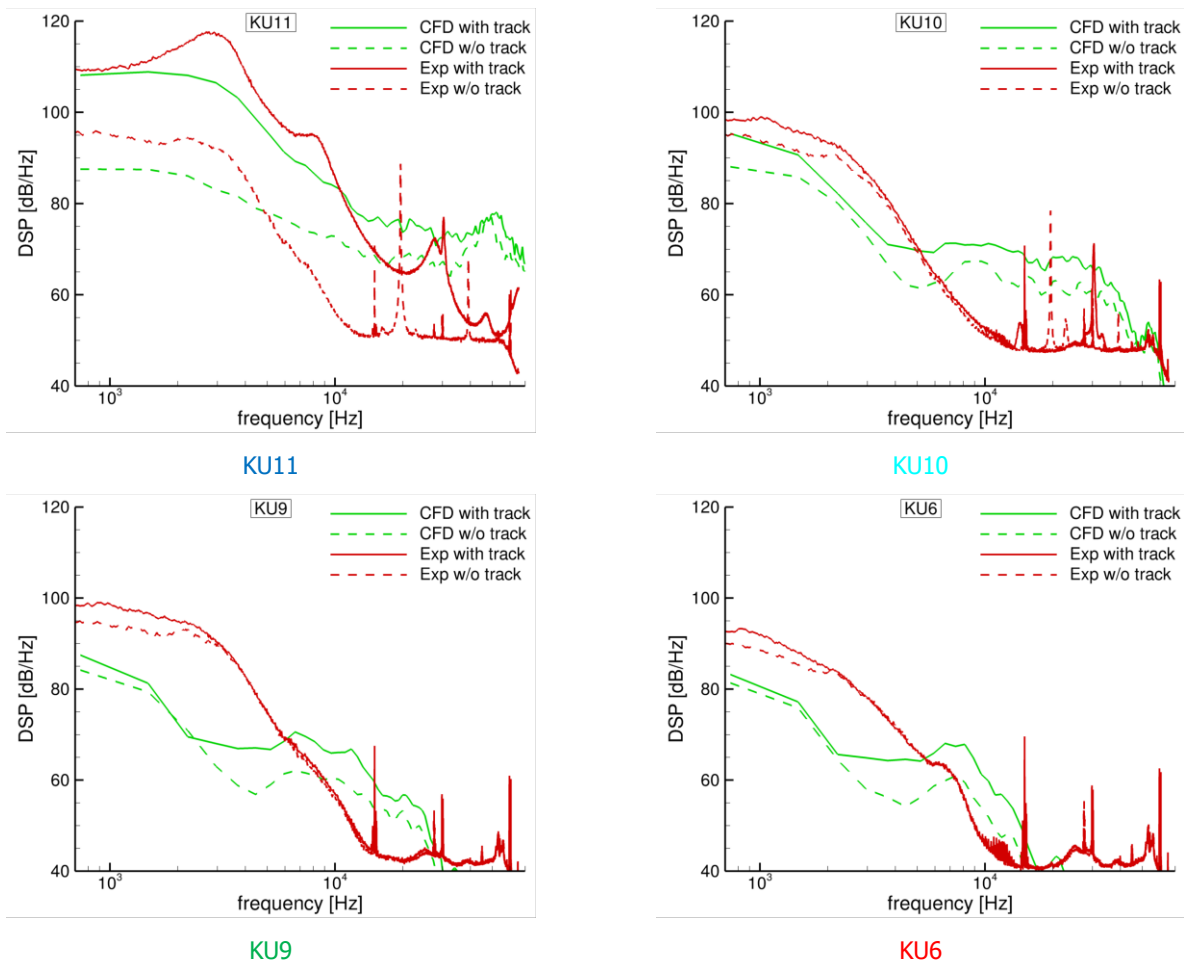
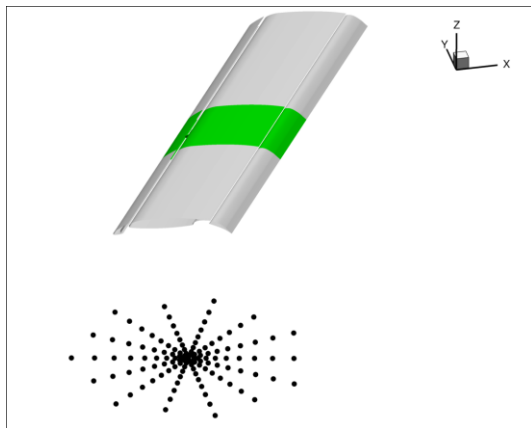
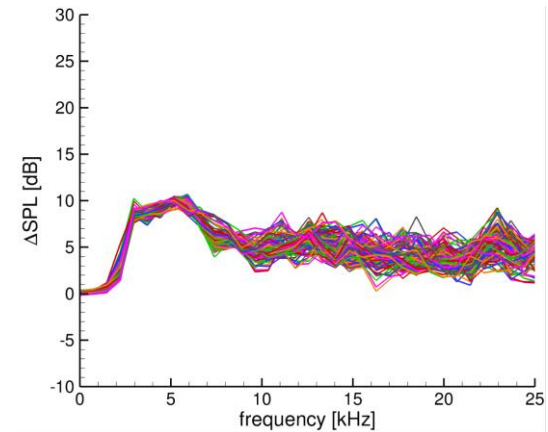


Figure 157: Comparison of pressure spectra at Kulites



Location of FWH surface (green) and acoustic array



Computed increase of SPL at acoustic array due to inclusion of slat track

Figure 158: Far-field noise due to slat track

5.4.8 Far-field noise computation and virtual beamforming

The far-field noise has been computed at the location of the acoustic array used in the F2 tunnel. The Ffowcs Williams & Hawkins (FWH) method has been employed, using the wing surface as source region, but limited in span ($-200 \text{ mm} < LY < 68.67 \text{ mm}$) as indicated in Figure 158 (green region). The right picture of Figure 158 shows the increase of the sound-pressure level due to the slat track at all points of the acoustic array. It shows an increase of at most 10 dB and in the order of 5 dB between 5 and 25 kHz. This is consistent with the previous measurements at NLR's acoustic tunnel (AWT), which also showed an increase in the order of 5 dB for the power integrated spectrum in the same frequency range [18]. The virtual time signals computed by NLR at the microphone positions were provided to ONERA, containing 10094 time steps corresponding to about 17 ms at a sampling frequency of 591.667 kHz. From these signals, ONERA computed the cross spectral matrix with 9 time averages of Fourier transform of blocks of 2048 samples ($\Delta f = 288 \text{ Hz}$), using a Hanning window, and an overlap of 66%.

Figure 159 compares the noise spectra computed at the position of the central microphone AW1 of the 120-microphone array in F2, for the baseline (no slat track) and for the slat track #11.

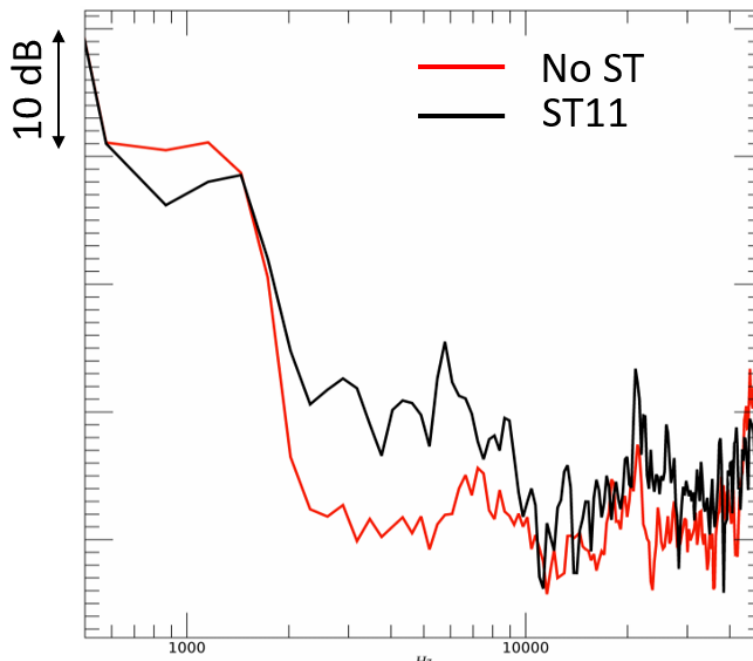


Figure 159: Noise spectra computed by NLR at the position of the central microphone of the 120-microphone array in F2, without slat track and with the slat track #11

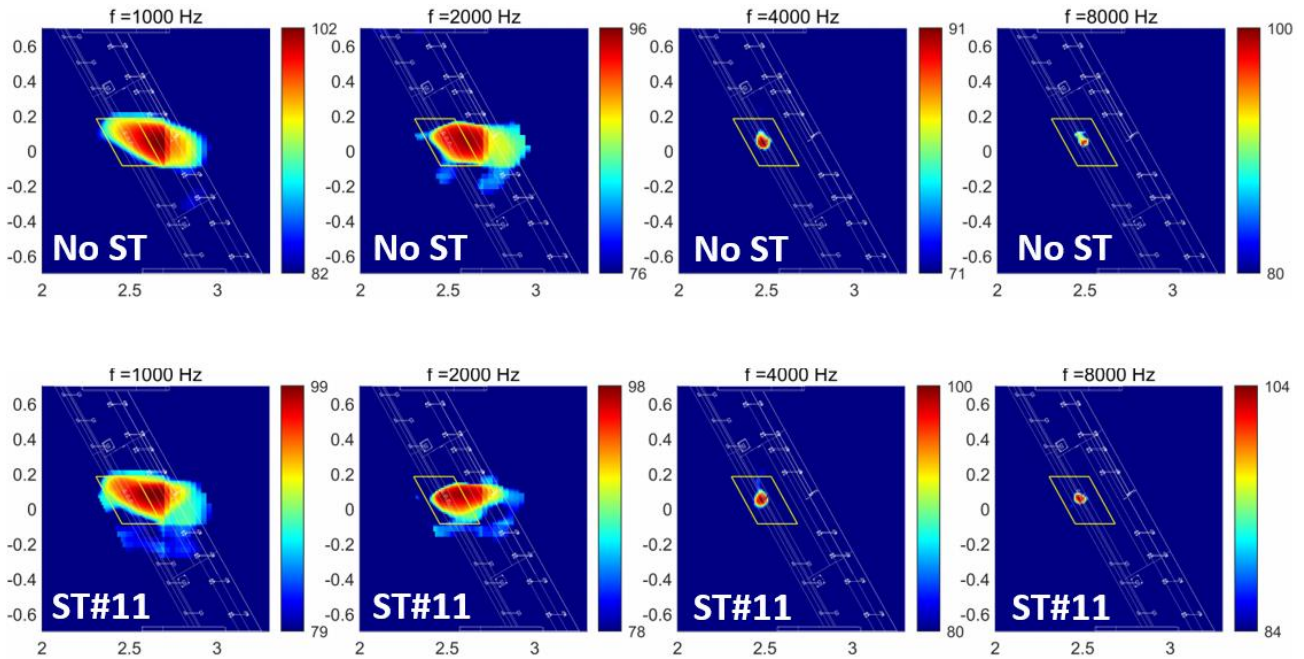


Figure 160: DAMAS noise maps at 1, 2, 4 and 8 kHz computed from the virtual acoustic signals computed by NLR on the positions of the 120 microphones without slat track (top) and with the slat track #11 (bottom)

The same array processing was applied by ONERA to the numerical signal as to the experimental data. Figure 160 shows DAMAS noise maps at 1, 2, 4 and 8 kHz computed from this cross spectral matrix without slat track (top) and with slat track #1 (middle) and #2 (bottom). The origin of the noise sources detected on the slat without slat track are not straightforward. When the slat track #11 is installed, the corresponding noise source clearly dominates the maps at all considered frequencies. These noise maps were integrated in the same slat track area (yellow zone on Figure 160) and the result (integrated spectra) are compared on Figure 161 with similar experimental data. The experimental relative ranking of noise levels between both cases is fairly reproduced by the numerical simulations. The numerical simulation underestimates the experimental F2 data by about 5 dB, which is reasonably good, knowing that the experimental data probably indirectly integrate other noise sources than only the sources contained in the yellow zones, especially the sources images generated by the reflections on the windtunnel walls.

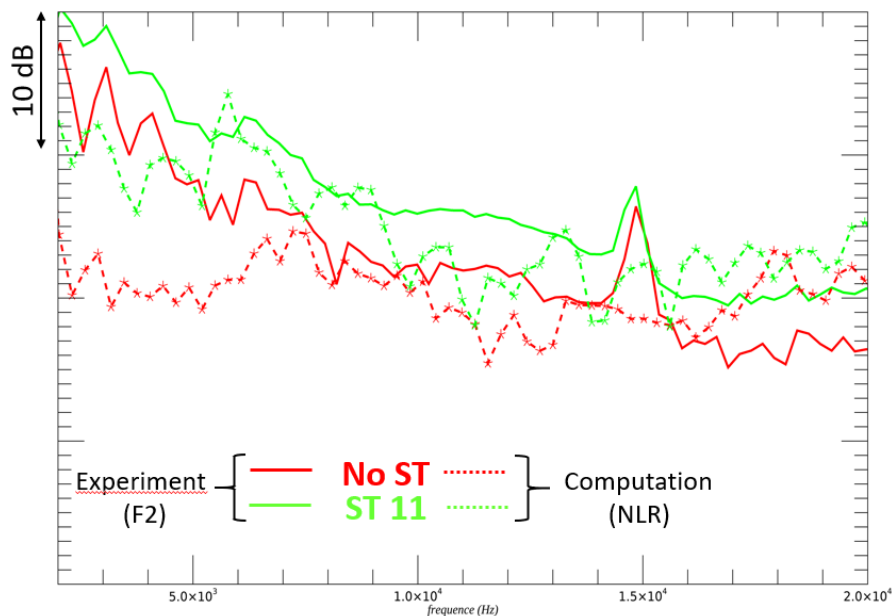


Figure 161: Noise spectra from the DAMAS noise maps integrated in the slat track area (yellow zone on Figure 160). Experimental results (solid) and numerical simulation (dashed) by NLR, without slat track and with slat track #11

5.5 Numerical simulations by DLR

5.5.1 Introduction

The results discussed in this section were conducted as part of the task planned in Workpackage 4, Subtask 4.2.4. The initial focus was to numerically investigate and assess an active slat-track Noise Reduction Technology (NRT) prior to experimental testing to assess the noise reduction potential and identify a priori promising design setups. The proposed idea was to achieve local flow control near the track using a steady blowing concept. This was realized by steadily blowing bleed air at the track to push away the oncoming free-stream flow, which will then go around the track, i.e., creating an air curtain around the track. Two different blowing strategies were investigated: the air was steadily blown along the streamwise (x -axis, parallel to the track) and the spanwise (z -axis, perpendicular to the track) direction. The discussion will be oriented towards the efficacy of the steady blowing concept and of an alternative passive slat-track measure that has been studied in addition to the planned concepts, i.e., porous material to reduce the extra noise induced by the presence of a slat-track in the slat cove.

To create a high-lift wing section, DLR's F16 high-lift wing cross-section was extruded in the spanwise direction. Figure 162 shows the F16 high-lift wing section used in the investigation, with a clean chord length (c) of 0.3 m. The simplified slat-track (ST#11) chosen for the investigation also served as a baseline track in several other DLR projects.

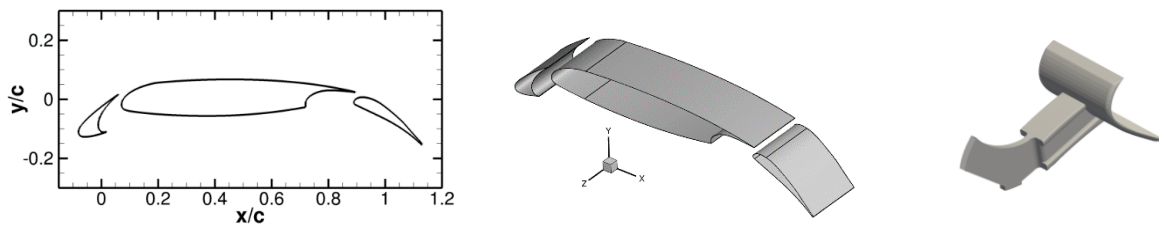


Figure 162: From the left – DLR's F16 high-lift wing cross-section, spanwise extruded high-lift wing section (20%c), simplified slat track (ST#11) used in the investigation.

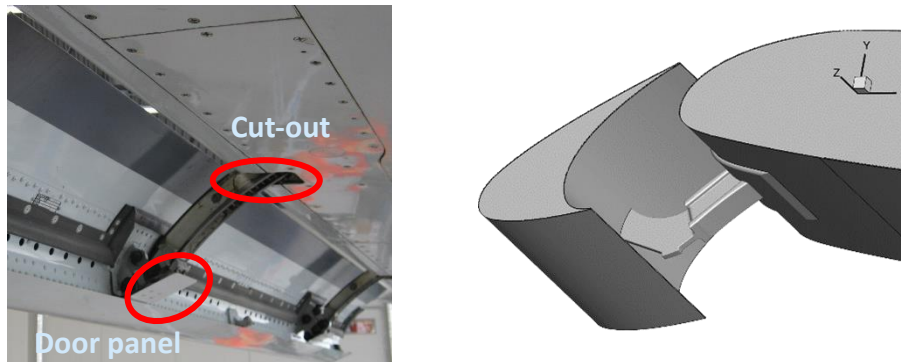


Figure 163: Left: Deployed slat configuration on the DLR A320 aircraft. Right: F16 high-lift wing section with a simplified track i.e. sealed cut-out, without door panel.

Simplifications included the sealing of the cut-out at the main element nose and neglecting the door panel at the slat cusp. Figure 163 shows a visual comparison between a real track aboard DLR-A320 aircraft and the F16 wing section with a simplified track.

Direct Noise Computation (DNC) of the F16 high-lift wing section was carried out using the Wall-Modelled LES (WM-LES) approach with the Lattice-Boltzmann-Method. ProLB [19] was used as a DNC tool, along with the acoustics resolved directly in the far-field. The complexity of the chosen test case was gradually increased to identify the effects of individual-applied changes. Starting from the unswept F16 high-lift wing section, the effect of sweep was first investigated. Using the swept F16 high-lift wing section case as a reference, the effect of a subsequent addition of slat track was studied.

Based on this outcome, the NRT was investigated, and their effectiveness in reducing track noise was assessed.

This section has the following structure:

- Part I: Effects of adding sweep and a slat track subsequently
- Part II: Active noise control
- Part III: Passive noise control

5.5.2 Numerical strategy and settings

The numerical strategy for realizing sweep will be described and discussed here. Figure 164 (a) shows the schematic arrangement of the F16 wing section without sweep. The figure includes two views, namely the side view (airfoil cross-section, x-y plane) and the top view (x-z plane). The wall model boundary condition was used on the high-lift wing surfaces. Velocity inlet and pressure outlet boundary conditions were applied in the far-field. Periodic boundaries were specified along the spanwise extent. Sponge zones were defined near the boundaries as non-reflecting far-field boundary condition.

The computations were carried out for free-field uniform flow conditions with $U_\infty = 61.53$ m/s, shown with a black arrow, at an angle of attack of 6.15° . The speed of sound a_0 was 343.20 m/s, and the Reynolds number of 1.23 million was used.

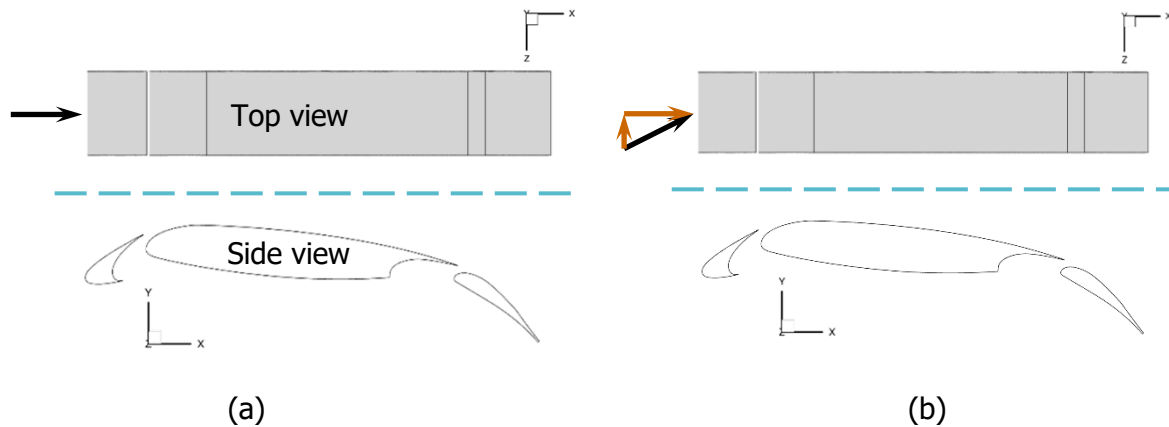


Figure 164: Numerical setup strategy for F16 wing section, without and with sweep

Figure 164 (b) shows the schematic arrangement of the F16 wing with sweep. This study does not perform a geometric sweep on the F16 wing section. To realize the sweep angle of 30° , the unswept F16 wing section is first rotated by 6.15° (the angle of attack) along the z-axis. The rotation of the uniform free-stream velocity (black arrow) by 30° occurs in the x-z plane. Brown arrows show the velocity components parallel and perpendicular to the wing leading edge. Based on this concept, periodic boundary conditions are still applicable in the z direction.

A swept configuration, on the contrary, would require, e.g., the definition of slip walls or a periodic boundary condition with x-offset to account for the resolved sweep. With ProLB, the only alternative option was to combine a sweep with a slip wall. However, this approach resulted in flow artifacts at the slip wall in other reference computations, as it blocked any lateral flow velocities at the boundary.

The velocity component parallel to the wing leading edge is the cross-flow component, i.e., along the -ve z-axis. In this study, we assume a swept wing section of an infinite span, i.e., periodically arranged tracks along the span. To realize this, periodic boundary condition is applied to a domain of with a span of 20% of the clean chord length c . Since the distance between the periodically arranged tracks in this study is smaller than what exists in reality, the noise contribution from the slat-track will be louder.

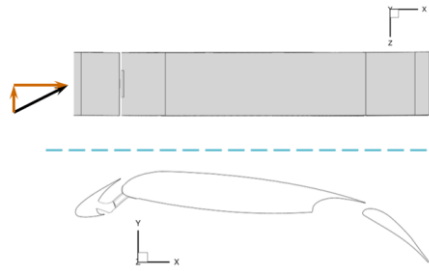


Figure 165. Numerical setup strategy for F16 wing section, slat-track.

The computational domain is a square box of dimension $30c \times 30c$. These dimensions include the thickness of sponge zones i.e. $3c$. Table 10 lists the numerical settings used for the simulations. Simulations with different complexities of F16 wing section, had these same numerical settings. All the cases discussed from now on had the acoustics resolved directly in the far-field.

Numerical settings.	Value
Finest grid size, Δ_f [m]	1.25e-04
Time step, [s]	2.1e-07
Total time, [s]	0.31
Refinement levels	9
No. of grid points	88 million

Table 10: Numerical Settings

ProLB is an industrial and research lattice Boltzmann solver that is developed within a scientific collaboration including CS GROUP, Renault, Airbus, Safran Group, Ecole Centrale de Lyon, Aix-Marseille University and in special scientific collaborations with ONERA and CERFACS. It is a node based solver that deploys a D3Q19 lattice. To ensure superior stability at higher Reynolds number a Hybrid Recursive Regularized Bhatnagar-Gross-Krook (HRR-BGK) [20] collision scheme is used instead of BGK. A logarithmic wall function is used to model the dynamics of turbulence at the first off wall cell with extra correcting terms for adverse pressure gradient and curvature corrections [21].

5.5.3 Adding sweep and slat-track

5.5.3.1 *F16 without and with sweep*

In this subsection, we will compare the time-averaged flow and far-field acoustic results between the F16 with and without sweep. From this point forward, all the velocity contours and profiles were extracted at the mid-span plane, i.e., $z = 0$. Figure 166 (a) shows a comparison of the C_p distribution between F16 with and without sweep. In the sweep case, we observe reduced suction peaks at all three elements, namely the slat, wing, and flap, compared to the suction peak levels in the unswept case. The different perpendicular velocity components realized at the leading edge of the F16 wing section under consideration here are responsible for this reduction. The transformation equation from the theory of the infinite swept wing verifies a reduction in the magnitude of suction peaks resulting from the inclusion of the sweep component. Figure 166 (b) and Figure 166 (c) show a comparison of the normalized velocity magnitude contour between the F16 with and without a sweep case. The F16 with a sweep case exhibits lower levels of normalized velocity.

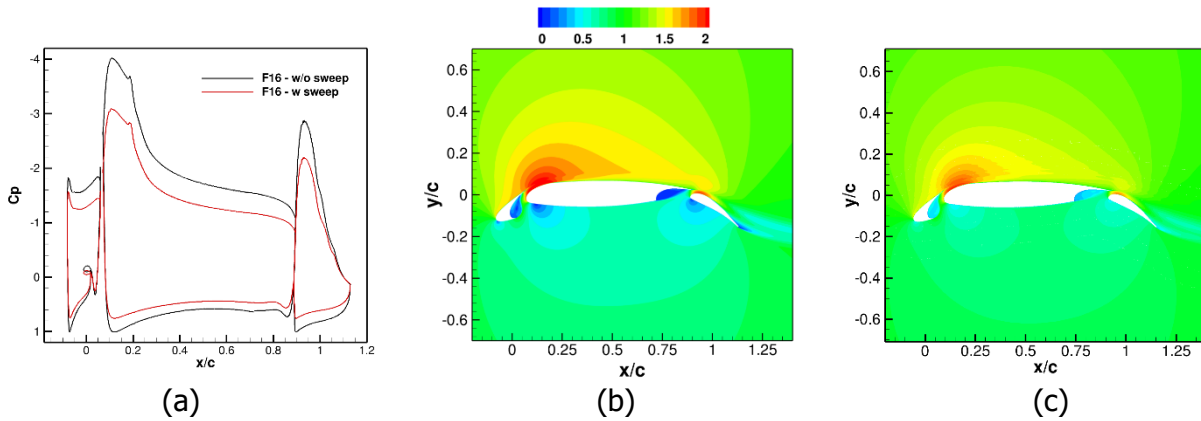


Figure 166: Time-averaged flow results, F16 without and with sweep. C_p distribution (a) and normalized velocity magnitude contour: without sweep (b) and with sweep (c)

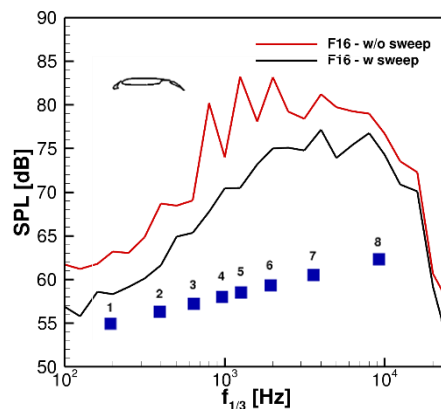


Figure 167: Farfield acoustic results, F16 without and with sweep.

Figure 167 exemplarily shows the far-field arrangement of microphones in the AWB with the F16 wing section. The acoustic spectra discussed now will be from the microphone numbered 5. Since we use a limited spanwise domain extent, i.e., 20% c , the spectra shown here were corrected to account for the full 3D propagation of acoustics in the far-field, span of the AWB and to account for "cut-on" type of jumps induced by periodicity; see Soni *et al.* [22] [23]. It is located roughly 1.32 m away from the coordinate center, i.e., the slat leading edge (retracted configuration). Figure 167 displays a comparison of the 1/3-octave band spectrum for F16 with and without sweep.

Two important observations can be drawn from this comparison: the tones observed in the unswept wing case are absent for the wing with sweep and the absolute noise levels, for the F16 with sweep case, over the entire frequency range is reduced. This reduction in the absolute noise levels can be justified as both arrangements will have different perpendicular velocity component.

5.5.3.2 F16 without and with slat-track

From now on, the sweep will be included in all the results of the F16 high-lift wing section shown and discussed. Figure 168 (a) compares the distribution of the F16 wing with and without slat-track. A noticeable difference from this comparison is the increase in flow acceleration on the suction side of the main element, i.e., the wing nose (see Figure 168). This type of flow acceleration occurs only over a limited portion of the main element's span, i.e., to a limited extent on either side of the slat-track. Shear-layers, rolling up from either side of the track and convecting further downstream, influence the local C_p distribution on the suction side of the main element. A visual comparison of the velocity magnitude contour between the F16 w/o and w track is shown in Figure 168 (b) and Figure 168 (c). When compared to the contour of the F16 w/o track, the presence of a track in the slat cove induces a completely different flow inside the cove, in the region near the slat trailing edge, and also in the slat gap. The track's surface shows the C_p plotted as a contour with lines. The side of the track

shown here faces the oncoming cross-flow. Starting from the side of the track in contact with the slat until the I-shaped region of the track, it faces only the recirculating cove flow and the shear layers originating from the slat cusp. It is the I-shaped region that will be exposed to the faster-moving cross-flow, hence the higher values of C_p there.

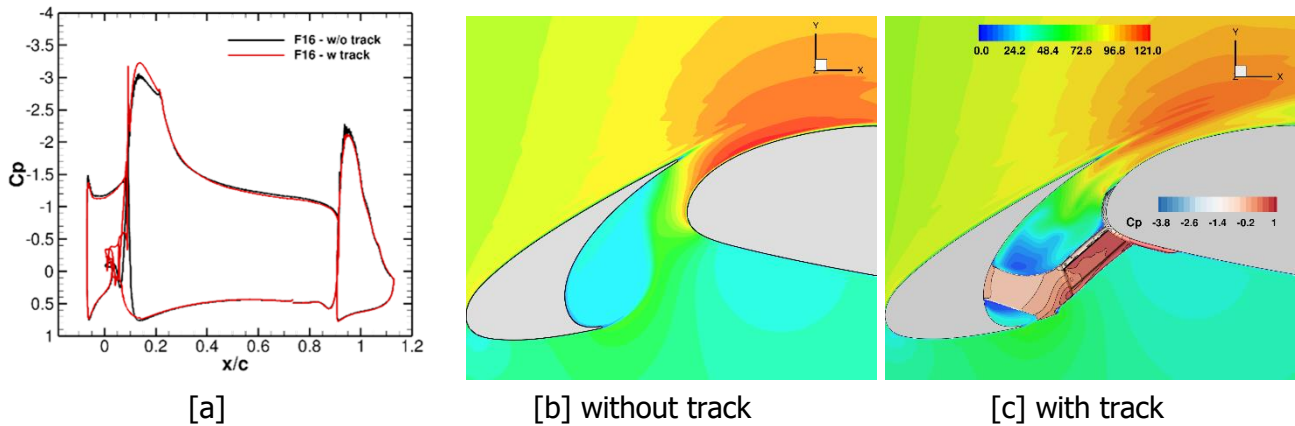


Figure 168: Static pressure coefficient C_p distribution (a) and velocity magnitude contour, m/s without (b) and with (c) track.

Figure 169 (a) shows the F16's sound pressure fluctuation contour with slat-track. A comparison of the 1/3-octave band pressure spectrum between F16 with and without slat-track is drawn in Figure 169 (b). It is clearly visible that there is an increase in absolute noise levels by ~ 5 dB over the entire frequency range when the track is present in the slat cove. The delta difference, averaged over the frequency range shown in Figure 169 (b), between the absolute noise levels of the F16 w/o track and the F16 w track is ΔSPL_{track} 4.93 dB.

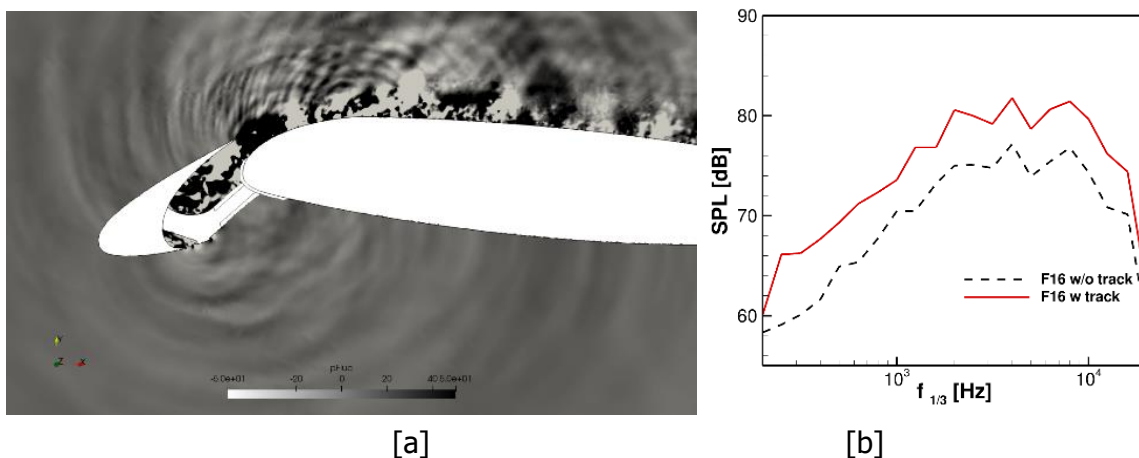


Figure 169: (a) sound pressure fluctuation contour with slat-track. (b) 1/3-octave band pressure spectrum with and without slat-track.

A simulated periodic LES section of 20% c span yielded the resolved pressure spectra shown in Figure 169 (b), which represent an infinite number of slat tracks arranged periodically with a 20% c spacing between them. We corrected the resulting pressure spectra from this periodic LES slice for the AWB span of 0.8 m. Considering the 20% c spacing between the tracks, roughly 12 tracks can fit in the chosen AWB span of 0.8 m. Firstly, we can identify the collective contribution of only those tracks by energetically subtracting the F16 w/o and with slat track spectra. When plotting the SPL for only track contribution, we see that the absolute levels are higher than those for the w/o track case (see Figure 170b).

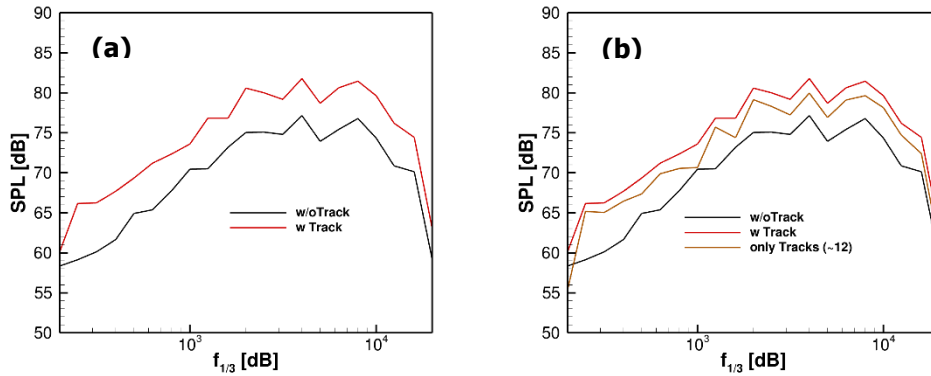


Figure 170: Contribution from tracks with 20% spacing

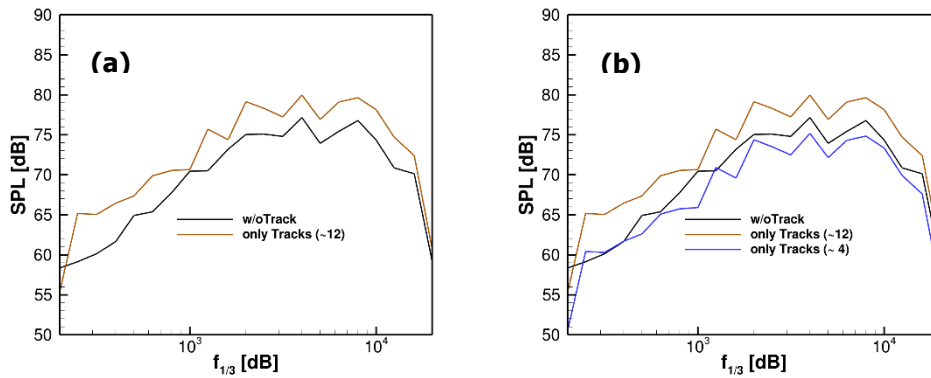


Figure 171: Contribution of tracks from 20% to 3.3*(slat chord length, c_s) spacing

To have a realistic track spacing i.e. $3.3 * c_s$ (~ 4 tracks within the AWB span) the contribution of only 12 tracks can be corrected for the 4 tracks, see Figure 171b, using the following correction:

$$SPL_4 = SPL_{12} + 10 * \log_{10}(4/12)$$

Absolute noise levels for the contribution from only four tracks lie below the F16 w/o track noise levels. Upon energetically adding the contribution of only 4 tracks with the F16 w/o track spectrum, the overall outcome is louder than the w/o track case by ~ 2 dB (absolute levels) over the entire frequency range, see Figure 172 (b). This exercise was carried out to identify how loud the tracks with realistic spacing, i.e., ~ 4 tracks in the AWB span, are and what their overall high-lift noise contribution is. Similar exercise can also be carried out for single track based on the output obtained from the periodic LES slice of a chosen span.

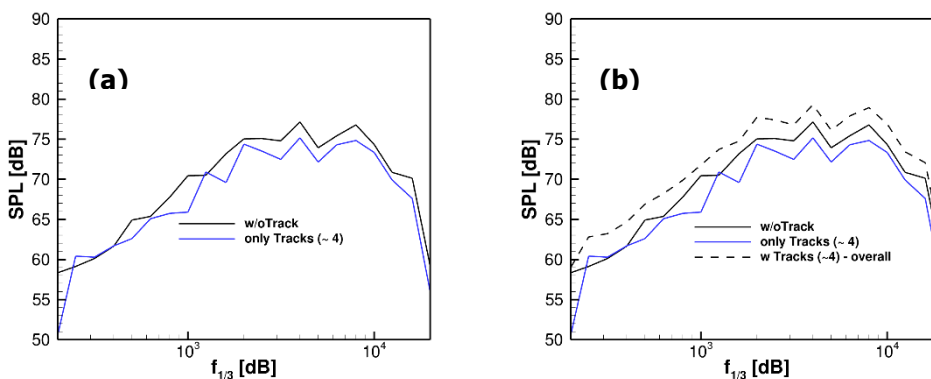


Figure 172: Contribution of tracks with $3.3 * c_s$ spacing

5.5.4 Active noise control

5.5.4.1 Concept

From the previous sub-section, it was clear that the presence of a slat-track in the slat cove increases the overall noise. As an active noise reduction measure, we have investigated a local flow control technique in the form of steadily blowing bleed air from around the track. Figure 173a visually illustrates this concept for a reference 2-D cross-section (y - z plane), which is perpendicular to the track. The idea here is to avoid direct contact between the oncoming cross-flow and the track. The purpose is to create a local stagnation point by steadily blowing air opposite to the oncoming cross-flow. This will cause the oncoming cross-flow to create an air-curtain around the track. Figure 173b illustrates the flow that develops around the track with steady blowing when viewed from behind the y - z plane.

In this work, we have investigated two different blowing strategies: streamwise (x -axis)- and spanwise (z -axis) flow directions. The streamwise concept steadily blows air along the +ve x -axis, which is parallel to the track. The spanwise blowing concept creates a steady flow of air that opposes the oncoming cross-flow along the +ve z -axis. We need to exert extra effort when exploring active noise control strategies to prevent any further flow acceleration in the slat gap. To realize steady air blowing in ProLB, a flow rate boundary condition was used. We chose a flow speed of 60 m/s for steady blowing based on some very preliminary tests in the DLR-AWB open tunnel.

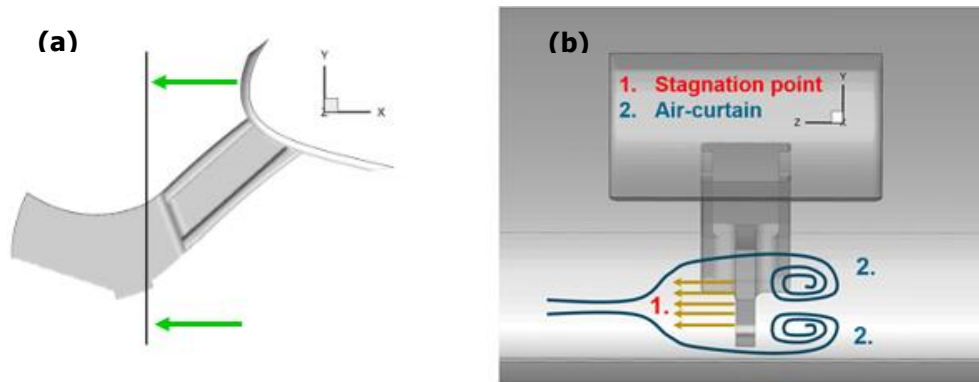


Figure 173: Blowing concept for F16 wing, slat-track.

5.5.4.2 Variants

The first idea of creating an air-curtain was to blow along the streamwise (x -axis) direction and create a stagnation point for the oncoming cross flow in front of the I-shaped track region. This will cause the oncoming flow to either slow down or go around the track, avoiding direct contact with the fast oncoming flow. Figure 174 (a) shows the arrangement of three nozzles protruding from the slat cove and placed alongside the track to create a curtain. The other purpose of such an arrangement was to shield a portion of the track from the oncoming flow.

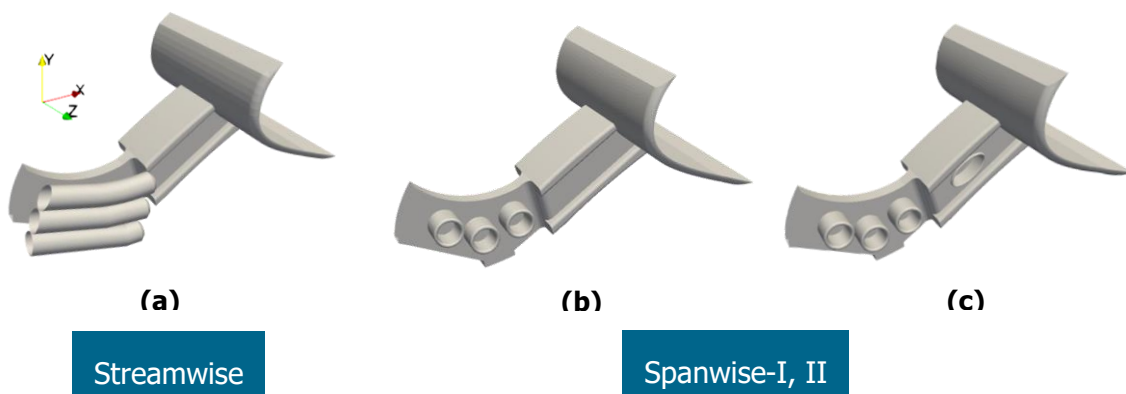


Figure 174: Variants of blowing.

The previous sub-section's conceptualization of the spanwise blowing concept served as the foundation for this one; see Figure 174 (b). The idea was to use a spanwise blowing direction (along +ve z-axis) to create a stagnation point in front of the track and inside the recirculating bubble. Three nozzles were arranged on the track portion, which will primarily face the re-circulating cove flow. Figure 174 (b) shows the spanwise, steady-blowing arrangement. The spanwise blowing-I strategy concentrated on positioning nozzles in the cove flow, yet the I-shaped region found itself fully exposed to the approaching faster cross-flow, as depicted in Figure 174 (b). The interaction of the cross-flow at the junction between the I-shaped region and the plate covering the cut-out on the main element, one of the prominent noise sources [7], could be modified by using local flow control there. Therefore, we positioned an extra nozzle at the I-shaped section to evaluate its efficiency, as illustrated in Figure 174 (c).

From the comparison of the C_p distribution between the F16 w/o and w streamwise blowing, slightly higher suction peak levels were observed on the slat and the main element of F16 with blowing, see Figure 175 (a).

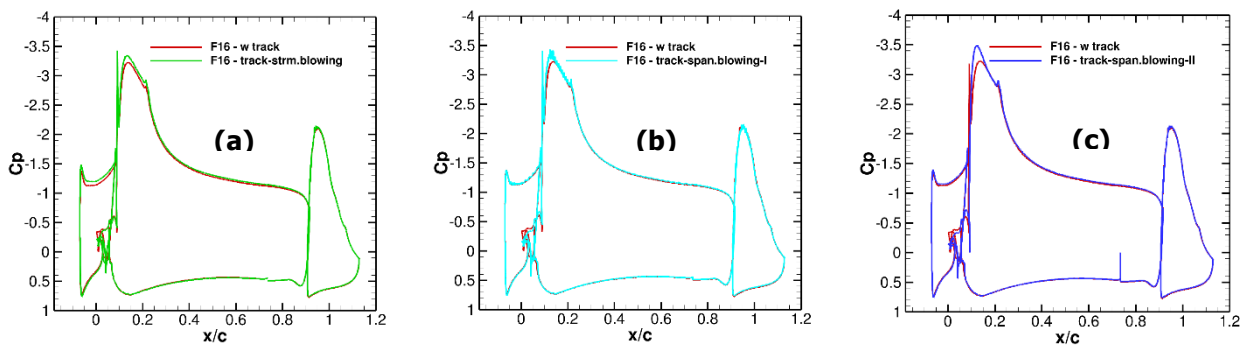


Figure 175: Time-averaged flow results.

Figure 175 (b) illustrates a similar outcome at the main element nose of the F16 in the spanwise blowing-I scenario. When looking at the F16 C_p distribution with and without blowing, you can see that the spanwise blowing-II variant has an even stronger suction peak on the main element nose (see Figure 175 (c)). Figure 176 illustrates the resolved unsteadiness in the complex flow that develops around the F16 wing section with slat-track and spanwise blowing-I.

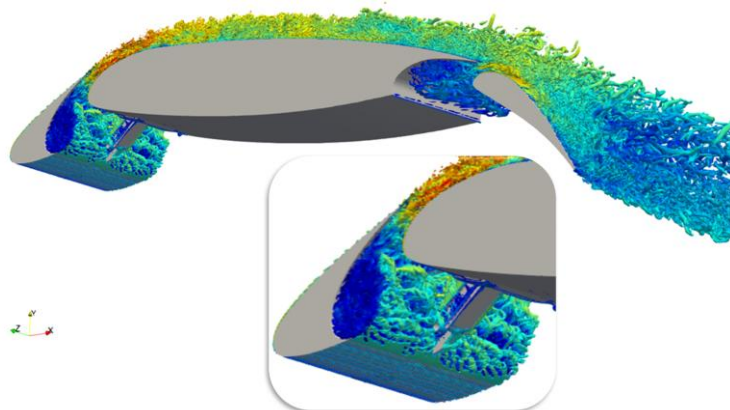


Figure 176: Iso-surfaces of Q-criterion, spanwise blowing-I.

Figure 177 (a) sketches a comparison of the 1/3-octave band pressure spectrum between the F16 without and with streamwise blowing systems. Over some frequencies, we observe subtle gains in terms of reduced noise levels and losses in terms of increased noise levels. The blowing case results in a slight increase in the maximum noise level, specifically at 4 kHz, when compared to the case without blowing.

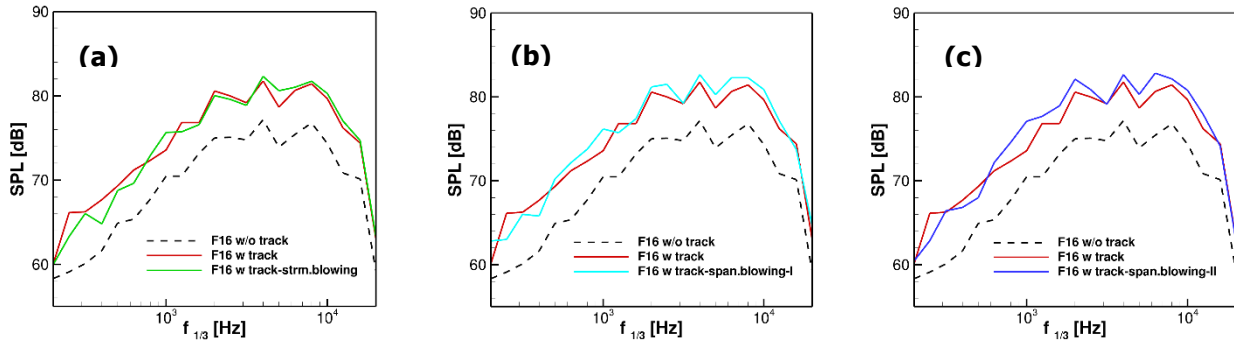


Figure 177: Far-field microphone comparison F16 without and with streamwise blowing, different variants.

Figure 177 (b) depicts the acoustic response of the spanwise blowing-I. The 1/3-octave band pressure spectra of the w/o and w spanwise blowing-I cases are compared. The w spanwise blowing-I case has higher absolute noise levels over a wider range of frequencies. Looking at the 1/3-octave band pressure spectrum plot, there is an increase in the noise levels at several frequencies, i.e., from 0.8 kHz - 11 kHz, along with an increase in the maximum noise level, see Figure 177 (c). One possible explanation could be that the faster moving cross-flow renders the flow from nozzle 4, specifically at the I-shaped portion, ineffective, as it instantly redirects it further downstream.

The delta difference between the absolute noise levels of F16 without track and F16 with different blowing variants, averaged over the frequency range shown in Figure 176, gives $\Delta SPL_{str.B} = 5.37$ dB, $\Delta SPL_{span.BI} = 5.755$ dB, and $\Delta SPL_{span.BII} = 6.05$ dB.

5.5.5 Passive noise control

In the previous section, we discussed attempts to achieve local flow control using steady blowing of air. A complex flow within the slat cove will evolve, given that the flow must circumnavigate the track. The applied variations demonstrated a partial success in reorienting the flow when trying to control it locally. However, the oncoming cross-flow, which carries a significantly higher velocity, pushes the stagnation point away from the nozzles, reducing the effectiveness of the active control measures. To mitigate the increase in overall high-lift noise due to the track's presence, we need to explore alternative options.

Instead of trying to control the flow locally, we will showcase how a passive noise reduction measure fared in terms of reducing the overall high-lift noise when a track is present in the flow. A passive measure was realized in the form of a porous glove around the track. The results presented and discussed here will serve as a proof-of-concept for this type of noise reduction measure. Figure 178 shows different views of the porous glove around the slat track.



Figure 178: Slat track with a porous glove

The computational domain and other numerical settings were kept similar to the cases discussed in the previous sections. The only additional setting required here was the definition of the porous

material which was introduced using the porous boundary condition in ProLB. For this case, a homogenous porous material was realized using the viscous resistance ($R_x = R_y = R_z = 1490 \text{ s}^{-1}$) based on the Darcy constant $k = 10^{-8} \text{ m}^2$. The glove had an equal offset of 2.5 mm from the surface of the slat-track in all directions.

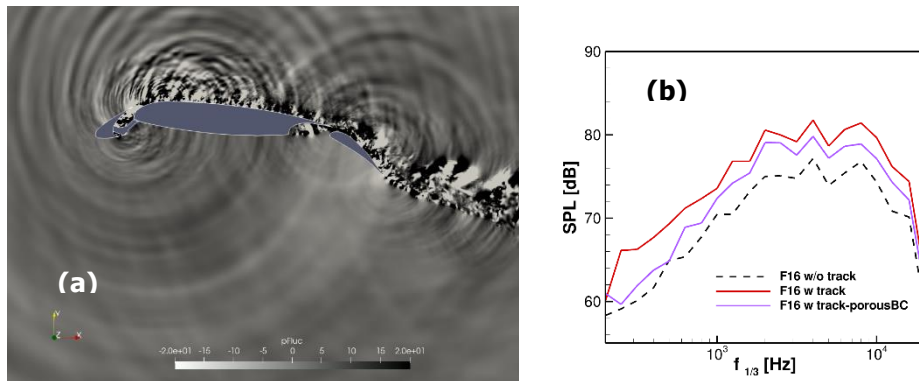


Figure 179: Sound pressure fluctuations, Pa and 1/3-octave spectrum comparison

When the far-field acoustic pressure spectra between the F16 w/o and with porous boundary condition applied is compared, we see a reduction in the absolute noise levels over the entire frequency range from 2 - 6 dB, see Figure 179b. This investigation with porous boundary condition serves as a proof of concept that passive measures, i.e. porous materials, can be an effective means to reduce the slat-track noise. The delta difference between the absolute noise levels of F16 w/o track and F16 w porous boundary condition averaged over the frequency range shown in Figure 179b, gives $\Delta SPL_{poroBC} = 2.85 \text{ dB}$.

5.5.6 Conclusions

The Direct Noise Computation (DNC) of high-lift wing sections with the WM-LES LBM approach was carried out. The complexity of DLR's F16 wing section, starting from the unswept F16, was increased subsequently by adding sweep and a slat-track. A comparison of F16 with and without slat-track revealed a 5 dB increase in the absolute noise level over the entire frequency range. To mitigate this increase in noise, we pursued both an active and a passive noise control measure. Using a steady blowing of bleed air, it was attempted to actively control the flow to go around the track via creating a stagnation point in front of the track.

	Active control			Passive control	
	ΔSPL_{track}	$\Delta SPL_{str.B}$	$\Delta SPL_{span.Bl}$	$\Delta SPL_{span.BlI}$	ΔSPL_{poroBC}
Outcome	4.93 dB	5.37 dB	5.755 dB	6.05 dB	2.85 dB

Table 11: Absolute noise level difference in dB, F16 w/o track vs. other NRT.

In this study, two different steady blowing strategies were investigated: streamwise and spanwise blowing. Locally controlling the flow on one side would cause the flow on the other side to behave differently, as the track will encounter flow from a multitude of directions. This distinct behavior was frequently the result of an increase in TKE in the slat cove (spanwise blowing) and an increase in gap flow velocity (streamwise blowing). From Table 11, it can be deduced that extra caution must be

exercised when using such local flow control measures, as they have the potential to increase the overall high-lift noise (compared against the ΔSPL_{track}).

Key takeaways from the active noise control technique include using it to control the flow around the I-shaped track region, as the cove flow rendered such measures ineffective. Also, the simulations with mass flow boundary conditions in ProLB functioned robustly.

Besides that, we investigated a passive noise reduction measure in the form of a porous glove around the track. The outcome of this type of measure was a reduction in the flow velocity around the track, a reduced TKE in the close vicinity of the track, and also the slat gap. This resulted in an overall reduction of 2–6 dB in absolute noise levels. This result serves as a proof of concept that porous materials are an effective choice to reduce the noise associated with the track.

Wrapping a thick porous layer around the slat track is technically impossible because it would obstruct the slats from retracting. This study demonstrates the effective use of porous materials in reducing noise on the slat track. The development of porous slat-track NRTs with higher technological readiness levels is a promising subject for upstream research activities.

The results of the investigation carried out under subtask 4.2.4 have been published as a conference paper; see Soni et al. [24].

5.5.7 Outlook

In our future work, we will explore the effective application of porous materials at the slat-track to reduce additional noise. Additionally, we will compare the experimental INVENTOR slat-track results with ProLB, utilizing directly resolved acoustics and extrapolating using FWH. These results will also serve as the basis for our work on the EU project FALCON.

5.5.8 Acknowledgements

The authors acknowledge the computational resources provided by the CARA cluster of the German Aerospace Center. The authors would also like to take this opportunity to acknowledge the CS GROUP for providing the ProLB 2.6.x licenses, and the ProLB consortium, in particular Alois Sengissen from Airbus, for their fruitful support of the high-lift device simulation activities.

5.6 Cross comparisons of computed and measured noise spectra

5.6.1 Introduction

In this last paragraph of section 5 devoted to the slat track flow and noise numerical simulations achieved by DAV, ONERA, NLR and DLR, we tentatively compare numerical simulations of the same slat track configurations achieved by different partners. Table 12 summarize the (relatively sparse) computational matrix, clearly showing (in bold rectangles) that the opportunities for such cross comparisons are limited.

	No ST	ST#1	ST#2	ST#11
DAV	x	x	x	
ONERA	x		x	
NLR	x			x
DLR	(x)			(x)

Table 12: Slat track noise computations: computational matrix and possible cross-comparisons (bold rectangles)

Actually, only the baseline or “no slat track” case was carried out by 3 partners (DAV, ONERA and NLR), whereas only one slat track, namely the ST#2, was computed by more than one partner, actually DAV and ONERA.

According to the DoW, DLR's focus was on the evaluation of the active blowing concept for noise reduction only and a participation into the cross-comparison exercise was not foreseen, therefore (X) refers to the baseline "no track" case and one case with a slat track (from the DLR's slat track design family), but evaluated from a simplified setup such that a direct cross-comparison with the experimental results is not possible. However, additional simulations to support the direct cross-comparison are certainly useful and will be provided by some supplementary activity for the cross-comparison publication yet to come.

Moreover, the chosen slat track design (Figure 162 (c)) apparently slightly differ from the design of ST#11 (Figure 145) computed by NLR, so a direct comparison of slat track noise prediction by DLR and NLR might be risky.

5.6.2 Cross-comparisons of computations of the baseline case (no slat track)

Figure 180 shows cross comparison of noise spectra (left side) derived from the integration of DAMAS noise maps (right side, example at 8 kHz) in the slat track area (yellow rectangle), predicted by NLR, ONERA and DAv, and measured in F2.

First point is that all predictions underestimate the measurement. One obvious reason is that the integration area (yellow rectangle) is typically larger than the considered computational domains, meaning that the experimental result might integrate more sources than the numerical predictions.

However, NLR's spectrum is the closest to the experimental spectrum above 6 kHz. In the same high frequency region, ONERA and DAv predictions are very close.

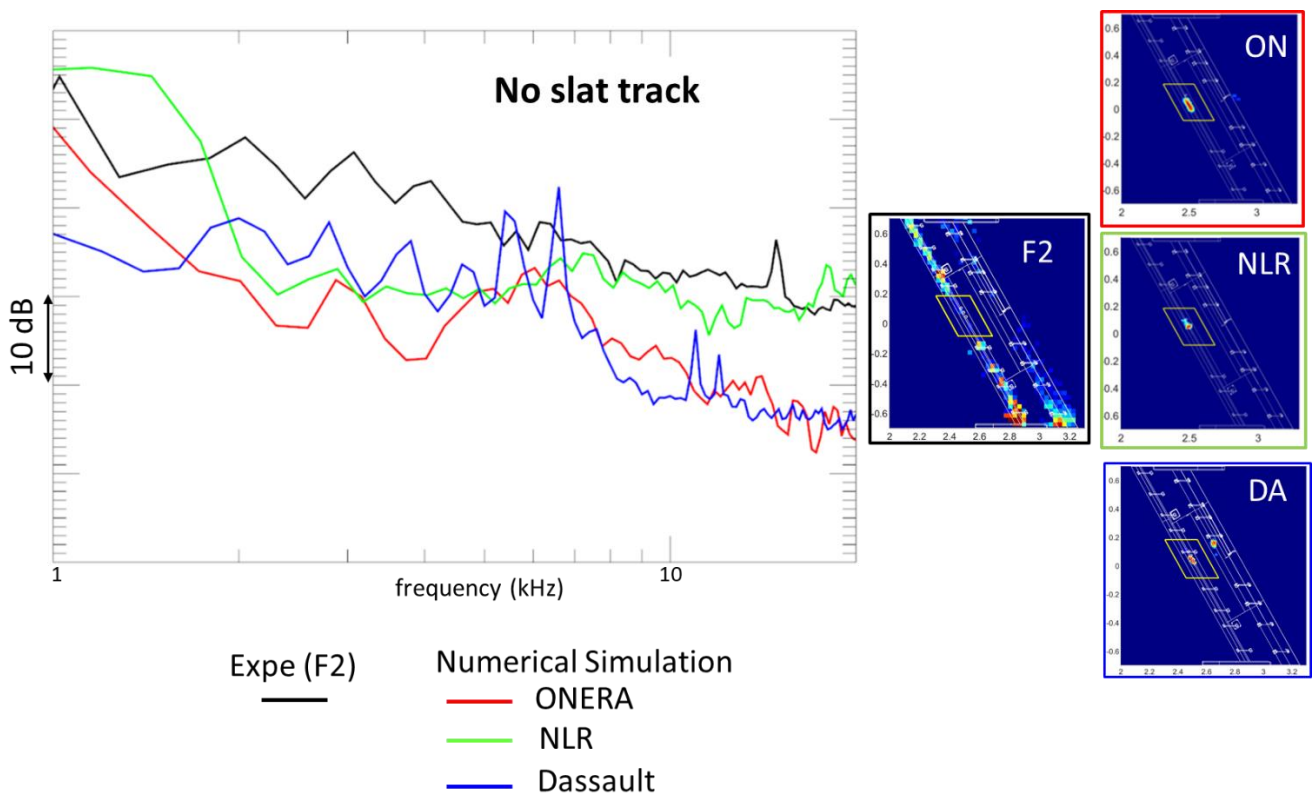


Figure 180: Cross comparison of noise spectra without slat track (left) derived from the integration of DAMAS noise maps (right, 8 kHz) in the slat track area (yellow rectangle), predicted by NLR, ONERA and DAv, and measured in F2.

5.6.3 Cross-comparisons of computations with the slat track ST#2

Figure 181 shows cross comparison of noise spectra without slat track (solid lines, already displayed on Figure 180) and with the slat track ST#2 (dashed lines). The spectra are derived from the

integration of DAMAS noise maps (right, measurement at 8 kHz) in the slat track area (yellow rectangle), and are based on ONERA's and DAV's simulation data and on the measurements in F2. It is interesting to look at the dashed line corresponding to predictions/measurement with the slat track ST#2. Just like in the baseline case, the predictions by ONERA significantly underestimate the experiment, for the same reason explained in the last section. DAV's simulation results of the ST#2 track are in pretty good agreement with the measurements above 4 kHz.

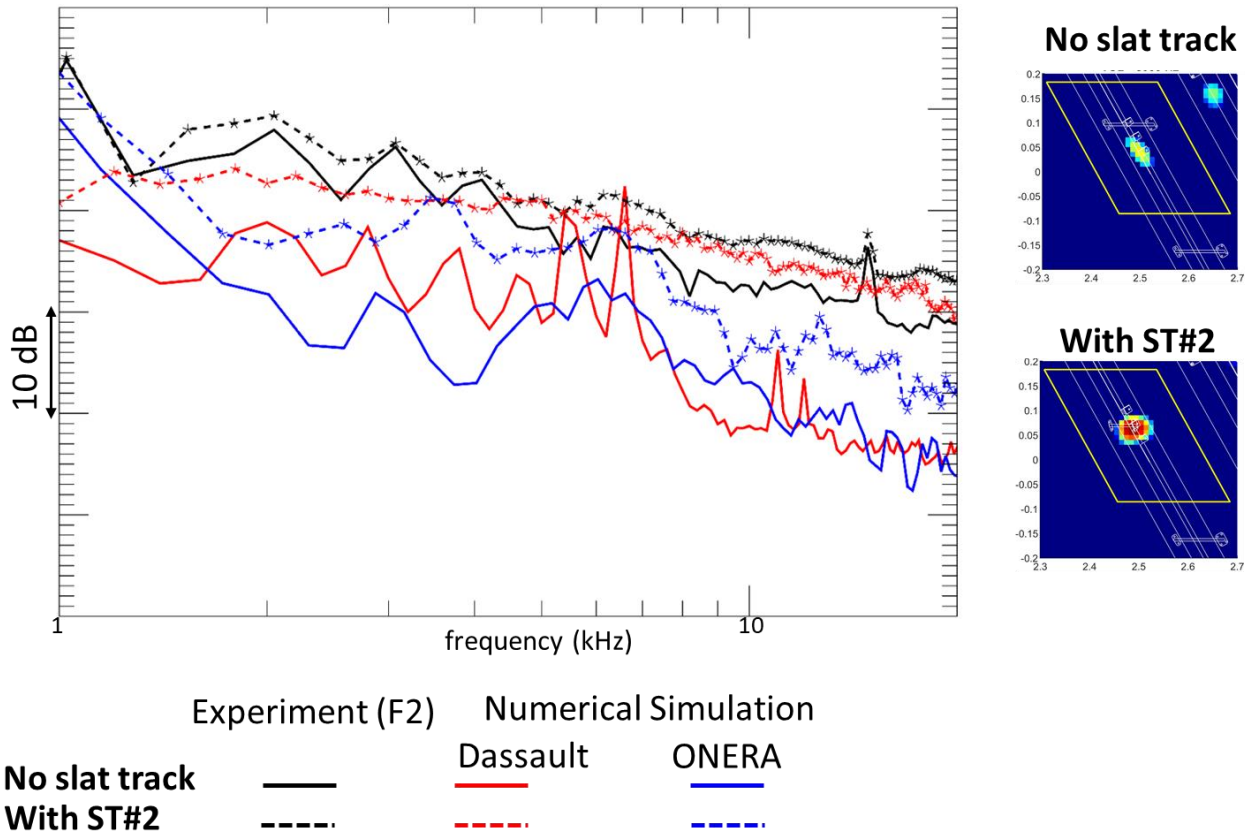


Figure 181: Cross comparison of noise spectra without slat track and with slat track ST#2 (left) derived from the integration of DAMAS noise maps (right, measurement at 8 kHz) in the slat track area (yellow rectangle), predicted by ONERA and DAV, and measured in F2.

6 Low noise slats numerical simulations by RWTH

6.1 Context

This section reports on the Subtask ST4.1.6, part of Task T4.1 "Preliminary assessment of slat noise reduction by innovative materials". Subtask ST4.1.6 was devoted to numerical simulations, achieved by RWTH, of the slat porous inserts installed on the flapless (VALIANT-like) configuration of the F16 model with 0° sweep, as it was tested in the acoustic windtunnel of the University of Bristol. These tests are summarized in the Section 3.4.2 of the present report. Note that these computations should have been reported in the deliverable D4.1 "Parametric study on slat noise reduction and selection of best NRTs based on porous treatments".

6.2 Objectives

The DLR's three-element F16 high lift wing model with detracted slat and Fowler flap has been the subject of numerous slat noise investigations. Within the LEISA2 project an exhaustive experimental database has been collected by ONERA and DLR, which was published as part of the BANC workshops in the category of high lift wing noise. Within the INVENTOR project, an unswept two-element wing configuration without a flap, derived from the F16 model is investigated. The slat and the front part of the F16 cross section were left unchanged, and only the trailing edge region is redesigned by ONERA, applying a constrained optimization based on RANS simulations (see the airfoil shape drawn with a red line on Figure 12). In doing so, the angle-of-attack and the shape of the trailing edge region were varied to achieve a similar flow field in the slat cove region compared to the original F16 wing at the reference angle of attack of 6.15° . Doing so, the total lift of the airfoil was reduced by a factor of about 3, with a significant reduction of the deflection of the open wind tunnel jet.

6.3 Incidence adjustment

To identify a suitable angle of attack for the noise mitigation simulations conducted by LES for free stream conditions, simulations were performed for three angles of attack using a 2D inhouse RANS solver using Menter's SST turbulence model and compared to the wind tunnel pressure distributions. The simulations were conducted for a Mach number of $M=0.109$ and a Reynolds number of $Re=760,000$, which match the conditions in the experiment with the full 3-element F16 model in the Aeroacoustic Windtunnel (AWB) at DLR Braunschweig. The best fit was identified for an angle of attack of 18° , which was then used for the LES, conducted for the solid slat and the slat with a porous insert.

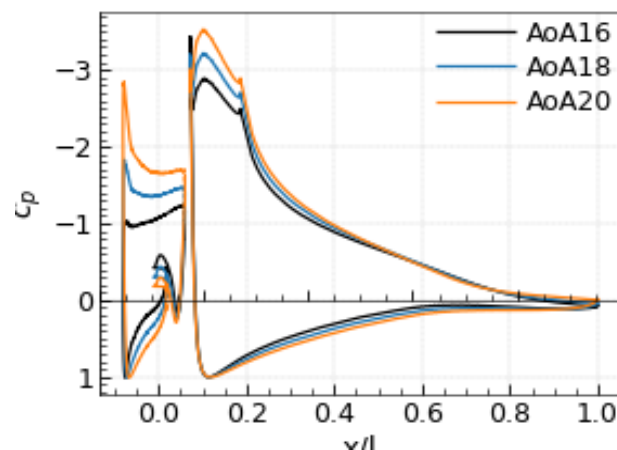


Figure 182: Non-dimensional pressure distribution c_p determined by simulations based on a RANS turbulence model along the chordwise direction x/L for three angles of attack AoA, i.e., 16° , 18° , and 20° .

6.4 Flow field results

Large eddy simulations for the flow field were conducted for an angle of attack of 18° , a Mach number of $M=0.109$ and a Reynolds number of $Re=760,000$, which are chosen according to the experiments in the acoustic wind tunnel of University of Bristol at a free stream velocity of 37 m/s. Two setups were used, the first with a conventional solid slat and the second with a porous insert. A schematic of the slat with the porous insert is shown in Figure 183. The porous material used was modelled as the diamond structured porous material designed by TU Delft with a characteristic unit length of $d_c=4.5$ mm. The porous material coefficients were determined with calibration simulations for a grazing flow setup experimentally investigated by VKI.

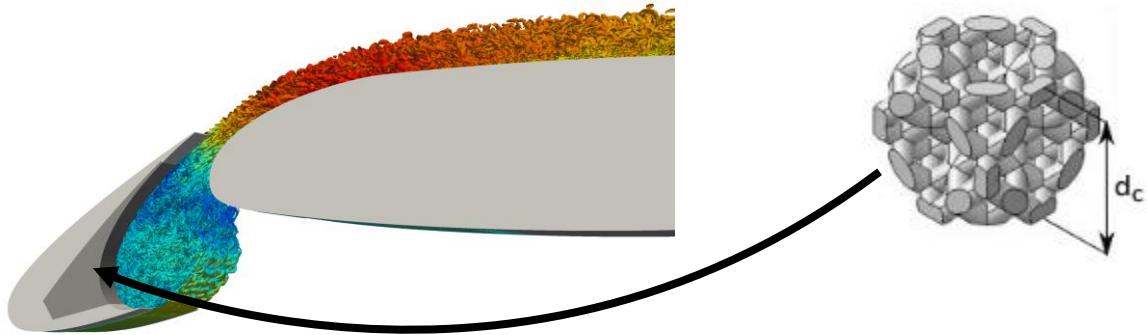


Figure 183: Zoom of the front part of the 2-element wing configuration, showing the porous insert in the slat and a visualization of the turbulent vortex structures in the slat cove region using the Q-criterion. The porous material is modelled as the diamond structure from TU Delft with a cell size of $d_c=4.5$ mm.

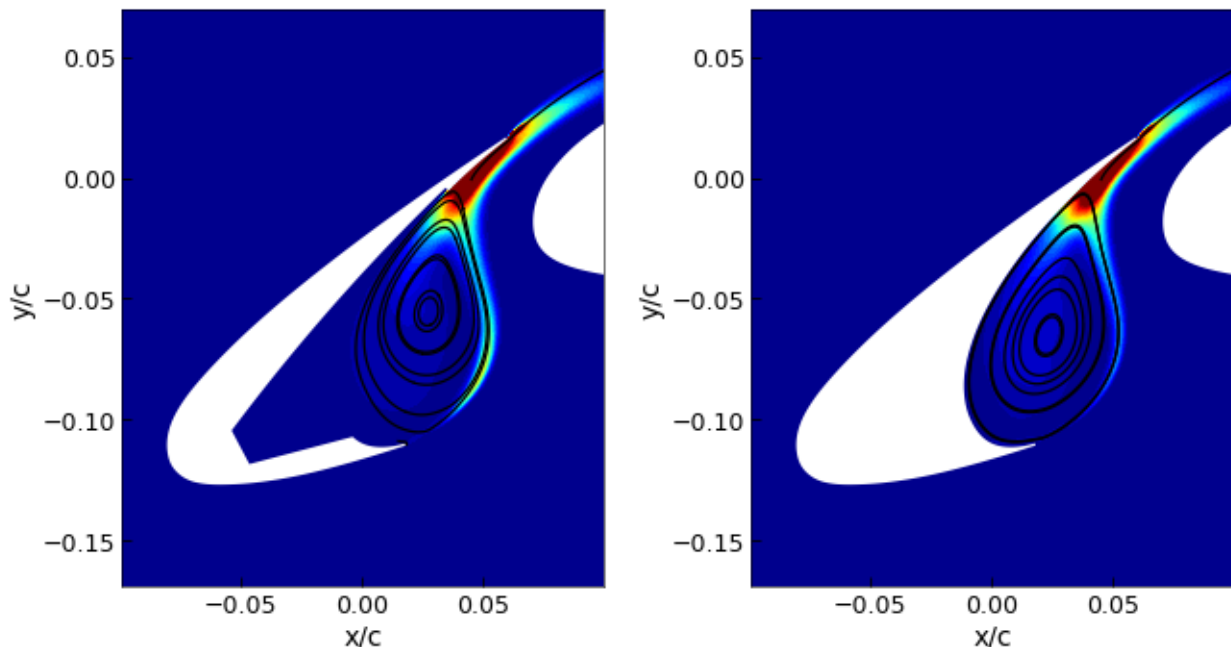


Figure 184: Turbulent kinetic energy contours for the wing configuration with the solid slat (left) and the slat with the porous insert (right). Streamlines are plotted in black.

The domain size was chosen to be $7C$ upstream, $9C$ downstream, $8C$ above and below the wing, where C is the chord length of the 2-element wing configuration. In the spanwise direction, an extent of $0.7C$ was used. Periodic boundary conditions were used in the spanwise direction, while non-reflecting boundary conditions combined with sponge layers were applied on all other domain

boundaries. A computational Cartesian mesh with 697 million cells was generated, which is refined around the wing such that a non-dimensional spatial step based on inner coordinates of $Dy^+ \sim 5$ is obtained at the wing surface. For the porous insert in the slat an additional 31 million cells is used. A finite-volume solver at second-order accuracy was used to solve the Navier-Stokes equations, where the MILES approach is used for conducting wall resolved LES. The flow field simulations are run for about 5 convective time units based on the chord length and the free stream velocity.

In Figure 184, turbulent kinetic energy contours are shown for the solid slat and the slat with the porous insert. The streamlines indicated a different slat vortex center and a different shape, showing that the porous insert has a non-negligible effect on the mean flow field. The spectra of the velocity fluctuations are shown in Figure 185 for various locations in the slat cove region. It can be seen that the major difference is obtained close to the cusp of the slat. The spectra for the solid slat show about 10 dB lower velocity fluctuations for frequencies higher than 103 Hz and the peak at around 104 Hz for the streamwise normal fluctuations is less broadband than for the solid slat. In all other positions, the velocity fluctuations are almost identical for frequencies above approximately 2000 Hz. For lower frequencies, the slat with the porous insert shows slightly lower amplitudes, where the difference in amplitudes is more pronounced closer to the cusp region.

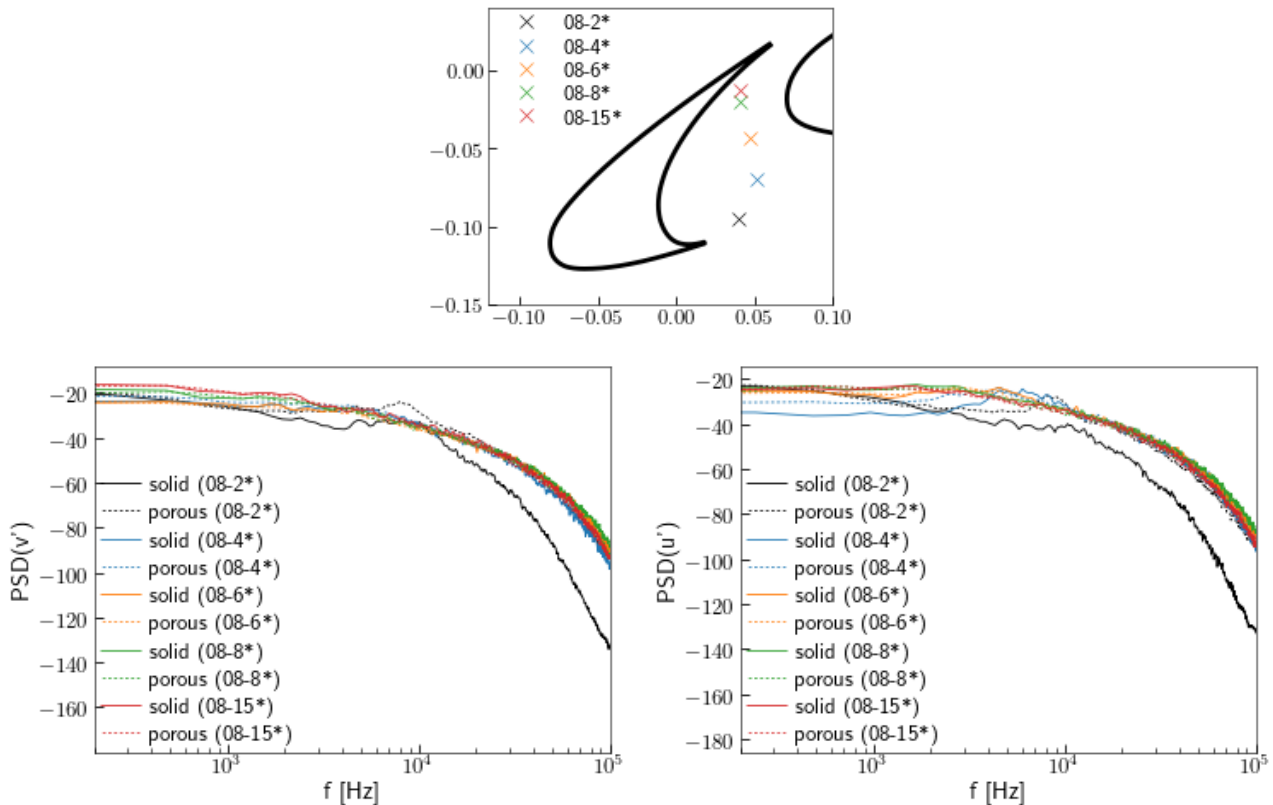


Figure 185: Velocity spectra in slat shear layer at various position in the slat cove region approximately following the reattachment streamline. Power spectral density of the velocity fluctuations at the positions indicated in the top figure. Bottom left: fluctuations of the velocity component in the streamwise direction u' , Bottom right: fluctuations of the velocity component normal to the streamwise direction v' .

6.5 Acoustic Field Results

After a fully developed turbulent flow field around the wing configuration is obtained, a coupled CFD/CAA simulation is conducted. A computational Cartesian mesh with the same partition level as for the flow field mesh is generated, which yields 335 million degrees of freedom, when a third-order polynomial degree is used for the discontinuous Galerkin solver for the acoustic perturbation equations. The CAA is run in parallel to the CFD simulation and uses the fluctuating Lamb vector as an acoustic source, determined at each time step from the LES. In Figure 186 contours of the acoustic

pressure field are visualized with the turbulent vortex structures around the 2-element wing configuration.

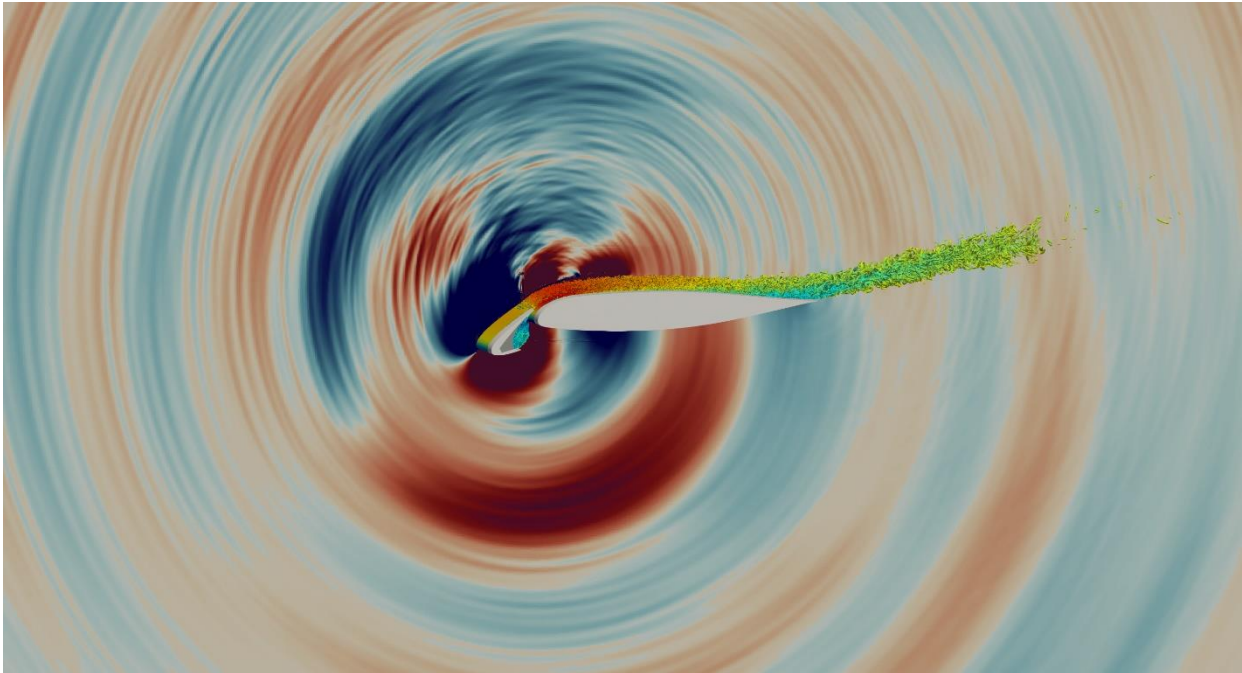


Figure 186: Acoustic pressure contours and turbulent vortex structures for the wing configuration and the slat with the porous insert.

After a fully developed acoustic field is obtained, spectra of the acoustic pressure field are determined at a distance of 1 m, i.e. $3.3C$ below the slat trailing edge. The octave and narrow band sound pressure levels are shown in Figure 187. As was already visible in the velocity spectra, the high frequency amplitudes are almost identical for both configurations. The porous insert, however, leads to a higher peak between 1000 Hz and 2000 Hz. At lower frequencies the porous insert leads to a slightly reduced sound pressure level.

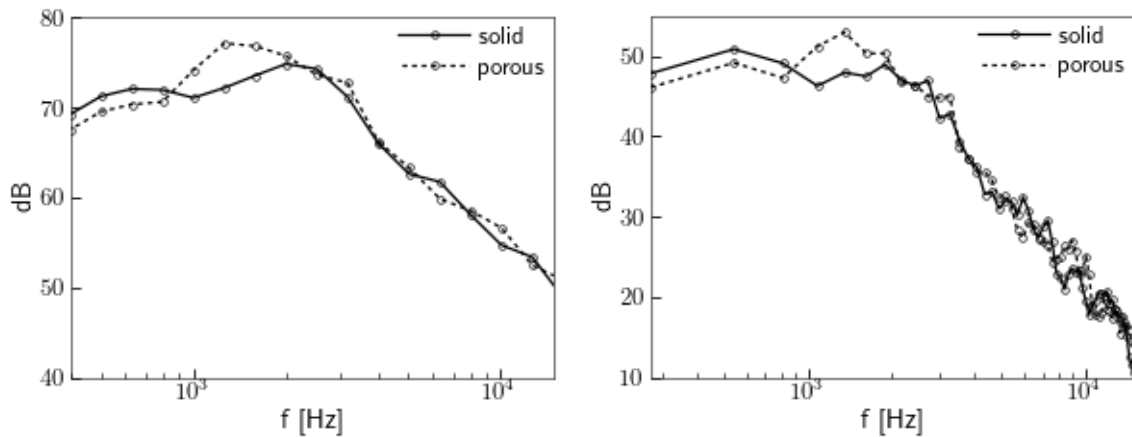


Figure 187: Far-field sound pressure level (SPL) in dB are shown at a distance of $3.3C$ below the slat trailing edge for octave band (left) and narrow band (right) filtering for the solid slat (solid) and the slat with the porous insert (porous).

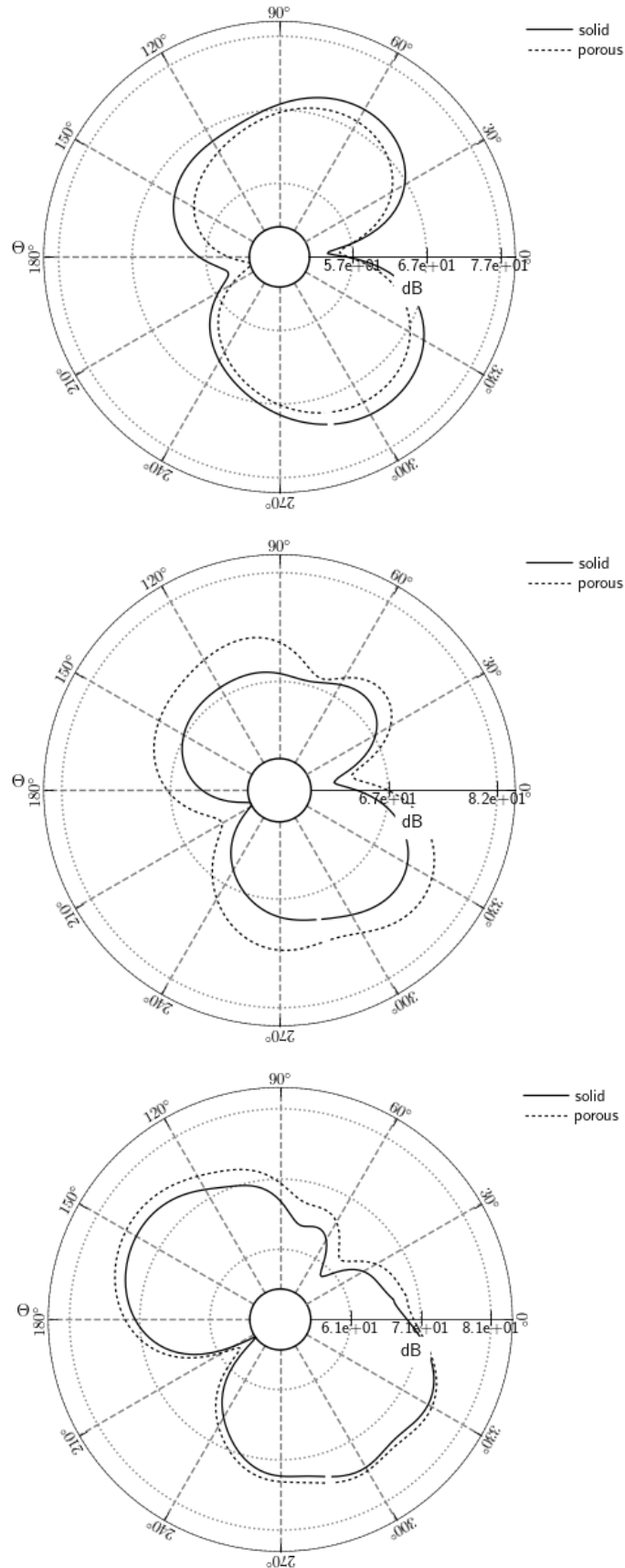


Figure 188: Directivity plots for a circle of 0.33 c diameter around the slat trailing edge for the OASPL in octave bands for center frequencies 500 Hz (top), 1000 Hz (middle), and 2000 Hz (bottom) for the wing configuration with the solid slat and the slat with the porous insert.

The directivity plots of the overall sound pressure levels confirm the results visible in the SPL spectra. Directivity plots are shown in Figure 188 for three different center frequencies of a low frequency of 500 Hz, a frequency where a higher peak is visible in the spectra of the SPL and a higher frequency of 2000 Hz. At the low frequencies of 500 Hz a lower OASPL can be observed in all directions for the slat with the porous insert. Due to the higher tonal peak, the opposite is visible for a center frequency of 1000 Hz, where the porous insert generates larger amplitudes. For higher frequencies the difference becomes much less pronounced.

6.6 Summary

The simulation results show that the porous insert in the slat has a non-negligible effect on the flow and the acoustic field. The present results with a specific porous material, however, do not show the desired noise mitigation. Although a slight noise reduction is obtained at lower frequencies, the higher broadband tonal component at around 1000 Hz is more pronounced, while no noise reduction is achieved at higher frequencies. It is an open question, whether an optimization of the geometry of the insert or of the properties of the porous material can improve the noise mitigation.

7 Acknowledgments



The EU INVENTOR (Innovative Design of Installed Airframe Components For Aircraft Noise Reduction) project receives funding from the European Union's Horizon 2020 Research and Innovation Programme under Grant Agreement No 860538. INVENTOR is a collaborative effort between ONERA (coordinator), Airbus Operations, Dassault Aviation, Safran Landing Systems, DLR, CERFACS, University of Southampton, TC Dublin, NLR, RWTH Aachen, Chalmers University, Von Karman Institute, University of Bristol, TU Delft, Upstream CFD and ERDYN Consultants.

8 References

- [1] Manoha, E., Pott-Pollenske, M., "*LEISA2: an experimental database for the validation of numerical predictions of slat unsteady flow and noise*", AIAA Aviation Forum, 22-26 June 2015, Dallas, TX, 21st AIAA/CEAS Aeroacoustics Conference. doi: 10.2514/6.2015-3137
- [2] Manoha, E., Davy, R., Pott-Pollenske, M., and Barré, S., "*SWAHILI: an experimental aerodynamic and acoustic database of a 2D high lift wing with sweep angle and flap side edge*", 2018 AIAA/CEAS Aeroacoustics Conference, 25-29 June 2018, Atlanta, Georgia. <https://doi.org/10.2514/6.2018-3459>
- [3] M. Jansen, M. Pott-Pollenske, S. Fauqueux, and E. Manoha, "*Interdependencies of Aerodynamic Test Conditions and High Lift System Noise Generation and Measurement*", AIAA AVIATION 2023 Forum, 12-16 June 2023, San Diego, CA. <https://doi.org/10.2514/6.2023-3497>
- [4] Hasan Kamliya Jawahar, Mahdi Azarpeyvand, Christophe Schram, Daniele Ragni, Alejandro Rubio Carpio, Gareth Bennett, Michael Pott-Pollenske, Matthias Meinke, Marc Terracol, Vincent Fleury, "*Report On Specifications For Experimental (Aawt/Uob) And Numerical Studies On Porous Slat Noise In Wp4*" – INVENTOR Deliverable D2.5, Public, July 2021
- [5] Hasan Kamliya Jawahar, Mahdi Azarpeyvand, Christophe Schram, Matthias Meinke, Daniele Ragni, Gareth Bennet, Michael Pott-Pollenske, Eric Manoha, Vincent Fleury, "*Parametric Study On Slat Noise Reduction And Selection Of Best NRTs Based On Porous Treatments*", – INVENTOR Deliverable D 4.1, Public, December 2022
- [6] Evelien van Bokhorst, Marc Terracol, Vincent Fleury, Johan Kok, Michael Pott-Pollenske, Marthijn Tuinstra, Eric Manoha, "*Report On Specifications For Preliminary Experimental (AWT/NLR) and Numerical Studies On Slat Track Noise In WP4*", – INVENTOR Deliverable D 2.3, Confidential, August 2021
- [7] Evelien van Bokhorst, Johan Kok, Marthijn Tuinstra, "*Parametric Study On Slat Track Noise Generation And Mitigation And Selection Of Best Low-Noise Slat Track Designs*", – INVENTOR Deliverable D 4.2, Public, October 2022
- [8] T. Brooks, W. H., "*A Deconvolution Approach for the Mapping of Acoustic Sources (DAMAS) Determined from Phased Microphone Array*", 10th AIAA/CEAS Aeroacoustics Conference, Manchester, Great Britain, n. 1, 10-12 May 2004. ISSN AIAA-2004-2954
- [9] T. Brooks, W. H. "*Extension of DAMAS Phased Array Processing for Spatial Coherence Determination (DAMAS-C)*", 12th AIAA/CEAS Aeroacoustics Conference, Cambridge, Massachusetts, n. 2, 8-10 May 2006. ISSN AIAA-2006-2654

-
- [10] Fleury, V., Coste, L., Davy, R., Mignosi, A., Cariou, C., and Prosper, J.-M., "Optimization of Microphone Array Wall-Mountings in Closed-Section Wind Tunnels," AIAA Journal, Vol. 50, No. 11, November 2012. doi:10.2514/1.J051336
- [11] Fleury, V., and Davy, R., "Beamforming-Based Noise Level Measurements in Hard-Wall Closed-Section Wind Tunnels," AIAA Paper 2012-2226, June 2012. doi:10.2514/6.2012.2226
- [12] Guo, Y., "Slat noise modeling and prediction", Journal of Sound and Vibration, Volume 331, Issue 15, 16 July 2012, Pages 3567-3586
- [13] Deck, S., & Renard, N. (2020). "Towards an enhanced protection of attached boundary layers in hybrid RANS/LES methods". Journal of Computational Physics, 400(108970).
- [14] Mary, I., & Sagaut, P. (2002). "Large eddy simulation of flow around an airfoil near stall". AIAA journal, 40(6), 1139-1145.
- [15] Dacles-Mariani, J., Zilliac, G. G., Chow, J. S., & Bradshaw, P. (1995). "Numerical/Experimental Study of a Wingtip Vortex in the Near Field". AIAA Journal, 33(9), 1561-1568.
- [16] Kok, J. C., 2017. "A Stochastic Backscatter Model for Grey-Area Mitigation in Detached Eddy Simulations". Flow, Turbulence and Combustion, Volume 99, pp. 119-150.
- [17] Kok, J. C., 2009. "A high-order low-dispersion symmetry-preserving finite-volume method for compressible flow on curvilinear grids". Journal of Computational Physics, Volume 228, pp. 6811-6832.
- [18] van Bokhorst, E., Kok, J. C. & Tuinstra, M., 2022. "Experimental study on slat track noise in the AWT at NLR", INVENTOR Deliverable D4.2
- [19] ProLB, www.prolb.com, 2024
- [20] Jacob, J., Malaspinas, O., and Sagaut, P., "A new hybrid recursive regularised Bhatnagar–Gross–Krook collision model for Lattice Boltzmann method-based large eddy simulation," Journal of Turbulence, Vol. 19, Nos. 11-12, 2018, pp. 1051–1076. <https://doi.org/10.1080/14685248.2018.1540879>
- [21] Leveque, E., Touil, H., Malik, S., Ricot, D., and Sengissen, A., "Wall-modeled large-eddy simulation of the flow past a rod-airfoil tandem by the Lattice Boltzmann method," International Journal of Numerical Methods for Heat and Fluid Flow, Vol. 28, No. 5, 2018, pp. 1096–1116. <https://doi.org/10.1108/HFF-06-2017-0258>
- [22] Soni, M., Ewert, R., Delfs, J., and Masilamani, K., "Towards Wall-Modeled LES with Lattice Boltzmann Method for Aeroacoustics: Application and Understanding," 2022. <https://doi.org/10.2514/6.2022-2918>
- [23] Soni, M., Ewert, R., Dierke, J., and Delfs, J., "Evaluation of the Noise Reduction Potential of a Krueger Flap High-Lift device via the Lattice Boltzmann Method," 2023. <https://doi.org/10.2514/6.2023-4477>
- [24] Soni, M., Ewert, R., Pott-Pollenske, M., and Delfs, J., "LBM-based Direct Noise Computation of a Swept High-Lift Wing Section with Slat-Track and Active Noise Control," AIAA 2024-3060. 30th AIAA/CEAS Aeroacoustics Conference (2024). June 2024.